Dissertation zur Erlangung des Doktorgrades

der Fakultät für Chemie und Pharmazie

der Ludwig-Maximilians-Universität München

Ammonothermal Synthesis of Functional Ternary and Multinary Nitrides

Jonas Häusler

aus

Ingolstadt, Deutschland

2018

Erklärung

Diese Dissertation wurde im Sinne von § 7 der Promotionsordnung vom 28. November 2011 von Herrn Prof. Dr. Wolfgang Schnick betreut.

Eidesstattliche Versicherung

Diese Dissertation wurde eigenständig und ohne unerlaubte Hilfe erarbeitet.

München, den 24.04.2018

.....

(Jonas Häusler)

Dissertation eingereicht am	01.03.2018
1. Gutachter	Prof. Dr. W. Schnick
2. Gutachter	Prof. Dr. R. Niewa
Mündliche Prüfung am	17.04.2018

Acknowledgements

Ich möchte mich herzlich bei Herrn Prof. Dr. Schnick für die Möglichkeit bedanken, meine Dissertation in seinem Arbeitskreis anfertigen zu können. Die hervorragenden Arbeitsbedingungen und die Freiheiten bei der Umsetzung neuer Ideen waren perfekte Voraussetzungen für die eigenständige Gestaltung meiner Promotion. Die Bearbeitung eines neuen Themenbereichs in der Arbeitsgruppe stellte außerdem eine besonders spannende und zugleich abwechslungsreiche Herausforderung dar. Ich möchte mich darüber hinaus für die zahlreichen positiven Anregungen und Gespräche bedanken und für die vielen Gelegenheiten, an Fachtagungen sowie an der ersten Summerschool für ammonothermale Kristallzucht in Erlangen und Santa Barbara teilnehmen zu können.

Ganz besonderer Dank gilt zudem Herrn Prof. Dr. Rainer Niewa für Übernahme des Koreferats meiner Dissertation sowie für die tolle Zusammenarbeit in unserer Forschergruppe und die große Hilfsbereitschaft bei jeglichen Diskussionen und Fragestellungen.

Herrn Prof. Dr. Wolfgang Beck, Herrn Prof. Dr. Hans-Christian Böttcher, Herrn Prof. Dr. Konstantin Karaghiosoff und Herrn Prof. Dr. Joost Wintterlin danke ich herzlich für ihre Bereitschaft, als Teil der Prüfungskommission meiner Doktorarbeit zur Verfügung zu stehen.

Vielen Dank an meine Laborkollegen Peter Wagatha, Mathias Mallmann, Niklas Cordes, Philipp Strobel, Kerstin Gottschling, Claudia Lermer und an meine Schreibstubenkollegen Eva Bertschler und Otto Zeman für die tolle Zeit und vielen spaßigen Abende. Danke auch an Christian Maak, Lukas Neudert, Lucien Eisenburger, Robin Niklaus und Eugenia Elzer, an Fabian Kessler und Jonathan Sappl, an Philipp Pust, Sebastian Schmiechen und Nicole Braml und natürlich an alle anderen Mitglieder des Arbeitskreises für die schöne Zeit und die vielen lustigen Schafkopf-, Film-, und Pokerrunden.

Ich möchte mich außerdem bei den Mitgliedern der Ammonothermal-Subgroup, Mathias Mallmann und Niklas Cordes, für die gute Zusammenarbeit in den letzten Jahren bedanken. Ebenfalls danke ich Philipp Pust und Sebastian Schmiechen für die Unterstützung und Hilfestellungen mit den Hochdruckautoklaven.

Darüber hinaus bedanke ich mich bei allen weiteren Beteiligten der DFG-Forschergruppe Ammono-FOR. Ohne die zahlreichen Kooperationen mit den Projektpartnern wäre diese Arbeit nicht möglich gewesen. Ich möchte mich dabei besonders bei Anna Kimmel, Thomas Steigerwald und Benjamin Hertweck für die große Hilfsbereitschaft bei Problemen jeglicher Art und die hervorragende Zusammenarbeit sowie bei Saskia Schimmel für die tolle Kooperation und die Röntgenmessungen bedanken. Herzlichen Dank auch an Prof. Rainer Niewa, Prof. Peter Wellmann und Prof. Eberhard Schlücker für die hervorragenden Anregungen und hilfreichen Gespräche bei unseren Forschergruppentreffen.

Ich bedanke mich natürlich auch bei Lukas Neudert, Lucien Eisenburger, Robin Niklaus, Prof. Ján Minár und Prof. Oliver Oeckler für die tolle Zusammenarbeit, aus der einige schöne Publikationen hervorgingen.

Vielen Dank auch an meine Praktikanten Stefan Strangmüller, Andreas Baumann, Gabriel Kiefl, Mathias Mallmann und David Schmidl, die alle einen hervorragenden Beitrag zu meiner Arbeit geleistet haben.

Großer Dank gilt auch Wolfgang Wünschheim, Thomas Miller und Olga Lorenz für die Hilfe bei allen technischen und organisatorischen Fragen. Durch euch war es möglich, sich ganz auf die eigene Forschung zu konzentrieren. Außerdem bedanke ich mich bei Christian Minke für die unzähligen REM-Messungen.

Darüber hinaus möchte ich mich herzlich bei den Organisatoren der Summerschool in Erlangen und Santa Barbara, Anna Kimmel, Siddha Pimputkar und allen weiteren Mithelfern, bedanken. Ich habe dort eine Menge toller Erfahrungen gesammelt und viele unglaublich nette Leute kennengelernt. Besonders die Gruppenausflüge waren wirklich einmalige Erlebnisse!

Ebenso danke ich natürlich auch allen anderen Mitgliedern der Arbeitskreise Schnick, Oeckler, Hoch, Johrendt und Lotsch für die super Arbeitsatmosphäre und die tolle Zeit im 2. Stock.

Meiner Freundin Martina und meinen Eltern und kann ich garnicht genug danken. Ohne eure Unterstützung wäre all das nie möglich gewesen!

„ Science is a field which grows continuously with ever expanding frontiers. “

(John Bardeen)

Table of Contents

1 Introduction

The global population is growing steadily and worldwide technologization is in full swing. The massively growing energy demands necessitate environment-friendly alternatives for conventional energy sources as well as ecological solutions for everyday life. Renewable energies, sustainable mobility and highly-efficient lighting technologies are thus of great importance in current research. Advanced functional materials with wide-ranging unique optical and electronic properties are fundamental to promote technical progress of such major innovations. Among these, semiconductors are of particular importance for a large variety of devices, e.g. computer processors, data storage media, mobile phones, light emitting diodes (LEDs) or photovoltaics. While the former are substantial for the advancing digitalization, LEDs and photovoltaics play a significant role in promoting the energy revolution. Moreover, such materials are essential for the evolution of photocatalytical hydrogen production providing renewable energy sources without collateral formation of greenhouse gases.[1-2] The increasing scarcity of industrially important elements like gallium or indium further necessitates the search for earth-abundant semiconductors with similar electronic and optical properties as well-suited alternatives for commonly used materials.[3] Regarding this wide range of applications, the exploration of new functional materials is an important aspect in solid-state chemistry enabling development of innovative and novel devices that can promote a sustainable future.

Semiconductors can be generally defined as solids with electronic conductivity ranging between that of conductors and insulators. Valence and conduction bands closest to the Fermi level are separated by a band gap in which electronic states are not existent due to the quantization of energy. Electrons can be excited from valence to the conduction band for example through thermal excitation or light. Both excited electrons and generated holes contribute to electrical conduction when a voltage is applied. The conductivity increases with temperature as additional electrons are thermally promoted to the conduction band. The charge carrier concentration can be greatly increased by introducing dopants into the material, namely donors that have more valence electrons (n-doping) and acceptors which have less valence electrons (p-doping) compared to the replaced atoms. The creation of heterojunctions between p- and n-doped materials results in formation of regions depleted of charge carriers which allows current to flow solely in one direction (Figure 1). This arrangement is the fundament of virtually all modern

semiconductor devices, e.g. transistors within integrated circuits, photodiodes for solar cells as well as light-emitting or laser diodes.

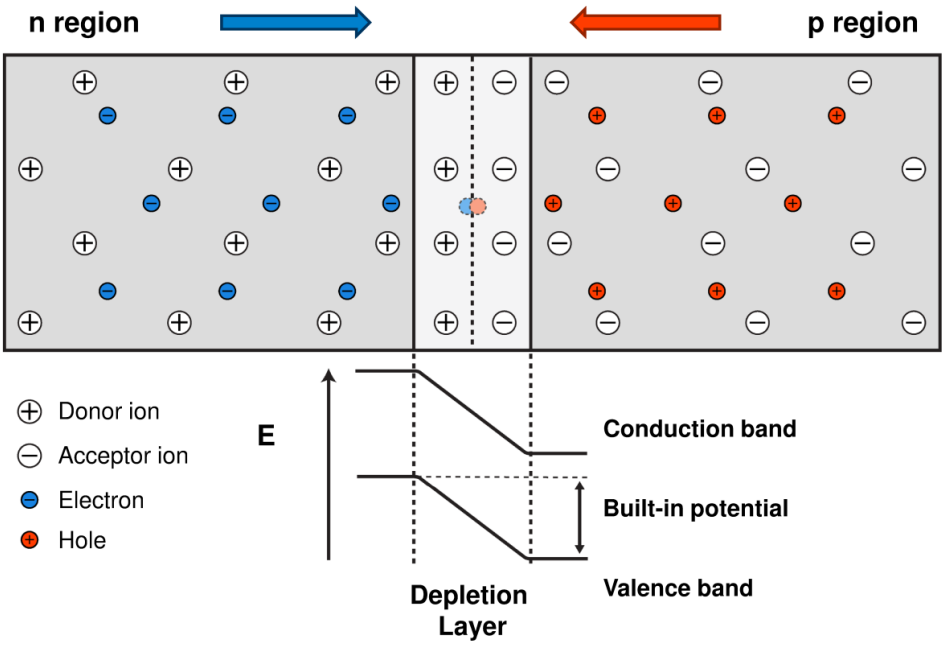

Figure 1. Schematic drawing of p-n junction between positively (p) and negatively (n) doped semiconducting material. Electrons of the n-region diffuse to the p-region, recombine with holes and vice versa leaving behind positively and negatively charged ions in the n- and p-regions, respectively. A space charge region near the p-n interface is formed which is depleted of charge carriers. The built-in potential is opposed to the diffusion of electrons and holes resulting in an equilibrium state.

At present, silicon represents the technologically most important semiconductor that is indispensable for the fabrication of integrated circuits implemented in various computer components as well as photovoltaics and liquid crystal displays. Similarly, germanium is partially used for photovoltaic cells, transistors and infrared optics. Materials with covalent character and valence electron concentration of four are structurally related to group 14 elements which is referred to as the Grimm-Sommerfeld rule.[4] Numerous binary semiconductors can be derived from this correlation, e.g. SiC, III-V semiconductors like GaN, GaAs or InP and II-VI semiconductors like ZnO, ZnS or CdTe. These compounds typically crystallize in wurtzite or sphalerite type structures and are mostly employed for optoelectronic applications. In particular gallium nitride is considered to be one of the most important semiconductors after silicon. GaN is a direct-gap semiconductor with excellent chemical and thermal stability as well as small electron and moderate hole effective

masses.[5] GaN and respective solid solutions (Al,Ga,In)N are of great industrial importance for highly efficient ultraviolet or blue LEDs and laser diodes covering band gaps between ~0.7 to 6.2 eV.[6] In particular the direct band gap of (Ga,In)N allows significantly increased efficiencies compared to formerly used SiC which exhibits an unfavorable indirect band gap. Within a p-n diode of $Ga_{1-x}In_xN$, voltage in forward direction enables electrons and holes to continually recombine which is accompanied by emission of photons. Their wavelengths correlate with the band gap of the adjustable $Ga_{1-x}In_xN$ composition. In 2014, the Nobel prize in physics was awarded to Isamu Akasaki, Hiroshi Amano and Shuji Nakamura for their development of highly efficient blue LEDs based on GaN.[7] The major challenge included the achievement of p-doping which was hampered by present impurities as well as by passivation of the dopant Mg with hydrogen. Irradiation of p-doped GaN employing a low-energy electron beam partially activated the acceptors by dissociation of hydrogen complexes. Nakamura showed that a similar effect can be achieved by thermal annealing of p-GaN. In this way, manufacturing of the first blue $Ga_{1-x}In_xN$ LED was achieved that paved the way to highly efficient white light sources and thus revolutionized optoelectronic technologies.

Phosphor-based conversion of ultraviolet or blue-emitting LEDs emerged as most efficient way to produce white light enabling a huge variety of lighting applications. Here, luminescent materials with specific emission characteristics are coated on $Ga_{1-x}In_xN$ LEDs, while mixing of complementary colors results in the generation of white light. Numerous rare-earth doped nitrides and oxonitrides, in particular (oxo)nitridosilicates and -aluminates, are excellently suitable as phosphors and industrially employed in pcLEDs.[8-11] These materials ideally feature wide band gaps in the range of 4.5 - 6 eV, where parameters like thermal luminescence behavior, photoionization and electronic states of dopants have to be considered.[12-15] A fraction of the irradiated light is transformed to longer wavelengths which is specified by the Stokes shift. This conversion is based on electronic transitions within activator ions, e.g. Eu^{2+} or Ce^{3+}, which are incorporated in the host lattice of the phosphor. Different phosphors with specific emission maxima and bandwidths are matched in a manner to achieve high luminous efficacies, i.e. an adaption of emission to the eye sensitivity curve, as well as an eminent color rendition within the visible spectral range.[11]

Next to the above mentioned application fields, nitride and oxonitride materials further attracted great interest for numerous other uses as well. For instance, several lithium containing nitrides feature promising ion conductivity characteristics for application in batteries, while oxonitride perovskites proved to be potential catalysts for photocatalytical

water splitting.[16-18] Moreover, materials like Si_3N_4 or SiAlONs emerged as industrially important ceramics due to their high mechanical strength as well as their high wear and oxidation resistances at high temperatures.[19-22] The diversity of intriguing optical, thermal, chemical, mechanical and electronic properties arises from the large structural variety of nitride compounds. Manifold structural possibilities occur due to the high structural flexibility of nitrogen within nitrides (feasible coordination modes $N^{[1]}$,$N^{[2]}$,$N^{[3]}$ and $N^{[4]}$) which also results in highly variable degrees of condensation.[23] With regard to previous findings and theoretical calculations in the field of nitrides, it can be expected that innumerable unprecedented nitride materials still await their discovery.[3,9,23-28] The advance of synthetic approaches and techniques represents the key enabling access to novel functional nitride compounds. Commonly, nitrides are synthesized by direct nitriding of metals, alloys or hydrides under nitrogen atmosphere, carbothermal reduction or solid-state metathesis reactions mostly at high temperatures in the range of 1300 - 2300 K. On the other hand, the ammonothermal method represents a highly promising technique which employs rather moderate temperatures with high-pressurized ammonia as reaction medium.[29] Here, the starting materials and respective mineralizers are placed into high-pressure autoclaves and dissolved in supercritical ammonia typically forming ternary or multinary amide or imide species. The high reactivity of supercritical ammonia and emerging intermediates facilitates the synthesis of nitrides with limited thermal stability and further promotes the discovery of compounds which are difficult to access by conventional methods.

In analogy to the hydrothermal growth of oxides, the ammonothermal approach is highly promising for the crystal growth of nitride materials as well. Both ammonia and water are polar and protic, albeit water exhibits a higher dielectric constant and dipole moment compared to liquid ammonia.[30] Solubilities of ionic solids within the latter are thus generally lower, though they can be significantly increased using high-pressurized supercritical ammonia leading to higher relative permittivities.[29] Several concepts like mineralizers, chemical transport, intermediates and crystal growth mechanisms can thus be derived from hydrothermal processes, yet require appropriate modification for the ammonothermal synthesis of nitrides. Crystal growth is commonly achieved by dissolution and recrystallization based transport reactions applying specific temperature gradients along the autoclave body. During the last decade, the ammonothermal method attracted great attention as it proved to be ideally suitable for the growth of bulk GaN single crystals. The prevalent lack of economic growth techniques forced the use of foreign substrates for GaN-based devices, most commonly sapphire or SiC, where numerous defects are created owing to the lattice mismatch which further leads to efficiency losses.

Native substrates can be fabricated from bulk GaN crystals that enable devices with significantly higher performances and are thus is of great industrial relevance.[31-32] For ammonothermal crystal growth, the nutrient, commonly polycrystalline GaN, is dissolved in the presence of mineralizers under formation of well-soluble complex species. To this end, alkali metal amides or ammonium halides are usually employed as ammonobasic or -acidic mineralizers, respectively. The formed intermediate species are transported to the seed crystal by convection, while chemical equilibrium of GaN recrystallization is adjusted via the applied temperature gradient. Intermediates have a major impact on solubilities, mass transport, growth rates, growth faces as well as predominant growth directions and are thus essential to elucidate and optimize crystal growth of nitrides. In recent years, several possible intermediate species were discovered depending on the type of mineralizer and applied growth conditions, such as $Li[Ga(NH_2)_4]$, $Na_2[Ga(NH_2)_4]NH_2$, $Ba[Ga(NH_2)_4]_2$ or $[Ga(NH_3)_6]I_3{\cdot}NH_3$.[33-35] Moreover, it has recently been demonstrated that reactions of $RbNH_2$ or $CsNH_2$ with Ga metal lead to liquids that are completely miscible with liquid ammonia.[36] A proposed reaction mechanism for chemical transport of GaN is illustrated in Figure 2.

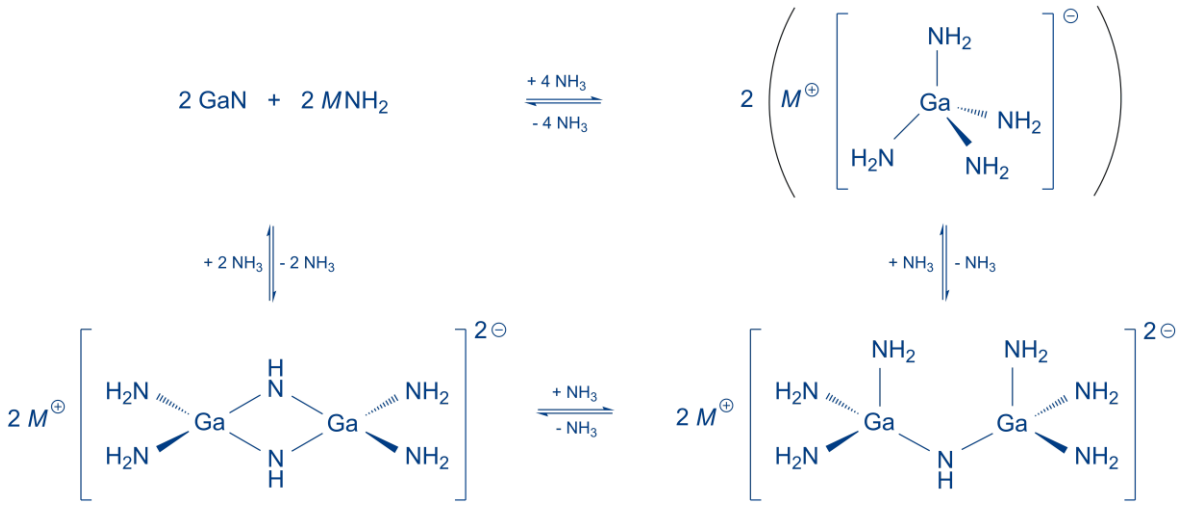

Figure 2. Proposed chemical equilibria of GaN dissolution and recrystallization in supercritical ammonia involving formation of $M_2[Ga(NH_2)_4]$ by dissolution of GaN with alkali metal amides MNH_2 as ammonobasic mineralizers (top) and possible formation mechanism of Ga-containing complex species for M = Cs (bottom).[36-37]

Baffle plates centred within the autoclave are employed which regulate mass transport and limit heat transfer between dissolution and growth zones. In this way, crystal growth can be effectively controlled, while the formation of defects is minimized by providing

constant temperatures close to the seed. Numerous other interacting parameters have to be considered for an effective crystal growth, most notably the type and concentration of mineralizer, fluid temperature, pressure, autoclave and baffle geometry, fluid convection, type of nutrient and seeds as well as oxygen or metal impurities.[29,38] Within the last decade, fundamental advances of ammonothermal GaN growth were achieved meanwhile attaining bulk crystals with excellent quality and diameters up to 50 mm.[39-42] Greatly improved growth rates along with excellent scalability via simultaneous growth on multiple seeds promote the industrial significance of the ammonothermal method. Notably, the GaN substrate market is estimated to grow by 75% within the next five years.[43] The major part of commercial GaN still originates from hydride vapor phase epitaxy (HVPE) growth, though it is expected that ammonothermal GaN will supersede epitaxial growth techniques within the next few years.

In comparison to the broad spectrum of hydrothermal research and its commercial application fields, the ammonothermal method is still much less explored. While currently most efforts are focused on the growth of GaN, only very few studies addressed the ammonothermal synthesis of other binary as well as ternary and multinary nitrides as yet (cf. Figure 3). During the second half of the 20th century, pioneering work in this field was conducted by Herbert Jacobs and coworkers, though prevalently focusing on crystal growth of amides, imides and ammoniates.[29,44] After Jacobs' retirement, ammonothermal research was virtually limited to GaN and explorative ammonothermal studies have been reported very rarely. In 2011, the interdisciplinary research group *Ammono-FOR* was found to re-establish the highly promising ammonothermal technology.[45] From technical point of view, syntheses in supercritical ammonia are quite challenging due to the high demands on autoclave materials and high-pressure facilities. Besides, commercially available autoclaves barely provide the required parameters for syntheses of well-crystalline nitrides in supercritical ammonia. Within the established research group, new autoclave technologies have been projected to be developed for explorative ammonothermal syntheses of nitrides and investigations on crystallization processes. Furthermore, growth techniques for nitrides are scarce since these are commonly not meltable at ambient pressure. Considering recent progress of bulk GaN crystal growth the ammonothermal method can be regarded as the most promising approach among feasible vapor phase, flux and solution based growth methods. Next to the utilization as substrates, large nitride single crystals would be of high interest for detailed investigation of physical and material properties as well as for optical applications such as nonlinear optics (NLO).[23]

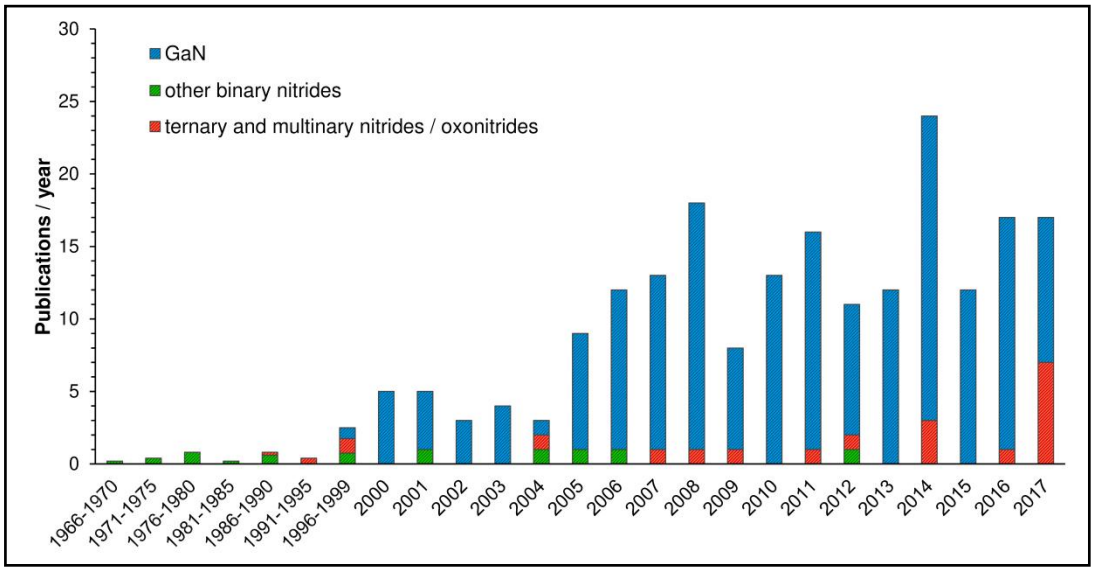

Figure 3. Number of publications per year referred to the ammonothermal synthesis of GaN (blue columns), other binary nitrides (green columns) and ternary / multinary nitrides or oxonitrides (red columns) based on SciFinder and Web of Science.[46-47]

The first objective of this thesis covers the evaluation of interacting parameters, customization of newly developed autoclave systems and the improvement of their design to efficiently obtain access to ternary and multinary nitrides using the ammonothermal method. In close cooperation with the chair of process technology and machinery at University of Erlangen-Nuremberg, high-pressure autoclaves have been developed using new nickel-based superalloys which meet extreme material demands featuring eminent chemical stability against supercritical ammonia solutions as well as high yield and tensile strengths at maximized process temperatures of up to 1100 K. In this way, the potential of ammonothermal syntheses has been greatly improved promoting the formation of highly crystalline ternary and multinary nitrides from supercritical ammonia solutions. Major steps for this objective included the systematic exploration of suitable reaction conditions, investigation of different mineralizer systems as well as probing highly reactive precursor species under ammonothermal reaction conditions.

On that basis, first systematic syntheses of Grimm-Sommerfeld analogous ternary nitrides from ammonothermal solution became possible during this thesis. This class of materials is of high current interest due to their structural analogy to (Al,Ga,In)N, the increased prospects for band-gap engineering and the earth-abundance of the constituting elements.[3,48-50] However, these semiconductors have rarely been studied so far and

experimental optical properties on bulk samples are virtually unexplored. In this work, detailed examination of mineralizers and synthesis parameters as well as optical properties of Grimm-Sommerfeld analogous nitride semiconductors will be presented. In addition, a proof of concept for possible dissolution and recrystallization based crystal growth processes is demonstrated employing in situ X-ray imaging techniques within a custom-built high-pressure optical cell. Moreover, it will be shown that the newly developed high-temperature autoclaves enable access to novel nitrides as well. For the first time, syntheses of novel multinary nitridosilicates and -germanates employing an ammonothermal approach have been accomplished. Highly reactive intermetallic precursors in combination with ammonobasic mineralizers at increased reaction temperatures up to 1070 K proved to be the key to synthesis of these new functional nitride materials.

The introducing minireview will first give a detailed overview on recent progress of the ammonothermal synthesis of nitrides, further presents different synthesis strategies and includes the latest developments of autoclave technologies. Moreover, challenges and future perspectives for the crystal growth of nitride materials and the discovery of novel nitrides are discussed. The following chapters cover the ammonothermal synthesis of addressed ternary and multinary functional nitride materials, detailed characterization of structural, optical and electronic properties in question as well as their great potential for wide-ranging optoelectronic applications.

References

[1] X. Li, J. Yu, J. Low, Y. Fang, J. Xiao, X. Chen, *J. Mater. Chem. A* **2015**, *3*, 2485-2534.

[2] S. Y. Tee, K. Y. Win, W. S. Teo, L.-D. Koh, S. Liu, C. P. Teng, M.-Y. Han, *Adv. Sci.* **2017**, *4*, 1600337.

[3] Y. Hinuma, T. Hatakeyama, Y. Kumagai, L. A. Burton, H. Sato, Y. Muraba, S. Iimura, H. Hiramatsu, I. Tanaka, H. Hosono, F. Oba, *Nat. Commun.* **2016**, 7:11962.

[4] H. G. Grimm, A. Sommerfeld, *Z. Phys.* **1926**, *36*, 36-59.

[5] H. Morkoç, *Handbook of Nitride Semiconductors and Devices, Materials Properties, Physics and Growth*, Wiley-VCH, Weinheim, Germany, **2009**.

[6] J. Wu, W. Walukiewicz, *Superlattices Microstruct.* **2003**, *34*, 63-75.

[7] S. Nakamura, *Angew. Chem.* **2015**, *127*, 7880-7899; S. Nakamura, *Angew. Chem. Int. Ed.* **2015**, *54*, 7770-7788.

[8] R. Mueller-Mach, G. Mueller, M. R. Krames, H. A. Höppe, F. Stadler, W. Schnick, T. Jüstel, P. Schmidt, *Phys. Status Solidi A* **2005**, *202*, 1727-1732.

[9] R.-J. Xie, H. T. Hintzen, *J. Am. Ceram. Soc.* **2013**, *96*, 665-687.

[10] P. Pust, V. Weiler, C. Hecht, A. Tucks, A. S. Wochnik, A. K. Henss, D. Wiechert, C. Scheu, P. J. Schmidt, W. Schnick, *Nat. Mater.* **2014**, *13*, 891-896.

[11] P. Pust, P. J. Schmidt, W. Schnick, *Nat. Mater.* **2015**, *14*, 454-458.

[12] P. Dorenbos, *J. Phys.: Condens. Matter* **2005**, *17*, 8103.

[13] T. M. Tolhurst, T. D. Boyko, P. Pust, N. W. Johnson, W. Schnick, A. Moewes, *Adv. Opt. Mater.* **2015**, *3*, 546-550.

[14] T. M. Tolhurst, S. Schmiechen, P. Pust, P. J. Schmidt, W. Schnick, A. Moewes, *Adv. Opt. Mater.* **2016**, *4*, 584-591.

[15] T. M. Tolhurst, P. Strobel, P. J. Schmidt, W. Schnick, A. Moewes, *Chem. Mater.* **2017**, *29*, 7976-7983.

[16] N. Tapia-Ruiz, M. Segalés, D. H. Gregory, *Coord. Chem. Rev.* **2013**, *257*, 1978-2014.

[17] E.-M. Bertschler, C. Dietrich, T. Leichtweiß, J. Janek, W. Schnick, *Chem. Eur. J.* **2018**, *24*, 196-205.

[18] G. Zhang, G. Liu, L. Wang, J. T. S. Irvine, *Chem. Soc. Rev.* **2016**, *45*, 5951-5984.

[19] K. H. Jack, *J. Mater. Sci.* **1976**, *11*, 1135-1158.

[20] A. Ziegler, J. C. Idrobo, M. K. Cinibulk, C. Kisielowski, N. D. Browning, R. O. Ritchie, *Science* **2004**, *306*, 1768-1770.

[21] N. Shibata, S. J. Pennycook, T. R. Gosnell, G. S. Painter, W. A. Shelton, P. F. Becher, *Nature* **2004**, *428*, 730.

[22] M. I. Jones, H. Hyuga, K. Hirao, Y. Yamauchi, *J. Am. Ceram. Soc.* **2004**, *87*, 714-716.

[23] M. Zeuner, S. Pagano, W. Schnick, *Angew. Chem.* **2011**, *123*, 7898-7920; *Angew. Chem. Int. Ed.* **2011**, *50*, 7754-7775.

[24] R. Niewa, F. J. DiSalvo, *Chem. Mater.* **1998**, *10*, 2733-2752.

[25] H. Yamane, F. J. DiSalvo, *Prog. Solid State Chem.* **2017**, DOI: 10.1016/j.progsolidstchem.2017.08.002.

[26] Z.-H. Cai, P. Narang, H. A. Atwater, S. Chen, C.-G. Duan, Z.-Q. Zhu, J.-H. Chu, *Chem. Mater.* **2015**, *27*, 7757-7764.

[27] H. Zhang, J. Ren, L. Wu, J. Zhang, *J. Solid State Chem.* **2017**, *245*, 184-189.

[28] P. Bielec, O. Janka, T. Block, R. Pöttgen, W. Schnick, *Angew. Chem. Int. Ed.* **2018**, DOI: 10.1002/anie.201713006.

[29] T. Richter, R. Niewa, *Inorganics* **2014**, *2*, 29-78.

[30] A. Rabenau, *Angew. Chem.* **1985**, *97*, 1017-1032; A. Rabenau, *Angew. Chem. Int. Ed.* **1985**, *24*, 1026-1040.

[31] T. Paskova, D. A. Hanser, K. R. Evans, *Proc. IEEE* **2010**, *98*, 1324-1338.

[32] S. Nakamura, M. R. Krames, *Proc. IEEE* **2013**, *101*, 2211-2220.

[33] S. Zhang, N. S. A. Alt, E. Schlücker, R. Niewa, *J. Cryst. Growth* **2014**, *403*, 22-28.

[34] J. Hertrampf, N. S. A. Alt, E. Schlücker, R. Niewa, *Eur. J. Inorg. Chem.* **2017**, *2017*, 902-909.

[35] S. Zhang, F. Hintze, W. Schnick, R. Niewa, *Eur. J. Inorg. Chem.* **2013**, *2013*, 5387-5399.

[36] J. Hertrampf, E. Schlücker, D. Gudat, R. Niewa, *Cryst. Growth Des.* **2017**, *17*, 4855–4863.

[37] B. Wang, M. J. Callahan, *Cryst. Growth Des.* **2006**, *6*, 1227-1246.

[38] D. Ehrentraut, E. Meissner, M. Bockowski, *Technology of Gallium Nitride Crystal Growth*, Springer Series in Materials Science, Springer, Berlin, Heidelberg, **2010**.

[39] R. Dwiliński, R. Doradziński, J. Garczyński, L. Sierzputowski, R. Kucharski, M. Zając, M. Rudziński, R. Kudrawiec, J. Serafińczuk, W. Strupiński, *J. Cryst. Growth* **2010**, *312*, 2499-2502.

[40] W. Jiang, D. Ehrentraut, J. Cook, D. S. Kamber, R. T. Pakalapati, M. P. D'Evelyn, *Phys. Status Solidi B* **2015**, *252*, 1069-1074.

[41] Y. Mikawa, T. Ishinabe, S. Kawabata, T. Mochizuki, A. Kojima, Y. Kagamitani, H. Fujisawa, *Proc. SPIE* **2015**, *9363*, 936302.

[42] J. B. Shim, G. H. Kim, Y. K. Lee, *J. Cryst. Growth* **2017**, *478*, 85-88.

[43] Gallium Nitride (GaN) Substrates Market - Forecasts from 2017 to 2022, *Research and Markets* **2017**, Dublin, Ireland.

[44] H. Jacobs, D. Schmidt, *Curr. Top. Mater. Sci.* **1982**, *8*, 387-427.

[45] Ammono-FOR, *research group chemistry and technology of the ammonothermal synthesis of nitrides*, http://www.ammono-for.org.

[46] SciFinder Database, American Chemical Society (ACS), Columbus, Ohio, USA, http://www.scifinder.cas.org.

[47] Web of Science Database, Clarivate Analytics, Philadelphia, Pennsylvania, USA, http://www.webofknowledge.com.

[48] P. Narang, S. Chen, N. C. Coronel, S. Gul, J. Yano, L.-W. Wang, N. S. Lewis, H. A. Atwater, *Adv. Mater.* **2014**, *26*, 1235-1241.

[49] P. C. Quayle, K. He, J. Shan, K. Kash, *MRS Commun.* **2013**, *3*, 135-138.

[50] A. D. Martinez, A. N. Fioretti, E. S. Toberer, A. C. Tamboli, *J. Mater. Chem. A* **2017**, *5*, 11418-11435.

2 Ammonothermal Synthesis of Nitrides: Recent Developments and Future Perspectives

published in: *Chem. Eur. J.* **2018**, DOI: 10.1002/chem.201800115

(**invited Minireview**)

authors: Jonas Häusler, and Wolfgang Schnick

http://onlinelibrary.wiley.com/doi/10.1002/chem.201800115/abstract

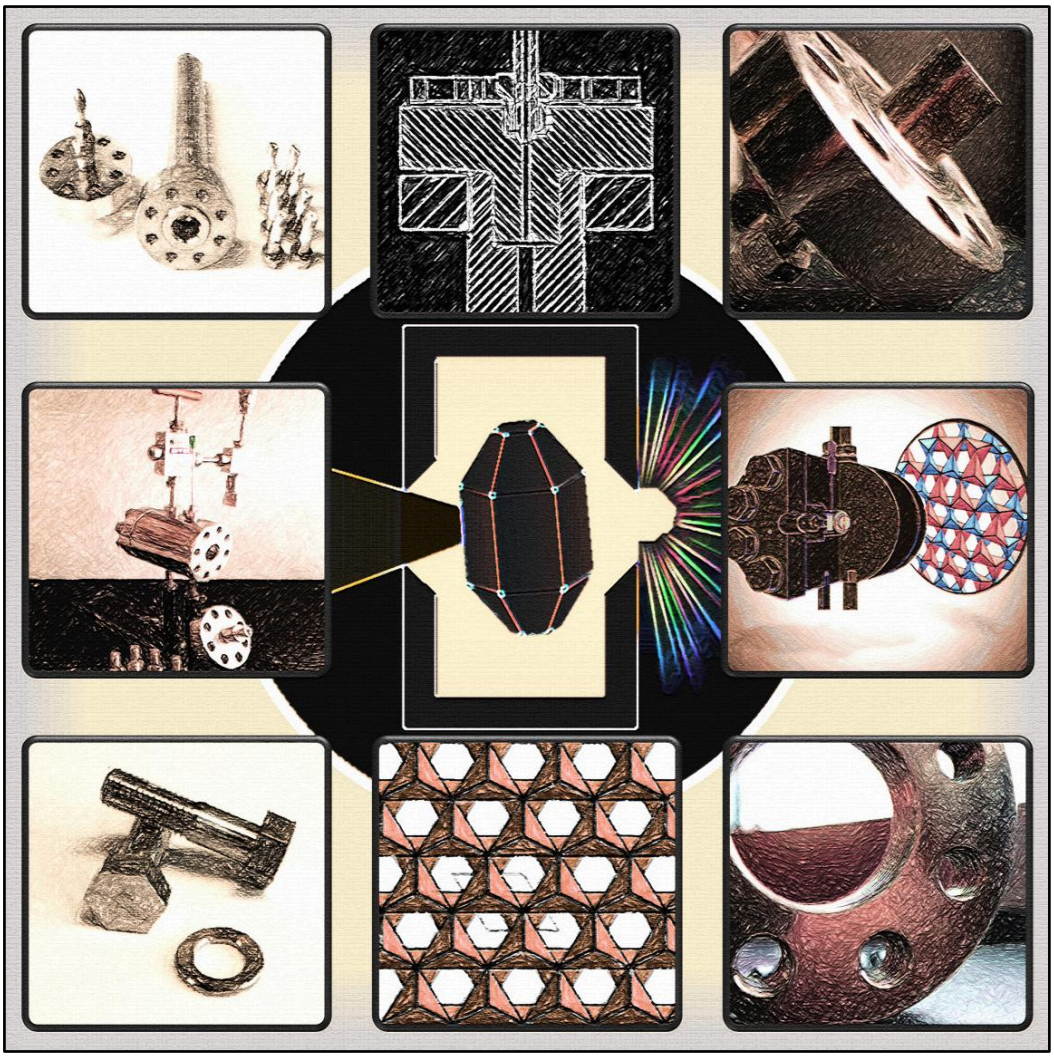

Abstract. Nitrides represent an intriguing class of functional materials with a broad range of application fields. Within the past decade, the ammonothermal method became increasingly attractive for the synthesis and crystal growth of nitride materials. The ammonothermal approach proved to be eminently suitable for the growth of bulk III-nitride semiconductors like GaN, and furthermore provided access to numerous ternary and multinary nitrides and oxonitrides with promising optical and electronic properties. In this minireview, we will shed light on the latest research findings covering the synthesis of nitrides by this method. An overview of synthesis strategies for binary, ternary, and multinary nitrides and oxonitrides, as well as their properties and potential applications will be given. The recent development of autoclave technologies for syntheses at high temperatures and pressures, in situ methods for investigations of crystallization processes, and solubility measurements by ultrasonic velocity experiments is briefly reviewed as well. In conclusion, challenges and future perspectives regarding the synthesis and crystal growth of novel nitrides, as well as the advancement of autoclave techniques are discussed.

2.1 Introduction

Solvothermal techniques are widely used for synthesis and crystal growth of various inorganic compounds. Probably the best-known example is the hydrothermal method, which is primarily used for the synthesis of oxides. For instance, over 3000 tons of bulk quartz crystals, an important source material for piezoelectronics, are industrially produced each year.[1] The term “hydrothermal” was first used by the British geologist Roderick Murchison to describe the natural formation of minerals in the earth's crust at elevated temperatures and pressures.[2] Already in the 1840s, the first hydrothermal experiments on the crystallization of silicates, carbonates, and quartz were conducted by Wöhler, Bunsen, and Schafhäutl, which rapidly initiated further research efforts in this field.[3,4] During the first half of the 20th century, systematic investigations on numerous hydrothermal systems, as well as the development of new autoclave technologies promoted the discovery of numerous novel inorganic compounds and the commercialization of hydrothermal crystal growth processes.[5,6]

Until then, non-aqueous solutions were only rarely studied at elevated temperatures and pressures. For instance, ammonia features similar physical properties compared to water, even though it is less protic, less polar, and has a lower relative permittivity.[7] Numerous amides and ammoniates were obtained from liquid ammonia solutions and several

ammonobasic and -acidic systems were thoroughly investigated at the beginning of the last century. However, crystallization was often hampered by the comparably low solubilities of many inorganic solids in liquid ammonia. To overcome this issue, Jacobs and co-workers initiated the first syntheses in supercritical ammonia during the 1960s, benefiting from the earlier developments in the field of hydrothermal syntheses.[8] In analogy to the latter, they used the term “ammonothermal” to describe these reactions. During the following years, they prevalently investigated the behavior of alkali, alkaline earth, and rare earth metals in supercritical ammonia. This new approach made numerous novel compounds accessible and enabled crystal growth of amides and nitrides by convection-driven transport reactions.[9] With the first ammonothermal synthesis of gallium nitride reported in 1995 by Dwiliński, Jacobs and co-workers, this route increasingly gained interest, since only few very specialized and expensive methods for the growth of bulk GaN crystals are available as yet.[10] Researchers started to examine mineralizer systems, intermediates, solution equilibria, and solubilities to gain insight into crystallization processes within the crystal growth of GaN. Meanwhile, growth rates beyond 300 µm day^{-1} in different crystallographic directions were achieved.[11,12] Bulk GaN crystals are of particular interest for the fabrication of substrates, which enable homoepitaxial growth of GaN layers for optoelectronic devices (“GaN-on-GaN”). Using this concept, semiconductor performances can be strongly increased due to the significantly lower defect concentrations in comparison to the prevailing heteroepitaxial-based devices.[13,14]

In recent years, the ammonothermal method was rediscovered as a powerful tool for the synthesis of ternary and multinary nitrides and oxonitrides as well. For instance, several II-IV-N_2 nitride semiconductors with similar optical and electronic properties compared to (Al,Ga)N, as well as luminescent materials for phosphor-converted light emitting diodes (pc-LEDs) and oxonitrides as potential photocatalysts were obtained from syntheses in supercritical ammonia.[15-18] The latest research findings on ammonothermal syntheses reveal a great potential for the crystal growth of ternary nitride semiconductors, as well as for the discovery of novel multinary nitrides and oxonitrides, which will be further discussed in this minireview.

2.2 Ammonothermal synthesis of nitrides

Nitrides comprise a huge class of compounds with large structural variety and manifold applications fields.[19-23] Common synthesis routes for nitrides include high-temperature approaches like direct nitriding of metals, alloys, or hydrides in nitrogen atmosphere, carbothermal reduction, or solid-state metathesis reactions. In contrast to these approaches, ammonothermal syntheses are solution-based reactions at comparatively low temperatures. Jacobs initially developed this method to obtain well-crystallized amides for X-ray structure analyses, as well as deuteroamides for neutron diffraction.[9] It was observed that various binary and ternary nitrides can likewise be synthesized in supercritical ammonia, particularly at elevated reaction temperatures. During the last decade, even quaternary and multinary nitrides and oxonitrides were obtained from supercritical ammonia solution. The ammonothermal technique further attracted great attention for the crystal growth of GaN, eminently contributing to the recent progress of advanced autoclave technologies. These developments will be presented in the following sections.

2.2.1 Binary nitrides

In this section, we will briefly summarize the most important findings covering the ammonothermal synthesis of binary nitrides, which provide fundamental concepts for current and future ammonothermal research. Recent developments regarding the crystal growth of GaN, as well as the latest study on the ammonothermal crystallization of InN will be reviewed. More detailed synthesis parameters of binary nitrides are given in a recent general review on the chemistry of ammonothermal synthesis.[24]

2.2.1.1 Overview

The first nitride obtained by ammonothermal synthesis, α-Be_3N_2, was reported in 1966.[8] In comparison to the conventional ammonolysis reaction in an ammonia flow, synthesis temperatures could be considerably lowered from 1270 to 670 K, applying an ammonia pressure of 20 MPa. α-Be_3N_2 was obtained as polycrystalline powder and crystallizes in the anti-bixbyite structure type, also referred to as the C-sesquioxide type. The first ammonothermal growth of single crystalline nitrides, LaN and EuN, was accomplished within studies on rare earth metals in ammonobasic and -acidic systems.[9,25] KNH_2 was used as an ammonobasic mineralizer, leading to the formation of intermediates like

$K_3[La(NH_2)_6]$ or $KEu(NH_2)_3$. Two different mechanisms for the crystal growth were proposed: chemical transport reactions along a temperature gradient within the autoclave, where ternary intermediates act as transporting agents, or the growth from a KNH_2 melt, both in supercritical ammonia.[9] Further rare earth metal nitrides (LnN, Ln=Y, Ce, Sm, Gd) were obtained as microcrystalline powders during systematic investigations on novel ternary amides.[26-29] YN and GdN were synthesized in an ammonoacidic environment with NH_4I as mineralizer, whereas in situ formed ammonobasic amides of Cs and K were used for the preparation of CeN and SmN, respectively.

Jacobs and co-workers also investigated the crystallization of 3d-element nitrides. η-Mn_3N_2 can be directly synthesized from Mn in supercritical ammonia at 670–870 K and 600 MPa.[30] The addition of 2–3 mol % of K, Rb, or I_2 facilitates the crystal growth by formation of well-soluble intermediates $M_2[Mn(NH_2)_4]$ (M=K, Rb) or $[Mn(NH_3)_6]I_2$ and subsequent conversion to η-Mn_3N_2. Using I_2, growth occurs in the cold zone of the autoclave along a temperature gradient from 870 to 570 K, whereas retrograde solubility was observed for K and Rb with chemical transport from 470 to 670 K. On the other hand, crystals of Cu_3N can be grown in an ammononeutral environment at 620–850 K and 600 MPa.[31] $[Cu(NH_3)_4](NO_3)_2$ and Cu are used as starting materials, which comproportionate to $[Cu(NH_3)_3](NO_3)$. Crystals of up to 1 mm^3 in size were observed in the hot zone of the autoclave. Single crystal X-ray diffraction confirmed the anti-ReO_3 type of structure of Cu_3N. The authors also showed that Cu_3N is stabilized by the resulting N_2 pressure from the nitrate decomposition. Whereas Cu_3N decomposes at 820 K and 800 MPa in pure supercritical NH_3, it is preserved by addition of NH_4NO_3. Further transition element nitrides were obtained by ammonothermal synthesis as well, namely γ′-Fe_4N, θ-Mn_6N_{5+x}, ϵ-Mn_4N, and Ni_3N. γ′-Fe_4N crystallizes in a perovskite-like structure, whereas θ-Mn_6N_{5+x}, ϵ-Mn_4N and Ni_3N can be classified as interstitial nitrides.[32-35]

2.2.1.2 Group 13 nitrides

Current research in the field of ammonothermal syntheses is primarily focused on the crystal growth of GaN, one of the most important semiconductor materials used in laser diodes, light emitting diodes, or field-effect transistors.[36,37] Only a very few specialized methods for the growth of bulk GaN crystals are available. Conventional methods like zone melting or the Czochralski process are not applicable for crystal growth, since GaN is not meltable at ambient pressure, and decomposes into Ga and N_2 above 1300 K.[38] Melting of GaN can be achieved at high pressures above 6 GPa and temperatures of

2500 K which is not practicable for bulk crystal growth processes.[39] Hence, growth technologies using vapor phase, flux, and solution based methods were developed, for example, ammonothermal synthesis, hydride vapor phase epitaxy (HVPE), and sodium flux growth.[40] The former is of particular interest in current research because of its excellent scalability and the feasible simultaneous growth of multiple crystals during one run; analogous to the hydrothermal growth of quartz.

Ammonothermal crystal growth of GaN can be conducted in ammonobasic or -acidic environments. Ammonobasic syntheses of GaN are typically performed using alkali metal amides MNH_2 (M=Li, Na, K, Rb, Cs) as mineralizers, with $NaNH_2$ and KNH_2 being the best studied systems to date. Recently, the first syntheses of GaN with $Sr(NH_2)_2$ and $Ba(NH_2)_2$ were reported as well.[41] Growth proceeds from the cold to the hot zone within the autoclave due to the retrograde solubility of GaN observed for basic systems. On the other hand, ammonium halides NH_4X (X=F, Cl, Br, I), as well as GaI_3 or $ZnCl_2$, can be employed for ammonoacidic crystal growth.[42-46] Both cubic and hexagonal GaN can be obtained depending on mineralizer and temperature.[47] While the solubility is commonly of regular type, retrograde solubility was observed at higher growth temperatures above 925 K for NH_4Cl. Syntheses of microcrystalline GaN powders in neutral environment were reported using LiCl, NaI, or KI, which are sometimes also added as co-mineralizers in combination with alkali metal amides.[40]

Evaluation of optimum growth conditions is challenging, due to varying experimental setups in different groups and numerous interacting parameters affecting crystal growth, for example, mineralizer concentration, type of nutrient and seeds, fluid temperature, temperature gradient, pressure, autoclave and baffle geometry, as well as oxygen or metal impurities. Next to these, the growth direction is a further fundamental parameter with regard to the desired crystal face polarity of GaN. For instance, strong piezoelectric and spontaneous polarizations occur in polar directions which limit device efficiencies.[40,48] These issues can be eliminated by growth on semipolar or nonpolar substrates, which in turn reduce or eliminate undesirable polarization effects. Different polar, nonpolar, and semipolar growth directions reported for ammonothermal syntheses[49-51] are illustrated in Figure 1.

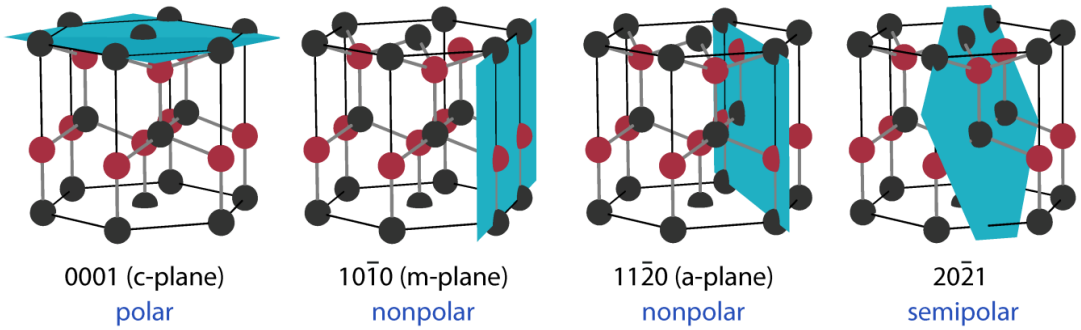

Figure 1. Selected growth directions reported for ammonothermal crystal growth of GaN (Ga black, N red, planes: turquoise).

During the last decade, a considerable increase of growth rates was achieved. In 2006, rates in the range of 10–50 µm day^{-1} were reported,[7] which could be improved to several hundreds of µm per day in different crystallographic directions.[49,52-54] Ehrentraut and co-workers reached growth rates up to 40 µm per hour in the *m*-direction using internally heated capsule-based reactors at comparable high temperatures up to 1020 K and pressures up to 600 MPa.[11] Saito et al. recently reported on growth rates >1000 µm day^{-1} employing Pt-lined autoclaves and ammonium halides as mineralizers.[55] Bulk crystals with 50 mm in diameter have also been demonstrated by different research groups.[56-59] Selected high-quality bulk GaN crystals grown by the ammonothermal method are shown in Figure 2.

To further optimize the crystal growth process, knowledge on intermediates and solubilities is fundamental. In recent years, several possible intermediate compounds for ammonobasic and -acidic systems were isolated.[60-63] Such intermediates act as transporting agents for GaN from dissolution to the growth zone, where dissolution and complexing equilibria are controlled through the applied temperature gradient. Numerical simulations additionally help to visualize fluid, mass, and heat flow of the convection-driven chemical transport reaction.[64-67] The kind of intermediate species affects solubility and growth rates of GaN and can further have an impact on N- or Ga-face growth, as well as the predominant growth directions.[68-70]

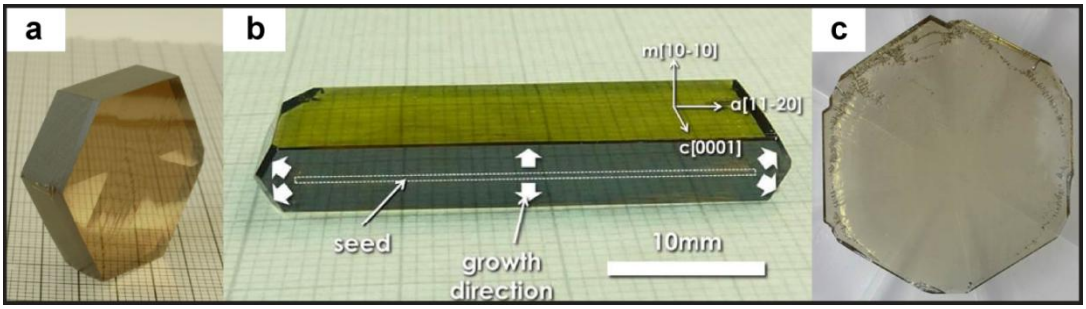

Figure 2. a) Photograph of a ≈25 mm *m*-plane GaN crystal grown in ammonobasic environment. Reproduced with permission from ref. [71], Copyright AIP Publishing 2009. b) Photograph of a ≈35 mm ammonoacidic *m*-plane GaN crystal. Reproduced with permission from ref. [58], Copyright SPIE 2015. c) Photograph of a ≈50 mm *c*-plane GaN crystal grown in ammonoacidic environment. Reproduced with permission from ref. [72], Copyright Elsevier 2014.

On the other hand, temperature and pressure-dependent solubility data for nutrient and intermediates are important for the choice of mineralizer, growth temperature, and temperature gradient. Solubilities are commonly determined gravimetrically by measuring the mass change of the starting material. Advanced in situ autoclave systems were developed for quantification of solubilities by X-ray imaging or ultrasonic velocity measurements (see Section 3). The key benefit of in situ methods is the determination of dissolution kinetics, which allows one to distinguish between saturation of the solution and dissolution based on mass transport. Besides, the dissolution rate can be directly monitored at varying temperatures. In situ data are available for $NaNH_2$, NH_4F, and NH_4Cl so far,[73,74] whereas gravimetrical measurements were reported for $NaNH_2$, KNH_2, and NH_4X (X=Cl, Br, I) as mineralizers.[68,75-78] Higher solubilities of GaN in acidic solutions were ascertained, according to present data, which coincide with the generally higher growth rates in acidic systems. Notably, different experimental parameters, as well as the evolution of Ga sinks and sources during the runs have to be considered, which can result in significant deviations of the evaluated solubilities.[75]

Impurities and defects in bulk GaN crystals represent another important aspect in current research. Suihkonen et al. studied and reviewed the formation and concentration of defects in ammonothermal GaN.[79,80] Impurities can be mainly ascribed to oxygen originating from nutrient and mineralizer, as well as transition metals from autoclave materials. Gallium vacancies and inclusions of hydrogen were also detected in both ammonobasic and -acidic grown crystals resulting in increased sub-band-gap absorption.[80-82] These point defects strongly affect electronic and optical properties of

GaN and cause lattice strain, which can even lead to cracking of the wafers. Transition element impurities are strongly reduced using liner systems or capsules, whereas oxygen getters can be employed to lower the oxygen concentration in GaN crystals. Feasible liner materials were examined for both basic and -acidic systems (see also Section 3.1). For instance, nearly transition metal free ($<1\times10^{17}$ cm^{-3}) GaN was obtained by implementing non-hermetically sealed silver or molybdenum capsules in the growth environment. Growth rates were even improved with Ag capsules, while Mo reduced the oxygen concentration in comparison to the source material and was thus proposed as possible oxygen getter. The transparency of bulk GaN can also be tuned by compensation of oxygen donors with Mg acceptors as recently examined for various spectral ranges.[83] Although previous developments provided ammonothermal GaN substrates with low dislocation densities and reduced impurity concentrations, additional studies will be necessary to further decrease the overall quantity of point defects.

Only few reports on the ammonothermal crystallization of other group 13 nitrides are available as yet. BN was obtained from boron and $LiNH_2$ or KNH_2 at 820 K and 100–500 MPa.[84] However, elemental boron still occurred as a side phase even after a reaction time of 21 days, which indicates a very low reactivity in basic supercritical ammonia. Polycrystalline AlN was synthesized in both ammonoacidic and -basic environment using NH_4Cl or KNH_2 as mineralizers.[85,86] Solid solutions (Al,Ga)N were also successfully formed starting from Al/Ga alloys and NH_4Cl.[87] Whereas acidic syntheses only yielded nanocrystalline products so far, the growth of AlN on GaN seeds up to 1.5 mm in thickness was reported with KN_3 as mineralizer.[88]

In an earlier study, the possible ammonothermal synthesis of InN, from metallic indium with KNH_2 at 720 K, was stated but not described in any detail.[7] Successful crystallization and characterization of InN was recently reported using $InCl_3$ and KNH_2 as starting materials.[89,90] InN was obtained at 630–770 K and 190–280 MPa employing a ratio $InCl_3$: KNH_2 of 1:3. The presence of an ammononeutral environment was suggested, considering the stoichiometric formation of KCl. Plate-like crystals up to 2 µm in diameter and rod-shaped crystals up to 5 µm in length were observed. Selected InN crystals are depicted in Figure 3. The successful ammonothermal synthesis of InN provides new opportunities for the crystal growth of (Ga,In)N solid solutions. It should be noted that indium metal reacts with nickel-based superalloys, forming intermetallics like In_3Ni_2 along the grain boundaries, which can lead to severe damage of the autoclave.[91] For this reason, ceramic BN- and Si_3N_4-liners were used for the ammonothermal reactions. Experimental band gaps of InN are somewhat contradictory in the literature ranging from

0.6 to 1.9 eV, which can be ascribed to various interacting factors, for example, oxygen impurities, dopant concentrations, the Moss–Burstein effect, as well as respective evaluation methods.[92] Photoluminescence spectra of ammonothermal InN indicated an optical band gap of ≈1.8 eV.[90]

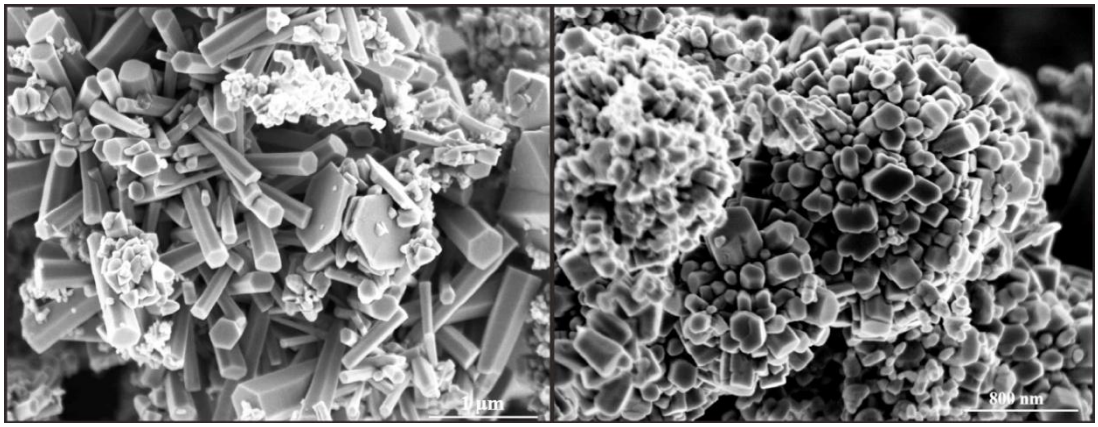

Figure 3. Scanning electron microscopy (SEM) images of InN crystals obtained by ammonothermal synthesis. Reproduced courtesy of J. Hertrampf.[90]

2.2.2 Ternary nitrides

The first ammonothermal syntheses of ternary nitrides were initiated by Jacobs and co-workers within systematic studies on alkali metal nitrides. They particularly investigated reactions of alkali amide melts with nitrides like Ta_3N_5, P_3N_5, and Si_3N_4. To improve the crystallinity of the products, synthesis temperatures had to be increased which in turn required high ammonia pressures to inhibit decomposition of the amides. Crystallization of the tantalum nitrides $MTaN_2$ (M=Na, K, Rb, Cs) was conducted between 673 and 1073 K and pressures up to 600 MPa (see Table 1). Ta_3N_5, Ta_2O_5, $TaCl_5$, or NH_4TaF_6 and an excess of alkali metal amides MNH_2 (M=Na, K, Rb, Cs) were used as starting materials.[93] Microcrystalline products were obtained, whereas single crystals of $NaTaN_2$ up to 30 µm in diameter were observed within syntheses of oxonitride perovskites.[18] The latter crystallizes in the α-$NaFeO_2$ type, whereas $KTaN_2$, $RbTaN_2$, and $CsTaN_2$ form a β-cristobalite like structure with K, Rb, and Cs occupied in all voids 12-fold coordinated by N. $NaTaN_2$ is chemically very stable, while the hydrolysis sensitivity increases from $KTaN_2$ to $CsTaN_2$. On the other hand, reactions of Ta_3N_5 with Li, Li_3N, or $LiNH_2$ result in the mixed valence tantalum nitride $Li_2Ta_3N_5$. Phase-pure products were obtained by ammonothermal synthesis at pressures of 600 MPa.[94] $Li_2Ta_3N_5$ crystallizes in a NaCl

superstructure with an ordered distribution of Li and Ta. The presence of Ta−Ta bonds was suggested with regard to the small interatomic distances, coinciding with reduced Ta^{3+} or Ta^{4+} ions next to Ta^{5+}.

Table 1. Ternary nitrides obtained by ammonothermal synthesis

Compound	Starting Material(s)	Mineralizer	Temp. [K]	Pressure [MPa]	Duration [h]	Lit.
$M TaN_2$ (M = Na, K, Rb, Cs)	Ta_3N_5, Ta_2O_5, $TaCl_5$ or NH_4TaF_6	MNH_2 (M = Na, K, Rb, Cs)	673 - 1073	≤ 600 [a]	120 - 600	[93]
$Li_2Ta_3N_5$	Ta_3N_5	$LiNH_2$	823	600	120	[94]
$K_3P_6N_{11}$	P_3N_5	KNH_2	773	600	168	[95]
$LiSi_2N_3$	Si	LiN_3	970 - 1070	100 - 170	100	[96]
$LiGe_2N_3$	Ge_3N_4	Li	900	150 - 230	100	[96]
$NaSi_2N_3$	Si	$NaNH_2$	923	600	120	[97]
$MgSiN_2$	Mg + Si	KN_3	1070	100 - 170	125	[96]
$MgGeN_2$	Mg + Ge	NaN_3	870	150 - 230	120	[96]
$MnSiN_2$	Mn + Si	KN_3	1070	100 - 170	125	[96]
$MnGeN_2$	Mn + Ge	NaN_3	870	150 - 230	120	[96]
$ZnSiN_2$	Zn + Si	LiN_3, NaN_3 or KN_3	870 - 1070	100 - 150	100	[15]
$ZnGeN_2$	Zn + Ge	LiN_3, NaN_3 or KN_3	870	150 - 230	95	[15]

[a] applied pressure dependent on synthesis temperature

Further, the behavior of silicon in ammonobasic and -acidic environments was examined. Jacobs et al. reported on the crystallization of a sodium nitridosilicate $NaSi_2N_3$, which is formed as polycrystalline powder by reaction of Si and excess $NaNH_2$ in supercritical

ammonia.[97] $NaSi_2N_3$ crystallizes in a wurtzite-derived superstructure in space group $Cmc2_1$. Reactions of Si with KNH_2 at 770–870 K and 600 MPa resulted in the formation of imidonitrides $K_3Si_6N_5(NH)_6$ and Si_2N_2NH.[98] $K_3Si_6N_5(NH)_6$ single crystals with a diameter of 300 µm were grown within 72 h, which indicates an adequate solubility of Si in ammonobasic KNH_2 solution. Si_2N_2NH was also obtained in acidic environment at 670 K and 200 MPa with NH_4Cl as mineralizer.[99] $NaSi_2N_3$ is structurally related to Si_2N_2NH, which is a defect variant of the wurtzite structure type with hydrogen bonded to the bridging twofold coordinated N atoms. Analogous attempted syntheses of $MSiN_2$ for M=K, Rb, Cs were not successful so far and resulted in unidentified products with low crystallinity.[97,99] Earlier studies in the system Li/Si indicated the formation of nanocrystalline $LiSi_2N_3$ in reactions of high surface area Si_3N_4 (HSA-Si_3N_4) with $LiNH_2$ at 570–670 K.[100] Well-crystalline products were obtained from Si and excess LiN_3 at higher reaction temperatures of 970 K, whereas Li_2SiN_2 was observed as second phase at 1070 K.[96] $LiGe_2N_3$ is isotypic to $LiSi_2N_3$ and can be synthesized from Ge_3N_4 with an excess of Li metal.[96]

The ammonolysis of P_3N_5 at 823 K and 600 MPa NH_3 results in microcrystalline phosphorus(V) nitride imide HPN_2. The latter is isoelectronic to SiO_2 and exhibits a distorted β-cristobalite-like structure. Deuterium positions in DPN_2, obtained from P_3N_5 and ND_3, were determined from synchrotron and neutron diffraction data.[101] Reactions of P_3N_5 with MNH_2 (M=Na, Rb, Cs) at 670–870 K yielded single crystals of imides and imidonitrides $Na_{10}[P_4(NH)_6N_4](NH_2)_6{\cdot}0.5\,NH_3$, $Rb_8[P_4N_6(NH)_4](NH_2)_2$ and $Cs_5[P(NH)_4](NH_2)_2$.[102-104] The former two compounds contain adamantane-like anions, with structural analogy to the lithium nitridophosphate $Li_{10}P_4N_{10}$.[105-107] On the other hand, $K_3P_6N_{11}$ represents the sole ammonothermally synthesized nitridophosphate so far, and can be obtained from P_3N_5 and KNH_2 at 773 K and 600 MPa NH_3 as microcrystalline powder.[95] The anionic P-N framework is analogous to the Si-N framework in the above mentioned $K_3Si_6N_5(NH)_6$, forming corner-sharing PN_4 tetrahedra, which can be separated in three symmetry equivalent chains along [1 0 0], [0 1 0], and [0 0 1] (Figure 4).[108] K^+ occupies the voids of the three-dimensional network with K(1) 8-fold and K(2) 9-fold coordinated by N.

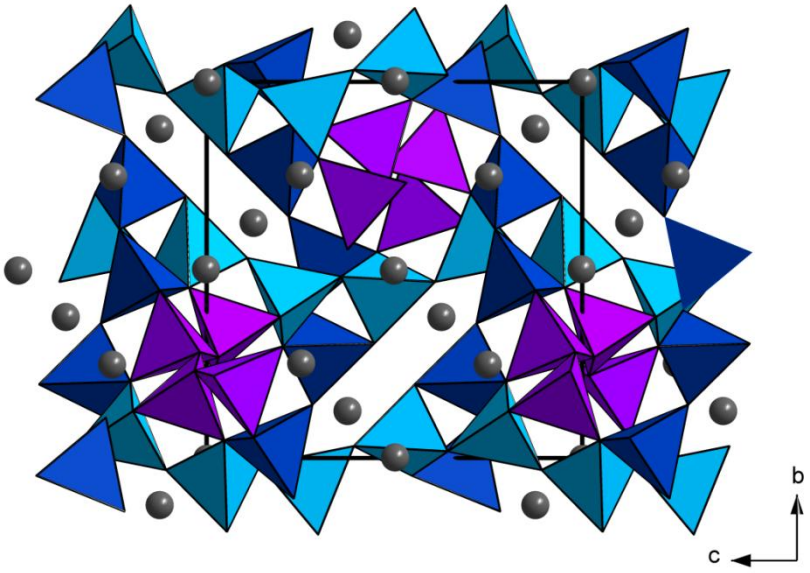

Figure 4. Crystal structure of $K_3P_6N_{11}$ viewed along [100] showing K atoms in gray and symmetry equivalent chains of PN_4 tetrahedra along [100] (purple), [010] (light blue) and [001] (dark blue).

Recently, we reported on the first ammonothermal synthesis of II-IV-N_2 nitrides with II=Mg, Mn, Zn and IV=Si, Ge. These materials are obtained by reaction of the respective elements with alkali metal azides NaN_3 or KN_3 as ammonobasic mineralizers. We observed that $MSiN_2$ (M=Mg, Mn, Zn) require high reaction temperatures of 1070 K to obtain well-crystalline products. On the other hand, lower temperatures are sufficient for $MGeN_2$, which in contrast are thermally less stable under specified ammonothermal conditions. The initial formation of intermediates and subsequent conversion to the nitrides at increasing reaction temperatures proved to be beneficial to obtain phase-pure products. Pressures above 100 MPa supported the crystallization process of these nitrides. Crystals were primarily in the nm to µm range, but exhibit well-defined faces as shown in Figure 5.[15,96]

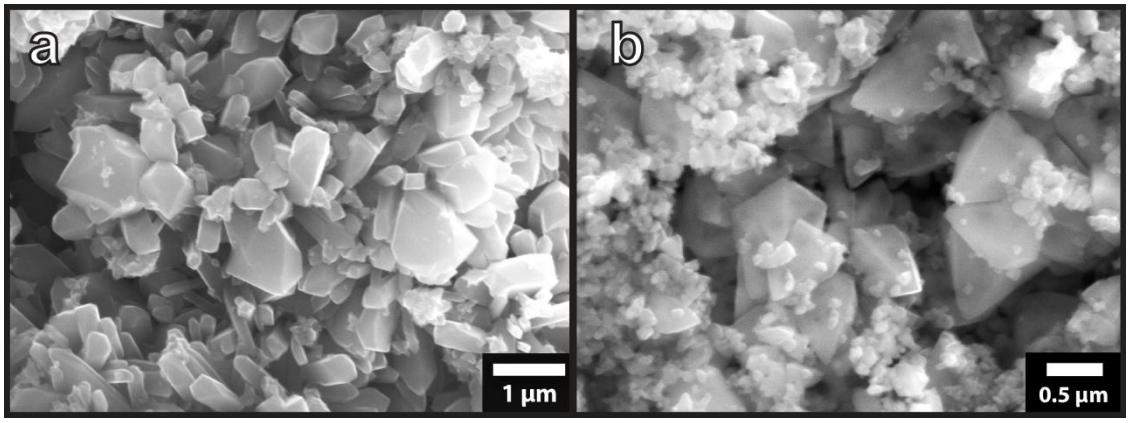

Figure 5. SEM images of $ZnSiN_2$ (a) and $ZnGeN_2$ crystals (b).[15]

Dissolution of $ZnGeN_2$ in ammonobasic supercritical ammonia was observed by in situ X-ray imaging, which exemplarily demonstrates a possible dissolution–recrystallization based mechanism of crystal growth. These findings are fundamental for the development of an ammonothermal growth process for ternary nitrides. Stated II-IV-N_2 compounds crystallize in a superstructure of hexagonal GaN with space group *Pna*2_1. Group-subgroup relations of III-N, II-IV-N_2, and I-IV_2-N_3 are illustrated in Figure 6.

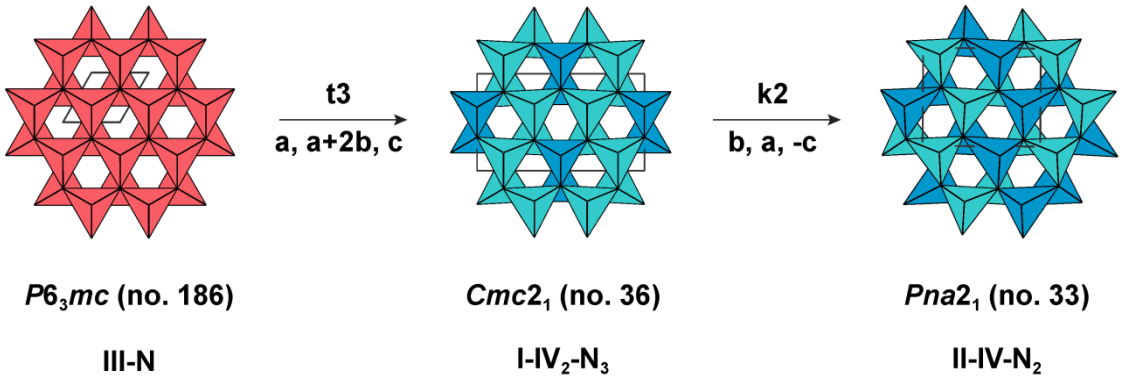

Figure 6. Group-subgroup relations of III-N, II-IV-N_2 and I-IV_2-N_3 type structures.[96]

Ternary II-IV-N_2 and I-IV_2-N_3 materials are of particular interest as possible next-generation semiconductors, due to their promising optical and electronic properties, the increased prospects for band-gap engineering compared to GaN, as well as the earth-abundance of the constituting elements.[96,109,110] Reported experimental band gaps for Grimm–Sommerfeld analogous nitrides are summarized in Figure 7. Similar lattice

parameters facilitate growth on GaN substrates, as well as formation of hybrid structures. For instance, spontaneous polarization differences of Zn-IV-nitrides are significantly smaller compared to (Al,Ga,In)N, which could suppress polarization fields in polar growth directions.[111] Besides, interesting luminescence properties for $MgSiN_2:Mn^{2+}$ were ascertained, while Mn-IV-N_2 materials could be attractive for spintronic applications.[112,113] However, this class of materials is still at an early stage of development and physical properties were scarcely investigated so far. The ammonothermal method could be well suitable for growth of larger single crystals, to facilitate detailed characterization of their optical and electronic properties.

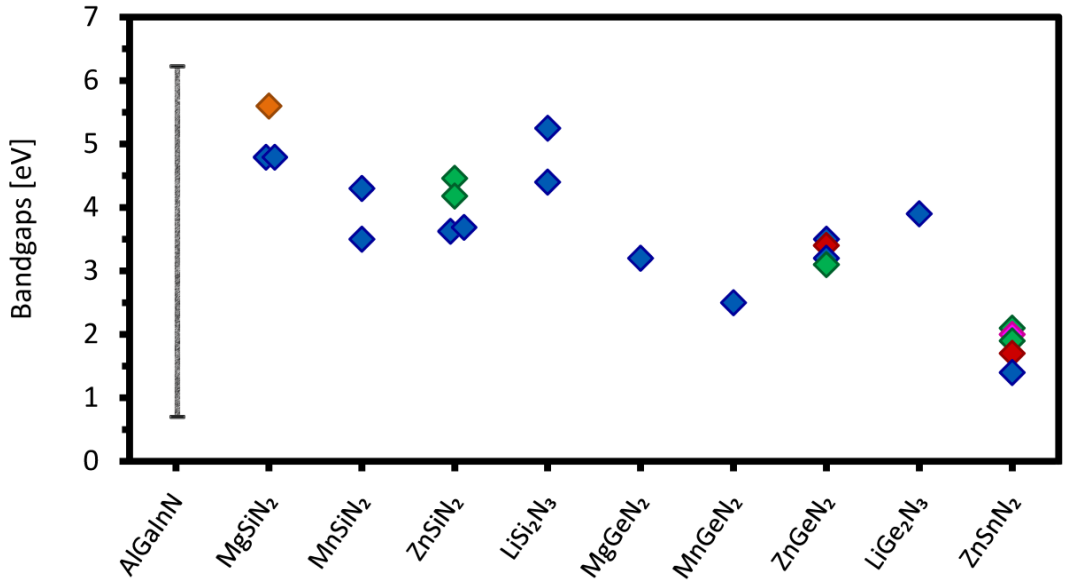

Figure 7. Band gap range of (Al,Ga,In)N solid solutions (gray) and experimental band gaps of Grimm-Sommerfeld analogous nitrides evaluated from UV-VIS spectroscopy (diffuse reflectance: blue, transmittance: green, absorption: pink), photoluminescence spectra (red) and X-ray absorption near-edge structure / X-ray emission spectroscopy (XANES / XES, orange). [15,96,112,114-126]

Another synthetic approach involves the ammonothermal synthesis of precursors and subsequent annealing at high temperatures, which was reported for $M_2Si_5N_8:Eu^{2+}$ (M=Sr, Ba). Dissolution of the starting materials in supercritical ammonia provides thorough mixing on an atomic level, and the formation of highly reactive amide or imide species. In this way, the synthesis temperature was considerably lowered compared to common high-temperature processes. Besides, uniformly shaped spherical particles with narrow

particle size distribution were obtained, which is favorable for luminescence applications of $M_2Si_5N_8:Eu^{2+}$.[127,128]

Overall, the ammonothermal method has been shown to be well suitable for the synthesis of ternary nitrides. In particular, compounds crystallizing in α-$NaFeO_2$ or β-cristobalite-analogous structures, as well as NaCl or wurtzite superstructures, were found to be stable in the examined systems. Other structures were observed for nitridophosphates ($K_3P_6N_{11}$) and also detected at higher reaction temperatures (Li_2SiN_2), or as a byproduct with CsN_3 as mineralizer ($Ca_{16}Si_{17}N_{34}$, Section 2.3).[16,96] All reported ternary nitrides were synthesized in an ammonobasic environment. Possible intermediates include binary and ternary amides containing monovalent and/or bivalent cations, as well as imides or imidonitrides of Si or P. [24,98,102-104] The formation of Ta or Ge intermediate species in supercritical ammonia has not been examined as yet. In addition, quantitative solubility data are virtually unknown, which hampers a controlled crystal growth of ternary nitrides. Crystal sizes in the range of up to 7 µm for $ZnSiN_2$ and 30 µm for $NaTaN_2$ were achieved so far. Converging solubilities of respective intermediates could be accomplished using new precursor compounds, which in turn would facilitate crystal growth by chemical transport reactions. On the other hand, growth from alkali metal amide melts or other flux agents within high-pressurized ammonia, as similarly proposed for lanthanide nitrides, might be feasible as well (Section 2.1.1).

2.2.3 Quaternary and multinary nitrides

During the last decade, the ammonothermal method was likewise employed for the synthesis of quaternary and multinary nitrides. In 2007, Li et al. reported on the ammonothermal synthesis of $CaAlSiN_3:Eu^{2+}$, an industrially important red phosphor for pc-LEDs.[129] $CaAlSiN_3:Eu^{2+}$ crystallizes in a superstructure of the wurtzite type with space group $Cmc2_1$ (Figure 8). Syntheses were conducted using intermetallic CaAlSi:Eu as starting material and $NaNH_2$ as mineralizer (see Table 2). The effect of temperature, pressure, and mineralizer concentration on crystallinity and luminescence properties was thoroughly investigated.[130,131] Initial formation of $CaAlSiN_3$ was observed between 770–870 K, albeit with poor crystallinity according to the powder X-ray diffraction data. The same holds for reactions in an ammonia flow, leading to very blurred and undefined reflections in the powder X-ray diffraction pattern. Crystallinity was considerably improved by employing higher reaction temperatures up to 1070 K. Here, the starting materials were first converted to reactive intermediates at 670 K, which were then slowly transformed to

the nitride with increasing temperature. This two-step approach is favorable since amides are preferably formed at lower temperatures and ammonia significantly decomposes at temperatures above 900 K at pressures in the order of 100 MPa. An average crystal size of ≈30–70 nm was estimated for $CaAlSiN_3$ using the Scherrer equation, while a few needle-shaped crystals with up to ≈600 nm in length were also observed by scanning electron microscopy. Crystallinity as well as photoluminescence efficiency revealed significant differences for varying pressures and mineralizer ratios. On the one hand, solid solutions with homeotypic $NaSi_2N_3$ according to $Na_xCa_{1-x}Al_{1-x}Si_{1+x}N_3$ are formed, dependent on mineralizer concentrations, which also affects the emission efficiencies. On the other hand, decomposition of intermediates could be promoted at reduced pressures, which decreased the observed Ca deficiency in the products. An atomic ratio Na:Ca between 2:1 and 5:1, as well as a pressure above 15 MPa, resulted in well-crystalline products, while pressures between 60 and 100 MPa yielded the highest photoluminescence intensity.

Table 2. Quaternary and multinary nitrides obtained by ammonothermal synthesis

Compound	Starting Material	Mineralizer	Temp. [K]	Pressure [MPa]	Duration [h]	Lit.
$CaAlSiN_3:Eu^{2+}$	CaAlSi:Eu	$NaNH_2$	773 - 1073	0.1 - 100	20 - 92	[129-131]
$CaAlSiN_3:Eu^{2+}$	Ca, Al, Si, Eu	NaN_3	850	100 - 200	240 - 720	[132]
$CaAlSiN_3:Li^+,Ce^{3+}$	CaAlSi: (Li,Ce)	$NaNH_2$ or Ca	1073	100	30 - 33	[133]
$SrAlSiN_3:Eu^{2+}$	SrAlSi:Eu	$NaNH_2$ or Sr	1073	100	30	[17,134]
$SrAlSiN_3:Na^+,Ce^{3+}$	SrAlSi: (Na,Ce)	Sr	1073	100	30	[135]
$CaGaSiN_3$ / $CaGaSiN_3:Eu^{2+}$	CaGaSi / CaGaSi:Eu	LiN_3 or NaN_3	1070	50 - 150	140 - 270	[16,136]
$Ca_{1-x}Li_xAl_{1-x}Ge_{1+x}N_3$ ($x \approx 0.2$)	$Ca_3Al_2Ge_2$	Li	925	185	95	[137]

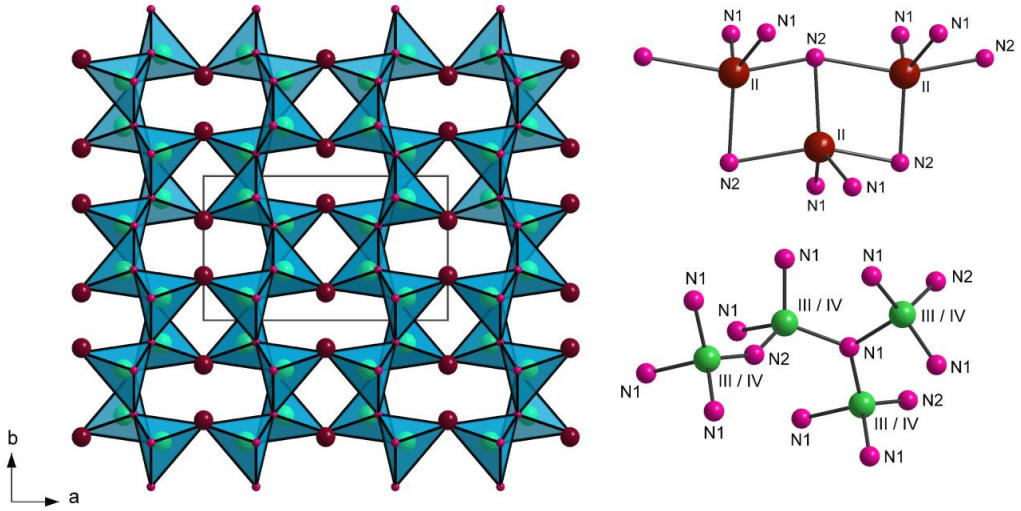

Figure 8. Left: Crystal structure of $M^{II}M^{III}M^{IV}N_3$ (cf. table 2) along [001] with M^{II} dark red, M^{III} / M^{IV} green, N pink. Right: Coordination of M^{II} and M^{III} / M^{IV} with nitrogen.

Synthesis of $CaAlSiN_3$ starting from the elements Ca, Al, Si and Eu was reported as well.[132] However, greatly prolonged reaction times are required for the nitride formation. The use of an intermetallic precursor provides a better mixing of intermediates on an atomic level and therefore facilitates the conversion to $CaAlSiN_3$. Low heating rates ensure a controlled nucleation and growth of the nitride by slow decomposition of the intermediates with increasing temperatures. An ammonia ratio of ≈13 % was calculated for 970 K and 100 MPa[138] and can be expected to be in the same order of magnitude, even though the internal temperature within the autoclave is not specified and the chemical equilibrium of ammonia decomposition is not necessarily reached within the reaction time (cf. Section 3). Nevertheless, much higher pressures would be required to enable dissolution-based processes, which in turn could facilitate the crystal growth of quaternary nitrides.

Isotypic $SrAlSiN_3:Eu^{2+}$ can be synthesized using an analogous route. Increased crystallinity and photoluminescence efficiency was achieved by using Sr instead of $NaNH_2$ as mineralizer, which can be attributed to a significant reduction of the Sr deficiency observed in ammonothermally formed $SrAlSiN_3$. The increased Sr concentration in the system resulted in bar- and plate-like crystals, whereas rather needle-shaped crystals were obtained with $NaNH_2$.[17,134] Phase-pure samples of $SrAlSiN_3$ were only attained by ammonothermal synthesis, as well as by high-pressure nitridation using a hot isostatic press (HIP).[139] Compared to the former, reported HIP syntheses yielded larger crystallites

with less defects and lower oxygen impurities. These differences also result in diverging photoluminescence properties of these materials, in particular a blueshift of the emission maximum for the ammonothermally obtained sample. The ammonothermal approach thus still requires further optimization, albeit a significant reduction of the synthesis temperature by ≈1100 K was achieved.

We recently reported on the ammonothermal synthesis of isotypic $CaGaSiN_3:Eu^{2+}$ which represents the first nitridosilicate containing GaN_4 tetrahedra within the anionic framework. The intermetallic CaGaSi:Eu and LiN_3 or NaN_3 were employed as starting materials. The use of KN_3 or CsN_3 as mineralizers resulted in $Ca_{16}Si_{17}N_{34}$ and GaN which indicates that $LiSi_2N_3$ or $NaSi_2N_3$, which are formed under similar conditions, might act as intermediates or crystallization seeds during these reactions. Crystals with up to 2 µm in length were obtained at 1070 K and 150 MPa (Figure 9), whereas rather poorly crystalline $CaGaSiN_3$ was formed at lower temperatures of 870 K or pressures below 100 MPa.[16] The crystal structure can be regarded as a superstructure of GaN; the formation of $CaGaSiN_3$ could thus underlie a similar mechanism within ammonothermal synthesis. Interestingly, the formation of $CaGaSiN_3$ is favored despite prevailing reaction conditions for the synthesis of GaN. This could be of particular interest for crystal growth strategies of further ordered superstructure compounds based on GaN. Eu^{2+} doped samples of $CaGaSiN_3$ show red luminescence by irradiation with blue light, with an emission maximum of 620 nm, which is in the same order as that of $SrAlSiN_3:Eu^{2+}$ obtained from HIP synthesis. Optical and electronic properties were examined by first-principles DFT calculations and compared to those of $CaAlSiN_3$.[136] The optical band gap of $CaGaSiN_3$ was estimated to be ≈3.2 eV by diffuse reflectance measurements and is thus considerably lower compared to $CaAlSiN_3$ (≈4.9 eV).[140]

Next to these nitridosilicates, we also reported on the novel nitridogermanate $Ca_{1-x}Li_xAl_{1-x}Ge_{1+x}N_3$ (x ≈0.2). This nitride was obtained from $Ca_3Al_2Ge_2$ and Li as mineralizer, and can be regarded as a solid solution of $LiGe_2N_3$ and hypothetical $CaAlGeN_3$. Ordering phenomena were investigated by scanning transmission electron microscopy high-angle annular dark-field (STEM-HAADF) imaging taking possible ordered structure models into account. The determined crystal structure was confirmed by *Z*-contrast imaging and is analogous to $CaAlSiN_3$ with Al/Ge disordered on Wyckoff site 8*b* and Ca/Li disordered on Wyckoff site 4*a*.[137] Well-defined crystals with up to 15 µm in length were observed, whereas the described nitridosilicates were found to be rather nanocrystalline. This indicates that Ge or its respective intermediates might possess higher solubilities in the supercritical fluid than Si-containing species. It was shown that

the ammonothermal approach represents a promising alternative to the common NaN_3 route for the synthesis of nitridogermanates.[23] The structural analogy to ternary nitrides like $LiSi_2N_3$ and $LiGe_2N_3$ further provides the opportunity for band gap engineering within these systems (Section 2.2).

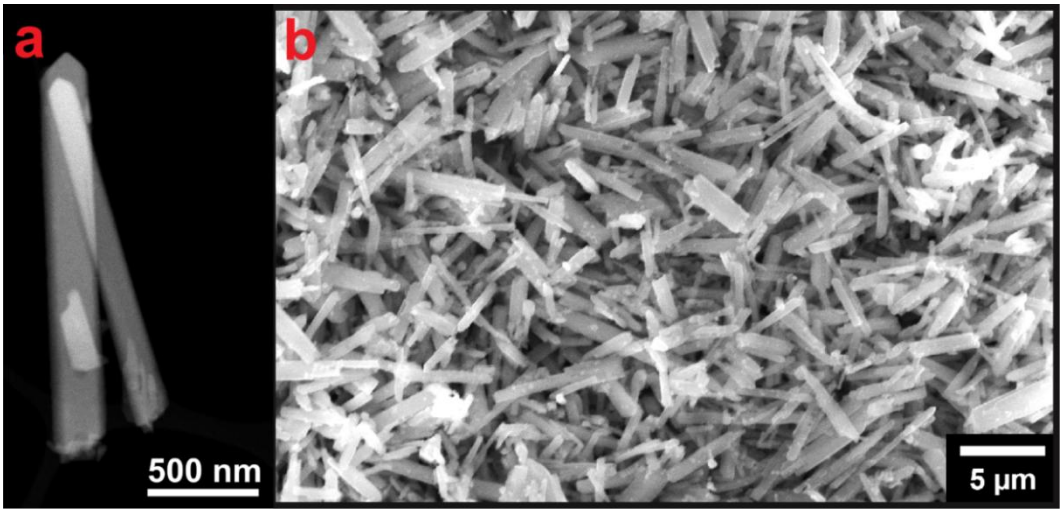

Figure 9. a) STEM dark-field image of $CaGaSiN_3:Eu^{2+}$ single crystals. b) SEM image of $Ca_{1-x}Li_xAl_{1-x}Ge_{1+x}N_3$ ($x \approx 0.2$).[16,137]

In summary, the above described systems offer a wide variability by cation substitutions and formation of solid solutions. Wurtzite-related nitridosilicates and -germanates seem to be preferably formed in the stated temperature and pressure ranges. However, the use of mineralizers like KN_3 or CsN_3 already indicated the possible formation of other nitridosilicates like $Ca_{16}Si_{17}N_{34}$ as well. Noteworthy, diverging solubilities and chemical reactivities of incorporated elements and respective intermediates have to be considered for ammonothermal synthesis of quaternary nitrides. Well-soluble species are partially transported to the colder peripheral parts of the autoclave, while hardly soluble compounds remain in the hot zone. In order to limit such transport, syntheses of mentioned nitrides were carried out in autoclaves with comparable small internal volumes of 5–10 mL. Considering the mole fraction of mineralizer, it can be assumed that alkali amide melts are present which could additionally confine chemical transport and promote crystal growth of the nitrides.

The ammonothermal approach proved to be particularly suitable for the synthesis of nitrides which are difficult to access by other methods. High temperatures of 2170 K with

nitrogen pressures of 190 MPa are required for an alternative synthesis of $SrAlSiN_3$, whereas $CaGaSiN_3$ and $Ca_{1-x}Li_xAl_{1-x}Ge_{1+x}N_3$ (x<1) were only obtained by the ammonothermal method as yet. Rather moderate temperatures for the ammonothermal synthesis of nitrides are sufficient, compared to other common routes, owing to the high reactivity of supercritical ammonia and respective intermediates. In particular synthesis of nitridogallates and -germanates is often hampered by their limited thermal stabilities. In this regard, the ammonothermal method could enable the discovery of further nitrides with unprecedented elemental compositions, as already demonstrated for $CaGaSiN_3$ and $Ca_{1-x}Li_xAl_{1-x}Ge_{1+x}N_3$. New autoclave technologies will be necessary to accomplish even higher pressures at 1070 K or above. In this way, dissolution and recrystallization based processes could be facilitated, and thus promote crystal growth of quaternary and multinary nitrides (see Section 3).

2.2.4 Oxonitrides

Oxonitrides comprise a further very intriguing class of compounds. For instance, various rare earth doped oxonitridosilicates possess excellent photoluminescence properties for possible application in light emitting diodes, whereas several novel oxonitridophosphates with unprecedented crystal structures were reported in recent years.[141-144] Inclusion of oxygen containing precursors in ammonothermal syntheses enables access to oxonitride materials as well. Previous studies focused on synthesis of oxonitrides with compositions $LnTaON_2$ (Ln=La, Pr, Nd, Sm, Ce, Gd), $LaNbON_2$, and $BaTaO_2N$ which all crystallize in the perovskite structure type (see Table 3). Watanabe et al. reported on the ammonothermal synthesis of $LaTaON_2$, where oxygen originated from impurities in the starting materials and autoclave walls. In other reports, NaOH was added as oxygen source and co-mineralizer. An alloy of La and Ta was used to accomplish a better mixing of the elements. Well-defined cube-shaped crystals were observed in the product. Reaction time and temperature did not significantly affect the crystal size or shape of $LaTaON_2$. Recent investigations on $LnTaON_2$ with Ln=La, Pr, Nd, Sm, Ce, Gd indicate that higher pressures could promote the crystal growth of oxonitrides, where sharp-edged crystals with up to 15 µm in size were observed.[18] SEM images of selected single crystals are shown in Figure 10.

Table 3. Oxonitrides obtained by ammonothermal synthesis

Compound	Starting Material	Mineralizer	Temp. [K]	Pressure [MPa]	Duration [h]	Lit.
$LaTaON_2$	LaTa [a]	$NaNH_2$	773 - 1073	100	15 - 75	[145]
Ln$TaON_2$ (*Ln* = La, Pr, Nd, Sm)	La, Pr, Nd or Sm + Ta	NaN_3 + NaOH	870	≤ 300	110	[18]
Ln$TaON_2$ (*Ln* = Ce, Gd)	Ce or Gd + Ta	NaN_3 + NaOH	1070	≤ 150	110	[18]
$LaNbON_2$	La_2Nb [a]	$NaNH_2$ + NaOH	1073	100	33	[146]
$BaTaO_2N$	Ba_3N_2 + TaON	$NaNH_2$ + NaOH	823 - 973	100	20	[147]

[a] nominal alloy composition

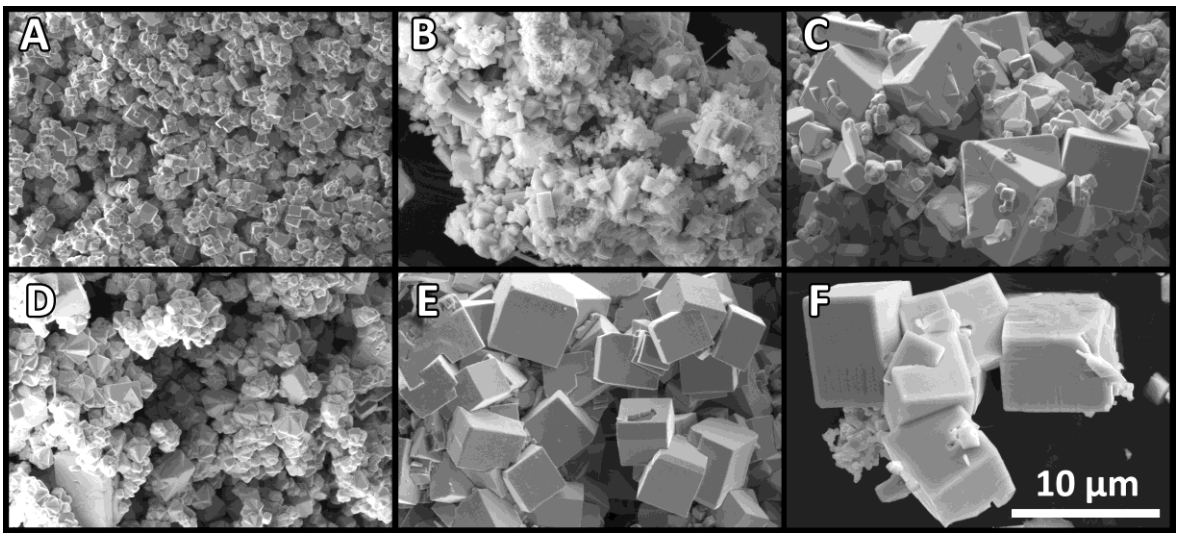

Figure 10. SEM images of a) $LaTaON_2$, b) $CeTaON_2$, c) $PrTaON_2$, d) $NdTaON_2$, e) $SmTaON_2$, f) $GdTaON_2$.[18]

This class of materials is of particular interest for photocatalytic water splitting. $LaNbON_2$ from ammonothermal synthesis showed marginal hydrogen evolution when doped with Sr or Ti. Higher rates were observed for $BaTaO_2N$, which can be synthesized from Ba_3N_2 and

TaON with mineralizers $NaNH_2$ and NaOH. Several parameters have to be addressed for an effective solar energy conversion, for example, photostability, positions of valance and conduction bands, crystallinity, morphology of the materials, and the type of co-catalyst.[148] In particular the control of morphology, crystallinity, defects, and particle size could be accomplished by a solution-based ammonothermal approach. For instance, the ammonothermal post-treatment of Ge_3N_4 and Ta_3N_5 effectively increased their photocatalytical activities, which was attributed to a decrease of defects in these nitrides.[149,150] Notably, hydrothermally synthesized $NaTaO_3$ showed far higher catalytic activity compared to conventional syntheses, which was attributed to high surface area, small particle size, and high crystallinity of the product.[151,152] Even though numerous studies addressed this field of research, photocatalyst efficiencies still require significant improvements to become economically attractive.

The deliberate inclusion of oxygen in ammonothermal processes strongly extends the potential of this method. While previous work is limited to perovskite oxonitrides, numerous new materials might be accessible within other systems as well. For instance, partial substitution of N by O in nitrido(alumino)silicates leads to the manifold class of Si(Al)ONs. Moreover, the linkage of (Al,Ga,In)N crystal growth to well-studied hydrothermal processes could pave the way to new semiconductors and photocatalysts such as ZnAlON or ZnGaON.[153,154]

2.3 Advance of autoclave technologies

2.3.1 Autoclaves and liner concepts

Autoclave materials for ammonothermal syntheses require high chemical stability against supercritical ammonia solutions, as well as high tensile strength, yield strength, and ductility at process temperatures. Nickel-based superalloys proved to be well-suited for ammonothermal reactors and components. Material properties of such alloys can be tailored by modulation of chemical compositions, as well as by thermal treatment of the raw material using post-fabrication processes like precipitation hardening. Typically employed materials in different research groups include Inconel 625, Inconel 718, René 41, as well as Haynes 282 alloy.[16,155-157] Exemplarily, autoclaves with upper temperature limits of 900 K at 300 MPa or 1100 K at 150–170 MPa were constructed, dependent on the respective material specifications and the autoclave design (Figure 11). Most of these materials are applicable for syntheses in ammonobasic environment, whereas severe

corrosion can occur with acidic mineralizers.[158,159] Liners or capsules are used to prevent corrosion of the autoclaves and to avoid incorporation of transition metals into the products. Recently, numerous materials were screened in terms of their chemical stability, using pure NH_3, $NaNH_2$, or NH_4Cl.[155] Another study investigated the behavior of NH_4X (X=F, Cl, I) solutions on diverse metallic samples.[160] Several materials were found to be applicable as liner materials, such as molybdenum for pure supercritical NH_3, $NaNH_2$, NH_4F, and NH_4Cl solutions, as well as silver for supercritical NH_3, $NaNH_2$, and NH_4F solutions. Non-hermetically sealed capsules made of silver or molybdenum were probed for ammonobasic growth of GaN, resulting in nearly transition metal free ($<1\times10^{17}$ cm^{-3}) crystals. Another approach implements liner-free titanium-zirconium-molybdenum (TZM) alloy autoclaves for acidic growth runs.[161] These autoclaves are designed for temperatures up to 925 K at pressures up to 150 MPa, and afford growth of GaN crystallites with negligible transition metal impurities as well.

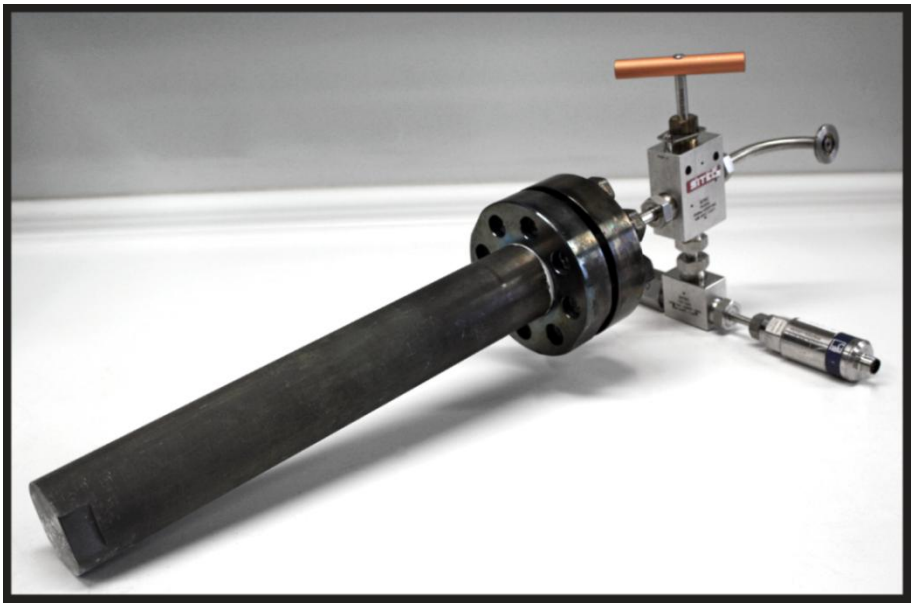

Figure 11. Autoclave made of Haynes 282 alloy with flange construction for explorative ammonothermal syntheses up to 1070 K and 170 MPa. The assembled head part consists of hand valve, pressure transmitter and safety head with integrated rupture disc.

Crystal growth of GaN is commonly performed at ≈800–900 K and 100–300 MPa, with an applied temperature gradient of ≈30–100 K. On the other hand, many ternary and quaternary nitrides were found to preferentially crystallize around the current upper temperature limit of ≈1100 K for common autoclave setups. From a thermodynamic point

of view, the ammonia equilibrium is strongly shifted to its decomposition products N_2 and H_2 even at the pressure limit of high-temperature autoclaves. Thereby, crystal growth is hampered due to insufficient quantity of solvent. Other effects of high nitrogen and hydrogen ratios are still unknown, though the latter can be expected to establish a reductive atmosphere within the autoclave.

Higher pressure inhibits the dissociation of ammonia, enables dissolution–recrystallization processes at high temperatures, and further increases solubility of ionic species. Very few materials could provide higher temperatures and pressures compared to the reported ones, for example, cobalt-based superalloys. However, such materials have not been examined with regard to long-term stability using supercritical ammonia and still require further investigations. Other concepts implement internal heaters, a thick ceramic inner shell, and an outer shell made of steel to circumvent material limitations of conventional reactors.[11,57] The low thermal conductivity of the ceramic retains the steel temperature below 470 K, where its high creep resistance is maintained. The reported vessel design sustains high pressures of up to 600 MPa at temperatures of 1025 K. Concepts from other high-pressure technologies like piston-cylinder or belt apparatus can be considered as well and have already been applied for hydrothermal processes.[5,6] An analogous setup for ammonothermal syntheses with considerable inner volume was developed employing sealed capsules placed in a high-pressure cell.[162] This alternative autoclave design was successfully tested for GaN crystal growth, and enables temperatures up to 1270 K with pressures up to 2 GPa. Using such techniques, novel autoclaves suitable for solution-based crystal growth of ternary and multinary nitrides at high temperatures could be designed. Besides, new nitrides might be accessible by extension of attainable parameter limits. Chemical stabilities of nitrides under ammonothermal conditions could additionally be increased by confining the reductive hydrogen atmosphere. Noteworthy, decomposition of ammonia is favored in the presence of catalysts, and the chemical equilibrium is not necessarily reached within the reaction time. Recent in situ Raman spectroscopy studies showed that ammonia decomposition is kinetically inhibited to some extent within common Inconel 718 autoclaves (Section 3.2.2).[163] Reduced decomposition of ammonia was also observed with silver capsules as the growth environment since silver is a poor catalyst for that process.[52] Pressure loss due to hydrogen diffusion through the autoclave walls is frequently observed at elevated temperatures, which was also restrained in experiments with silver capsules.

2.3.2 In situ autoclave technologies

Investigations of chemo-physical processes are fundamental to gain a deeper understanding of crystal growth in ammonothermal reactions. However, only little is known about the formation of intermediates, solution equilibria, and mass transport in supercritical ammonia. Direct insights into the autoclave chamber during running reactions help to illuminate crystallization mechanisms and to optimize technological processes. In situ X-ray techniques can be used to monitor dissolution and growth of crystals, and to determine solubilities of nitrides. Fundamental data on chemical reactions and solution equilibria can be obtained from spectroscopic in situ analyses. Besides, ultrasonic velocity measurements were recently employed for concentration determination of mineralizers or other dissolved species.

2.3.2.1 In situ X-ray imaging

High-pressure optical cells for in situ investigations are equipped with specially designed windows to provide improved X-ray transmission (see Figure 12). Sapphire was successfully applied as a window material for temperatures up to 925 K and pressures up to 300 MPa using $NaNH_2$, NH_4F, or NH_4Cl as mineralizers.

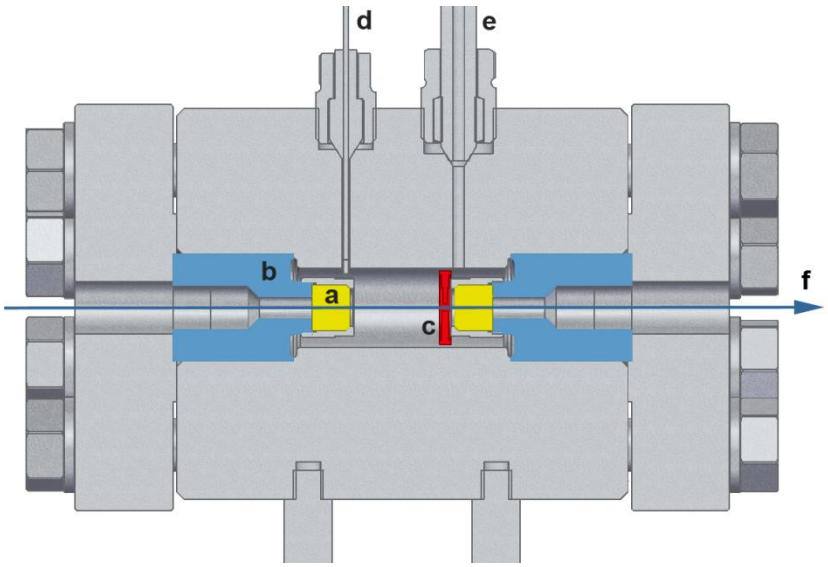

Figure 12. Schematic view of optical cell for in situ X-ray imaging and in situ Raman experiments. a) Sapphire windows, b) mount for windows, c) crystal mount, d) thermocouple, e) filling tube, f) beam path.

Other materials with improved X-ray transparency were also investigated as potential window or coating materials, identifying diamond as a material compatible with various mineralizers, and boron carbide as an excellent window material for experiments with Na-based mineralizers.[164]

For solubility measurements, crystals are clamped between two bolts of an Inconel 718 mount (gold-coated for acidic reactions) with an attached Inconel 718 fixing spring. The size of the crystal is monitored by 2D X-ray visualization probing different crystallographic directions (Figure 13). The dissolved volume over reaction time gives information about initiating dissolution as well as dissolution kinetics.[73,74] Hence, it is possible to differentiate between reaching the saturation point and dissolution by mass transport. Pressed pellets of powder samples can be used for dissolution monitoring as well. In this way, dissolvability of $ZnGeN_2$ was ascertained, which is a first fundamental step towards crystal growth of ternary nitride materials.[15]

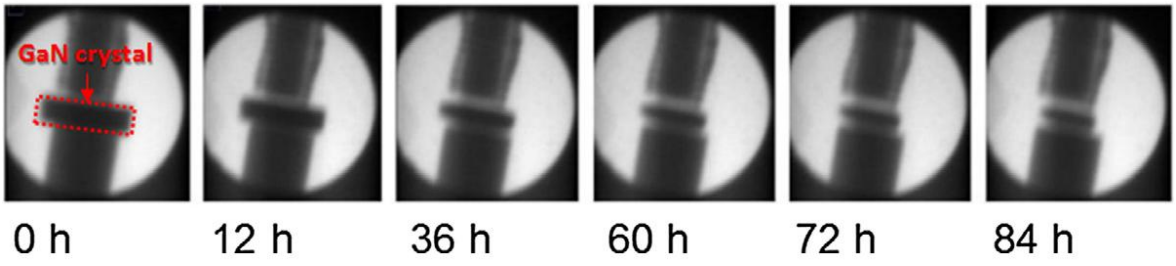

Figure 13. GaN crystal within Inconel 718 mount (0 h) and GaN dissolution over time at 815 K and 240–275 MPa (12–84 h) with NaN_3 as mineralizer monitored by in situ X-ray imaging. Reproduced with permission from ref. [74], Copyright Elsevier 2017.

2.3.2.2 In situ spectroscopy

The described optical cell can be employed for in situ spectroscopic studies as well. Raman spectra of supercritical ammonia solutions can be recorded using a backscattering setup where a laser beam is deflected on a dichroic mirror and focused into the optical cell. The backscattered light is detected in an angle of 0° and collected by a spectrometer. In this way, the formation of hydrogen and nitrogen, as well as possible intermediate compounds, can be monitored. A recent study showed that ammonia decomposition is restrained in common Inconel 718 autoclaves, which was attributed to passivation layers on the autoclave walls partially shielding the catalytically active metal surface. Besides, in situ formation of $NaNH_2$ from NaN_3 was monitored by Raman and UV/Vis spectroscopy.

The investigations indicate that degradation of dissolved NaN_3 to Na, and subsequent formation of $NaNH_2$, proceeds between 600 and 650 K.[163] Future studies could further give information about dissolved intermediates, as well as their formation and degradation conditions.

2.3.2.3 In situ ultrasonic velocity measurements

The velocity of ultrasonic waves passing through solutions is dependent on the kind of solvent, temperature, and pressure, as well as the concentration of dissolved species. For instance, the solubility of specific mineralizers can be determined in situ by measuring the ultrasonic velocity for different concentrations. The ultrasonic velocity remains constant as soon as the saturation point is reached. First indicative experiments have been reported for NaN_3 solutions in liquid ammonia up to 385 K.[165] A conventional Inconel 718 autoclave is employed, with an attached ultrasonic sensor at the outer wall for both generating and receiving the ultrasonic signals. The applicability for supercritical ammonia has been demonstrated as well, although the authors indicated that measurements for supercritical solutions are still in progress. Such investigations could provide accurate solubility data for different mineralizers, as well as further dissolved species under ammonothermal reaction conditions.

2.4 Future challenges and perspectives

During the last decade, the ammonothermal crystal growth of GaN has taken a major step forward, with significantly increased growth rates in different crystallographic directions, as well as improved crystal qualities. Meanwhile, ammonothermal GaN with superior crystal quality compared to HVPE GaN was demonstrated, however with generally higher concentrations of gallium vacancy complexes. Such complexes form deep levels in the band gap and cause increased sub-band-gap absorption, though the effect on device performances is still unclear. Exploring and confining the formation of point defects will be an important issue in future research. Besides, knowledge on crystallization and growth mechanisms is still fragmentary. Further data on solubilities, intermediates, and solution equilibria are required to effectively optimize growth rates of GaN. In situ X-ray and spectroscopic technologies are currently at an early stage of development, though, they will help to illuminate occurring crystallization processes, and can additionally provide fundamental data for the potential ammonothermal growth of (Al,Ga,In)N solid solutions.

While most current GaN devices are based on foreign substrates, their performances could be significantly increased using homoepitaxial processes. However, the price of sapphire or silicon carbide is still orders of magnitude lower compared to GaN substrates. The latter are thus preferred for specialized applications like high-performance laser diodes and not yet cost-effective for a broad range of devices. Maximum growth rates are limited by solubilities, transport rates and surface kinetics, though, ammonothermal growth processes offer excellent scalability growing on multiple seeds simultaneously. In this context, fundamental progress has already been made by different companies, in particular Ammono (Ammono-GaN), Soraa (scalable compact rapid ammonothermal, SCoRA™), and Mitsubishi (supercritical acidic ammonia technology, SCAAT™).[58,166,167] A considerable price reduction of ammonothermal GaN wafers could be accomplished by means of a commercial-scale manufacturing with significantly increased output volume.

The ammonothermal method further provided access to numerous ternary and multinary nitrides and thus accelerates fundamental solid-state chemistry. Recent studies showed that wurtzite-derived ternary and quaternary nitrides are preferably formed under ammonothermal conditions. Many of the reported compounds are merely difficult to access by other synthetic methods. In particular Grimm–Sommerfeld analogous II-IV-N_2 and I-IV_2-N_3 nitrides are of high interest as possible next-generation semiconductor materials, as they are predominantly composed of earth-abundant elements and offer a wide range of attainable band gaps. However, this class of compounds is still at an early stage of development and reported crystal sizes are merely in the low µm range. Larger single crystals could facilitate the precise characterization of optical and electronic properties. Besides, ammonothermal growth on GaN substrates could be promising to open up new application fields as well. The development of growth processes will be challenging due to the diverging solubilities of included elements. The exemplary dissolvability of $ZnGeN_2$ in ammonobasic supercritical ammonia has been demonstrated by in situ X-ray imaging, which is a first important step for a possible dissolution–recrystallization based growth process. In situ measurements are also beneficial to illuminate interaction of intermediates and their influence on crystallization and growth mechanisms. For instance, in situ spectroscopic methods can be used for identification of dissolved species, as well as their formation and degradation conditions, as indicated in recent investigations.[90] The use of new precursors, mineralizers or co-solvents with high relative permittivities could help to increase the solubility of Si or Ge containing species and to promote crystal growth of these nitrides. Apart from that, significantly higher pressures will be required to facilitate solution-based growth at temperatures of 1000 K

and beyond. The same holds for reported quaternary nitridosilicates, which are partially affected by lower crystallinity compared to common high-temperature methods.

The increase of synthesis temperature and pressure can be accomplished by means of new autoclave materials or internally heated capsule-based autoclave systems as described above. Exceeding the degradation temperature of amides within ammonothermal syntheses could afford crystal growth of other promising nitride materials as well. For instance, Zn_3N_2 represents an intriguing narrow-gap semiconductor material featuring small carrier effective masses and high carrier mobility.[109,168] Supposable intermediates in ammonobasic and -acidic systems were already reported, while its ammonothermal synthesis was assumed to require considerably higher process temperatures.[169,170] Moreover, new element combinations and mineralizer systems, along with an extension of parameter limits, could promote the discovery of novel multinary nitride materials as our recent studies already demonstrated. Explorative ammonothermal investigations are particularly promising for nitrides that are difficult to access by conventional high-temperature methods, as well as nitrides with limited thermal stability. On the other hand, the deliberate inclusion of oxygen within the starting materials, as well as an interlinking with hydrothermal approaches are promising strategies for the discovery of new oxonitride materials with unprecedented physical properties.

2.5 Conclusions

In the last few years, intriguing findings and discoveries have been made within ammonothermal research. Growth rates and quality of GaN were significantly improved and the access to ternary and multinary nitrides and oxonitrides with promising optical and electronic properties was achieved. New high-temperature autoclaves were developed to extend the maximum parameter limits, which enabled the synthesis of novel nitride materials. Further, new in situ technologies provided fundamental insights into dissolution and crystallization processes.

While native substrates are state of the art for virtually all commercial semiconductors, evolution of bulk GaN is still in progress. It can be expected that ammonothermal synthesis will supersede other growth techniques in the near future. The first light emitting diodes based on native ammonothermal GaN substrates, with very high efficiency, are already available on the market, yet still in the highly-priced segment. Upscaling comparable to hydrothermal growth of quartz could significantly decrease their production costs. Besides, further knowledge on solubilities, intermediates, and crystallization

mechanisms are beneficial to effectively optimize growth rates and to examine and reduce occurring point defects.

With regard to the ammonothermal synthesis of ternary nitrides, Grimm–Sommerfeld analogous II-IV-N_2 and I-IV_2-N_3 materials are of particular interest as they feature similar optical and electronic properties compared to (Al,Ga,In)N, and offer a wide range of attainable band gaps. Besides, they are predominantly composed of earth-abundant elements whereas elements like indium are becoming increasingly scarce. Further ternary zinc nitrides were recently screened regarding their band gaps and electronic properties, with the possible inclusion of divalent cations like Mg^{2+} or Mn^{2+} additionally increasing their variability.[96,109] In this way, design and tailoring of new materials with desired physical properties can be achieved using the ammonothermal approach as an explorative tool for their synthesis.

The deliberate inclusion of oxygen within the starting material further provided access to highly crystalline oxonitride perovskites. Such perovskites could be promising photocatalyst materials for water splitting, but still require additional research efforts and optimization. Ammonothermal syntheses also exhibit great potential for the exploratory discovery and crystal growth of novel nitride or oxonitride materials with intriguing optical and electronic properties as recently demonstrated for $CaGaSiN_3$ and $Ca_{1-x}Li_xAl_{1-x}Ge_{1+x}N_3$. The further extension of current parameter limits could unleash the full potential of this method and thereby pave the way to new innovative functional materials.

2.6 References

[1] G. Dhanaraj, K. Byrappa, V. Prasad, M. Dudley, *Springer Handbook of Crystal Growth* **2010**, Springer Berlin Heidelberg, Germany.

[2] S.-I. Hirano, S. Sōmiya, *Hydrothermal Reactions for Materials Science and Engineering*, Springer Dordrecht, Netherlands, **1989**.

[3] K. E. v. Schafhäutl, *Gelehrte Anzeigen Bayer. Akad.* **1845**, *20*, 557-596.

[4] R. W. Bunsen, *Ann. Chem. Pharm.* **1848**, *65*, 70-85.

[5] A. Rabenau, *Angew. Chem.* **1985**, *97*, 1017-1032; A. Rabenau, *Angew. Chem. Int. Ed.* **1985**, *24*, 1026-1040.

[6] K. Byrappa, M. Yoshimura, *Handbook of Hydrothermal Technology*, William Andrew Publishing, New York, USA, **2001**.

[7] B. Wang, M. J. Callahan, *Cryst. Growth Des.* **2006**, *6*, 1227-1246.

[8] R. Juza, H. Jacobs, H. Gerke, *Ber. Bunsenges. Phys. Chem.* **1966**, *70*, 1103-1105.

[9] H. Jacobs, D. Schmidt, *Curr. Top. Mater. Sci.* **1982**, *8*, 387-427.

[10] R. Dwiliński, A. Wysmołek, J. Baranowski, M. Kamińska, R. Doradziński, J. Garczyński, L. Sierzputowski, H. Jacobs, *Acta Phys. Pol. A* **1995**, *88*, 833-836.

[11] E. Dirk, T. P. Rajeev, S. K. Derrick, J. Wenkan, W. P. Douglas, C. D. Bradley, M. Melvin, P. D. E. Mark, *Jpn. J. Appl. Phys.* **2013**, *52*, 08JA01.

[12] S. Pimputkar, J. S. Speck, S. Nakamura, *J. Cryst. Growth* **2016**, *456*, 15-20.

[13] T. Paskova, D. A. Hanser, K. R. Evans, *Proc. IEEE* **2010**, *98*, 1324-1338.

[14] S. Nakamura, M. R. Krames, *Proc. IEEE* **2013**, *101*, 2211-2220.

[15] J. Häusler, S. Schimmel, P. Wellmann, W. Schnick, *Chem. Eur. J.* **2017**, *23*, 12275 - 12282.

[16] J. Häusler, L. Neudert, M. Mallmann, R. Niklaus, A.-C. L. Kimmel, N. S. A. Alt, E. Schlücker, O. Oeckler, W. Schnick, *Chem. Eur. J.* **2017**, *23*, 2583-2590.

[17] T. Watanabe, K. Nonaka, J. Li, K. Kishida, M. Yoshimura, *J. Ceram. Soc. Jpn.* **2012**, *120*, 500-502.

[18] N. Cordes, W. Schnick, *Chem. Eur. J.* **2017**, *23*, 11410-11415.

[19] M. Zeuner, S. Pagano, W. Schnick, *Angew. Chem.* **2011**, *123*, 7898-7920; *Angew. Chem. Int. Ed.* **2011**, *50*, 7754-7775.

[20] R.-J. Xie, H. T. Hintzen, *J. Am. Ceram. Soc.* **2013**, *96*, 665-687.

[21] R. Niewa, F. J. DiSalvo, *Chem. Mater.* **1998**, *10*, 2733-2752.

[22] N. Tapia-Ruiz, M. Segalés, D. H. Gregory, *Coord. Chem. Rev.* **2013**, *257*, 1978-2014.

[23] H. Yamane, F. J. DiSalvo, *Prog. Solid State Chem.* **2017**, DOI: 10.1016/j.progsolidstchem.2017.08.002.

[24] T. Richter, R. Niewa, *Inorganics* **2014**, *2*, 29-78.

[25] H. Jacobs, U. Fink, *Z. Anorg. Allg. Chem.* **1978**, *438*, 151-159.

[26] A. Stuhr, H. Jocobs, R. Juza, *Z. Anorg. Allg. Chem.* **1973**, *395*, 291-300.

[27] H. Jacobs, D. Kablitz, *Z. Anorg. Allg. Chem.* **1979**, *454*, 35-42.

[28] H. Jacobs, H. Kistrup, *Z. Anorg. Allg. Chem.* **1977**, *435*, 127-136.

[29] G. Linde, R. Juza, *Z. Anorg. Allg. Chem.* **1974**, *409*, 191-198.

[30] H. Jacobs, C. Stüve, *J. Less Common Met.* **1984**, *96*, 323-329.

[31] U. Zachwieja, H. Jacobs, *J. Less Common Met.* **1990**, *161*, 175-184.

[32] H. Jacobs, J. Bock, *J. Less Common Met.* **1987**, *134*, 215-220.

[33] G. Kreiner, H. Jacobs, *J. Alloys Compd.* **1992**, *183*, 345-362.

[34] M. Zając, J. Gosk, E. Grzanka, S. Stelmakh, M. Palczewska, A. Wysmołek, K. Korona, M. Kamińska, A. Twardowski, *J. Alloys Compd.* **2008**, *456*, 324-338.

[35] A. Leineweber, H. Jacobs, S. Hull, *Inorg. Chem.* **2001**, *40*, 5818-5822.

[36] S. P. DenBaars, D. Feezell, K. Kelchner, S. Pimputkar, C.-C. Pan, C.-C. Yen, S. Tanaka, Y. Zhao, N. Pfaff, R. Farrell, M. Iza, S. Keller, U. Mishra, J. S. Speck, S. Nakamura, *Acta Mater.* **2013**, *61*, 945-951.

[37] K. Shinohara, D. C. Regan, Y. Tang, A. L. Corrion, D. F. Brown, J. C. Wong, J. F. Robinson, H. H. Fung, A. Schmitz, T. C. Oh, S. J. Kim, P. S. Chen, R. G. Nagele, A. D. Margomenos, M. Micovic, *IEEE Trans. Electron Dev.* **2013**, *60*, 2982-2996.

[38] H.-D. Xiao, H.-L. Ma, Z.-J. Lin, J. Ma, F.-J. Zong, X.-J. Zhang, *Mater. Chem. Phys.* **2007**, *106*, 5-7.

[39] W. Utsumi, H. Saitoh, H. Kaneko, T. Watanuki, K. Aoki, O. Shimomura, *Nat. Mater.* **2003**, *2*, 735-738.

[40] D. Ehrentraut, E. Meissner, M. Bockowski, *Technology of Gallium Nitride Crystal Growth*, Springer Series in Materials Science, Springer, Berlin, Heidelberg, **2010**.

[41] J. Hertrampf, N. S. A. Alt, E. Schlücker, M. Knetzger, E. Meissner, R. Niewa, *J. Cryst. Growth* **2016**, *456*, 2-4.

[42] A. P. Purdy, R. J. Jouet, C. F. George, *Cryst. Growth Des.* **2002**, *2*, 141-145.

[43] Q. Bao, M. Saito, K. Hazu, K. Furusawa, Y. Kagamitani, R. Kayano, D. Tomida, K. Qiao, T. Ishiguro, C. Yokoyama, S. F. Chichibu, *Cryst. Growth Des.* **2013**, *13*, 4158-4161.

[44] Q. Bao, T. Hashimoto, F. Sato, K. Hazu, M. Saito, Y. Kagamitani, T. Ishinabe, R. Kayano, D. Tomida, K. Qiao, S. F. Chichibu, T. Ishiguro, C. Yokoyama, *CrystEngComm* **2013**, *15*, 5382-5386.

[45] A. P. Purdy, *Chem. Mater.* **1999**, *11*, 1648-1651.

[46] C. Yokoyama, T. Hashimoto, Q. Bao, Y. Kagamitani, K. Qiao, *CrystEngComm* **2011**, *13*, 5306-5308.

[47] D. Ehrentraut, N. Hoshino, Y. Kagamitani, A. Yoshikawa, T. Fukuda, H. Itoh, S. Kawabata, *J. Mater. Chem.* **2007**, *17*, 886-893.

[48] L. Y. Kuritzky, J. S. Speck, *MRS Commun.* **2015**, *5*, 463-473.

[49] R. Dwiliński, R. Doradziński, J. Garczyński, L. Sierzputowski, R. Kucharski, M. Zając, M. Rudziński, R. Kudrawiec, W. Strupiński, J. Misiewicz, *Phys. Status Solidi A* **2011**, *208*, 1489-1493.

[50] R. Kucharski, M. Zając, R. Doradziński, M. Rudziński, R. Kudrawiec, R. Dwiliński, *Semicond. Sci. Technol.* **2012**, *27*, 024007.

[51] S. Pimputkar, S. Kawabata, J. S. Speck, S. Nakamura, *J. Cryst. Growth* **2013**, *368*, 67-71.

[52] S. Pimputkar, S. Kawabata, J. S. Speck, S. Nakamura, *J. Cryst. Growth* **2014**, *403*, 7-17.

[53] Q. Bao, M. Saito, K. Hazu, Y. Kagamitani, K. Kurimoto, D. Tomida, K. Qiao, T. Ishiguro, C. Yokoyama, S. F. Chichibu, *J. Cryst. Growth* **2014**, *404*, 168-171.

[54] S. Pimputkar, *Dissertation*, University of California, Santa Barbara, USA, **2012**.

[55] M. Saito, Q. Bao, K. Kurimoto, D. Tomida, K. Kojima, Y. Kagamitani, R. Kayano, T. Ishiguro, S. F. Chichibu, in *10th International Workshop on Bulk Nitride Semiconductors (IWBNS-X)*, Espoo, Finland, **2017**.

[56] R. Dwiliński, R. Doradziński, J. Garczyński, L. Sierzputowski, R. Kucharski, M. Zając, M. Rudziński, R. Kudrawiec, J. Serafińczuk, W. Strupiński, *J. Cryst. Growth* **2010**, *312*, 2499-2502.

[57] W. Jiang, D. Ehrentraut, J. Cook, D. S. Kamber, R. T. Pakalapati, M. P. D'Evelyn, *Phys. Status Solidi B* **2015**, *252*, 1069-1074.

[58] Y. Mikawa, T. Ishinabe, S. Kawabata, T. Mochizuki, A. Kojima, Y. Kagamitani, H. Fujisawa, *Proc. SPIE* **2015**, *9363*, 936302.

[59] J. B. Shim, G. H. Kim, Y. K. Lee, *J. Cryst. Growth* **2017**, *478*, 85-88.

[60] S. Zhang, F. Hintze, W. Schnick, R. Niewa, *Eur. J. Inorg. Chem.* **2013**, *2013*, 5387-5399.

[61] S. Zhang, N. S. A. Alt, E. Schlücker, R. Niewa, *J. Cryst. Growth* **2014**, *403*, 22-28.

[62] J. Hertrampf, N. S. A. Alt, E. Schlücker, R. Niewa, *Eur. J. Inorg. Chem.* **2017**, *2017*, 902-909.

[63] J. Hertrampf, E. Schlücker, D. Gudat, R. Niewa, *Cryst. Growth Des.* **2017**, *17*, 4855–4863.

[64] J. Erlekampf, J. Seebeck, P. Savva, E. Meissner, J. Friedrich, N. S. A. Alt, E. Schlücker, L. Frey, *J. Cryst. Growth* **2014**, *403*, 96-104.

[65] I. Mirzaee, M. Charmchi, H. Sun, *Numer. Heat Transfer, Part A* **2016**, *70*, 460-491.

[66] H. Enayati, A. J. Chandy, M. J. Braun, *Int. J. Therm. Sci.* **2018**, *123*, 42-57.

[67] M. Yoshio, S. Osamu, T. Daisuke, Y. Chiaki, *Jpn. J. Appl. Phys.* **2016**, *55*, 05FC03.

[68] D. Ehrentraut, Y. Kagamitani, C. Yokoyama, T. Fukuda, *J. Cryst. Growth* **2008**, *310*, 891-895.

[69] D. Tomida, Y. Kagamitani, Q. Bao, K. Hazu, H. Sawayama, S. F. Chichibu, C. Yokoyama, T. Fukuda, T. Ishiguro, *J. Cryst. Growth* **2012**, *353*, 59-62.

[70] D. Bliss, B. Wang, M. Suscavage, R. Lancto, S. Swider, W. Eikenberry, C. Lynch, *J. Cryst. Growth* **2010**, *312*, 1069-1073.

[71] R. Kucharski, M. Rudziński, M. Zając, R. Doradziński, J. Garczyński, L. Sierzputowski, R. Kudrawiec, J. Serafińczuk, W. Strupiński, R. Dwiliński, *Appl. Phys. Lett.* **2009**, *95*, 131119.

[72] W. Jiang, D. Ehrentraut, B. C. Downey, D. S. Kamber, R. T. Pakalapati, H. D. Yoo, M. P. D'Evelyn, *J. Cryst. Growth* **2014**, *403*, 18-21.

[73] S. Schimmel, M. Lindner, T. G. Steigerwald, B. Hertweck, T. M. M. Richter, U. Künecke, N. S. A. Alt, R. Niewa, E. Schlücker, P. J. Wellmann, *J. Cryst. Growth* **2015**, *418*, 64-69.

[74] S. Schimmel, M. Koch, P. Macher, A.-C. L. Kimmel, T. G. Steigerwald, N. S. A. Alt, E. Schlücker, P. Wellmann, *J. Cryst. Growth* **2017**, *479*, 59-66.

[75] S. Griffiths, S. Pimputkar, J. S. Speck, S. Nakamura, *J. Cryst. Growth* **2016**, *456*, 5-14.

[76] R. Dwiliński, R. Doradziński, J. Garczyński, L. P. Sierzputowski, A. Puchalski, Y. Kanbara, K. Yagi, H. Minakuchi, H. Hayashi, *J. Cryst. Growth* **2008**, *310*, 3911-3916.

[77] D. Tomida, K. Kuroda, N. Hoshino, K. Suzuki, Y. Kagamitani, T. Ishiguro, T. Fukuda, C. Yokoyama, *J. Cryst. Growth* **2010**, *312*, 3161-3164.

[78] D. Tomida, T. Kuribayashi, K. Suzuki, Y. Kagamitani, T. Ishiguro, T. Fukuda, C. Yokoyama, *J. Cryst. Growth* **2011**, *325*, 52-54.

[79] S. Sintonen, P. Kivisaari, S. Pimputkar, S. Suihkonen, T. Schulz, J. S. Speck, S. Nakamura, *J. Cryst. Growth* **2016**, *456*, 43-50.

[80] S. Suihkonen, S. Pimputkar, S. Sintonen, F. Tuomisto, *Adv. Electron. Mater.* **2017**, *3*, 1600496.

[81] W. Jiang, M. Nolan, D. Ehrentraut, M. P. D'Evelyn, *Appl. Phys. Express* **2017**, *10*, 075506.

[82] F. Tuomisto, T. Kuittinen, M. Zając, R. Doradziński, D. Wasik, *J. Cryst. Growth* **2014**, *403*, 114-118.

[83] R. Kucharski, Ł. Janicki, M. Zajac, M. Welna, M. Motyka, C. Skierbiszewski, R. Kudrawiec, *Crystals* **2017**, *7*, 187.

[84] R. Dwiliński, R. Doradziński, J. Garczyński, L. Sierzputowski, M. Palczewska, A. Wysmolek, M. Kamińska, *MRS Internet J. Nitride Semicond. Res.* **1998**, *3*, e25.

[85] Y. C. Lan, X. L. Chen, Y. G. Cao, Y. P. Xu, L. D. Xun, T. Xu, J. K. Liang, *J. Cryst. Growth* **1999**, *207*, 247-250.

[86] D. Peters, *J. Cryst. Growth* **1990**, *104*, 411-418.

[87] Y. G. Cao, X. L. Chen, Y. C. Lan, J. Y. Li, Y. Zhang, Z. Yang, J. K. Liang, *Appl. Phys. A* **2001**, *72*, 125-127.

[88] B. T. Adekore, K. Rakes, B. Wang, M. J. Callahan, S. Pendurti, Z. Sitar, *J. Electron. Mater.* **2006**, *35*, 1104-1111.

[89] J. Hertrampf, N. S. A. Alt, E. Schlücker, R. Niewa, *Z. Kristallogr. Suppl.* **2016**, *36*, 73.

[90] J. Hertrampf, *Dissertation*, University of Stuttgart, Stuttgart, Germany, **2017**.

[91] B. Hertweck, *Dissertation*, University of Erlangen-Nuremberg, Erlangen, Germany, **2016**.

[92] K. S. A. Butcher, T. L. Tansley, *Superlattices Microstruct.* **2005**, *38*, 1-37.

[93] H. Jacobs, E. von Pinkowski, *J. Less Common Met.* **1989**, *146*, 147-160.

[94] T. Brokamp, H. Jacobs, *J. Alloys Compd.* **1991**, *176*, 47-60.

[95] H. Jacobs, R. Nymwegen, *Z. Anorg. Allg. Chem.* **1997**, *623*, 429-433.

[96] J. Häusler, R. Niklaus, J. Minár, W. Schnick, *Chem. Eur. J.* **2017**, DOI: 10.1002/chem.201704973.

[97] H. Jacobs, H. Mengis, *Eur. J. Solid State Inorg. Chem.* **1993**, *30*, 45-54.

[98] D. Peters, E. F. Paulus, H. Jacobs, *Z. Anorg. Allg. Chem.* **1990**, *584*, 129-137.

[99] H. Mengis, *Dissertation*, University of Dortmund, Dortmund, Germany, **1993**.

[100] S. Kaskel, M. Khanna, B. Zibrowius, H.-W. Schmidt, D. Ullner, *J. Cryst. Growth* **2004**, *261*, 99-104.

[101] H. Jacobs, R. Nymwegen, S. Doyle, T. Wroblewski, W. Kockelmann, *Z. Anorg. Allg. Chem.* **1997**, *623*, 1467-1474.

[102] H. Jacobs, S. Pollok, F. Golinski, *Z. Anorg. Allg. Chem.* **1994**, *620*, 1213-1218.

[103] F. Golinski, H. Jacobs, *Z. Anorg. Allg. Chem.* **1995**, *621*, 29-33.

[104] H. Jacobs, F. Golinski, *Z. Anorg. Allg. Chem.* **1994**, *620*, 531-534.

[105] W. Schnick, U. Berger, *Angew. Chem.* **1991**, *103*, 857-858; W. Schnick, U. Berger, *Angew. Chem. Int. Ed.* **1991**, *30*, 830-831.

[106] E.-M. Bertschler, C. Dietrich, T. Leichtweiß, J. Janek, W. Schnick, *Chem. Eur. J.* **2017**, DOI: 10.1002/chem.201704305.

[107] E.-M. Bertschler, R. Niklaus, W. Schnick, *Chem. Eur. J.* **2017**, DOI: 10.1002/chem.201704975.

[108] K. Landskron, W. Schnick, *J. Solid State Chem.* **2001**, *156*, 390-393.

[109] Y. Hinuma, T. Hatakeyama, Y. Kumagai, L. A. Burton, H. Sato, Y. Muraba, S. Iimura, H. Hiramatsu, I. Tanaka, H. Hosono, F. Oba, *Nat. Commun.* **2016**, 7:11962.

[110] A. D. Martinez, A. N. Fioretti, E. S. Toberer, A. C. Tamboli, *J. Mater. Chem. A* **2017**, *5*, 11418-11435.

[111] T. R. Paudel, W. R. L. Lambrecht, *Phys. Rev. B* **2009**, *79*, 245205.

[112] C. J. Duan, A. C. A. Delsing, H. T. Hintzen, *J. Lumin.* **2009**, *129*, 645-649.

[113] D. Naveh, L. Kronik, *Phys. Status Solidi B* **2006**, *243*, 2159-2163.

[114] C. M. Fang, R. A. d. Groot, R. J. Bruls, H. T. Hintzen, G. d. With, *J. Phys.: Condens. Matter* **1999**, *11*, 4833-4842.

[115] T. de Boer, T. D. Boyko, C. Braun, W. Schnick, A. Moewes, *Phys. Status Solidi RRL* **2015**, *9*, 250-254.

[116] T. Endo, Y. Sato, H. Takizawa, M. Shimada, *J. Mater. Sci. Lett.* **1992**, *11*, 424-426.

[117] J. Muth, A. Cai, A. Osinsky, H. Everitt, B. Cook, I. Avrutsky, *Mater. Res. Soc. Symp. Proc.* **2005**, *831*, E11.45.1-5.

[118] A. Osinsky, V. Fuflyigin, L. D. Zhu, A. B. Goulakov, J. W. Graff, E. F. Schubert, in *Proc. 2000 IEEE / Cornell Conference on High Performance Devices*, **2000**, pp. 168-172.

[119] F. Liang, L. Tian, H. Zhang, F. Liang, S. Liu, R. Cheng, S. Zhang, *RSC Adv.* **2016**, *6*, 68615-68618.

[120] K. Du, C. Bekele, C. C. Hayman, J. C. Angus, P. Pirouz, K. Kash, *J. Cryst. Growth* **2008**, *310*, 1057-1061.

[121] M. Shang, J. Wang, J. Fan, H. Lian, Y. Zhang, J. Lin, *J. Mater. Chem. C* **2015**, *3*, 9306-9317.

[122] F. Kawamura, N. Yamada, M. Imai, T. Taniguchi, *Cryst. Res. Technol.* **2016**, *51*, 220-224.

[123] P. C. Quayle, K. He, J. Shan, K. Kash, *MRS Commun.* **2013**, *3*, 135-138.

[124] F. Deng, H. Cao, L. Liang, J. Li, J. Gao, H. Zhang, R. Qin, C. Liu, *Opt. Lett.* **2015**, *40*, 1282-1285.

[125] C.-H. Kuo, K.-S. Chang, *Cryst. Growth Des.* **2017**, *17*, 4694-4702.

[126] N. Feldberg, B. Keen, J. D. Aldous, D. O. Scanlon, P. A. Stampe, R. J. Kennedy, R. J. Reeves, T. D. Veal, S. M. Durbin, *IEEE PVSC* **2012**, 002524-002527.

[127] M. Zeuner, F. Hintze, W. Schnick, *Chem. Mater.* **2009**, *21*, 336-342.

[128] M. Zeuner, P. J. Schmidt, W. Schnick, *Chem. Mater.* **2009**, *21*, 2467-2473.

[129] J. Li, T. Watanabe, H. Wada, T. Setoyama, M. Yoshimura, *Chem. Mater.* **2007**, *19*, 3592-3594.

[130] J. Li, T. Watanabe, N. Sakamoto, H. Wada, T. Setoyama, M. Yoshimura, *Chem. Mater.* **2008**, *20*, 2095-2105.

[131] J. Li, T. Watanabe, H. Wada, T. Setoyama, M. Yoshimura, *J. Am. Ceram. Soc.* **2009**, *92*, 344-349.

[132] J. Cho, B. K. Bang, S. J. Jeong, C. H. Kim, *RSC Adv.* **2014**, *4*, 23218-23222.

[133] Y. Maruyama, T. Watanabe, *J. Ceram. Soc. Jpn.* **2016**, *124*, 66-69.

[134] K. Nonaka, K. Kishida, C. Izawa, T. Watanabe, *J. Ceram. Soc. Jpn.* **2014**, *122*, 17-20.

[135] Y. Maruyama, Y. Yanase, T. Watanabe, *J. Ceram. Soc. Jpn.* **2017**, *125*, 399-401.

[136] R. Niklaus, J. Minar, J. Häusler, W. Schnick, *PCCP* **2017**, *19*, 9292-9299.

[137] J. Häusler, L. Eisenburger, O. Oeckler, W. Schnick, *Eur. J. Inorg. Chem.* **2017**, DOI: 10.1002/ejic.201701314.

[138] A. T. Larson, *J. Am. Chem. Soc.* **1924**, *46*, 367-372.

[139] H. Watanabe, H. Yamane, N. Kijima, *J. Solid State Chem.* **2008**, *181*, 1848-1852.

[140] L. Wang, R.-J. Xie, Y. Li, X. Wang, C.-G. Ma, D. Luo, T. Takeda, Y.-T. Tsai, R.-S. Liu, N. Hirosaki, *Light Sci Appl.* **2016**, *5*, e16155.

[141] M. Seibald, T. Rosenthal, O. Oeckler, C. Maak, A. Tücks, P. J. Schmidt, D. Wiechert, W. Schnick, *Chem. Mater.* **2013**, *25*, 1852-1857.

[142] C. Maak, R. Niklaus, F. Friedrich, A. Mähringer, P. J. Schmidt, W. Schnick, *Chem. Mater.* **2017**, *29*, 8377-8384.

[143] S. J. Sedlmaier, M. Döblinger, O. Oeckler, J. Weber, J. Schmedt auf der Günne, W. Schnick, *J. Am. Chem. Soc.* **2011**, *133*, 12069-12078.

[144] A. Marchuk, L. Neudert, O. Oeckler, W. Schnick, *Eur. J. Inorg. Chem.* **2014**, *2014*, 3427-3434.

[145] T. Watanabe, K. Tajima, J. Li, N. Matsushita, M. Yoshimura, *Chem. Lett.* **2011**, *40*, 1101-1102.

[146] C. Izawa, T. Kobayashi, K. Kishida, T. Watanabe, *Adv. Mater. Sci. Eng.* **2014**, *465720*, 1-5.

[147] T. Toshima, K. Kishida, Y. Maruyama, T. Watanabe, *J. Ceram. Soc. Jpn.* **2017**, *125*, 643-647.

[148] P. Zhang, J. Zhang, J. Gong, *Chem. Soc. Rev.* **2014**, *43*, 4395-4422.

[149] Y. Lee, T. Watanabe, T. Takata, M. Hara, M. Yoshimura, K. Domen, *J. Phys. Chem. B* **2006**, *110*, 17563-17569.

[150] K. Kishida, T. Watanabe, *J. Ceram. Soc. Jpn.* **2014**, *122*, 156-160.

[151] J. W. Liu, G. Chen, Z. H. Li, Z. G. Zhang, *Int. J. Hydrogen Energy* **2007**, *32*, 2269-2272.

[152] L. Yungi, W. Tomoaki, T. Tsuyoshi, H. Michikazu, Y. Masahiro, D. Kazunari, *Bull. Chem. Soc. Jpn.* **2007**, *80*, 423-428.

[153] K. Maeda, T. Takata, M. Hara, N. Saito, Y. Inoue, H. Kobayashi, K. Domen, *J. Am. Chem. Soc.* **2005**, *127*, 8286-8287.

[154] M. Zhong, Y. Ma, P. Oleynikov, K. Domen, J.-J. Delaunay, *Energy Environ. Sci.* **2014**, *7*, 1693-1699.

[155] S. Pimputkar, T. F. Malkowski, S. Griffiths, A. Espenlaub, S. Suihkonen, J. S. Speck, S. Nakamura, *J. Supercrit. Fluids* **2016**, *110*, 193-229.

[156] T. G. Steigerwald, N. S. A. Alt, B. Hertweck, E. Schluecker, *J. Cryst. Growth* **2014**, *403*, 59-65.

[157] K. Yoshida, K. Aoki, T. Fukuda, *J. Cryst. Growth* **2014**, *393*, 93-97.

[158] B. Hertweck, T. G. Steigerwald, N. S. A. Alt, E. Schluecker, *Chem. Eng. Technol.* **2014**, *37*, 1903-1906.

[159] B. Hertweck, T. G. Steigerwald, N. S. A. Alt, E. Schluecker, *J. Supercrit. Fluids* **2014**, *95*, 158-166.

[160] B. Hertweck, S. Zhang, T. G. Steigerwald, N. S. A. Alt, R. Niewa, E. Schluecker, *Chem. Eng. Technol.* **2014**, *37*, 1835-1844.

[161] T. F. Malkowski, S. Pimputkar, J. S. Speck, S. P. DenBaars, S. Nakamura, *J. Cryst. Growth* **2016**, *456*, 21-26.

[162] M. P. D'Evelyn, H. C. Hong, D. S. Park, H. Lu, E. Kaminsky, R. R. Melkote, P. Perlin, M. Lesczynski, S. Porowski, R. J. Molnar, *J. Cryst. Growth* **2007**, *300*, 11-16.

[163] T. G. Steigerwald, J. Balouschek, B. Hertweck, A.-C. L. Kimmel, N. S. A. Alt, E. Schlücker, *J. Supercrit. Fluids* **2017**, DOI: 10.1016/j.supflu.2017.12.028.

[164] S. Schimmel, U. Künecke, M. Meisel, B. Hertweck, T. G. Steigerwald, C. Nebel, N. S. A. Alt, E. Schlücker, P. Wellmann, *J. Cryst. Growth* **2016**, *456*, 33-42.

[165] H. Baser, W. Schwieger, D. Freitag, T. G. Steigerwald, E. Schluecker, *Chem. Eng. Technol.* **2017**, *40*, 1101-1106.

[166] M. P. D'Evelyn, D. Ehrentraut, W. Jiang, D. S. Kamber, B. C. Downey, R. T. Pakalapati, H. D. Yoo, *ECS Trans.* **2013**, *58*, 287-294.

[167] R. Stevenson, *IEEE Spectrum* **2010**, *47*, 40-45.

[168] X. Cao, Y. Ninomiya, N. Yamada, *Phys. Status Solidi A* **2017**, *214*, 1600472.

[169] T. M. M. Richter, N. S. A. Alt, E. Schlücker, R. Niewa, *Z. Anorg. Allg. Chem.* **2016**, *642*, 1207-1211.

[170] T. M. M. Richter, S. LeTonquesse, N. S. A. Alt, E. Schlücker, R. Niewa, *Inorg. Chem.* **2016**, *55*, 2488-2498.

3 Ammonothermal Synthesis of Earth-abundant Nitride Semiconductors $ZnSiN_2$ and $ZnGeN_2$ and Dissolution Monitoring by In Situ X-ray Imaging

published in: *Chem. Eur. J.* **2017**, *23*, 12275 - 12282.

authors: Jonas Häusler, Saskia Schimmel, Peter Wellmann, and Wolfgang Schnick

DOI: 10.1002/chem.201701081

http://onlinelibrary.wiley.com/doi/10.1002/chem.201701081/abstract

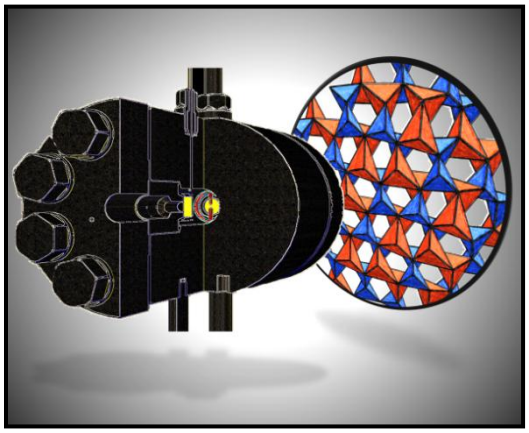

Abstract. In this contribution, first synthesis of semiconducting $ZnSiN_2$ and $ZnGeN_2$ from solution is reported with supercritical ammonia as solvent and KNH_2 as ammonobasic mineralizer. The reactions were conducted in custom-built high-pressure autoclaves made of nickel-based superalloy. The nitrides were characterized by powder X-ray diffraction and their crystal structures were refined by the Rietveld method. $ZnSiN_2$ (a = 5.24637(4), b = 6.28025(5), c = 5.02228(4) Å, Z = 4, R_{wp} = 0.0556) and isotypic $ZnGeN_2$ (a = 5.46677(10), b = 6.44640(12), c = 5.19080(10) Å, Z = 4, R_{wp} = 0.0494) crystallize in the orthorhombic space group $Pna2_1$ (no. 33). The morphology and elemental composition of the nitrides were examined by electron microscopy and energy-dispersive X-ray spectroscopy (EDX). Well-defined single crystals with a diameter up to 7 µm were grown by ammonothermal synthesis at temperatures between 870 and 1070 K and pressures up to 230 MPa. Optical properties have been analyzed with diffuse reflectance measurements. The band gaps of $ZnSiN_2$ and $ZnGeN_2$ were determined to be 3.7 and 3.2 eV at room temperature, respectively. In situ X-ray measurements were performed to exemplarily investigate the crystallization mechanism of

$ZnGeN_2$. Dissolution in ammonobasic supercritical ammonia between 570 and 670 K was observed which is quite promising for the crystal growth of ternary nitrides under ammonothermal conditions.

3.1 Introduction

Gallium nitride and respective solid solutions (Al,Ga,In)N represent one of the most important materials for optoelectronic semiconductor devices. The development of new semiconducting materials is a key aspect of current research due to the rapidly growing market, the increasing number of application fields, and in addition the scarcity of elements like gallium and indium. Recently, various ternary zinc nitrides have been screened in terms of electronic structure, dopability, and stability using first-principle calculations.[1] In particular, the Grimm–Sommerfeld analogous compounds $Zn(Si,Ge,Sn)N_2$ feature similar structural, optical, and electronic properties to (Al,Ga,In)N.[2,3] Promising superior properties have been predicted as well, such as similar spontaneous polarization parameters which could diminish the issue of polarization fields in heterostructures.[3,4] The ternary zinc nitrides also offer excellent band gap tunability and additional substitution sites, which enable a further modification of the electronic band structure. Besides, they are comprised of earth-abundant elements and feature high chemical and thermal stability.

About 25 years ago, Endo et al. demonstrated the synthesis of $ZnSiN_2$ and $ZnGeN_2$ using a high-pressure belt-type apparatus.[5] Powder samples were synthesized starting from the binary nitrides at pressures up to 6.5 GPa and temperatures between 1300 and 1900 K. With the exploration of the semiconducting properties, these compounds attracted increasing interest, which promoted the development of new epitaxy processes. Thin films of $ZnMN_2$ (M = Si, Ge, Sn) can be deposited on specific substrates by metalorganic vapor phase epitaxy (MOVPE) or molecular beam epitaxy (MBE) techniques.[6-8] However, no synthetic approach for the growth of bulk single crystals of these ternary nitrides have been developed as yet.

Ammonothermal syntheses comprise solvothermal reactions using supercritical ammonia as the solvent. In analogy to the well-studied hydrothermal crystal growth of quartz, single crystals of binary nitrides like AlN and GaN can be grown from solution by convection-driven chemical transport reactions.[9] The autoclaves are sectioned in dissolution and growth zones applying specific temperature gradients. Specially designed baffle plates are used to reach a constant temperature around the crystallization seed and to control the

convection flow of the supercritical fluid. Mineralizers like alkali metal amides or ammonium halides are added to increase the solubility of the starting materials and to form intermediates, which also act as transporting agents.

Semiconductor performance can be extensively increased using single crystalline GaN wafers for homoepitaxial growth processes instead of conventional substrates like sapphire.[10] Meanwhile, GaN growth rates over 300 µm per day in different crystallographic directions and single crystals with more than 50 mm in diameter have been demonstrated by the ammonothermal method.[11-13] Ternary and quaternary nitrides can be synthesized ammonothermally as well, such as $NaSi_2N_3$, $K_3P_6N_{11}$, and $CaGaSiN_3$.[14-16] While the optimization of AlN and GaN growth processes is still an important aspect in current research, the ammonothermal crystal growth of ternary nitrides has not been reported in literature so far. In addition, only little is known about occurring intermediates and their solubilities under ammonothermal reaction conditions.

In this contribution, we report on the ammonothermal synthesis, as well as on the structural and optical characterization, of the ternary zinc nitrides $ZnSiN_2$ and $ZnGeN_2$. Specially designed autoclaves equipped with sapphire windows were used to investigate the dissolution behavior and kinetics by in situ X-ray imaging.

3.2 Results and Discussion

3.2.1 Synthesis

$ZnSiN_2$ and $ZnGeN_2$ were synthesized by the ammonothermal method under ammonobasic conditions. Different mineralizers were found to be suitable for the synthesis, notably MNH_2 with M = Li, Na, and K. The alkali metal amides were formed in situ using the respective azides MN_3. The latter were preferred as they exhibit long-term stability towards oxygen and moisture. The decomposition of the azides at elevated temperatures and the subsequent reaction of the alkali metal with ammonia leads to the formation of MNH_2. Our experiments showed that the best crystallinity of the nitrides is obtained using KNH_2 as the mineralizer. Since KNH_2 exhibits the highest solubility of the investigated mineralizers, we assume that a higher basicity of the supercritical ammonia solution might support crystal growth.[17] The reactions were conducted in two steps taking the preferential formation of amides at lower temperatures and the significant decomposition of ammonia beyond 850 K into account:[18,19] Reactive intermediate compounds were formed at 570–670 K which were gradually decomposed to the nitrides

at temperatures up to 1070 K. After the reaction, the residual mineralizer and zinc intermediates were removed by washing the product with water and 1 M HCl. $ZnSiN_2$ and $ZnGeN_2$ were obtained as pale beige and light yellow powders, respectively. We observed that pressures above 100 MPa were necessary to obtain well-crystallized products, which can be explained with higher NH_3 mole fractions and better solubilities of ionic compounds with increasing pressures.[19,20] Zn was used in 25 % excess due to a higher expected solubility of $Zn(NH_2)_2$ and ternary zinc amides in comparison to Si, Ge, or respective intermediates. Amorphous side-phases were detected when employing 1:1 mixtures of Zn:Si/Ge, which can be attributed to unreacted Si/Ge-containing intermediates. With regard to $ZnSiN_2$, only small particles in the range up to 50 nm were obtained at 870 K, while well-defined crystals with diameters beyond 5 µm could be grown at 1070 K (see electron microscopy section). On the other hand, lower temperatures were sufficient for the synthesis of well-crystalline $ZnGeN_2$. We ascertained that $ZnGeN_2$ decomposed at reaction temperatures above 950 K. While the majority of the crystals were in the range of 200 nm, several crystals up to 1 µm in diameter were observed as well. The lower average crystal size compared to $ZnSiN_2$ can be attributed to slower growth kinetics at 870 K. Due to the well-defined morphology of the crystals, a growth mechanism from solution is likely. The growth of significantly larger crystals could then be performed using crystallization seeds and transport reactions with specific temperature gradients. To corroborate a dissolution–recrystallization based mechanism, we performed dissolution experiments in analogy to the formation of intermediates during the ammonothermal crystal growth of GaN (see section dissolution monitoring by in situ X-ray imaging).

3.2.2 Powder X-ray diffraction (PXRD)

Indexing of the PXRD patterns indicated that both $ZnSiN_2$ and $ZnGeN_2$ crystallize with orthorhombic metrics. Systematic absences suggest space group $Pna2_1$ which coincides with the investigations of Endo et al.[5] Rietveld refinement was carried out using Wyckoff positions and atomic coordinates from the literature as starting values.[5] No side-phases were detected in the powder X-ray diffraction patterns (see Figure 1). The crystallographic data obtained from Rietveld refinement are represented in Table 1, atomic coordinates are listed in Tables S1 and S2 (see the Supporting Information).

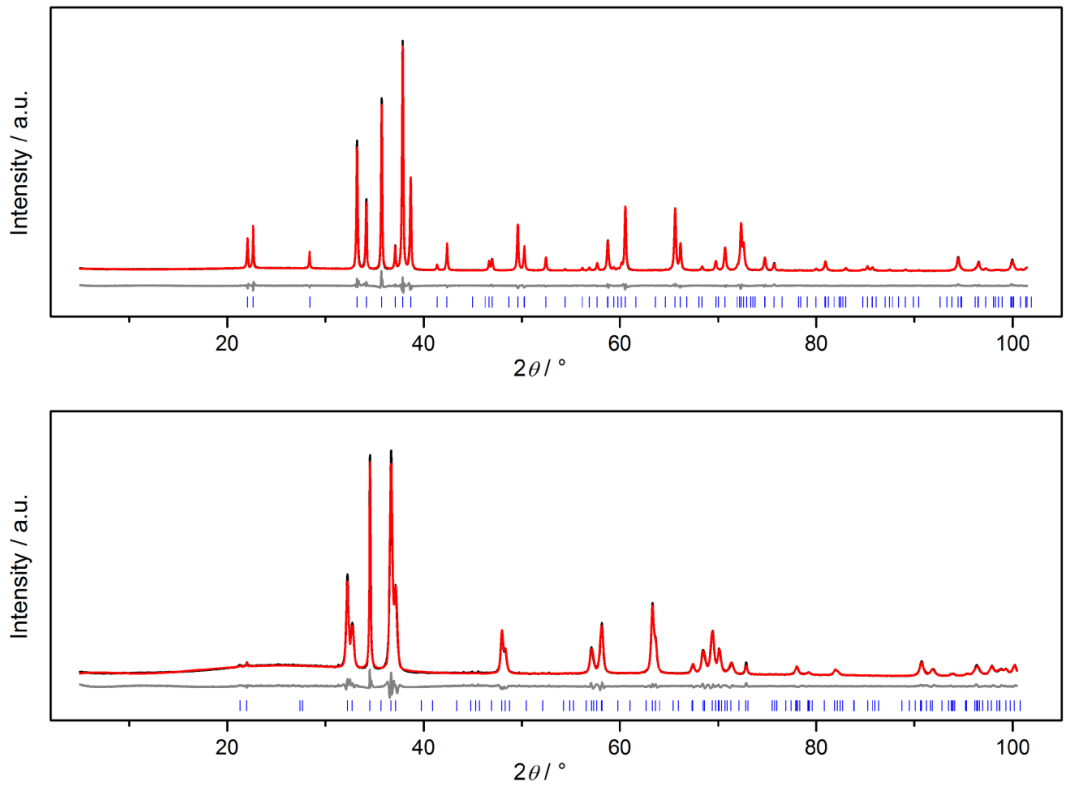

Figure 1. Rietveld refinement of $ZnSiN_2$ (top) and $ZnGeN_2$ (bottom) with experimental data (black lines, Cu-$K_{\alpha1}$ radiation, λ = 1.540596 Å), calculated patterns (red lines), difference profiles (gray lines) and positions of Bragg reflections (blue bars).

In $ZnMN_2$ (M = Si, Ge), Zn and M are tetrahedrally coordinated by N. The ZnN_4 and MN_4 tetrahedra are corner-sharing forming a three-dimensional network with a degree of condensation (i.e., the atomic ratio (Zn,M) : N) of κ = 1 (see Figure 2). The crystal structure is isotypic to β-$NaFeO_2$ and represents a 2×√3 superstructure of the wurtzite structure type.[21] For $ZnGeN_2$, some other studies proposed a disordered wurtzite-type structure with hexagonal space group $P6_3mc$ which is apparently dependent on the synthesis method and reaction conditions.[22] Recently, it was also shown that the degree of ordering can be increased by annealing disordered phases at 1120 K.[23] In comparison to wurtzite-type $ZnGeN_2$, peak splitting was observed in the PXRD, which is consistent with the described orthorhombic structure. The expected (1 1 0) and (0 1 1) superstructure reflections were identified in the diffraction pattern,[23] albeit these are very weak due to the similar scattering factors of Zn and Ge.

Table 1. Crystallographic data of $ZnSiN_2$ and $ZnGeN_2$ obtained from Rietveld refinement

Formula	**$ZnSiN_2$**	**$ZnGeN_2$**
Crystal system	orthorhombic	
Space group	*Pna*2_1 (no. 33)	
a [Å]	5.24637(4)	5.46677(10)
b [Å]	6.28025(5)	6.44640(12)
c [Å]	5.02228(4)	5.19080(10)
Cell volume [Å^3]	165.477(2)	182.929(6)
Density [g·cm^{-3}]	4.8764	6.0279
Formula units per cell	4	
T [K]	293(2)	
Diffractometer	STOE STADI P	
Radiation [Å]	Cu-$K_{\alpha1}$ (λ = 1.540596 Å)	
2θ range [°]	5.0 ≤ 2θ ≤ 101.5	
Profile function	fundamental parameters model	
Background function	Shifted Chebyshev	
Data points	6432	6365
Number of reflections	102	110
Refined parameters	53	50
R values	R_p = 0.0419 R_{wp} = 0.0556 R_{Bragg} = 0.0198	R_p = 0.0387 R_{wp} = 0.0494 R_{Bragg} = 0.0150
GoF	2.433	2.539

Interatomic Zn−N and Si−N distances in $ZnSiN_2$ are between 2.04–2.08 Å and 1.70–1.79 Å, while the Zn−N and Ge−N distances in $ZnGeN_2$ range from 2.01–2.07 Å and 1.85–1.93 Å, respectively. The calculated distances from Rietveld refinement are comparable to earlier reported values.[5]

Temperature-programmed powder X-ray diffraction (TP-PXRD) up to 1270 K was performed to investigate the thermal stability of $ZnSiN_2$ and $ZnGeN_2$ as well as possible changes in the crystal structure (see Figures S1 and S2 in the Supporting Information). According to the diffraction patterns, $ZnSiN_2$ is stable up to temperatures beyond 1270 K, while $ZnGeN_2$ decomposes between 1170 and 1220 K. Both compounds retain the above described orthorhombic crystal structure in the specified temperature range.

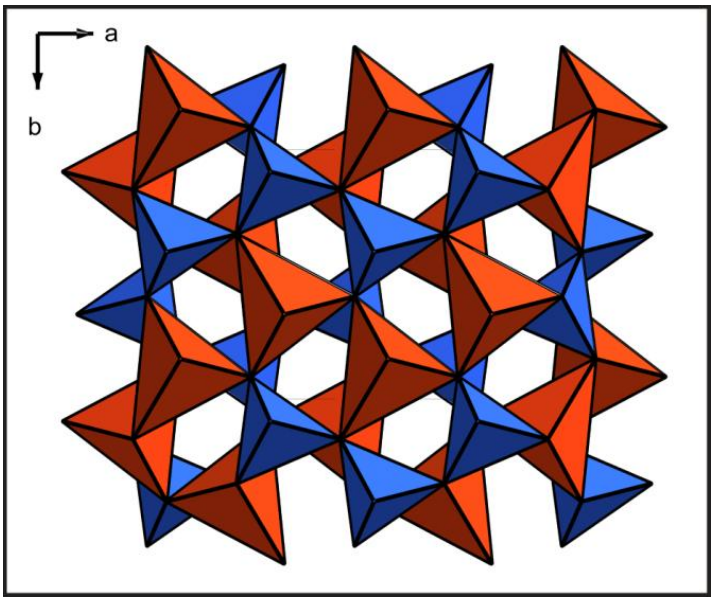

Figure 2. Crystal structure of Zn*M*N_2 (*M* = Si, Ge) viewed along [001]. The ZnN_4 tetrahedra are depicted in blue, the *M*N_4 tetrahedra in orange.

3.2.3 Scanning/transmission electron microscopy (SEM/TEM)

SEM images show that individual crystals of $ZnSiN_2$ up to 7 µm in diameter were grown during the reactions, while the majority exhibits a size around 1 µm (see Figure 3 a and b). On the other hand, the crystals of $ZnGeN_2$ are in the range up to 1 µm due to the lower feasible reaction temperatures (see Figure 3 c and d). The well-shaped morphology indicates a solution-based growth mechanism of the crystals, which is quite promising for potential growth processes of bulk single crystals of ternary nitrides.

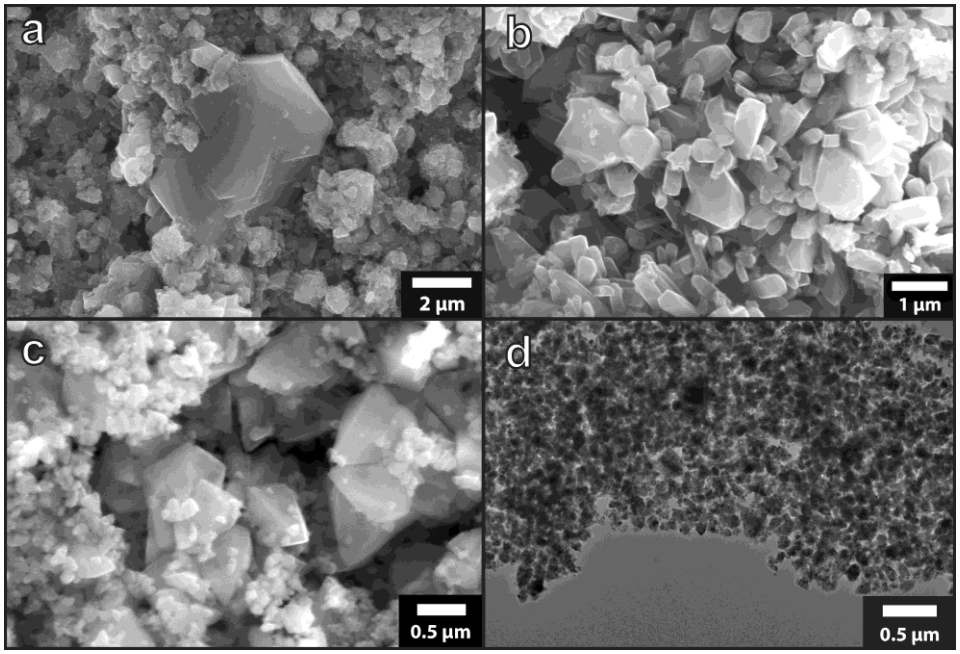

Figure 3. SEM images of $ZnSiN_2$ (a, b) crystals. SEM (c) and TEM (d) images of $ZnGeN_2$ crystals.

The EDX data coincide with the composition of $ZnSiN_2$ and $ZnGeN_2$ within the measurement accuracy (see Table 2). The residual mineralizer was almost entirely removed from the product. Small oxygen and chloride impurities most likely arise from the washing treatment with H_2O and 1 M HCl.

Table 2. SEM EDX measurements of $ZnSiN_2$ and $ZnGeN_2$ in atom %; mean values of five crystallites

$ZnSiN_2$	**Zn**	**Si**	**N**	**O**	**K**	**Cl**
	21.3	22.1	53.4	3.0	0.1	0
$ZnGeN_2$	**Zn**	**Ge**	**N**	**O**	**K**	**Cl**
	24.4	26.7	45.2	3.3	0.2	0.1

3.2.4 UV/Vis spectroscopy

Diffuse reflectance spectra were measured to investigate the optical properties of the synthesized materials. The reflectance (R) spectra were first converted to pseudo-absorption through the Kubelka–Munk function $F(R) = (1-R)^2/2R$.[24] Tauc plots were then used to determine the optical band gaps by drawing a tangent at the inflection points (see

Figure 4).[25] While $ZnGeN_2$ is a direct band gap semiconductor, calculations for $ZnSiN_2$ predict an indirect band gap (U_v–Γ_c) which is ≈0.2 eV smaller in comparison to the direct gap (Γ_v–Γ_c).[21] The observed absorption in the spectrum was primarily attributed to the direct transition with regard to the minor difference between the direct and indirect band gap, which also coincides with optical measurements of $ZnSiN_2$ from the literature.[26] The evaluated band gaps are 3.7 and 3.2 eV for $ZnSiN_2$ and $ZnGeN_2$, respectively.

Numerous diverging values for the band gaps have been reported for ternary zinc nitrides. Calculations for $ZnGeN_2$ yielded values between 1.57 and 3.99 eV, while indirect and direct band gaps of $ZnSiN_2$ range from 3.23 to 6.01 eV and 3.45 to 6.26 eV, respectively.[1,21,27] These discrepancies can be ascribed to different approximation methods which partially lead to considerable under- or overestimation of the band gaps. On the other hand, the experimentally determined band gaps reveal significant differences as well. Reported values for $ZnGeN_2$ and $ZnSiN_2$ range from 2.7 to 3.5 eV and 3.6 to 4.5 eV, respectively.[5,26,28-30] This divergence can have various reasons such as differing synthesis conditions, measuring methods, defect and impurity concentrations, or the degree of ordering. Yet, the diffuse reflectance measurements of ammonothermally synthesized $ZnSiN_2$ and $ZnGeN_2$ are in the same range as the other referred experimental band gaps.

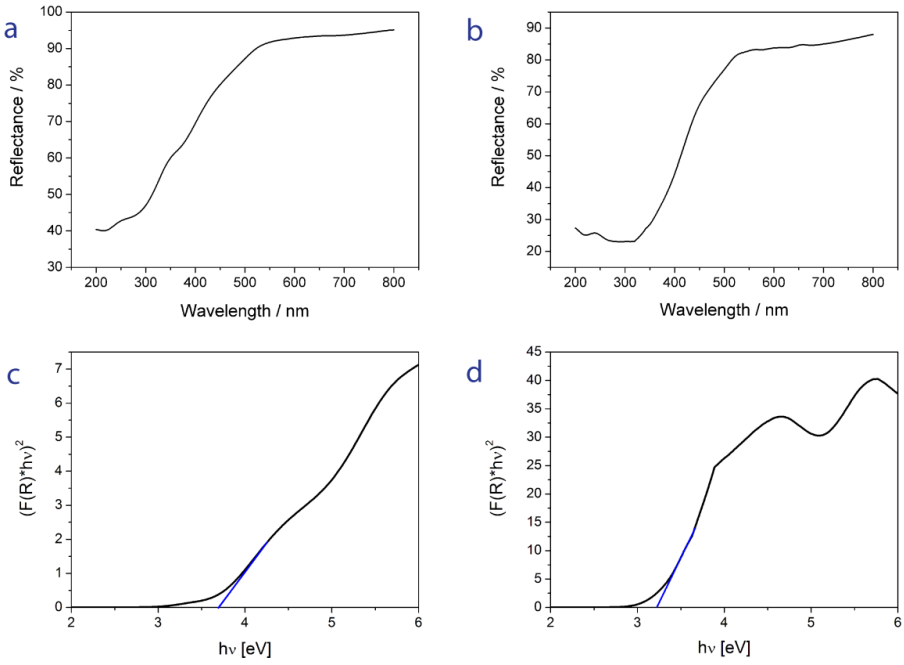

Figure 4. Diffuse reflectance measurements of $ZnSiN_2$ (a), $ZnGeN_2$ (b), and respective Tauc plots (c, d).

3.2.5 Dissolution monitoring by in situ X-ray imaging

Crystal growth by solvothermal methods is commonly carried out utilizing temperature-dependent reversible dissolution and crystallization of the materials. Commonly, a temperature gradient is applied to obtain dissolution and growth zones, which enable chemical transport of the materials. To evaluate the pressure and temperature range for dissolution, orienting dissolution experiments with $ZnGeN_2$ were performed and monitored by in situ X-ray imaging. Temperature and pressure over time for this experiment are shown in Figure 5. The term “internal temperature” refers to the temperatures measured inside the autoclave close to the inner wall of the reaction chamber whereas ′external temperature′ refers to the temperature in the heating sleeve that was used to heat the autoclave. Selected in situ X-ray images are shown in Figure 6. As it can be seen from the first images (0:00 h and 7:29 h), the $ZnGeN_2$ pellet is well visible and yields a contrast that is comparable to GaN (GaN images for comparison and considerations regarding contrast can be seen in our previous in situ investigations).[31,32]

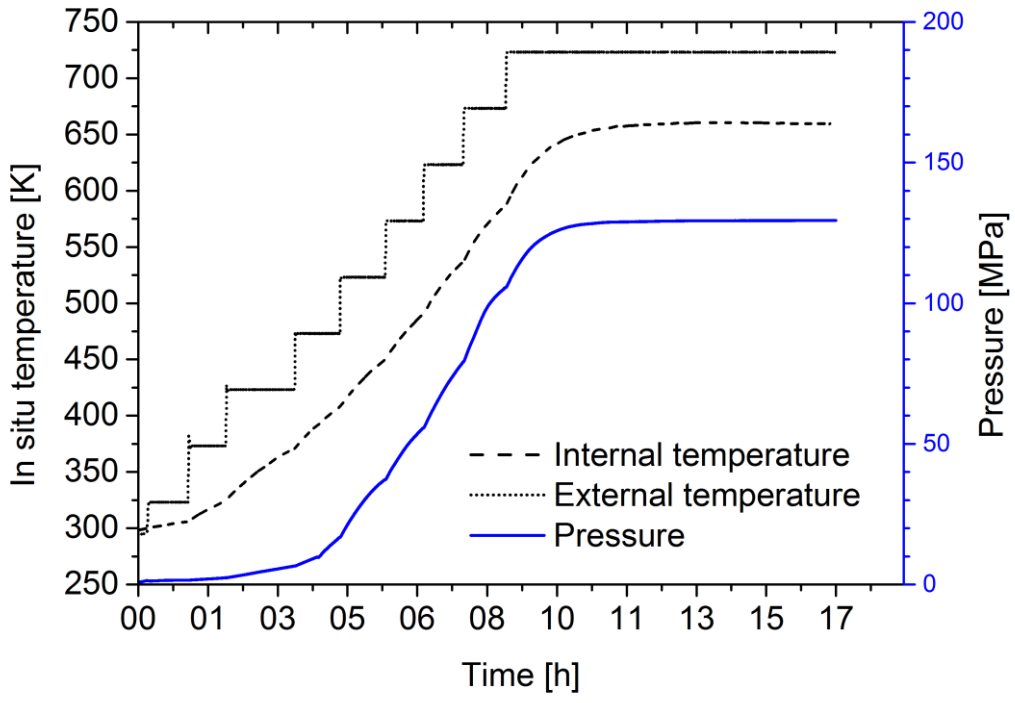

Figure 5. Experimental parameters (*T*, *p*) of $ZnGeN_2$ dissolution experiment with in situ X-ray imaging.

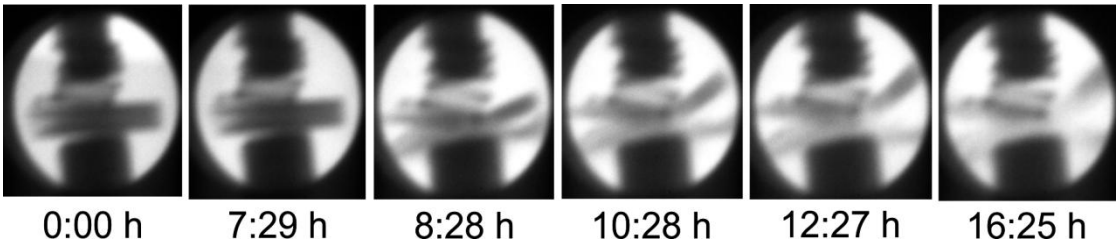

Figure 6. X-ray images showing the dissolution of the $ZnGeN_2$ pellet.

The reference image in the beginning of the experiment (0:00 h) was taken before reaching the critical point of the solvent. In this image, the phase boundary can thus still be seen since X-ray transmission decreases with increasing density. The third image shown in Figure 6 represents the first image showing a visible geometry change of the pellet (8:28 h, 570 K, 100 MPa). Since a geometry change could be caused not only by dissolution but also by mechanical disintegration of the powder particles, changes of X-ray absorption were analyzed for both the pellet and the surrounding fluid. Profile lines as depicted in Figure 7 give quantitative insight into the changes of X-ray transmission both with respect to different areas within one image and with respect to changes from one measurement to another.

In Figure 7, the six selected images showing subsequent dissolution of the pellet are analyzed using profile lines. As expected, the areas of the supercritical fluid (before onset of $ZnGeN_2$ dissolution, 7:29 h) show an intermediate transmission between that of the gas and liquid phases of the subcritical fluid (0:00 h). The profile lines indicate that the length of the radiographed path through $ZnGeN_2$ becomes shorter due to dissolution, that is, the transmitted intensity in the areas of the pellet parts increases as the pellet dissolves. Noteworthy, the transmitted intensity in the areas of the fluid decreases as the pellet dissolves. This indicates that the geometry change of the pellet coincides with increased absorption of the fluid which can be attributed to dissolved species containing elements that are heavier than those originally present in the fluid. Zn and Ge possess the highest atomic weight of the expectable elements in the fluid and they have atomic numbers on average identical to Ga. Comparable changes of the X-ray absorption of the fluid have been observed in dissolution experiments with bulk GaN crystals as well in which the mechanical disintegration of the sample can be excluded. This further supports that intermediate species containing Zn, Ge, or both are present in the fluid after dissolution of $ZnGeN_2$. The partial dissolution of $ZnGeN_2$ was monitored both below the specified

synthesis temperatures and within a short reaction time which is very promising for possible reversible transport reactions with applied dissolution and growth zones.

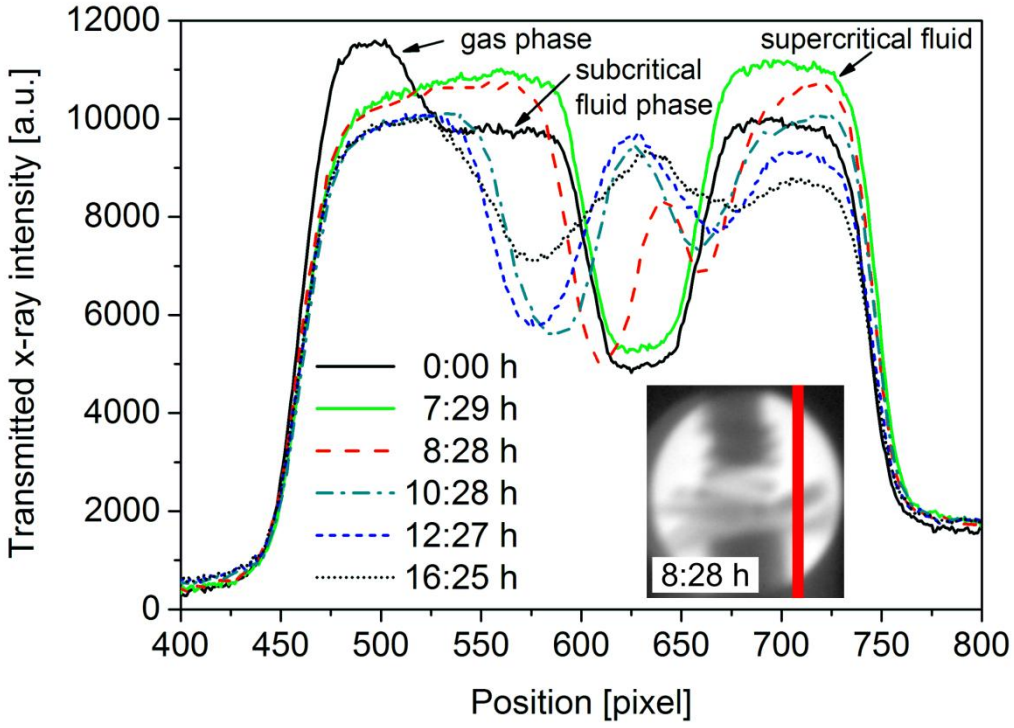

Figure 7. Profile lines extracted from the grayscale values of the X-ray images corresponding to the transmitted X-ray intensity. The inset shows the position of the profile line within the image using the first image showing dissolution of the pellet as an example.

To support the specified in situ measurements, we additionally performed dissolution experiments with regular high-pressure autoclaves used for synthesis. We observed that $ZnGeN_2$ dissolves at 670 K and 240 MPa using a 2 mol % $NaNH_2$ in NH_3 solution. Powder X-ray diffraction revealed unknown reflections next to $NaNH_2$, which can be attributed to the formation of intermediate compounds. Moreover, no characteristic reflections of $ZnGeN_2$ were detectable in the diffraction pattern. The product of this reaction completely dissolved in 1 M HCl, which also verifies that $ZnGeN_2$ formed reactive intermediates under the specified reaction conditions. Such compounds play the key role as transporting agents for ammonothermal crystal growth processes. Several alkali metal amidozincates have been identified so far, such as $Li_4[Zn(NH_2)_4](NH_2)_2$, $Na_2[Zn(NH_2)_4]\cdot 0.5NH_3$, and $K_2[Zn(NH_2)_4]$.[33-35] While only few compounds in the MNH_2–Si–NH_3 system were obtained

from supercritical ammonia, namely Si_2N_2NH, $K_3Si_6N_5(NH)_6$, and MSi_2N_3 (M = Li, Na),[14,36-38] no supposable Ge-containing intermediates have been reported in literature as yet.

3.3 Conclusions

The synthesis of the ternary nitrides $ZnSiN_2$ and $ZnGeN_2$ was performed by the ammonothermal method using custom-built high-pressure autoclaves. Different ammonobasic mineralizers were probed, where the employment of KNH_2 yielded the best crystallinity of the products. Powder X-ray diffraction showed that the nitrides crystallize in an ordered wurtzite-derived superstructure with space group *Pna*2_1. Temperature-programmed PXRD indicated a pronounced thermal stability of at least 1270 K for $ZnSiN_2$ and up to 1220 K for $ZnGeN_2$ with retention of the orthorhombic crystal structure. Respective band gaps of 3.7 and 3.2 eV for $ZnSiN_2$ and $ZnGeN_2$ were determined using diffuse reflectance measurements.

The well-defined morphology of the products indicates a solution-based growth mechanism, which is very promising for future crystal growth experiments. To corroborate a dissolution and recrystallization based mechanism analogous to the crystal growth of GaN, the dissolution of $ZnGeN_2$ in ammonobasic supercritical ammonia was monitored by in situ X-ray visualization. Partial dissolution of a $ZnGeN_2$ pellet was ascertained within a short reaction time by evaluating the transmitted X-ray intensity. Additional experiments verified a complete dissolution of $ZnGeN_2$ in a 2 mol % $NaNH_2$ in NH_3 solution after 75 h at 670 K. These findings demonstrate the feasibility of a dissolution and recrystallization based crystal growth by convection-driven transport reactions in analogy to GaN. The identification of intermediates as well as the determination of solubilities in dependence of pressure, temperature gradient and mineralizer will be essential for the development of ammonothermal growth strategies. Further development of Raman and X-ray diffraction in situ techniques will help to gain a better understanding of the crystallization processes. The synthesis of solid solutions $Zn(Si,Ge,Sn)N_2$, the insertion of dopants, as well as their influence on the optical and electronic properties will be of further interest in future studies. Notably, our results are very promising for potential ammonothermal syntheses of novel earth-abundant nitride semiconductor materials.

3.4 Experimental Section

The autoclaves were filled and sealed within Ar-filled glove boxes (Unilab, MBraun, Garching, O_2 <1 ppm, H_2O <1 ppm) to rigorously exclude oxygen and moisture during syntheses. A vacuum line (≤0.1 Pa) with connected argon and ammonia supply was used for the condensation procedure. Ar (Air Liquide, 99.999 %) and NH_3 (Air Liquide, 99.999 %) were passed through gas purification cartridges (MicroTorr FT400-902 and MC400-702FV, SAES Pure Gas Inc., San Luis Obispo, CA, USA) to obtain a purity level of <1 ppbV H_2O, O_2 and CO_2.

3.4.1 Ammonothermal synthesis

Syntheses in supercritical ammonia were performed in custom-built autoclaves made of nickel-based superalloys Inconel® 718 (max. 900 K, 300 MPa) or Haynes® 282® (max. 1100 K, 170 MPa). The autoclave body is sealed with a flange construction using silver-coated metal-C-rings (GFD seals) made of Inconel® 718 as sealing gaskets. The hand valve (SITEC), pressure transmitter (HBM P2VA1/5000 bar), and safety head with integrated bursting disc (SITEC) are connected to the autoclave lid through high-pressure pipes. For the synthesis of $ZnSiN_2$, Si (Alfa Aesar, 99.99 %) was first ball-milled under argon for 10 h using a planetary ball mill (Retsch PM 400). Zn (10 mmol, Alfa Aesar, 99.9 %), Si (8 mmol) and KN_3 (20 mmol, Sigma–Aldrich, 99.9 %) were then mixed and placed into a Mo-Liner, which was transferred into a Haynes 282 autoclave. For the synthesis of $ZnGeN_2$, Ge (smart-elements, 99.99 %) was ground for 15 min with an oscillating mixer mill (Specac Specamill). Zn (20 mmol, Alfa Aesar, 99.9 %), Ge (16 mmol) and KN_3 (50 mmol, Sigma–Aldrich, 99.9 %) were then mixed and directly placed into an Inconel 718 autoclave. The autoclaves were closed under argon, evacuated and cooled with ethanol/liquid nitrogen to 198 K. Ammonia was condensed into the autoclaves through a pressure regulating valve. For the synthesis of $ZnSiN_2$, the autoclave body was heated in a custom-built vertical tube furnace (Loba, HTM Reetz) to 570 K with a rate of 3 $K\,min^{-1}$, kept at this temperature for 15 h, heated to 1070 K with a rate of 1 $K\,min^{-1}$, and held for further 75 h. The pressure was kept between 100 MPa and 150 MPa during the heating periods and was appropriately reduced if necessary. For the synthesis of $ZnGeN_2$, the autoclave body was heated to 570 K with a rate of 3 $K\,min^{-1}$, kept at this temperature for 15 h, heated to 870 K with a rate of 2 $K\,min^{-1}$, and held for further 75 h. The pressure was kept between 150 MPa and 230 MPa. The autoclaves were cooled down to room temperature by switching off the furnace. The products were washed with water and 1 M

HCl to remove residual mineralizer and intermediates. The obtained powders were dried at 350 K in air. Analogous reactions at up to 870 K were performed with LiN_3 and NaN_3 as mineralizer.

3.4.2 Powder X-ray diffraction

Samples were filled in glass capillaries (0.3 mm diameter, Hilgenberg GmbH) for XRD measurements in modified Debye–Scherrer geometry. The diffraction patterns were recorded with a Stoe STADI P diffractometer (Cu $K\alpha_1$, λ = 1.540596 Å, Ge(1 1 1) monochromator, Mythen 1 K detector). Temperature-programmed powder X-ray diffraction was performed on a Stoe STADI P diffractometer (Mo-K α_1 , λ = 0.70930 Å, Ge(1 1 1) monochromator, image plate position sensitive detector) equipped with a high-temperature graphite furnace. The diffraction patterns were recorded in segments of 50 K up to 1270 K with a heating rate of 5 K min^{-1}.

Indexing and Rietveld refinement were performed with TOPAS-Academic software.[39] The fundamental parameters model with direct convolution of source emission profiles, axial instrument contributions, crystallite size, and microstrain effects was used for the peak shape function.[40] Capillary absorption correction (inner diameter 0.28 mm) was carried out using the calculated absorption coefficient.

Further details on the crystal structure investigations may be obtained from the Fachinformationszentrum Karlsruhe, 76344 Eggenstein-Leopoldshafen, Germany (fax: +49–7247-808-666; email:crysdata@fiz-karlsruhe.de, https://www.fiz-karlsruhe.de/en/leistungen/kristallographie/kristallstrukturdepot/order-form-request-for-deposited-data.html), on quoting the depository numbers CSD-432701 and CSD-432702.

3.4.3 Electron microscopy

The morphology and chemical composition of the samples was examined with a FEI Helios G3 UC scanning electron microscope (SEM; field emission gun, acceleration voltage 30 kV) equipped with an energy-dispersive X-ray (EDX) detector for elemental analyses. The samples were placed on an adhesive carbon pad and coated with a conductive carbon film using a high-vacuum sputter coater (BAL-TEC MED 020, Bal Tec AG). Transmission electron microscopy (TEM) was performed on a FEI Titan Themis 60–300 with X-FEG, monochromator, Cs-corrector and windowless, 4-quadrant Super-X EDX-detector. The powder was sonicated in absolute ethanol for 30 min, drop cast on

copper finder grids with holey carbon film (S166-2, Plano GmbH, Germany), and transferred into the microscope on a double-tilt holder.

3.4.4 UV/VIS spectroscopy

Diffuse reflectance measurements were conducted at room temperature using a Jasco V-650 UV/VIS spectrophotometer equipped with Czerny–Turner mount, photomultiplier tube detector, and deuterium (190–350 nm)/halogen (330–900 nm) lamps as light sources.

3.4.5 Dissolution monitoring by in situ X-ray imaging

For monitoring the dissolution of $ZnGeN_2$, pellets of ammonothermally synthesized $ZnGeN_2$ were placed within the field of view of the autoclave used for in situ X-ray imaging experiments (optical cell). Polycrystalline $ZnGeN_2$ was cold pressed to a pellet (4 mm in diameter) using a manual hydraulic press with an applied pressure of 10 kN. The setup for dissolution experiments with in situ X-ray monitoring was identical to the one described in a previous publication,[31] except for the following modifications. An unlined Inconel® 718 autoclave (12.3 mL internal volume) was used since NaN_3 was applied as mineralizer and no adjustments to the fill level were performed during the experiment. A cylinder-shaped pellet produced from powder was used instead of a bulk cuboid-shaped single crystal. The fill level was adjusted to about 55 % with an initial weight of 0.4549 g NaN_3 (7 mmol). A series of five X-ray images was recorded approximately once an hour. These five images were averaged in order to reduce noise. The profile lines were extracted from the averaged images by selecting a vertical stripe of 10 pixels (at the position indicated by the red bar in the inset in Figure 7) and averaging these 10 profile lines.

For the complementary dissolution experiments, ammonothermally synthesized $ZnGeN_2$ (1 mmol) was mixed with NaN_3 (50 mmol) and placed into an autoclave. NH_3 (≈60 mL at 198 K, 2.6 mol) was condensed into the autoclave resulting in a mineralizer concentration of about 2 mol %. The autoclave was heated in a vertical tube furnace to 670 K and kept at this temperature for 75 h. A maximum pressure of 240 MPa was attained during the reaction. To confirm a complete conversion of $ZnGeN_2$ to intermediates, the colorless product was slowly poured in an isopropanol/H_2O (80:20) solution. In this way, a controlled decomposition of the amides was achieved. The formed colorless precipitate entirely dissolved in 1 M HCl.

3.5 References

[1] Y. Hinuma, T. Hatakeyama, Y. Kumagai, L. A. Burton, H. Sato, Y. Muraba, S. Iimura, H. Hiramatsu, I. Tanaka, H. Hosono, F. Oba, *Nat. Commun.* **2016**, 7:11962.

[2] V. L. Shaposhnikov, A. V. Krivosheeva, F. Arnaud D'Avitaya, J. L. Lazzari, V. E. Borisenko, *Phys. Status Solidi B* **2008**, *245*, 142-148.

[3] P. C. Quayle, K. He, J. Shan, K. Kash, *MRS Commun.* **2013**, *3*, 135-138.

[4] T. R. Paudel, W. R. L. Lambrecht, *Phys. Rev. B* **2009**, *79*, 245205.

[5] T. Endo, Y. Sato, H. Takizawa, M. Shimada, *J. Mater. Sci. Lett.* **1992**, *11*, 424-426.

[6] A. Mintairov, J. Merz, A. Osinsky, V. Fuflyigin, L. D. Zhu, *Appl. Phys. Lett.* **2000**, *76*, 2517-2519.

[7] T. Misaki, A. Wakahara, H. Okada, A. Yoshida, *J. Cryst. Growth* **2004**, *260*, 125-129.

[8] N. Feldberg, J. D. Aldous, W. M. Linhart, L. J. Phillips, K. Durose, P. A. Stampe, R. J. Kennedy, D. O. Scanlon, G. Vardar, R. L. Field, T. Y. Jen, R. S. Goldman, T. D. Veal, S. M. Durbin, *Appl. Phys. Lett.* **2013**, *103*, 042109.

[9] B. Wang, M. J. Callahan, *Cryst. Growth Des.* **2006**, *6*, 1227-1246.

[10] A. D. Hanser, K. R. Evans, in *Technology of Gallium Nitride Crystal Growth* (Eds.: D. Ehrentraut, E. Meissner, M. Bockowski), Springer Berlin Heidelberg, **2010**, pp. 3-27.

[11] D. Ehrentraut, R. T. Pakalapati, D. S. Kamber, W. Jiang, D. W. Pocius, B. C. Downey, M. McLaurin, M. P. D'Evelyn, *Jpn. J. Appl. Phys.* **2013**, *52*, 08JA01.

[12] S. Pimputkar, J. S. Speck, S. Nakamura, *J. Cryst. Growth* **2016**, *456*, 15-20.

[13] R. Dwiliński, R. Doradziński, J. Garczyński, L. Sierzputowski, R. Kucharski, M. Zając, M. Rudziński, R. Kudrawiec, J. Serafińczuk, W. Strupiński, *J. Cryst. Growth* **2010**, *312*, 2499-2502.

[14] H. Jacobs, H. Mengis, *Eur. J. Solid State Inorg. Chem.* **1993**, *30*, 45-54.

[15] H. Jacobs, R. Nymwegen, *Z. Anorg. Allg. Chem.* **1997**, *623*, 429-433.

[16] J. Häusler, L. Neudert, M. Mallmann, R. Niklaus, A.-C. L. Kimmel, N. S. A. Alt, E. Schlücker, O. Oeckler, W. Schnick, *Chem. Eur. J.* **2017**, *23*, 2583-2590.

[17] R. Juza, *Angew. Chem.* **1964**, *76*, 290-300; R. Juza, *Angew. Chem. Int. Ed.* **1964**, *3*, 471-481.

[18] T. Richter, R. Niewa, *Inorganics* **2014**, *2*, 29-78.

[19] S. Pimputkar, S. Nakamura, *J. Supercrit. Fluids* **2016**, *107*, 17-30.

[20] H. Jacobs, D. Schmidt, *Curr. Top. Mater. Sci.* **1982**, *8*, 387-427.

[21] A. Punya, W. R. L. Lambrecht, M. van Schilfgaarde, *Phys. Rev. B* **2011**, *84*, 165204.

[22] K. Du, C. Bekele, C. C. Hayman, J. C. Angus, P. Pirouz, K. Kash, *J. Cryst. Growth* **2008**, *310*, 1057-1061.

[23] E. W. Blanton, K. He, J. Shan, K. Kash, *J. Cryst. Growth* **2017**, *461*, 38-45.

[24] R. López, R. Gómez, *J. Sol-Gel Sci. Technol.* **2012**, *61*, 1-7.

[25] J. Tauc, R. Grigorovici, A. Vancu, *Phys. Status Solidi B* **1966**, *15*, 627-637.

[26] A. Osinsky, V. Fuflyigin, L. D. Zhu, A. B. Goulakov, J. W. Graff, E. F. Schubert, in *Proc. 2000 IEEE / Cornell Conference on High Performance Devices*, **2000**, pp. 168-172.

[27] T. Misaki, X. Wu, A. Wakahara, A. Yoshida, in *IPAP Conference Series*, **2000**, pp. 685-688.

[28] W. L. Larson, H. P. Maruska, D. A. Stevenson, *J. Electrochem. Soc.* **1974**, *121*, 1673-1674.

[29] T. Misaki, A. Wakahara, H. Okada, A. Yoshida, *Phys. Status Solidi C* **2003**, *0*, 2890-2893.

[30] M. Shang, J. Wang, J. Fan, H. Lian, Y. Zhang, J. Lin, *J. Mater. Chem. C* **2015**, *3*, 9306-9317.

[31] S. Schimmel, M. Lindner, T. G. Steigerwald, B. Hertweck, T. M. M. Richter, U. Künecke, N. S. A. Alt, R. Niewa, E. Schlücker, P. Wellmann, *J. Cryst. Growth* **2015**, *418*, 64-69.

[32] S. Schimmel, U. Künecke, H. Baser, T. G. Steigerwald, B. Hertweck, N. S. A. Alt, E. Schlücker, W. Schwieger, P. Wellmann, *Phys. Status Solidi C* **2014**, *11*, 1439-1442.

[33] T. M. M. Richter, N. S. A. Alt, E. Schlücker, R. Niewa, *Z. Anorg. Allg. Chem.* **2015**, *641*, 1016-1023.

[34] B. Fröhling, H. Jacobs, *Z. Anorg. Allg. Chem.* **1998**, *624*, 1148-1153.

[35] T. M. M. Richter, S. Zhang, R. Niewa, *Z. Kristallogr.* **2013**, *228*, 351-358.

[36] D. Peters, H. Jacobs, *J. Less Common Met.* **1989**, *146*, 241-249.

[37] D. Peters, E. F. Paulus, H. Jacobs, *Z. Anorg. Allg. Chem.* **1990**, *584*, 129-137.

[38] S. Kaskel, M. Khanna, B. Zibrowius, H.-W. Schmidt, D. Ullner, *J. Cryst. Growth* **2004**, *261*, 99-104.

[39] A. Coelho, *TOPAS Academic*, Version 4.1, Coelho Software, Brisbane (Australia), **2007**.

[40] R. W. Cheary, A. A. Coelho, J. P. Cline, *J. Res. Natl. Inst. Stand. Technol.* **2004**, *109*, 1-25.

4 Ammonothermal Synthesis and Optical Properties of Ternary Nitride Semiconductors Mg-IV-N_2, Mn-IV-N_2 and Li-IV_2-N_3 (IV = Si, Ge)

published in: *Chem. Eur. J.* **2018**, *24*, 1686-1693.

authors: Jonas Häusler, Robin Niklaus, Ján Minár, and Wolfgang Schnick

DOI: 10.1002/chem.201704973

http://onlinelibrary.wiley.com/doi/10.1002/chem.201704973/abstract

Abstract. Grimm–Sommerfeld analogous nitrides $MgSiN_2$, $MgGeN_2$, $MnSiN_2$, $MnGeN_2$, $LiSi_2N_3$ and $LiGe_2N_3$ (generally classified as II-IV-N_2 and I-IV_2-N_3) are promising semiconductor materials with great potential for application in (opto)electronics or photovoltaics. A new synthetic approach for these nitride materials was developed using supercritical ammonia as both solvent and nitride-forming agent. Syntheses were conducted in custom-built high-pressure autoclaves with alkali metal amides $LiNH_2$, $NaNH_2$ or KNH_2 as ammonobasic mineralizers, which accomplish an adequate solubility of the starting materials and promote the formation of reactive intermediate species. The reactions were performed at temperatures between 870 and 1070 K and pressures up to 230 MPa. All studied compounds crystallize in wurtzite-derived superstructures with orthorhombic space groups *Pna*2_1 (II-IV-N_2) and *Cmc*2_1 (I-IV_2-N_3), respectively, which was confirmed by powder X-ray diffraction. Optical bandgaps were estimated from diffuse reflectance spectra using the Kubelka–Munk function ($MgSiN_2$: 4.8 eV, $MgGeN_2$: 3.2 eV, $MnSiN_2$: 3.5 eV, $MnGeN_2$: 2.5 eV,

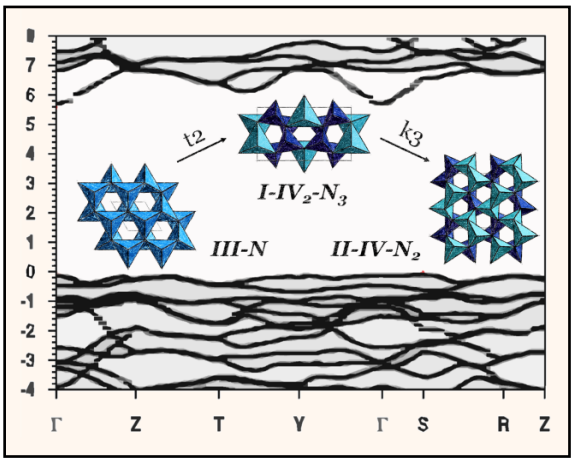

$LiSi_2N_3$: 4.4 eV, $LiGe_2N_3$: 3.9 eV). Complementary DFT calculations were carried out to gain insight into the electronic band structures of these materials and to corroborate the optical measurements.

4.1 Introduction

Prospecting new semiconducting materials is an important issue in current research to meet the rapid development and high demands of modern electronic technologies. At present, gallium nitride and its solid solutions (Al,Ga,In)N (III-N) represent the most important nitride semiconductors for numerous applications, for example, light-emitting diodes, laser diodes or field-effect transistors.[1,2] In recent decades, a large number of new ternary nitrides were discovered, with many of them recently gaining increasing attention due to their promising optical and electronic properties.[3] In particular, ternary nitrides with structural relationships to group 13 nitrides are good candidates as next-generation semiconductor materials as they feature similar ranges of bandgaps and increased prospects for bandgap engineering. Furthermore, implied ternary nitrides are generally composed of earth-abundant elements, whereas metals like gallium or indium are becoming increasingly scarce. Zn-IV-nitrides (IV = Si, Ge, Sn) are currently the most prominent examples for such Grimm–Sommerfeld analogous compounds showing good bandgap tunability and small carrier effective masses.[3-6] Besides this, isotypic $MgSiN_2$ is also well-studied in terms of its electronic band structure, the photoluminescence of Mn^{2+} doped or rare-earth-doped materials as well as its ceramic properties.[7-10] On the other hand, further II-IV-N_2 compounds as well as wurtzite-related I-IV_2-N_3 nitrides have scarcely been investigated with regard to their optical and electronic properties so far. Previous experimental studies are mainly limited to the photoluminescence and ion conductivity of $LiSi_2N_3$, magnetic and optical properties of $MnSiN_2$ as well as the formation and optical tuning of $Mg_xMn_{1-x}SiN_2$ solid solutions.[11-16] Experimental analyses of optical parameters of the respective germanium compounds $MgGeN_2$, $MnGeN_2$ and $LiGe_2N_3$ have so far not been reported.

Common synthetic methods for Mg-IV-N_2, Mn-IV-N_2 and Li-IV_2-N_3 nitrides include high-temperature techniques under N_2 atmosphere, ammonolysis and vapor–liquid–solid (VLS) deposition.[15,17-19] In this contribution, we present an ammonothermal approach for bulk synthesis of these compounds using highly pressurized ammonia as the reaction medium. The ammonothermal technique is widely used for the crystal growth of binary nitrides like GaN,[20] whereas very few ternary nitrides were synthesized by this method so far. Recently, we described solution-based syntheses of $ZnSiN_2$ and $ZnGeN_2$ using

ammonobasic supercritical ammonia.[21] In the present study, we report on synthesis and optical characterization of the ternary nitride semiconductors $MgSiN_2$, $MgGeN_2$, $MnSiN_2$, $MnGeN_2$, $LiSi_2N_3$ and $LiGe_2N_3$. The products were analyzed by powder X-ray diffraction, bandgaps were evaluated using diffuse reflectance spectroscopy and electronic structure was determined by DFT calculations based on the Korringa–Kohn–Rostoker (KKR) Green's function method.

4.2 Results and Discussion

4.2.1 Synthesis

The ternary nitrides $MgSiN_2$, $MgGeN_2$, $MnSiN_2$, $MnGeN_2$, $LiSi_2N_3$ and $LiGe_2N_3$ were synthesized by the ammonothermal method using custom-built high-pressure autoclaves. Ammonobasic mineralizers MNH_2 (M = Li, Na, K) were added to increase solubility of the starting materials. The alkali metal amides were obtained in situ starting from the azides because of the available purity and chemical stability of the latter. In analogy to the synthesis of Zn-IV-nitrides,[21] KNH_2 was preferred for syntheses of $MgSiN_2$ and $MnSiN_2$, while phase-pure samples of $MgGeN_2$ and $MnGeN_2$ were only obtained with $NaNH_2$ as the mineralizer. Mg/Mn were used in 20 % excess and Li in 50 % excess to facilitate complete conversion of the intermediates to the nitrides (see Experimental Section). Residual alkali or alkaline earth metal amides were easily washed out after the reactions (see below). The syntheses of II-IV-N_2 were carried out in two temperature steps, since intermediate species like amides or imides are preferentially formed at temperatures below 700 K.[22] In case of the Li-IV_2-N_3 compounds, the autoclaves were directly heated to the final desired temperature. Otherwise, a nearly complete transport of $LiNH_2$ into the colder peripheral parts of the vessels was observed. Lower heating rates were applied for the synthesis of $LiSi_2N_3$, taking the considerable decomposition of NH_3 at temperatures above 850 K into account.[23] All Si-containing products were synthesized at up to 1070 K with an autogenous pressure of 170 MPa. Phase-pure $LiSi_2N_3$ was obtained at 970 K, while Li_2SiN_2 was detected as a side-phase at 1070 K.[24] Besides, synthesis of $LiGe_2N_3$ was only successful starting from Ge_3N_4 instead of Ge. Since the Ge compounds are thermally less stable than the Si compounds, the former were synthesized at lower temperatures up to 900 K and a pressure of 230 MPa. Residual intermediates and mineralizer were dissolved in 5 M HCl ($MgSiN_2$, $MnSiN_2$, $LiSi_2N_3$), EtOH ($MgGeN_2$, $LiGe_2N_3$) or H_2O ($MnGeN_2$). The respective solvent was selected taking the chemical stability of the products and the formation of side-phases during the purification process into account.

Crystal sizes of the obtained nitrides are in the range of 100 nm to 1 µm as shown in scanning electron microscopy (SEM) images (Figure S1).

4.2.2 Powder X-ray diffraction and crystal structures

The purified products were analyzed by powder X-ray diffraction (see Figure 1). Wyckoff positions and atomic coordinates for Rietveld refinement were taken from literature.[17,25-27] The obtained crystallographic data are listed in Table 1, refined atomic coordinates and displacement parameters are given in Tables S1–S6 (see the Supporting Information). All referred compounds crystallize in orthorhombic symmetry. The crystal structures of both II-IV-N_2 and I-IV_2-N_3 can be derived from the wurtzite structure type (space group $P6_3mc$); ordering of the tetrahedrally coordinated cations results in space groups $Pna2_1$ and $Cmc2_1$, respectively.

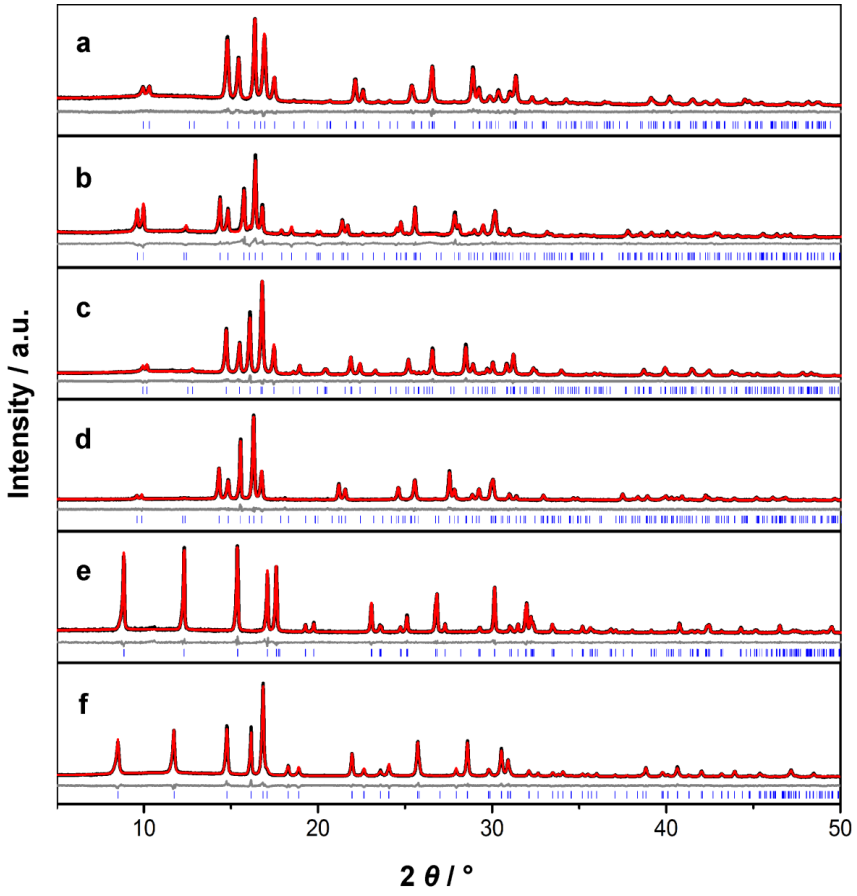

Figure 1. Rietveld refinements of $MgSiN_2$ (a), $MgGeN_2$ (b), $MnSiN_2$ (c), $MnGeN_2$ (d), $LiSi_2N_3$ (e) and $LiGe_2N_3$ (f) with experimental data (black lines, Mo-Kα_1 radiation, λ = 0.70930 Å), calculated patterns (red lines), difference profiles (gray lines) and positions of Bragg reflections (blue bars).

Table 1. Crystallographic data of Mg-IV-N_2, Mn-IV-N_2 and Li-IV_2-N_3 (IV = Si, Ge) obtained by Rietveld refinement

Formula	**$MgSiN_2$**	**$MgGeN_2$**	**$MnSiN_2$**	**$MnGeN_2$**	**$LiSi_2N_3$**	**$LiGe_2N_3$**
Crystal system	orthorhombic					
Space group	*Pna*2_1	*Pna*2_1	*Pna*2_1	*Pna*2_1	*Cmc*2_1	*Cmc*2_1
a [Å]	5.2825(2)	5.5018(2)	5.2679(1)	5.4974(2)	9.2135(2)	9.5570(4)
b [Å]	6.4593(2)	6.6254(3)	6.5125(1)	6.6639(2)	5.2980(1)	5.5198(2)
c [Å]	4.9862(2)	5.1835(3)	5.0742(1)	5.2508(1)	4.7800(1)	5.0486(1)
Cell volume [$Å^3$]	170.132(9)	188.949(15)	174.082(6)	192.359(9)	233.324(9)	266.326(15)
Density [$g \cdot cm^{-3}$]	3.1391	4.3916	4.2367	5.3715	2.9929	4.8429
Formula units [cell]	4					
T [K]	293(2)					
Diffractometer	STOE STADI P					
Radiation [Å]	Mo-Kα_1 (λ = 0.70930 Å)					
2θ range [°]	$5.0 \leq 2\theta \leq 50$					
Profile function	fundamental parameters model					
Background function	Shifted Chebyshev					
Data points	3001					
Number of reflections	143	183	170	187	125	143
Refined parameters	56	50	35	51	33	54
R values	R_p = 0.0331 R_{wp} = 0.0417 R_{Bragg} = 0.0193	R_p = 0.0430 R_{wp} = 0.0578 R_{Bragg} = 0.0394	R_p = 0.0338 R_{wp} = 0.0434 R_{Bragg} = 0.0177	R_p = 0.0480 R_{wp} = 0.0632 R_{Bragg} = 0.0135	R_p = 0.0658 R_{wp} = 0.0877 R_{Bragg} = 0.0211	R_p = 0.0349 R_{wp} = 0.0453 R_{Bragg} = 0.0212
Goodness of fit	1.240	1.991	1.686	1.035	0.935	1.946

Crystal structures and group–subgroup relationships are illustrated in Figure 2. The three-dimensional networks are built up of corner-sharing cation-centered tetrahedra forming *sechser*-rings along [001]. As expected, a slight tilting and distortion of the tetrahedra in II-IV-N_2 and I-IV_2-N_3 compared to the hypothetical superstructures based on III-N can be

observed. Calculated lattice parameters and interatomic distances from Rietveld refinement are in the same range as earlier reported values.[17-25-27]

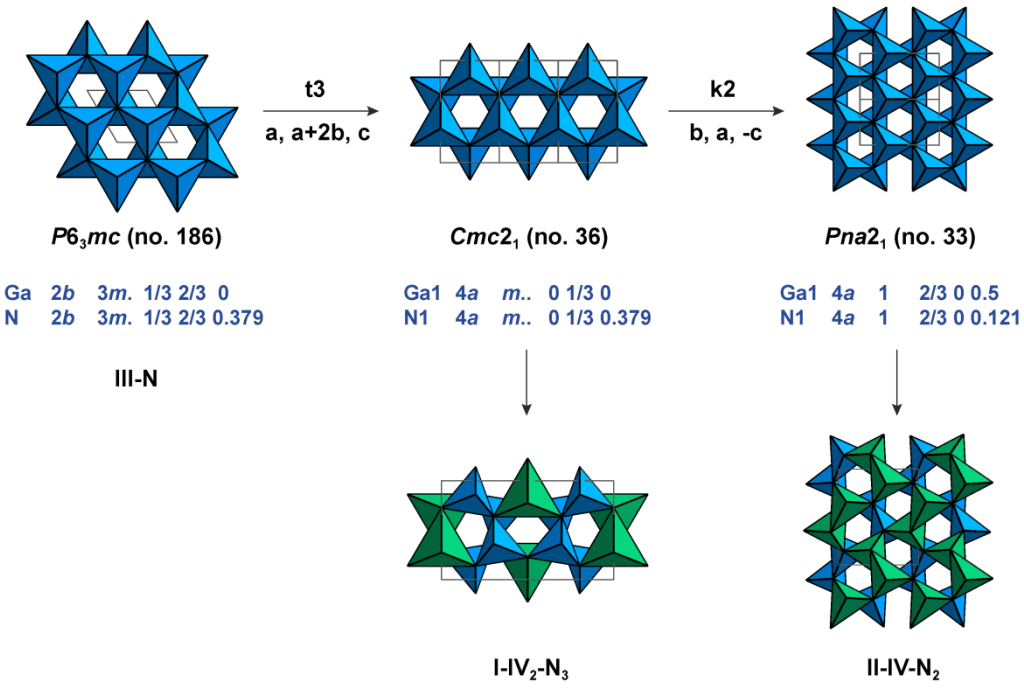

Figure 2. Group–subgroup relations of the wurtzite structure type ($P6_3mc$) and wurtzite superstructures of I-IV_2-N_3 ($Cmc2_1$) and II-IV-N_2 ($Pna2_1$) compounds viewed along [001]. GaN_4 (III-N) and MN_4 (M = Si, Ge in I-IV_2-N_3 and II-IV-N_2) tetrahedra are depicted in blue, $M'N_4$ tetrahedra (M' = Li, Mg or Mn) in green. Wyckoff positions of GaN were taken from literature.[28]

In addition, thermal stabilities of the synthesized nitrides were analyzed by temperature-programmed powder X-ray diffraction (TP-XRD). Degradation initiates at 770 K for $MgGeN_2$, 920 K for $MnSiN_2$ and between 1000–1200 K for the other nitrides as indicated by emerging reflections of the decomposition products (see Figure S2–S7 in the Supporting Information).

4.2.3 UV/Vis reflectance spectroscopy

Diffuse reflectance of the purified powder samples was measured to investigate the optical properties of the materials. The recorded spectra show broad absorption bands between 200–400 nm ($MgSiN_2$, $MnSiN_2$, $LiSi_2N_3$) and 300–500 nm ($MgGeN_2$, $MnGeN_2$, $LiGe_2N_3$), see Figure S8 in the Supporting Information. Pseudo-absorption spectra were

calculated using the Kubelka–Munk function $F(R) = (1-R)^2/2R$ (R = reflectance).[29] The optical bandgaps were determined using Tauc plots $h\nu$ versus $(F(R)\cdot h\nu)^{1/n}$ with $n = 1/2$ for direct allowed transitions (Figure 3 and Table 2).[30] The observed absorption bands in the spectra were primarily attributed to direct transitions due to the similarity of direct and indirect bandgaps in the materials (section DFT calculations).

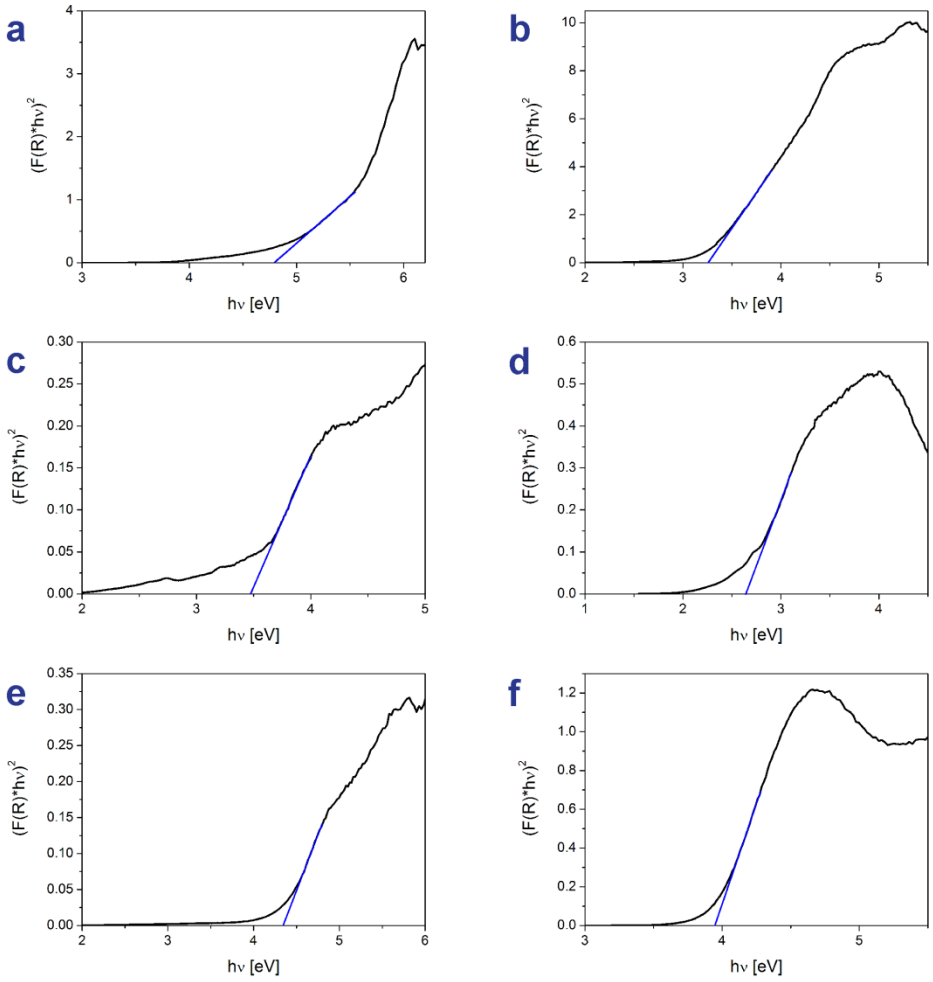

Figure 3. Tauc plots of $MgSiN_2$ (a), $MgGeN_2$ (b), $MnSiN_2$ (c), $MnGeN_2$ (d), $LiSi_2N_3$ (e) and $LiGe_2N_3$ (f).

Table 2. Evaluated optical bandgaps of Mg-IV-N_2, Mn-IV-N_2 and Li-IV_2-N_3 (IV = Si, Ge) from Tauc plots [eV] at room temperature

$MgSiN_2$	$MnSiN_2$	$LiSi_2N_3$	$MgGeN_2$	$MnGeN_2$	$LiGe_2N_3$
4.8	3.5	4.4	3.2	2.5	3.9

Apart from $MgSiN_2$, material properties of these nitrides have scarcely been investigated so far. Optical measurements were only reported for the respective Si nitrides $MgSiN_2$, $MnSiN_2$ and $LiSi_2N_3$. The evaluated bandgap of $MgSiN_2$ coincides well with previously determined values in the literature, ranging from 4.8 to 5.6 eV.[10,31] A deviation of ≈0.8 eV in comparison to other reported data was observed for $MnSiN_2$ and $LiSi_2N_3$ which can be attributed to different evaluation techniques for the bandgaps as well as different synthetic methods.[16,32] To some extent, variances can also arise from crystallographic defects within the materials. $MgGeN_2$, $MnGeN_2$ and $LiGe_2N_3$ exhibit smaller optical bandgaps in comparison to the respective Si nitrides, which is consistent with comparable systems.[3] Notably, sub-bandgap absorption was observed for $MnSiN_2$ and $MnGeN_2$ which was previously attributed to spin-forbidden d–d-transitions and associated selection rule relaxations.[15,16] This also explains the tails observed in the Tauc plots as well as the red and brown colors of the products (see Experimental section), which is in line with previous studies.[15,19]

4.2.4 DFT calculations

In order to corroborate the experimental data, DFT calculations were carried out. Plots of the total and atom resolved density of states (DOS) are shown in Figure 4 for $MnSiN_2$ and $MnGeN_2$ (for specific bandgap region see Figure S9, supporting information) and in Figure S10 for Mg-IV-N_2 and Li-IV_2-N_3 (IV = Si, Ge). Excluding temperature effects, $MnSiN_2$ and $MnGeN_2$ exhibit spin polarization which is in agreement with previous calculations.[33] The spin polarization seen in Figure 4 a–b arises from the Mn atoms, in particular their 5d states. For Mn total magnetic moment values of 4.49 μB and 4.45 μB are obtained for $MnSiN_2$ and $MnGeN_2$, respectively.

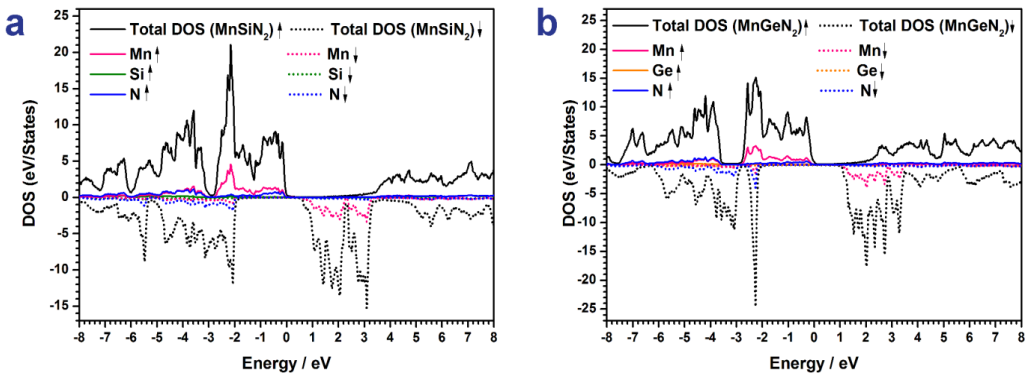

Figure 4. Total and atom resolved DOS of $MnSiN_2$ (a) and $MnGeN_2$ (b) within the SPRKKR formalism.

In order to estimate the optical absorption, the joint density of states (JDOS) was subsequently calculated for each compound as depicted in Figure 5 a–f in line with previous works[34] and was further validated by additional optical calculations within linear response formalism. E_g was then determined by means of a linear fit of the first steep ascend of the JDOS. Its values agree well with the evaluated optical bandgap from experimental data with merely minor deviations (Tables 2 and 3).

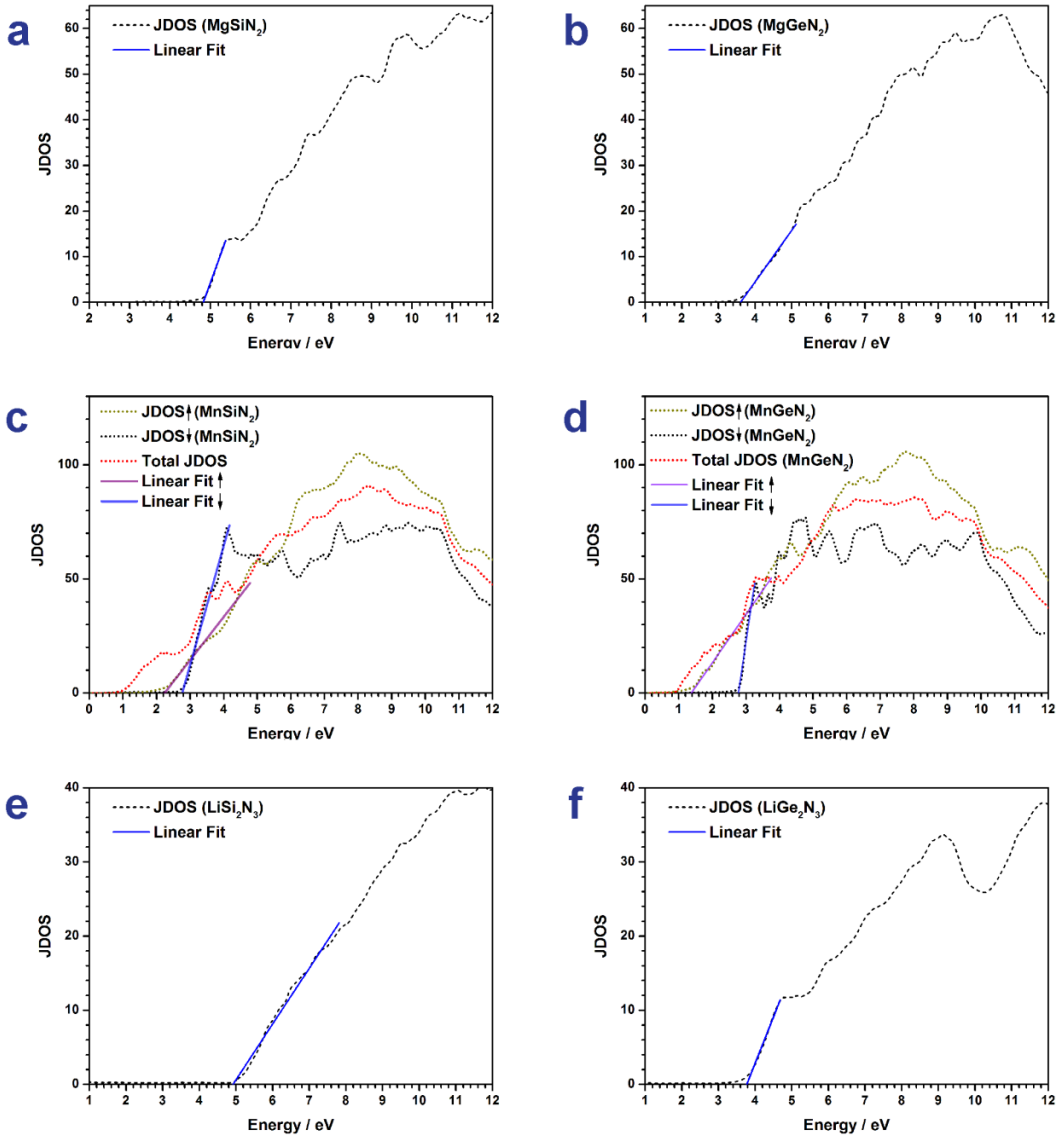

Figure 5. Calculated JDOS of $MgSiN_2$ (a), $MgGeN_2$ (b), $MnSiN_2$ (c), $MnGeN_2$ (d), $LiSi_2N_3$ (e) and $LiGe_2N_3$ (f) within the SPRKKR formalism. Extrapolated linear fits are used to evaluate E_g.

Table 3. Electronic (El.) and optical (Opt.) bandgaps (eV) for Mg-IV-N_2, Mn-IV-N_2 (spin up ↑ / spin down ↓) and Li-IV_2-N_3 (IV = Si, Ge) as calculated by SPRKKR formalism (EV-GGA)

	$MgSiN_2$	**$MnSiN_2$**	**$LiSi_2N_3$**	**$MgGeN_2$**	**$MnGeN_2$**	**$LiGe_2N_3$**
El.	4.2	$0.6^{\uparrow}$ $1.0^{\downarrow}$	5.6	3.0	$0.1^{\uparrow}$ $1.0^{\downarrow}$	3.6
Opt.	4.8	$2.2^{\uparrow}$ $2.8^{\downarrow}$	4.9	3.6	$1.4^{\uparrow}$ $2.8^{\downarrow}$	3.8

Due to the spin polarization of $MnSiN_2$ and $MnGeN_2$ their JDOS was calculated for both the spin up and spin down channel. Early absorption (1–2 eV) in the total JDOS would mainly represent Mn-3d–3d transitions that are deemed forbidden due to dipole selection rules. However, selection rule relaxations can induce absorption in this energy range to some extent.[15,16] Hence, E_g can be estimated from a mean value of the spin up and down JDOS. This appears to be a reasonable approximation for the optical bandgap in line with the experimental absorption starting at around 2 eV for both Mn compounds while the strong incline in absorption can likely be attributed to N 2p to Mn 3d transitions. Electronic bandgaps were determined from the Bloch spectral functions depicted in Figure 6 a–h. Mg-IV-N_2 and Li-IV_2-N_3 (IV = Si, Ge) exhibit direct and indirect bandgaps of very similar magnitude, while Mn-IV-N_2 reveal both direct and indirect gaps with respect to their spin channels.

Up to now, bandgap calculations referred to these nitrides were reported for $MgSiN_2$, $MgGeN_2$ and $LiSi_2N_3$. Estimated bandgaps range from 3.8 to 6.3 eV for $MgSiN_2$,[10,25,35-40] 2.9 to 5.4 eV for $MgGeN_2$[25,35-37,41] and 5.0 to 5.6 eV for $LiSi_2N_3$.[13,42] The large discrepancies result from different calculation methods which can lead to a significant under- or overestimation of the bandgaps. In general, the applied SPRKKR formalism seems to provide reasonable values with regard to the experimental data.

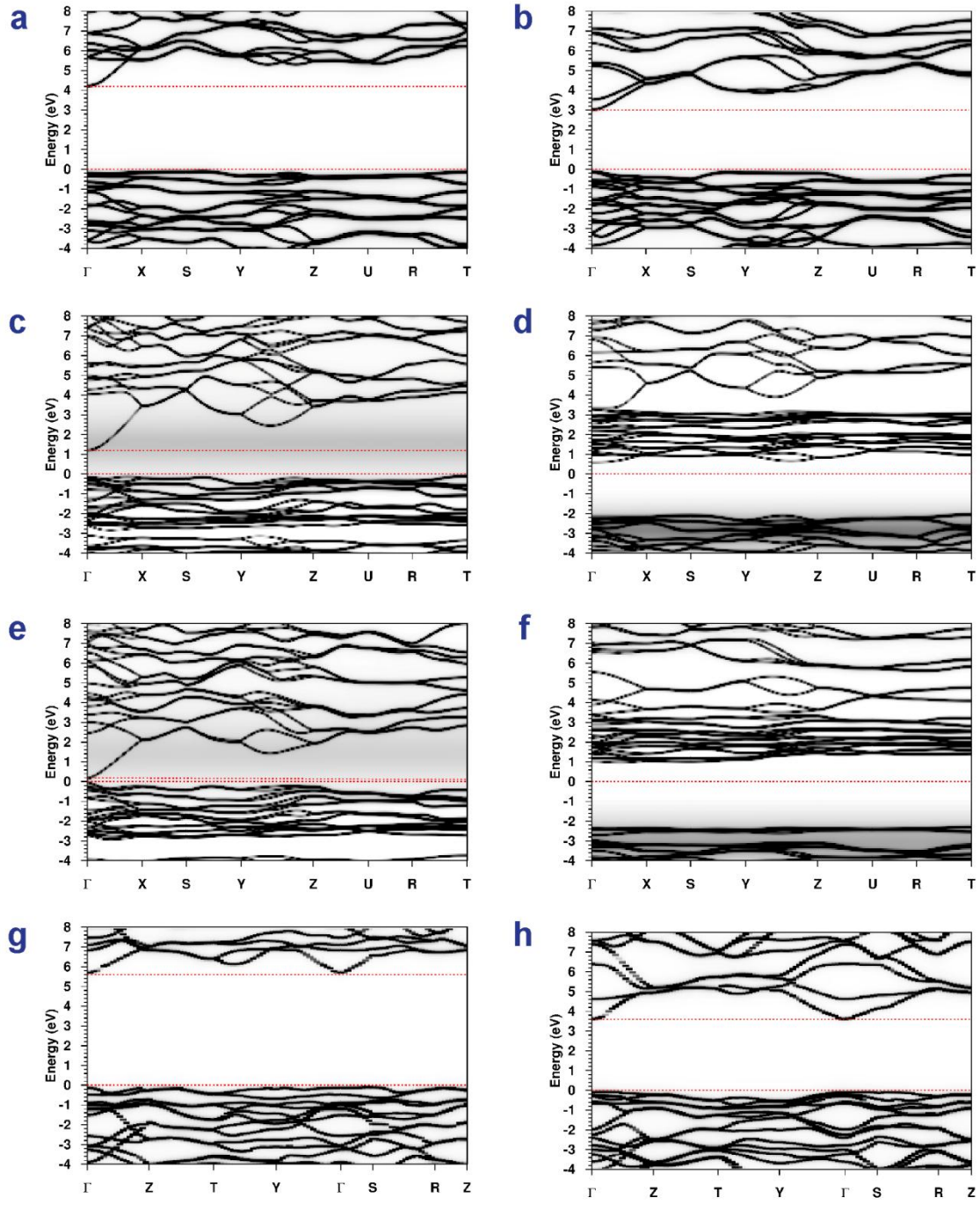

Figure 6. Bloch spectral functions of $MgSiN_2$ (a), $MgGeN_2$ (b), $MnSiN_2$ (↑c/↓d), $MnGeN_2$ (↑e/↓f), $LiSi_2N_3$ (g) and $LiGe_2N_3$ (h) as calculated by SPRKKR formalism (EV-GGA). ↑ and ↓ indicate spin up and down channels, respectively.

4.3 Conclusions

We developed a new synthetic approach for the ternary nitrides Mg-IV-N_2, Mn-IV-N_2 and Li-IV_2-N_3 (IV = Si, Ge) implementing solutions of supercritical ammonia (p_{crit} = 11.3 MPa, T_{crit}=405.5 K)[43] with alkali metal amides as ammonobasic mineralizers. Custom-built high-pressure autoclaves made of nickel-based superalloys Inconel 718 (max. 900 K, 300 MPa) and Haynes alloy 282 (max. 1100 K, 170 MPa) provided the required temperature and pressure for the formation of these materials. Evaluation of observed absorption bands in diffuse reflectance spectra resulted in a range of bandgaps between 2.5 eV ($MnGeN_2$) and 4.8 eV ($MgSiN_2$). Band structures and the type of band transitions were calculated by DFT, which corroborated the estimated optical bandgaps, further providing new insights into electronic and optical properties of the materials in question. Calculated Bloch spectral functions show bandgaps similar in magnitude to the optical bandgaps with direct bandgaps for the majority of discussed compounds. $MnSiN_2$ and $MnGeN_2$ exhibit much lower electronic bandgaps than estimated from experimental and calculated optical bandgaps however with low transition probabilities as indicated by DOS and JDOS calculations.

Up to now, only few reports on ammonothermal synthesis of ternary and multinary nitrides can be found in literature. Syntheses in supercritical ammonia are still challenging due to the high demands on autoclave materials and high-pressure facilities. However, recent achievements in this research field are very intriguing for future studies.[21,34,44,45] With regard to the structural relationship of III-N, II-IV-N_2 and I-IV_2-N_3 nitrides, bandgap engineering and further tuning of optical properties by formation of solid solutions is very promising. Even more attainable compositions for wurtzite-derived superstructures have been proposed by Parthé and Baur.[46-48] For instance, the thermodynamic stability of wurtzite-related quaternary nitride semiconductors like $LiAlGe_2N_4$ and $LiGaGe_2N_4$ was recently predicted as well.[49] On the basis of our latest studies, the ammonothermal approach is thus very promising for the discovery and design of novel and innovative next-generation semiconductors.

4.4 Experimental Section

The autoclaves were loaded and sealed in Ar-filled glove boxes (Unilab, MBraun, Garching, O_2<1 ppm, H_2O<1 ppm) to avoid oxygen and moisture contamination of the starting materials. A vacuum line (≤0.1 Pa) with connected argon and ammonia supply was used for the condensation procedure. Ar (Air Liquide, 99.999 %) and NH_3 (Air Liquide,

99.999 %) were passed through gas purification cartridges (Micro torr FT400-902 and MC400-702FV, SAES Pure Gas Inc., San Luis Obispo, CA, USA) providing a purity level of <1 ppbV H_2O, O_2 and CO_2.

Custom-built autoclaves manufactured from nickel-based superalloys Inconel 718 (max. 900 K, 300 MPa, 10 mL/97 mL) or Haynes 282 (max. 1100 K, 170 MPa, 10 mL) were used for ammonothermal syntheses. The autoclave body and lid is sealed via flange joints using silver-coated Inconel 718 metal-C-rings (GFD seals) as sealing gaskets. The hand valve (SITEC), pressure transmitter (HBM P2VA1/5000 bar) and safety head with integrated bursting disc (SITEC) are connected to the autoclave lid via 3/8″ high-pressure tubing connections.

4.4.1 Synthesis of $MgSiN_2$, $MnSiN_2$ and $LiSi_2N_3$

To facilitate a complete conversion to intermediate compounds, Si (Alfa Aesar, 99.9 %) was ball-milled under argon for 10 h using a planetary ball mill (Retsch PM 400). Mg (10 mmol, Alfa Aesar, 99.8 %), Si (8 mmol) and KN_3 (25 mmol, Sigma–Aldrich, 99.9 %), Mn (10 mmol, Alfa Aesar, 99.95 %), Si (8 mmol) and KN_3 (25 mmol) or LiN_3 (5 mmol, synthesized according to the procedure of Fair et al.)[50] and Si (5 mmol) were placed in Mo liners, respectively. The Mo liners were transferred into Haynes 282 autoclaves. The autoclaves were closed under argon, evacuated and cooled with ethanol/liquid nitrogen to 198 K. Ammonia was condensed into the autoclaves via a pressure regulating valve. For the synthesis of $MgSiN_2$ and $MnSiN_2$, the autoclave body was heated in a custom-built vertical tube furnace (Loba, HTM Reetz) to 570 K with a rate of 3 K min^{-1}, held at this temperature for 15 h, heated to 1070 K with a rate of 1 K min^{-1} and held for further 100 h. For the synthesis of $LiSi_2N_3$, the autoclave body was heated to 970 K with a rate of 1.5 K min^{-1} and maintained at this temperature for 100 h. The pressure was kept between 100 MPa and 170 MPa during the heating periods and was appropriately reduced if necessary. The autoclaves were cooled down to room temperature by switching off the furnace. The products were washed with H_2O and 5 M HCl to remove the residual mineralizer and intermediates and dried at 350 K in air. $MgSiN_2$ and $LiSi_2N_3$ where obtained as white powders and $MnSiN_2$ as red powder, respectively.

4.4.2 Synthesis of $MgGeN_2$, $MnGeN_2$ and $LiGe_2N_3$

Ge (smart-elements, 99.99 %) was ground for 15 min with an oscillating mixer mill (Specac Specamill) prior to the syntheses. Mg (20 mmol, Alfa Aesar, 99.8 %), Ge (16

mmol) and NaN_3 (50 mmol, Sigma–Aldrich, 99.5 %), Mn (20 mmol, Alfa Aesar, 99.95 %), Ge (16 mmol) and NaN_3 (50 mmol) or Li (25 mmol, Alfa Aesar, 99 %) and Ge_3N_4 (3 mmol, ABCR, 99.9 %) were directly placed into Inconel 718 autoclaves, respectively. The autoclaves were closed under argon, evacuated and cooled with ethanol/liquid nitrogen to 198 K. Ammonia was condensed into the autoclaves via a pressure regulating valve. For the synthesis of $MgGeN_2$ and $MnGeN_2$, the autoclave body (97 mL internal volume) was heated in a custom-built vertical tube furnace (Loba, HTM Reetz) to 670 K with a rate of 3 K min^{-1}, kept at this temperature for 15 h, heated to 870 K with a rate of 2 K min^{-1} and held for further 100 h. For the synthesis of $LiGe_2N_3$, the autoclave body (10 mL internal volume) was heated to 900 K with a rate of 3 K min^{-1} and maintained at this temperature for 100 h. The pressure was kept between 150 MPa and 230 MPa during the heating periods and was appropriately reduced if necessary. The autoclaves were cooled down to room temperature by switching off the furnace. The products were washed with EtOH ($MgGeN_2$, $LiGe_2N_3$) or H_2O ($MnGeN_2$) to remove the residual mineralizer and intermediates and dried at 350 K in air. $MgGeN_2$, $MnGeN_2$ and $LiGe_2N_3$ where obtained as beige, light brown and white powders, respectively.

4.4.3 Powder X-ray diffraction

The products were finely ground and loaded in glass capillaries (0.3 mm diameter, 0.01 mm wall thickness, Hilgenberg GmbH). XRD measurements were performed using a Stoe STADI P diffractometer (Mo $K\alpha_1$, λ = 0.70930 Å, Ge(111) monochromator, Mythen 1 K detector) in modified Debye–Scherrer geometry. Temperature-programmed powder X-ray diffraction was conducted on a Stoe STADI P diffractometer (Mo $K\alpha_1$, λ = 0.70930 Å, Ge(111) monochromator, image plate position sensitive detector) which is equipped with a high-temperature graphite furnace. The diffraction patterns were recorded in segments of 50 K up to 1270 K with a heating rate of 5 K min^{-1}.

TOPAS-Academic Software was used for Rietveld refinement applying the fundamental parameters model with direct convolution of source emission profiles, axial instrument contributions, crystallite size and microstrain effects for the peak shape function.[51,52] Capillary absorption correction (inner diameter 0.28 mm) was performed with the calculated absorption coefficient.

Further details on the crystal structure investigations may be obtained from the Fachinformationszentrum Karlsruhe, 76344 Eggenstein-Leopoldshafen, Germany (E-mail: crysdata@fiz-karlsruhe.de), on quoting the depository numbers CSD-433631 ($MgSiN_2$),

CSD-433632 ($MgGeN_2$), CSD-433633 ($MnSiN_2$), CSD-433634 ($MnGeN_2$), CSD-433635 ($LiSi_2N_3$) and CSD-433636 ($LiGe_2N_3$).

4.4.4 Scanning electron microscopy (SEM)

The crystal morphology of the products was investigated using a FEI Helios G3 UC scanning electron microscope (SEM; field emission gun, acceleration voltage 30 kV). The purified products were placed on an adhesive carbon pad and subsequently coated with a conductive carbon film using a high-vacuum sputtercoater (BAL-TEC MED 020, Bal Tec AG).

4.4.5 UV/Vis spectroscopy

A Jasco V-650 UV/Vis spectrophotometer equipped with Czerny–Turner mount, photomultiplier tube detector and deuterium (190–350 nm)/halogen (330–900 nm) lamps as light sources was used for diffuse reflectance measurements. The intensity artifacts at 330 nm arising from the deuterium—halogen lamp switch were corrected for a reliable determination of the bandgap.

4.4.6 DFT calculations

Bloch spectral functions and DOS calculations were conducted based on Rietveld refinements of the experimental structures as shown in Table 2 within the fully relativistic Korringa–Kohn–Rostoker (KKR) Green's function method as implemented in the Munich SPRKKR package.[53,54] The Brillouin zone was sampled with *k*-meshes of 12×10×13 (II-IV-N_2) and 12×12×11 (Li-IV_2-N_3) respectively. An angular momentum expansion of l = 3 was used for all calculations. Electronic convergence was achieved based on the local density approximation (LDA) of Vosko, Wilk, and Nusair and further by the EV-GGA (Engel Vosko) in order to compare the electronic bandgaps to the experimental measurements.[55,56] For the Li-IV_2-N_3 phases *k*-dependent convergence parameters for the structure constant matrix had to be set manually to values of ETA = 2.0, RMAX = 2.5 and GMAX = 2.5 in order to achieve reasonable results.

4.5 References

[1] S. P. DenBaars, D. Feezell, K. Kelchner, S. Pimputkar, C.-C. Pan, C.-C. Yen, S. Tanaka, Y. Zhao, N. Pfaff, R. Farrell, M. Iza, S. Keller, U. Mishra, J. S. Speck, S. Nakamura, *Acta Mater.* **2013**, *61*, 945-951.

[2] K. Shinohara, D. C. Regan, Y. Tang, A. L. Corrion, D. F. Brown, J. C. Wong, J. F. Robinson, H. H. Fung, A. Schmitz, T. C. Oh, S. J. Kim, P. S. Chen, R. G. Nagele, A. D. Margomenos, M. Micovic, *IEEE Trans. Electron Dev.* **2013**, *60*, 2982-2996.

[3] Y. Hinuma, T. Hatakeyama, Y. Kumagai, L. A. Burton, H. Sato, Y. Muraba, S. Iimura, H. Hiramatsu, I. Tanaka, H. Hosono, F. Oba, *Nat. Commun.* **2016**, 7:11962.

[4] P. Narang, S. Chen, N. C. Coronel, S. Gul, J. Yano, L.-W. Wang, N. S. Lewis, H. A. Atwater, *Adv. Mater.* **2014**, *26*, 1235-1241.

[5] P. C. Quayle, K. He, J. Shan, K. Kash, *MRS Commun.* **2013**, *3*, 135-138.

[6] A. D. Martinez, A. N. Fioretti, E. S. Toberer, A. C. Tamboli, *J. Mater. Chem. A* **2017**, *5*, 11418-11435.

[7] R. J. Bruls, A. A. Kudyba-Jansen, P. Gerharts, H. T. Hintzen, R. Metselaar, *J. Mater. Sci. Mater. Electron.* **2002**, *13*, 63-75.

[8] C. Kulshreshtha, J. H. Kwak, Y.-J. Park, K.-S. Sohn, *Opt. Lett.* **2009**, *34*, 794-796.

[9] J. B. Quirk, M. Råsander, C. M. McGilvery, R. Palgrave, M. A. Moram, *Appl. Phys. Lett.* **2014**, *105*, 112108.

[10] T. de Boer, T. D. Boyko, C. Braun, W. Schnick, A. Moewes, *Phys. Status Solidi RRL* **2015**, *9*, 250-254.

[11] H. Yamane, S. Kikkawa, M. Koizumi, *Solid State Ion.* **1987**, *25*, 183-191.

[12] E. Narimatsu, Y. Yamamoto, T. Nishimura, N. Hirosaki, *J. Ceram. Soc. Jpn.* **2010**, *118*, 837-841.

[13] Y. Q. Li, N. Hirosaki, R. J. Xie, T. Takeka, M. Mitomo, *J. Solid State Chem.* **2009**, *182*, 301-311.

[14] Q. Wu, Y. Li, X. Wang, Z. Zhao, C. Wang, H. Li, A. Mao, Y. Wang, *RSC Adv.* **2014**, *4*, 39030-39036.

[15] S. Esmaeilzadeh, U. Hålenius, M. Valldor, *Chem. Mater.* **2006**, *18*, 2713-2718.

[16] C. J. Duan, A. C. A. Delsing, H. T. Hintzen, *J. Lumin.* **2009**, *129*, 645-649.

[17] M. Orth, W. Schnick, *Z. Anorg. Allg. Chem.* **1999**, *625*, 1426-1428.

[18] Z. Lenčéš, K. Hirao, Y. Yamauchi, S. Kanzaki, *J. Am. Ceram. Soc.* **2003**, *86*, 1088-1093.

[19] J. Guyader, M. Maunaye, J. Lang, *C. R. Acad. Sci. Ser. C* **1971**, *272*, 311-313.

[20] G. Dhanaraj, K. Byrappa, V. Prasad, M. Dudley, *Springer Handbook of Crystal Growth* **2010**, Springer Berlin Heidelberg, Germany.

[21] J. Häusler, S. Schimmel, P. Wellmann, W. Schnick, *Chem. Eur. J.* **2017**, *23*, 12275 - 12282.

[22] T. Richter, R. Niewa, *Inorganics* **2014**, *2*, 29-78.

[23] S. Pimputkar, S. Nakamura, *The Journal of Supercritical Fluids* **2016**, *107*, 17-30.

[24] S. Pagano, M. Zeuner, S. Hug, W. Schnick, *Eur. J. Inorg. Chem.* **2009**, *2009*, 1579-1584.

[25] Y. H. Jung, L. C. Tang, M. H. Lee, *J. Phys.: Condens. Matter* **2001**, *13*, 10417.

[26] M. Maunaye, R. Marchand, J. Guyader, Y. Laurent, J. Lang, *Bull. Soc. Fr. Miner. Cristallogr.* **1971**, *94*, 561-564.

[27] J. David, J. P. Charlot, J. Lang, *Rev. Chim. Miner.* **1974**, *11*, 405-413.

[28] W. Paszkowicz, S. Podsiadło, R. Minikayev, *J. Alloys Compd.* **2004**, *382*, 100-106.

[29] R. López, R. Gómez, *J. Sol-Gel Sci. Technol.* **2012**, *61*, 1-7.

[30] J. Tauc, R. Grigorovici, A. Vancu, *Phys. Status Solidi B* **1966**, *15*, 627-637.

[31] C. M. Fang, R. A. d. Groot, R. J. Bruls, H. T. Hintzen, G. d. With, *J. Phys.: Condens. Matter* **1999**, *11*, 4833-4842.

[32] F. Liang, L. Tian, H. Zhang, F. Liang, S. Liu, R. Cheng, S. Zhang, *RSC Adv.* **2016**, *6*, 68615-68618.

[33] D. Naveh, L. Kronik, *Phys. Status Solidi B* **2006**, *243*, 2159-2163.

[34] R. Niklaus, J. Minar, J. Häusler, W. Schnick, *PCCP* **2017**, *19*, 9292-9299.

[35] A. P. Jaroenjittichai, W. R. L. Lambrecht, *Phys. Rev. B* **2016**, *94*, 125201.

[36] Y. M. Basalaev, P. V. Demushin, *J. Struct. Chem.* **2010**, *51*, 1191-1194.

[37] T. Misaki, X. Wu, A. Wakahara, A. Yoshida, *Proc. Int. Workshop on Nitride Semiconductors, IPAP Conf. Series 1* **2000**, 685-688.

[38] M. Råsander, M. A. Moram, *Mater. Res. Express* **2016**, *3*, 085902.

[39] C. M. Fang, H. T. Hintzen, G. de With *Appl. Phys. A* **2004**, *78*, 717-719.

[40] H. M. Huang, S. J. Luo, K. L. Yao, *J. Supercond. Nov. Magn.* **2014**, *27*, 257-261.

[41] L. C. Tang, Y. C. Chang, J. Y. Huang, C. S. Chang, *Proc. SPIE Vol. 7056, Photonic Fiber and Crystal Devices: Advances in Materials and Innovations in Device Applications II* **2008**, *7056*, 705605.

[42] H. Zhang, J. Ren, L. Wu, J. Zhang, *J. Solid State Chem.* **2017**, *245*, 184-189.

[43] E. Brunner, *J. Chem. Thermodyn.* **1988**, *20*, 273-297.

[44] J. Häusler, L. Neudert, M. Mallmann, R. Niklaus, A.-C. L. Kimmel, N. S. A. Alt, E. Schlücker, O. Oeckler, W. Schnick, *Chem. Eur. J.* **2017**, *23*, 2583-2590.

[45] N. Cordes, W. Schnick, *Chem. Eur. J.* **2017**, *23*, 11410-11415.

[46] E. Parthé, *Z. Kristallogr. Cryst. Mater.* **1964**, *119*, 204.

[47] T. J. McLarnan, W. H. Baur, *J. Solid State Chem.* **1982**, *42*, 283-299.

[48] W. H. Baur, T. J. McLarnan, *J. Solid State Chem.* **1982**, *42*, 300-321.

[49] Z.-H. Cai, P. Narang, H. A. Atwater, S. Chen, C.-G. Duan, Z.-Q. Zhu, J.-H. Chu, *Chem. Mater.* **2015**, *27*, 7757-7764.

[50] H. D. Fair, R. F. Walker, *Energetic Materials, Physics and Chemistry of Inorganic Azides, 1st ed.*, Springer, New York **1977**.

[51] A. Coelho, *TOPAS Academic*, *Version 4.1*, Coelho Software, Brisbane (Australia), **2007**.

[52] R. W. Cheary, A. A. Coelho, J. P. Cline, *J. Res. Natl. Inst. Stand. Technol.* **2004**, *109*, 1-25.

[53] H. Ebert, D. Ködderitzsch, J. Minár, *Rep. Prog. Phys.* **2011**, *74*, 096501.

[54] H. Ebert et al., *The Munich SPR-KKR Package, Version 7.7*, http://olymp.cup.uni-muenchen.de/ak/ebert/SPRKKR, **2012**.

[55] S. H. Vosko, L. Wilk, M. Nusair, *Can. J. Phys.* **1980**, *58*, 1200-1211.

[56] E. Engel, S. H. Vosko, *Phys. Rev. B* **1993**, *47*, 13164-13174.

5 Ammonothermal Synthesis of Novel Nitrides: Case Study on $CaGaSiN_3$

published in: *Chem. Eur. J.* **2017**, *23*, 2583–2590.

authors: Jonas Häusler, Lukas Neudert, Mathias Mallmann, Robin Niklaus, Anna-Carina L. Kimmel, Nicolas S. A. Alt, Eberhard Schlücker, Oliver Oeckler, and Wolfgang Schnick

DOI: 10.1002/chem.201605344

http://onlinelibrary.wiley.com/doi/10.1002/chem.201605344/abstract

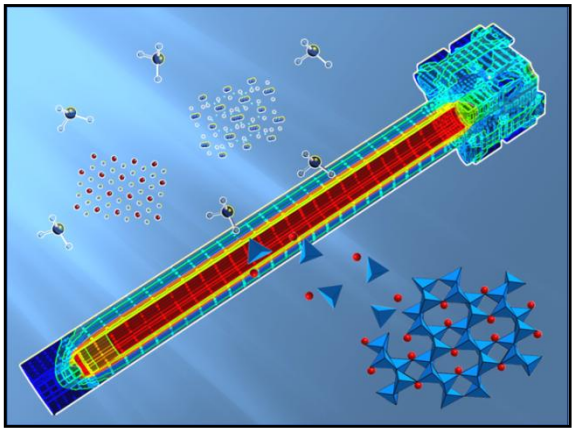

Abstract. The first gallium-containing nitridosilicate $CaGaSiN_3$ was synthesized in newly developed high-pressure autoclaves using supercritical ammonia as solvent and nitriding agent. The reaction was conducted in an ammonobasic environment starting from intermetallic CaGaSi with NaN_3 as a mineralizer. At 770 K, intermediate compounds were obtained, which were subsequently converted to the crystalline nitride at temperatures up to 1070 K (70–150 MPa). The impact of other mineralizers (e.g., LiN_3, KN_3, and CsN_3) on the product formation was investigated as well. The crystal structure of $CaGaSiN_3$ was analyzed by powder X-ray diffraction and refined by the Rietveld method. The structural results were further corroborated by transmission electron microscopy, ^{29}Si MAS-NMR, and first-principle DFT calculations. $CaGaSiN_3$ crystallizes in the orthorhombic space group $Cmc2_1$ (no. 36) with lattice parameters a = 9.8855(11), b = 5.6595(1), c = 5.0810(1) Å, (Z = 4, R_{wp} = 0.0326), and is isostructural with $CaAlSiN_3$ (CASN). Eu^{2+} doped samples exhibit red luminescence with an emission maximum of 620 nm and FWHM of 90 nm.

Thus, $CaGaSiN_3:Eu^{2+}$ also represents an interesting candidate as a red-emitting material in phosphor-converted light-emitting diodes (pc-LEDs). In addition to the already known substitution of alkaline-earth metals in $(Ca,Sr)AlSiN_3:Eu^{2+}$, inclusion of Ga is a further and promising perspective for luminescence tuning of widely used red-emitting CASN type materials.

5.1 Introduction

In analogy to hydrothermal processes, the ammonothermal method comprises solution-based reactions using supercritical ammonia as the solvent. A wide range of inorganic compounds can be synthesized by this technique, notably amides, imides, and ammoniates, preferably at temperatures up to 800 K, and nitrides at higher temperatures up to more than 1000 K.[1] The solubility of many metals and ionic compounds can be strongly increased by employing high pressures and ammonobasic or -acidic mineralizers like alkali metal amides or ammonium halides. The ammonothermal method is therefore well-suited for the growth of single crystals from solution.

In the 1960s, Jacobs and co-workers investigated the behavior of various chemical elements in supercritical ammonia. In this way, many new multinary amide and imide compounds were synthesized.[2] Even single crystals of binary nitrides (e.g., Be_3N_2, LaN, Cu_3N) could be grown by chemical transport reactions during ammonothermal syntheses.[3-5] The pioneering work of Jacobs laid the foundation for today's research on the ammonothermal crystal growth of group 13 nitrides. The interest in the ammonothermal technique has strongly increased in the last few years, as it emerged as a powerful alternative for the industrial growth of high-quality bulk GaN crystals.[6] Starting from polycrystalline GaN in ammonobasic or -acidic environment, the growth process is conducted by convection-driven chemical transport reactions maintaining specific temperature gradients in the autoclaves. High growth rates of up to 40 µm h^{-1} in the *m*-direction were reported by employing NH_4F as the mineralizer.[7] The crystals are processed for the fabrication of wafers that can be used as substrates for semiconductor devices.

It has been shown that ternary nitrides can be synthesized ammonothermally as well, for example $LiSi_2N_3$, $NaSi_2N_3$ and $K_3P_6N_{11}$, using ammonobasic mineralizers at pressures between 100–600 MPa and temperatures up to 870 K.[8-10] Moreover, Watanabe et al. demonstrated the synthesis of $CaAlSiN_3:Eu^{2+}$ (CASN) and $SrAlSiN_3:Eu^{2+}$ (SASN), the first quaternary nitrides obtained by this method.[11,12] These nitrides are industrially used red-

emitting luminescent materials for phosphor-converted light-emitting diodes (pc-LEDs) with an emission maximum between 650 nm (CASN) and 610 nm (SASN).[13,14] Studies on substitutions of the *p*-block elements Al or Si in CASN or SASN with the heavier homologs Ga and Ge have not been mentioned in the literature as yet.

Only a few reports about explorative ammonothermal syntheses of nitrides were published since Jacob's research studies, even though the technique has proven to be promising, especially for the synthesis of hardly accessible compounds. To unleash its full potential, we developed new high-temperature autoclaves that are applicable for pressures up to 170 MPa and temperatures of 1100 K (see Figure 1). In this contribution, we report the ammonothermal synthesis of the first nitridogallosilicate $CaGaSiN_3$ in an ammonobasic environment. Its crystal structure was analyzed by powder X-ray diffraction. Indexing and Rietveld refinement results were confirmed by electron diffraction, ^{29}Si solid-state NMR, and first-principles DFT calculations. Additionally the luminescence characteristics of Eu^{2+}-doped $CaGaSiN_3$ were investigated and revealed interesting properties for possible applications as red-emitting phosphor in pc-LEDs.

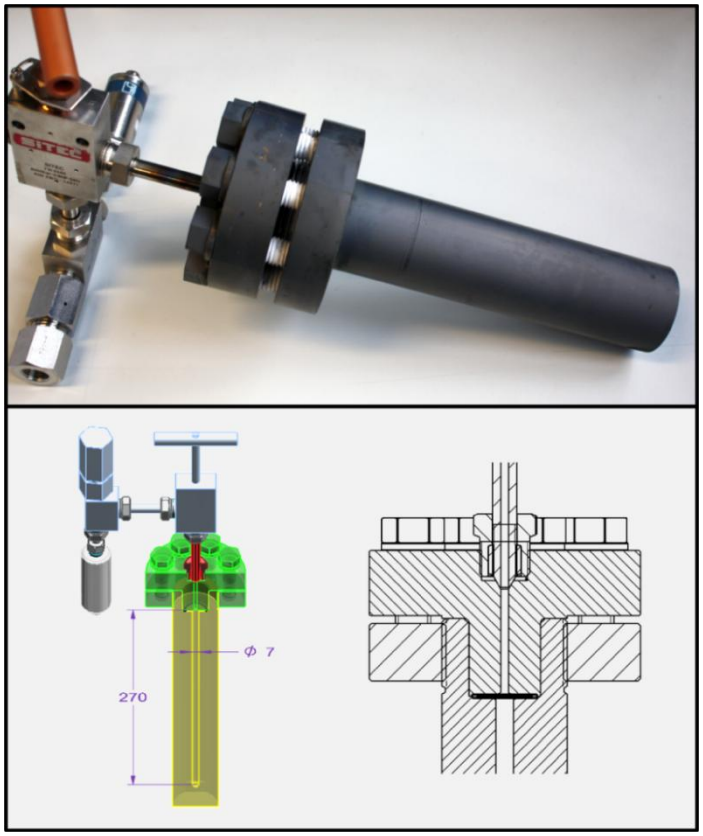

Figure 1. Top: Autoclave made of nickel-based superalloy for ammonothermal syntheses. Bottom: Left: Cross-sectional drawing of autoclave with assembled head part. Right: Flange construction and sealing concept.

5.2 Results and Discussion

5.2.1 Synthesis

The new compound $CaGaSiN_3:Eu^{2+}$ was synthesized by the ammonothermal method using custom-built autoclaves. NaN_3 was used as a mineralizer because of its stability with respect to oxygen and moisture and availability in high purity. NaN_3 forms $NaNH_2$ in situ by reaction with supercritical ammonia at elevated temperatures.[6] $NaNH_2$ is the actual basic mineralizer which increases the solubility of the starting materials by forming intermediate compounds like amides, imides, or ammoniates. The first heating step was conducted to convert the intermetallic precursor CaGaSi:Eu to intermediates such as $NaCa(NH_2)_3$, $NaGa(NH_2)_4$, Si_2N_2NH, and amorphous species, which are formed at temperatures around 770 K.[15-17] These compounds are slowly decomposed during the subsequent heating step between 770 and 1070 K leading to controlled formation of $CaGaSiN_3:Eu^{2+}$. The use of an intermetallic precursor facilitates this conversion because of a better mixing of intermediates on a molecular level. The product was further annealed at 1070 K under slow reduction of the pressure to support decomposition of the remaining intermediates and to increase its crystallinity. The residual mineralizer and crystalline intermediates were easily removed by washing the product with water and 1 M HCl. Analogous reactions with LiN_3 as the mineralizer yielded GaN as a side-phase next to $CaGaSiN_3:Eu^{2+}$. Because $LiNH_2$ exhibits a very low solubility in ammonia, the formation of intermediates is expected to be slower compared to $NaNH_2$.[18] This might facilitate the formation of GaN, as Si is not sufficiently converted to reactive intermediates. On the other hand, the ternary nitride $Ca_{16}Si_{17}N_{34}$[19], in addition to GaN, was obtained by reactions with alkali azides KN_3 and CsN_3, which can presumably be attributed to the formation of different intermediates; ternary amides $MCa(NH_2)_3$ (M = Na, K, Cs) or $MGa(NH_2)_4$ (M = Li, Na, K) are formed in reactions of alkali amides with Ca or Ga, whereas syntheses with Si lead to imidonitrides Si_2N_2NH and $K_3Si_6N_5(NH)_6$ or nitrides $LiSi_2N_3$ and $NaSi_2N_3$.[8,9,17,20] NaN_3 was therefore assessed as the most suitable mineralizer for the ammonothermal synthesis of $CaGaSiN_3$. We also discovered that ammonothermal reactions at 870 K or pressures below 100 MPa resulted in formation of $CaGaSiN_3$ with poor crystallinity. Accordingly, the employment of high temperatures and pressures was found to be crucial for the synthesis of crystalline $CaGaSiN_3$.

5.2.2 Crystal structure analysis

Powder X-ray diffraction (PXRD) under inert conditions showed the occurrence of $NaNH_2$, $NaCa(NH_2)_3$, and amorphous byphases in addition to $CaGaSiN_3:Eu^{2+}$. After purification, $CaGaSiN_3:Eu^{2+}$ was the only crystalline phase in the product. The reflections were indexed with an orthorhombic unit cell; systematic absences indicated the space group $Cmc2_1$. Wyckoff positions and coordinates of isotypic $CaAlSiN_3$ were taken as starting values for the Rietveld refinement.[21] Displacement parameters and occupancy factors could not be refined to reasonable values because of crystallite size broadening and overlapping of reflections in the X-ray diffraction pattern. Therefore, the displacement parameters were fixed at reasonable values and full occupancy of the crystallographic sites with the ideal composition $Ca_{0.99}Eu_{0.01}GaSiN_3$ was assumed. The PXRD data are represented in Figure 2 and Table 1; Wyckoff positions and atomic coordinates are listed in Table S1 (see the Supporting Information). A marked background in the powder patterns hints at amorphous side-phases. Presumably, these arise from polymerized amide or imide compounds, which remained stable in the reaction mixture. Additional temperature-dependent PXRD measurements (see Figure S2 in the Supporting Information) show that $CaGaSiN_3$ is stable up to ≈820 K and retains orthorhombic metrics in this temperature range.

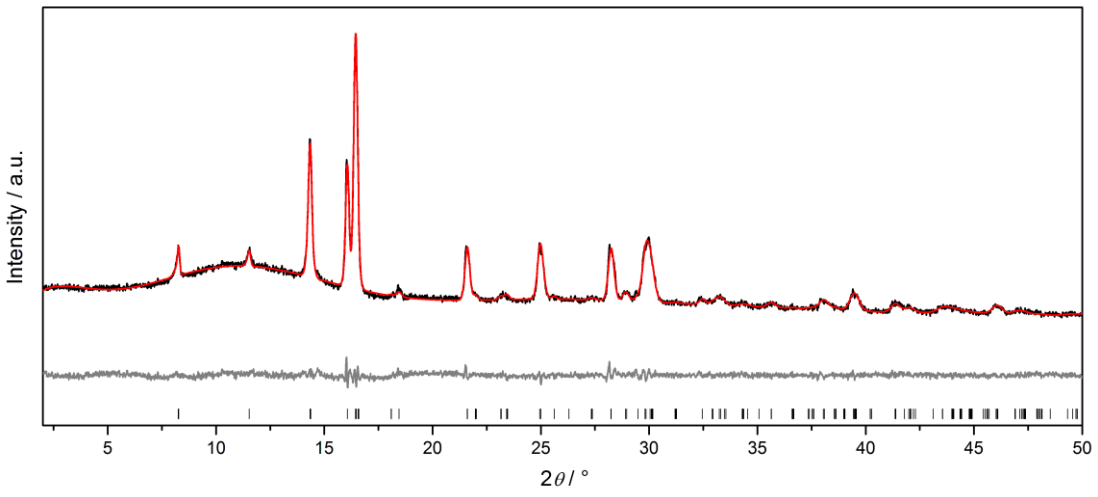

Figure 2. Rietveld refinement of X-ray powder diffraction pattern of $CaGaSiN_3:Eu^{2+}$ with experimental data (black line), calculated pattern (red line), difference profile (gray line), and positions of Bragg reflections (black bars).

Table 1. Crystallographic data of $CaGaSiN_3:Eu^{2+}$ obtained by Rietveld refinement

Formula	**$Ca_{0.99}Eu_{0.01}GaSiN_3$**
Crystal system	orthorhombic
Space group	Cmc21 (no. 36)
a [Å]	9.8855(11)
b [Å]	5.6595(6)
c [Å]	5.0810(4)
Cell volume [$Å^3$]	284.26(5)
Formula units [cell]	4
Density [$g \cdot cm^{-3}$]	4.230
T [K]	295(2)
Diffractometer	STOE STADI P
Radiation [Å]	Mo-Kα1 (λ = 0.70930 Å)
θ range [°]	$2.0 \leq 2\theta \leq 50.0$
Data points	3283
Total number of reflections	166
Refined parameters	29
Background function	Shifted Chebyshev
R values	$R_p = 0.0248$ $R_{wp} = 0.0326$
Goodness of fit	1.518

$CaGaSiN_3$ crystallizes in space group $Cmc2_1$ (no. 36), which is a maximal non-isomorphic subgroup of $P6_3mc$ (no. 186). Its crystal structure can be regarded as a strongly distorted superstructure variant of the wurtzite structure type (space group $P6_3mc$) and is isotypic with $CaAlSiN_3$. In analogy with the latter, Ga and Si are disordered on Wyckoff site 8*b* and are tetrahedrally coordinated by nitrogen. The $(Ga/Si)N_4$ tetrahedra share vertices, forming a network of six-membered rings extending in (001) (see Figure 3). Ca occupies

the 4*b* site and is coordinated by five nitrogen atoms. Intermetallic CaGaSi, which crystallizes in the AlB_2 structure type, is structurally unrelated to $CaGaSiN_3$. CaGaSi exhibits a disordered Ga/Si site as well, but it remains unclear if this could favor Ga/Si disorder in $CaGaSiN_3$.

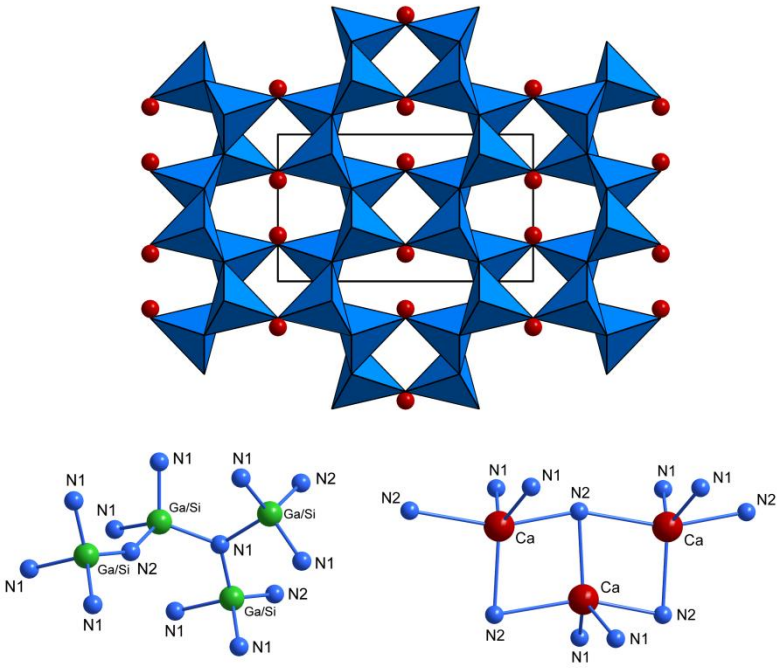

Figure 3. Top: Crystal structure of $CaGaSiN_3:Eu^{2+}$ viewed along [001] with $(Ga/Si)N_4$ tetrahedra depicted in blue, Ca^{2+} in red. Bottom: Coordination of Ga/Si (left) and Ca (right) with nitrogen.

The ionic radii of Al and Ga in nitride compounds are 41 and 48 pm, respectively.[22] As expected, substitution of Al by Ga leads to an increased cell volume, which is about 3 % larger in comparison to ammonothermally synthesized $CaAlSiN_3$.[23] Traces of sodium originating from the mineralizer might be incorporated into the structure, as also discussed below in the electron microscopy section. A solid-solution of $CaGaSiN_3$ and $NaSi_2N_3$ according to $Na_xCa_{1-x}Ga_{1-x}Si_{1+x}N_3$ is presumably formed, as these compounds are isostructural and exhibit similar lattice parameters. $NaSi_2N_3$ can be synthesized by reaction of Si with $NaNH_2$ under similar ammonothermal conditions.[9] During our systematic investigations we found that reactions with LiN_3 as mineralizer yielded $CaGaSiN_3$ with reduced cell parameters, which corroborates the formation of solid solutions of $M_xCa_{1-x}Ga_{1-x}Si_{1+x}N_3$ (M = Li, Na). Therefore, the lattice parameter of the ideal composition of $CaGaSiN_3$ might slightly deviate from the obtained data.

The reflections in the powder pattern of ammonothermally synthesized $CaGaSiN_3$ are affected by crystallite size broadening. The average crystal size was refined to a value of about 20 nm (Gaussian convolution),[24] which is in the same order of magnitude as reported values for ammonothermally synthesized $CaAlSiN_3$.[23] Microstrain probably contributes to peak broadening as well, as the crystal size observed by transmission electron microscopy deviates from this value (see electron microscopy analyses).

The (Ga/Si)−N interatomic distances range between 1.701 and 1.943 Å, which reveals a marked distortion of the $(Ga/Si)N_4$ tetrahedra. Ca is coordinated by five N atoms with distances between 2.317 and 2.714 Å. Similar values are observed in comparable nitrides: Typical Si−N and Ga−N bond lengths range from 1.60 to 1.80 Å in nitridosilicates and from 1.92 to 2.06 Å in nitridogallates, respectively.[9,25-29] The Ca−N distances in $CaAlSiN_3:Eu^{2+}$ are between 2.32 and 2.69 Å,[21] and on average slightly shorter than in $CaGaSiN_3:Eu^{2+}$. The Ca−Ca distances amount to 3.31 Å and are therefore similar to those in other calcium nitridosilicates like $CaSiN_2$ (3.05–3.30 Å) and $CaAlSiN_3$ (3.27 Å).[21,30]

5.2.3 Electron microscopy

SEM images show that $CaGaSiN_3$ forms plate- and needle-shaped crystallites with typical diameters from 0.05–0.1 µm (see Figure S1 in the Supporting Information). The morphology is similar to that of ammonothermally synthesized $CaAlSiN_3$.[23] TEM investigations were performed to obtain information about the crystallite sizes, chemical composition on the nanometer scale, and to confirm the orthorhombic metrics. Despite sample preparation using ultrasonic methods, the majority of the $CaGaSiN_3:Eu^{2+}$ crystallites form agglomerates (see Figure 4 left). A few separated crystals were suitable for EDX analysis and selected area electron diffraction (SAED). $CaGaSiN_3$ is stable in the electron beam. The diameter of the crystals varies between 10 and 100 nm; the length between 0.5 and 2 µm (see Figure 4 right). EDX measurements on different microcrystals showed an atomic ratio of the heavy atoms approximately matching the sum formula $CaGaSiN_3$ (see Table 2). Small amounts of Na up to 5 atom % were detected in several crystals, which points to a possible formation of solid solutions between $CaGaSiN_3$ and $NaSi_2N_3$ as discussed above. The small amount of oxygen detected might arise from surface hydrolysis caused by the washing treatment or from partial substitutions of Ca/N by Na/O maintaining charge neutrality.

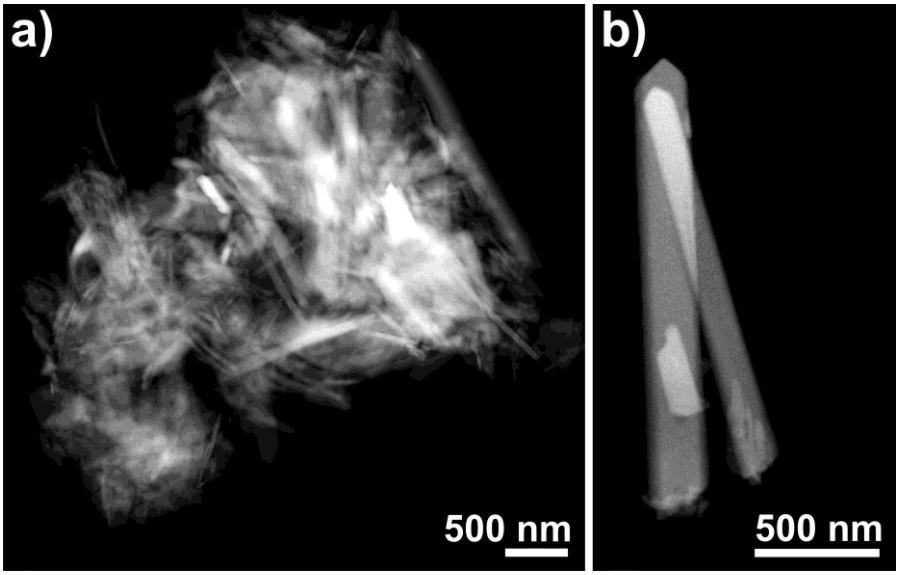

Figure 4. STEM dark-field images of representative crystals of $CaGaSiN_3:Eu^{2+}$; (a) agglomerates and (b) separated crystals.

Table 2. TEM EDX measurements of $CaGaSiN_3$ microcrystals in atom %, mean values with standard deviations

	Ca	Ga	Na	Si	N	O
K1	13	22	2	21	38	4
K2	13	20	3	21	39	6
K3	11	18	4	20	44	3
K4	14	21	1	21	39	3
K5	14	18	4	20	38	7
K6	15	17	4	20	40	4
K7	16	17	5	19	40	5
average	14(1)	19(2)	3(1)	20(1)	40(2)	5(1)

Electron diffraction (see Figure 5) confirmed the orthorhombic metrics of $CaGaSiN_3$. Lattice parameters a = 9.9 Å, b = 5.7 Å, and c = 5.1 Å were determined from SAED patterns along [100] and [010]. SAED patterns or Fourier transformed HRTEM images along various zone axes of different crystals of $CaGaSiN_3:Eu^{2+}$ exhibited no additional reflections. Although short-range ordering of Ga and Si may be possible, there is no evidence for a superstructure.

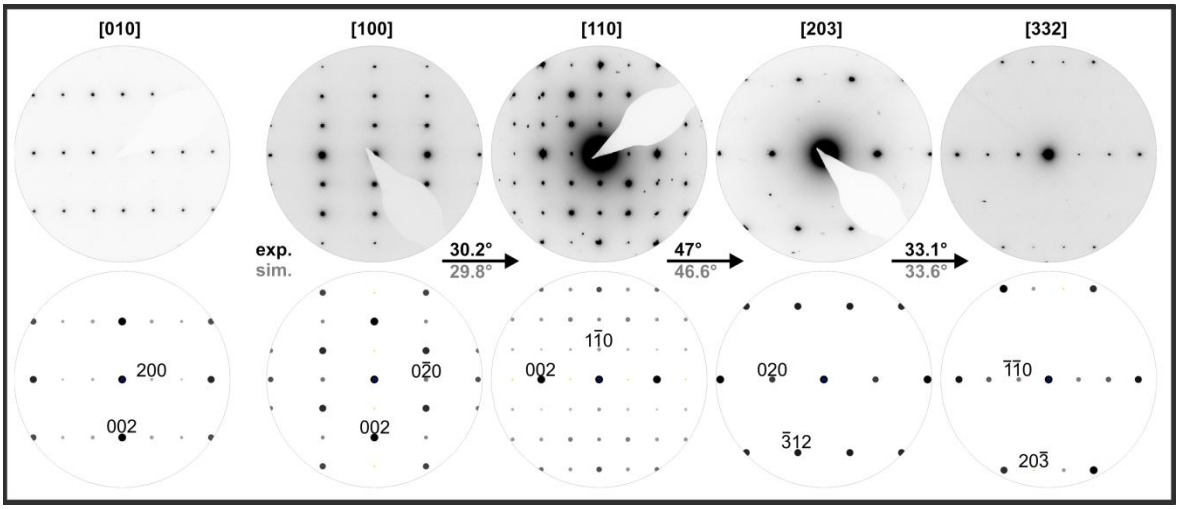

Figure 5. SAED patterns of a microcrystal of $CaGaSiN_3:Eu^{2+}$; left: for [010] zone axis, right: SAED tilt series, experimental patterns and tilt angles (top) and simulated data based on structure model from powder X-ray data (bottom), selected reflections labeled with indices.

5.2.4 Solid-state NMR spectroscopy

^{29}Si MAS-NMR spectra were recorded to corroborate the previous analyses. The ^{29}Si spectrum exhibits one signal at −50.7 ppm (see Figure 6), which is in accordance with one crystallographic site of Si in the structure. The chemical shift of SiN_4-tetrahedra in nitrides is commonly between −40 and −60 ppm.[31-35] Signals around −50 ppm have been detected for isostructural $CaAlSiN_3$, which coincides very well with the measurement.[36]

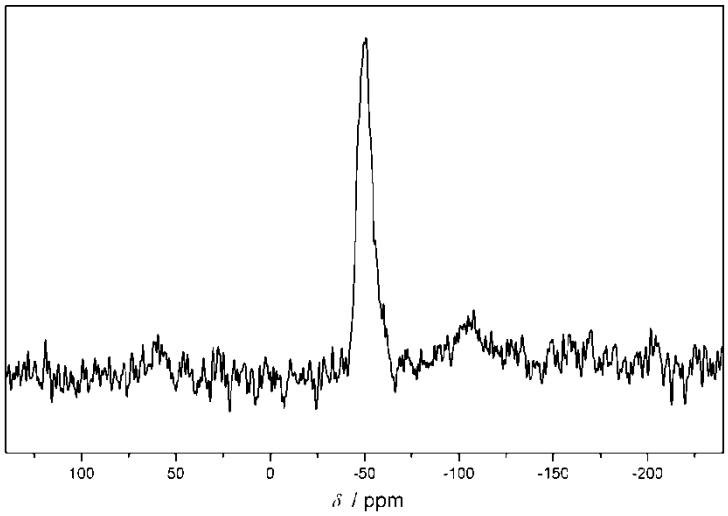

Figure 6. ^{29}Si MAS-NMR spectrum of $CaGaSiN_3:Eu^{2+}$ with one signal at −50.7 ppm.

5.2.5 Luminescence

Red luminescence is observed when samples of $CaGaSiN_3:Eu^{2+}$ are irradiated with UV light. A broadband excitation was observed with a maximum of about 470 nm (see Figure 7). The phosphor can therefore be efficiently excited by a blue (Ga,In)N-based LED. The emission spectrum shows a maximum of 620 nm with full width at half-maximum (FWHM) of 90 nm. The luminescence is originating from the $4f^6(^7F)5d^1 \rightarrow 4f^7(^8S_{7/2})$ transition in Eu^{2+}. In comparison to $CaAlSiN_3:Eu^{2+}$ (λ_{max} = 650 nm),[13] the increased bond lengths lead to a less distinctive crystal field splitting of the 5d-states. Therefore, the Stokes shift of the excitation light is smaller and in the same order of isostructural $SrAlSiN_3:Eu^{2+}$.[37]

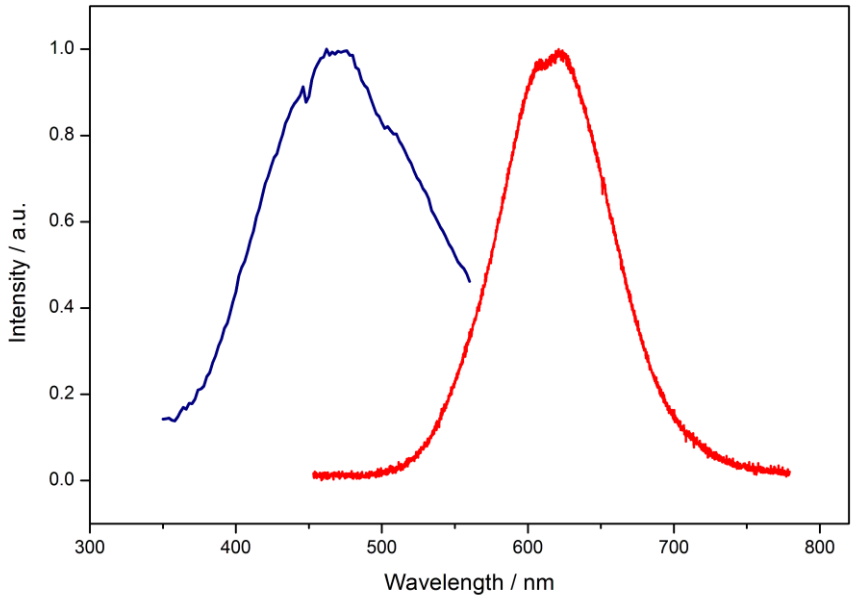

Figure 7. Excitation (blue) and emission spectrum (red) of $CaGaSiN_3:Eu^{2+}$ (1 mol % Eu) with λ_{exc} = 450 nm.

5.2.6 DFT calculations

To explain the Ga/Si disorder, crystallographically ordered structure models were constructed for the ab initio calculations. The Niggli-reduced cell includes two tetrahedrally coordinated Ga and Si atoms, respectively. Six structure models are obtained by arranging the Ga and Si atoms in an ordered manner, three of which are different from a crystallographic point of view (see Figure 8).[38] The calculated lattice constants and total energies are listed in Table 3.

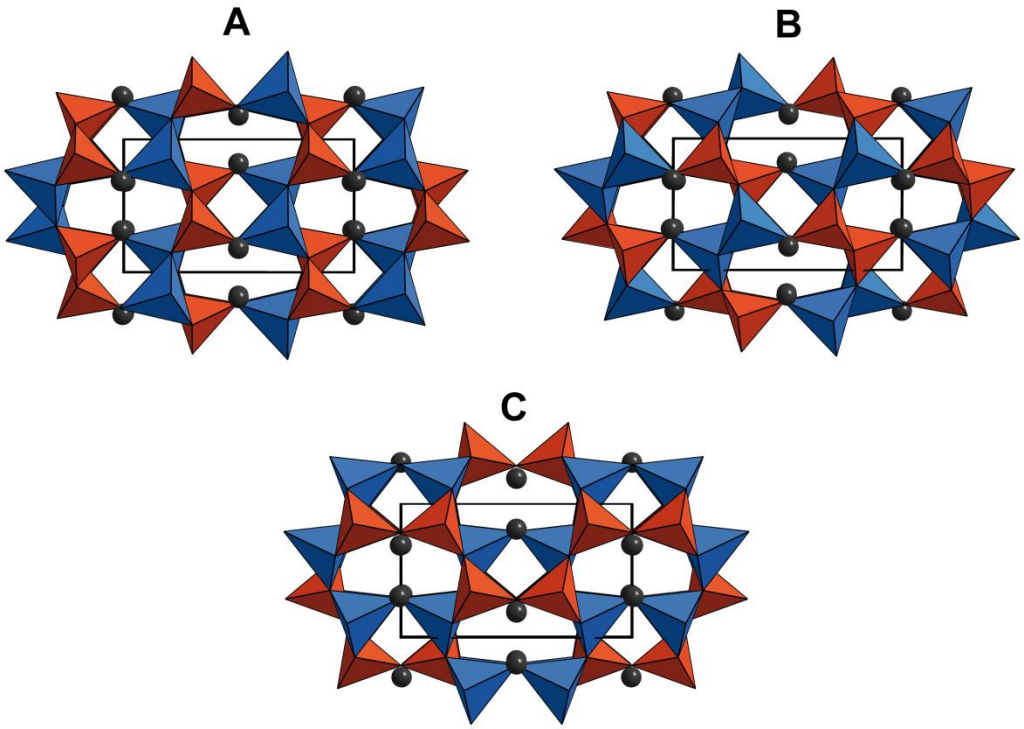

Figure 8. Ordered structure models for first-principles DFT calculations.

Table 3. Lattice parameters and total energies of $CaGaSiN_3$ for three different ordered structure models calculated by the generalized gradient approximation (GGA)

Lattice parameter [Å]	Model A	Model B	Model C
a	10.063	10.080	9.987
b	5.794	5.785	5.746
c	5.137	5.136	5.224
Total energies [eV / formula unit]	-41.132	-41.140	-40.885

As usual, the cell parameters approximated are overestimated by generalized gradient approximations (GGA); the values determined by Rietveld refinement are expectedly lower. Comparing theoretical and experimental data, the observed deviation of 1–2 % is in the same range as for $CaAlSiN_3$.[39,40] Incorporation of traces of sodium could additionally

lead to slightly decreased cell parameters. Whereas total energies of model A and B are quite similar, the structure of model C seems to be less stable. This might arise from the fact that two GaN_4-tetrahedra are connected by a twofold-coordinated N (N[2]) atom, which seems to be less favorable, as already stated for respective AlN_4-tetrahedra in $CaAlSiN_3$.[38] The overall similarity of total energies corroborates the disorder of Ga and Si on the 8*b* site.

5.3 Conclusion

$CaGaSiN_3:Eu^{2+}$ was synthesized by the ammonothermal method starting from intermetallic precursor CaGaSi:Eu in an ammonobasic environment employing NaN_3 as a mineralizer. Rietveld refinement showed that $CaGaSiN_3:Eu^{2+}$ crystallizes in space group $Cmc2_1$ as a distorted superstructure variant of the wurtzite structure type. Though nanocrystals are preferentially formed during the reaction, TEM investigations revealed that a minority of crystals with up to 2 µm in length were formed. Electron diffraction patterns suggest that the size of the coherently scattering domains in the $CaGaSiN_3:Eu^{2+}$ microcrystal is in the range of nm. Cation ordering could be possible due to symmetry reduction without additional reflections; however, no evidence for such ordering was observed. TEM investigations confirm chemical composition and orthorhombic metrics of $CaGaSiN_3:Eu^{2+}$. The magnitude of the determined lattice parameters was further verified by ab initio DFT calculations.

The crystal size, morphology, and X-ray diffraction patterns are similar to those of ammonothermally synthesized $CaAlSiN_3$. Different alkali metal azides were probed as mineralizers, where NaN_3 proved to be the best choice, with no detectable crystalline side-phases in the product. Some evidence of possible incorporation of Na was observed in the product, which coincides with analogous syntheses of $CaAlSiN_3$.[23]

It was also shown that the formation of $CaGaSiN_3$ is favored despite prevailing reaction conditions for the ammonothermal crystal growth of GaN. The use of an intermetallic precursor facilitates the conversion to the nitride because of a better mixing of the intermediates on a molecular level. Furthermore, it was found that $CaGaSiN_3:Eu^{2+}$ is best accessible with LiN_3 and NaN_3 as mineralizer. Employment of KN_3 and CsN_3 leads to formation of K and Cs amides or imides, which behave differently compared with Li and Na. Additionally, no ternary K or Cs nitridosilicates are known so far, whereas the nitrides $LiSi_2N_3$ and $NaSi_2N_3$ might act as precursors and crystallization seeds.

In addition, promising photoluminescence characteristics for the application in phosphor-converted LEDs were ascertained. Solid solutions with $CaAlSiN_3:Eu^{2+}$, but also with other wurtzite derivatives, establish numerous substitution options in this structure type. For instance, recent studies on $Li_xCa_{1-x}Al_{1-x}Si_{1+x}N_3$ demonstrated either a slight blue- or strong redshift of the emission maximum dependent on the degree of cation cosubstitution.[41] With regard to $CaGaSiN_3:Eu^{2+}$ and respective solid solutions, new luminescence tuning opportunities are opened up in the CASN and SASN system.

This study demonstrates that the ammonothermal technique is a powerful tool for the synthesis of novel multinary nitrides. With the development of new high-temperature autoclaves, the synthetic potential of this method is strongly extended. Notably, the formation of wurtzite derivatives seems to be favored in particular, which might be promising for the crystal growth of new semiconductors like Zn_2PN_3 or analogous substitutional compounds.[42]

5.4 Experimental Section

Unless otherwise stated, all manipulations were performed in flame-dried Schlenk-type glassware connected to a vacuum line (≤0.1 Pa) or in Ar-filled glove boxes (Unilab, MBraun, Garching, O_2<1 ppm, H_2O<1 ppm) to rigorously exclude oxygen and moisture during syntheses. Argon (Air Liquide, 99.999 %) was purified by passage through columns filled with KOH (Merck, ≥85 %), silica gel (Merck), dried molecular sieve (Fluka, 3 Å), P_4O_{10} (Roth, ≥99 %) and titanium sponge (Johnson Matthey, 99.5 %) at 970 K. Ammonia (Air Liquide, 99.999 %) was passed through a gas purification cartridge (Micro torr MC400-702FV, SAES Pure Gas Inc., San Luis Obispo, CA, USA) to obtain a purity level of <1 ppbV H_2O, O_2, and CO_2.

5.4.1 Preparation of starting materials

The precursor CaGaSi:Eu (1 %) was prepared according to the reported procedure of Czybulka et al.[43] Stoichiometric amounts of Ca (Sigma–Aldrich, 99.99 %), Ga (smart elements, 99.999 %), Si (Alfa Aesar, 99.99 %) and 1 % Eu as dopant (smart elements, 99.99 %) were placed in a tantalum ampule, which was sealed in a water-cooled arc furnace under argon atmosphere. The tantalum ampule was then placed in a silica tube, which was evacuated and inserted in a tube furnace. The ampule was heated to 1300 K at a rate of 5 K min^{-1}, kept at this temperature for 48 h and then cooled to room temperature

at a rate of 0.5 K min^{-1}. The product was thoroughly ground in an agate mortar and stored under argon.

5.4.2 Ammonothermal synthesis

Syntheses in supercritical ammonia were carried out in custom-built autoclaves made of nickel-based superalloy (Haynes® 282®), sustaining a maximum pressure of 170 MPa at 1100 K. The autoclave body (10 mL internal volume) is connected to the head part, consisting of hand valve (SITEC), pressure transmitter (HBM P2VA1/5000 bar), and safety head with integrated bursting disc (SITEC). Silver-coated metal C-rings (GFD seals) made of Inconel 718 were used as sealing gaskets. CaGaSi:Eu (5 mmol) and NaN_3 (10 mmol, Acros, 99 %) were placed in a tantalum liner, which was then transferred into the autoclave. The assembled autoclave was evacuated and cooled with ethanol/liquid nitrogen to 198 K. Subsequently, purified ammonia was directly condensed into the autoclave through a pressure regulating valve. The autoclave body was heated in a custom-built vertical tube furnace (Loba, HTM Reetz) to 770 K with a rate of 3 K min^{-1}, kept at this temperature for 20 h, heated to 1070 K with a rate of 0.05 K min^{-1}, and held for a further 150 h. The pressure was always kept between 100 and 150 MPa during the heating periods and was appropriately reduced if necessary. At 1070 K, the attained pressure of 103 MPa was slowly reduced to 70 MPa over 150 h. The autoclave was then cooled down to room temperature by switching off the furnace. The product was washed with water and 1 M HCl to remove residual mineralizer and intermediates. The obtained pale orange powder was dried at 350 K in air.

Analogous reactions were performed with LiN_3, KN_3, and CsN_3 to investigate the influence of the mineralizer.

5.4.3 Powder X-ray diffraction

For the XRD measurements, the samples were filled in glass capillaries (0.3 mm diameter, Hilgenberg GmbH). Diffraction patterns were recorded using a Stoe STADI P diffractometer ($Cu_{K\alpha1}$ radiation, Ge(111) monochromator, Mythen 1 K detector) in modified Debye–Scherrer geometry. Indexing and Rietveld refinement were carried out with the TOPAS package.[24]

Further details on the crystal structure investigations may be obtained from the Fachinformationszentrum Karlsruhe, 76344 Eggenstein- Leopoldshafen, Germany (fax: +49–7247-808-666; e-mail: crysdata@fiz-karlsruhe.de, http://www.fiz-karlsruhe.de/request_for_deposited_data.html), on quoting the depository number CSD-432259.

5.4.4 Electron microscopy

The morphology of the powder was examined with a JEOL JSM 6500 F scanning electron microscope (SEM; field emission gun, acceleration voltage 20 kV) equipped with an energy-dispersive X-ray spectroscopy (EDX) detector (Oxford Instruments, IncaEnergy) for elemental analyses. Transmission electron microscopy (TEM) was done on a FEI Titan Themis 60–300 with X-FEG, monochromator, Cs-corrector, and windowless, 4-quadrant Super-X EDX-detector. The TEM was operated at 300 kV and the images were recorded using a 4k×4k FEI Ceta CMOS camera. Microcrystals of $CaGaSiN_3:Eu^{2+}$ were ground in absolute ethanol and sonicated for 60 min. These were subsequently drop-cast on copper finder grids with holey carbon film (S166-2, Plano GmbH, Germany) and transferred into the microscope on a double-tilt holder. Samples for scanning transmission electron microscopy (STEM) were plasma cleaned for 20 s. For the evaluation of the TEM data, the following software was used: Digital Micrograph,[44] JEMS, and ProcessDiffraction7[45] for indexing and simulation of SAED patterns, and ES Vision[46] for EDX spectra.

5.4.5 Solid-state MAS-NMR spectroscopy

^{29}Si solid-state MAS-NMR experiments were carried out on a Bruker 500 Advance III FT spectrometer equipped with a commercial 4 mm triple-resonance MAS-NMR probe at a magnetic field of 11.74 T. The measurements were performed on Eu^{2+}-doped samples in ZrO_2 rotors at a ^{29}Si resonance frequency of 99.4 MHz. $Si(CH_3)_4$ (1 %) in $CDCl_3$ was used as reference.

5.4.6 Luminescence

An in-house-built spectrofluorimeter equipped with a 150 W Xe lamp, two 500 mm Czerny–Turner monochromators, 1800 l mm^{-1} lattices and 250/500 nm lamps was used for excitation measurements. The emission spectrum was recorded with an Ocean Optics USB4000 fiber spectrometer using an Avantes AvaLight LED with a wavelength of 450 nm as light source and a Thorlabs LongPass-Filter with 495 nm.

5.4.7 DFT calculations

First-principles DFT calculations were conducted using the Vienna ab initio simulation package (VASP).[47-50] The generalized gradient approximation of Perdew, Burke, and Ernzerhof (PBE-GGA) with the projector-augmented-wave function (PAW) was applied.[51,52] An (8×10×10) k-point mesh was generated with the method of Monkhorst and Pack using a plane-wave cut-off of 535 eV.[53] Optimized atom coordinates, lattice parameters and total energies were calculated through relaxation of the structure. The convergence criteria of total energy and residual atomic forces were set to 1×10^{-7} eV per unit cell and 4×10^{-3} eV $Å^{-1}$, respectively.

5.5 References

[1] T. Richter, R. Niewa, *Inorganics* **2014**, *2*, 29-78.

[2] H. Jacobs, D. Schmidt, *Curr. Top. Mater. Sci.* **1982**, *8*, 387-427.

[3] R. Juza, H. Jacobs, H. Gerke, *Ber. Bunsenges. Phys. Chem.* **1966**, *70*, 1103-1105.

[4] H. Jacobs, H. Scholze, *Z. Anorg. Allg. Chem.* **1976**, *427*, 8-16.

[5] U. Zachwieja, H. Jacobs, *J. Less Common Met.* **1990**, *161*, 175-184.

[6] B. Wang, M. J. Callahan, *Cryst. Growth Des.* **2006**, *6*, 1227-1246.

[7] D. Ehrentraut, R. T. Pakalapati, D. S. Kamber, W. Jiang, D. W. Pocius, B. C. Downey, M. McLaurin, M. P. D'Evelyn, *Jpn. J. Appl. Phys.* **2013**, *52*, 08JA01.

[8] S. Kaskel, M. Khanna, B. Zibrowius, H.-W. Schmidt, D. Ullner, *J. Cryst. Growth* **2004**, *261*, 99-104.

[9] H. Jacobs, H. Mengis, *Eur. J. Solid State Inorg. Chem.* **1993**, *30*, 45-54.

[10] H. Jacobs, R. Nymwegen, *Z. Anorg. Allg. Chem.* **1997**, *623*, 429-433.

[11] J. Li, T. Watanabe, H. Wada, T. Setoyama, M. Yoshimura, *Chem. Mater.* **2007**, *19*, 3592-3594.

[12] T. Watanabe, K. Nonaka, J. Li, K. Kishida, M. Yoshimura, *J. Ceram. Soc. Jpn.* **2012**, *120*, 500-502.

[13] H. Watanabe, N. Kijima, *J. Alloys Compd.* **2009**, *475*, 434-439.

[14] T. Suehiro, R.-J. Xie, N. Hirosaki, *Ind. Eng. Chem. Res.* **2014**, *53*, 2713-2717.

[15] H. Jacobs, J. Kockelkorn, J. Birkenbeul, *J. Less Common Met.* **1982**, *87*, 215-224.

[16] H. Jacobs, B. Nöcker, *Z. Anorg. Allg. Chem.* **1993**, *619*, 381-386.

[17] D. Peters, H. Jacobs, *J. Less Common Met.* **1989**, *146*, 241-249.

[18] R. Juza, *Angew. Chem.* **1964**, *76*, 290-300.

[19] S. M. Hick, M. I. Miller, R. B. Kaner, R. G. Blair, *Inorg. Chem.* **2012**, *51*, 12626-12629.

[20] D. Peters, E. F. Paulus, H. Jacobs, *Z. Anorg. Allg. Chem.* **1990**, *584*, 129-137.

[21] H. S. Kim, K. Machida, T. Horikawa, H. Hanzawa, *J. Alloys Compd.* **2015**, *633*, 97-103.

[22] W. H. Baur, *Crystallogr. Rev.* **1987**, *1*, 59-83.

[23] J. Li, T. Watanabe, N. Sakamoto, H. Wada, T. Setoyama, M. Yoshimura, *Chem. Mater.* **2008**, *20*, 2095-2105.

[24] A. Coelho, *TOPAS Academic*, Version 4.1, Coelho Software, Brisbane (Australia), **2007**.

[25] T. Schlieper, W. Schnick, *Z. Anorg. Allg. Chem.* **1995**, *621*, 1037-1041.

[26] H. Yamane, H. Morito, *J. Alloys Compd.* **2013**, *555*, 320-324.

[27] S. J. Clarke, F. J. DiSalvo, *Inorg. Chem.* **1997**, *36*, 1143-1148.

[28] G. Goglio, A. Denis, E. Gaudin, C. Labrugère, D. Foy, A. Largeteau, *Z. Naturforsch. B* **2008**, *63*, 730.

[29] F. Hintze, F. Hummel, P. J. Schmidt, D. Wiechert, W. Schnick, *Chem. Mater.* **2012**, *24*, 402-407.

[30] Z. A. Gál, P. M. Mallinson, H. J. Orchard, S. J. Clarke, *Inorg. Chem.* **2004**, *43*, 3998-4006.

[31] G. R. Hatfield, B. Li, W. B. Hammond, F. Reidinger, J. Yamanis, *J. Mater. Sci.* **1990**, *25*, 4032-4035.

[32] T. Sekine, M. Tansho, M. Kanzaki, *Appl. Phys. Lett.* **2001**, *78*, 3050-3051.

[33] F. Stadler, O. Oeckler, J. Senker, H. A. Höppe, P. Kroll, W. Schnick, *Angew. Chem. Int. Ed.* **2005**, *44*, 567-570.

[34] C. Hecht, F. Stadler, P. J. Schmidt, J. S. auf der Günne, V. Baumann, W. Schnick, *Chem. Mater.* **2009**, *21*, 1595-1601.

[35] M. Zeuner, S. Pagano, S. Hug, P. Pust, S. Schmiechen, C. Scheu, W. Schnick, *Eur. J. Inorg. Chem.* **2010**, *2010*, 4945-4951.

[36] S.-S. Wang, W.-T. Chen, Y. Li, J. Wang, H.-S. Sheu, R.-S. Liu, *J. Am. Chem. Soc.* **2013**, *135*, 12504-12507.

[37] H. Watanabe, H. Yamane, N. Kijima, *J. Solid State Chem.* **2008**, *181*, 1848-1852.

[38] M. Mikami, K. Uheda, N. Kijima, *Phys. Status Solidi A* **2006**, *203*, 2705-2711.

[39] Z. Wang, B. Shen, F. Dong, S. Wang, W.-S. Su, *PCCP* **2015**, *17*, 15065-15070.

[40] X. Piao, K.-i. Machida, T. Horikawa, H. Hanzawa, Y. Shimomura, N. Kijima, *Chem. Mater.* **2007**, *19*, 4592-4599.

[41] T. Wang, Q. Xiang, Z. Xia, J. Chen, Q. Liu, *Inorg. Chem.* **2016**, *55*, 2929-2933.

[42] Y. Hinuma, T. Hatakeyama, Y. Kumagai, L. A. Burton, H. Sato, Y. Muraba, S. Iimura, H. Hiramatsu, I. Tanaka, H. Hosono, F. Oba, *Nat. Commun.* **2016**, 7:11962.

[43] A. Czybulka, B. Pinger, H.-U. Schuster, *Z. Anorg. Allg. Chem.* **1989**, *579*, 151-157.

[44] Digital Micrograph, *v3.6.1, Gatan Software Team*, Pleasanton, USA, **1999**.

[45] J. L. Lábár, *Ultramicroscopy* **2005**, *103*, 237-249.

[46] ES Vision, *v4.0.164, Emispec Systems Inc*., Tempe, USA, **1994 – 2002**.

[47] G. Kresse, J. Hafner, *Phys. Rev. B* **1993**, *47*, 558-561.

[48] G. Kresse, J. Hafner, *Phys. Rev. B* **1994**, *49*, 14251-14269.

[49] G. Kresse, J. Furthmüller, *Comput. Mater. Sci.* **1996**, *6*, 15-50.

[50] G. Kresse, J. Furthmüller, *Phys. Rev. B* **1996**, *54*, 11169-11186.

[51] J. P. Perdew, K. Burke, M. Ernzerhof, *Phys. Rev. Lett.* **1996**, *77*, 3865-3868.

[52] J. P. Perdew, K. Burke, M. Ernzerhof, *Phys. Rev. Lett.* **1997**, *78*, 1396-1396.

[53] H. J. Monkhorst, J. D. Pack, *Phys. Rev. B* **1976**, *13*, 5188-5192.

6 Ammonothermal Synthesis and Crystal Structure of the Nitridoalumogermanate $Ca_{1-x}Li_xAl_{1-x}Ge_{1+x}N_3$ ($x \approx 0.2$)

published in: *Eur. J. Inorg. Chem.* **2018**, *2018*, 759-764.

authors: Jonas Häusler, Lucien Eisenburger, Oliver Oeckler, and Wolfgang Schnick

DOI: 10.1002/ejic.201701314

http://onlinelibrary.wiley.com/doi/10.1002/ejic.201701314/abstract

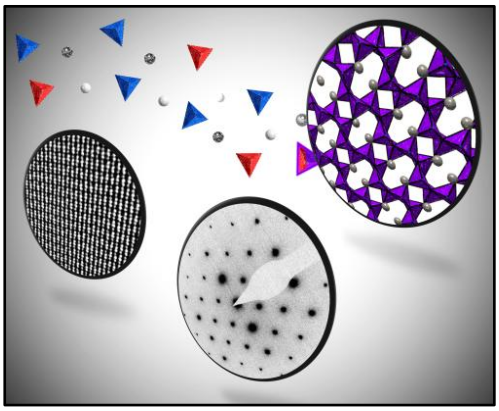

Abstract. The new nitridoalumogermanate $Ca_{1-x}Li_xAl_{1-x}Ge_{1+x}N_3$ ($x \approx 0.2$) was synthesized from supercritical ammonia at 925 K and 185 MPa starting from the intermetallic precursor $Ca_3Al_2Ge_2$ and Li as mineralizer. The crystal structure was refined by the Rietveld method; $Ca_{1-x}Li_xAl_{1-x}Ge_{1+x}N_3$ with $x \approx 0.2$ [a = 9.9822(5), b = 5.7763(2), c = 5.1484(1) Å, Z = 4, R_{wp} = 0.0492] crystallizes in orthorhombic space group $Cmc2_1$ (no. 36). Needle-shaped crystals with up to 15 µm in length were detected by scanning electron microscopy. Possible cation ordering was analyzed by transmission electron microscopy. No superstructure reflections were observed in electron diffraction patterns and the structure model was confirmed by Z-contrast imaging. The composition was verified by energy-dispersive X-ray spectroscopy on single crystals and inductively coupled plasma optical emission spectrometry. Optical properties were studied by diffuse reflectance spectroscopy, showing a broad absorption band between 250 and 300 nm. The optical band gap was estimated to be 4.3 eV at room temperature using the Tauc method.

6.1 Introduction

During the last two decades, the compound class of nitrides gained increasing importance for numerous technological applications. For instance, gallium nitride emerged as one of the most important semiconductors for optoelectronics, while various rare-earth doped nitridosilicates and -aluminates proved to be excellent luminescent materials for light-emitting diodes.[1-3] On the other hand, only a small number of nitridogermanates has been discovered so far and their physical properties were only rarely investigated. However, recent calculations predicted promising optical and electronic properties for several nitridogermanates as well.[4,5] Since these nitrides are thermally less stable than nitridosilicates, conventional high-temperature approaches are not applicable for their syntheses. The common access to nitridogermanates is based on the sodium azide route employing sodium as a flux and NaN_3 as a nitrogen source.[6] High diffusion rates at relatively low temperatures of around 1000 K as well as an increased solubility of nitrogen in liquid sodium in the presence of alkaline earth metals promote the formation of these nitrides. In this way, several new ternary and quaternary nitridogermanates have been synthesized in recent years, such as $Sr_5Ge_2N_6$, $M[Mg_3GeN_4]$ (M = Sr, Ba) and $Ca_2[Mg_5GeN_6]$.[7-10] Nitridosilicates and -gallates like $Ba_4Mg[Si_2N_6]$, $Ba_5Si_2N_6$ and $Ba[Mg_2Ga_2N_4]$ are accessible by this route as well.[11-13] While corner- or edge-sharing GeN_4 tetrahedra constitute the common structural entities in nitridogermanates, other Ge-N compounds contain structural motifs like Zintl anions Ge^{4-} (e.g. $Sr_{11}Ge_4N_6$), Ge^{2-} chains (e.g. $Sr_3Ge_2N_2$) or dumbbell-shaped $(GeN_2)^{4-}$ anions (e.g. Ca_2GeN_2).[14-16]

The ammonothermal method represents a further promising low-temperature approach for the synthesis of nitrides. While most inorganic compounds are rather hardly soluble in liquid ammonia, the solubility of ionic solids is strongly increased using high-pressurized supercritical ammonia due to the increasing relative permittivity with increasing density. In addition, the applied mineralizers, commonly alkali metal amides MNH_2 (M = Li–Cs), act as complexing agents forming species like ternary amides, imides or ammoniates by reaction with the starting materials and ammonia.[17] Such intermediates provide significantly improved solubilities in supercritical ammonia as well. These benefits are fundamental for the synthesis of nitrides from solution and for crystal growth processes by convection-driven transport reactions. While this method is prevalently used for the growth of bulk single crystals of GaN, syntheses of ternary and quaternary nitrides such as Zn-IV-N_2 (IV = Si, Ge), $K_3P_6N_{11}$ or $CaGaSiN_3$ have been reported as well.[18-21] Elements, alloys or nitrides are mixed with mineralizers and placed into special high-pressure autoclaves. A specific amount of ammonia is condensed into the vessel, which is then

closed and heated in a tube furnace. Amides or imides are preferentially formed below 700 K and also act as reactive intermediates, while most nitrides are obtained at elevated temperatures up to 1100 K.

Here we report on a new low-temperature synthesis approach for nitridogermanates using the ammonothermal method. While all currently known nitridogermanates are comprised of alkali and/or alkaline earth metals and germanium as cations, we also present the first nitridoalumogermanate, which contains corner-sharing AlN_4 and GeN_4 tetrahedra.

6.2 Results and Discussion

6.2.1 Synthesis

The intermetallic phase $Ca_3Al_2Ge_2$ was used as starting material and Li was applied as mineralizer for ammonothermal synthesis. With respect to the composition of $Ca_{1-x}Li_xAl_{1-x}Ge_{1+x}N_3$ calcium is included in excess since we have observed that calcium-containing intermediates were transported to the colder zone of the autoclave to some extent during analogous reactions. To facilitate a complete conversion of the starting materials to intermediates, Li was also used in excess. Li dissolves in liquid ammonia and forms $LiNH_2$ at elevated temperatures.[22] The synthesis of $Ca_{1-x}Li_xAl_{1-x}Ge_{1+x}N_3$ ($x \approx 0.2$) was carried out in two temperature steps, i.e. the formation of intermediates at 625 K and the conversion of the latter to the nitride at 925 K. We observed that the nitride degraded at an elevated reaction temperature of ≈ 975 K. An increased formation of hydrogen at higher temperatures could promote the decomposition due to the reducing atmosphere. $Ca_{1-x}Li_xAl_{1-x}Ge_{1+x}N_3$ is slightly moisture-sensitive and dissolves in water entirely. For this reason, 100 % ethanol and 100 % acetic acid were chosen as solvents for the purification. In order to completely remove residual intermediates, mineralizer and formed side-phases by washing, multiple ultrasonication steps were performed.

6.2.2 Crystal Structure Analysis

Powder X-ray diffraction data indicated that the untreated product contained $Ca(NH_2)_2$ and the mineralizer $LiNH_2$ as side-phases. Indexing of the diffraction patterns after purification indicated orthorhombic metrics; systematic absences suggested space group $Cmc2_1$. Atomic coordinates of isotypic $CaGaSiN_3$ were used as starting values for the Rietveld refinement.[21] No side-phases were detected in the powder X-ray diffraction pattern (see

Figure 1). Crystallographic data and atomic coordinates from Rietveld refinement are listed in Table 1 and Table 2, respectively.

Table 1. Crystallographic data of $Ca_{1-x}Li_xAl_{1-x}Ge_{1+x}N_3$ obtained by Rietveld refinement

Formula	**$Ca_{0.8}Li_{0.2}Al_{0.8}Ge_{1.2}N_3$**
Crystal system	orthorhombic
Space group	*Cmc*2_1 (no. 36)
Lattice parameters /Å	*a* = 9.9822(5)
	b = 5.7763(2)
	c = 5.1484(1)
Cell volume /Å^3	296.86(2)
Formula units / cell	4
Density /g·cm^{-3}	4.120
T / K	295(2)
Diffractometer	STOE STADI P
Radiation /Å	Mo-$K_{\alpha1}$ (λ = 0.70930 Å)
θ range /°	$2.0 \leq 2\theta \leq 50.0$
Data points	3283
Total number of reflections	153
Refined parameters	55 (thereof 14 for background)
Background function	shifted Chebyshev
Constraints	6
R values	R_p = 0.0365
	R_{wp} = 0.0492
	R_{Bragg} = 0.00835
Goodness of fit	2.056

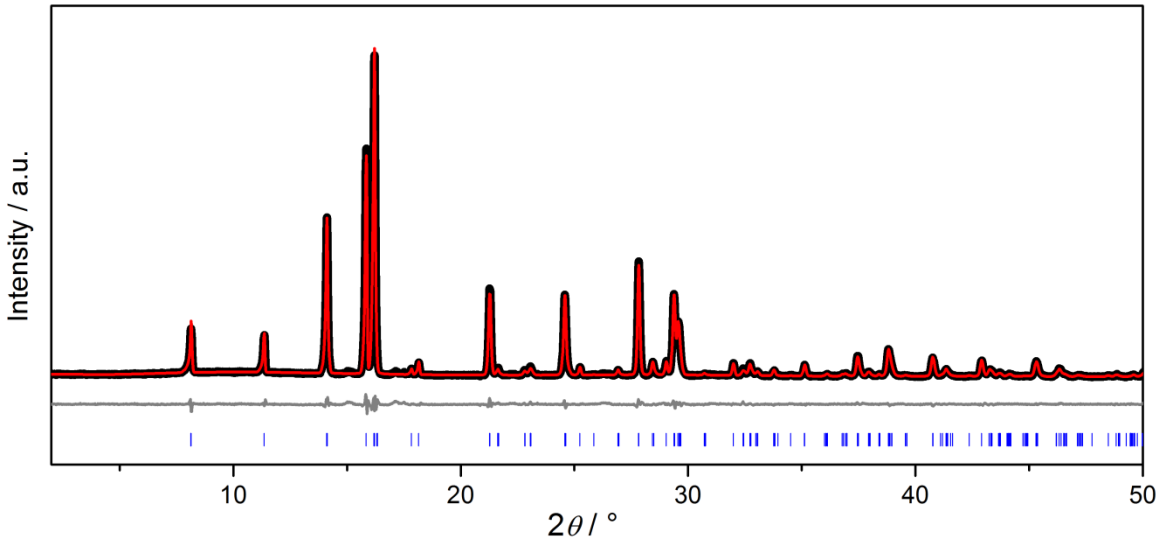

Figure 1. Rietveld refinement of $Ca_{1-x}Li_xAl_{1-x}Ge_{1+x}N_3$ (x = 0.2) with experimental data (black line, Mo-K_α1 radiation, λ = 0.70930 Å), calculated patterns (red line), difference profiles (gray line) and positions of Bragg reflections (blue bars).

Table 2. Wyckoff positions and atomic coordinates of $Ca_{1-x}Li_xAl_{1-x}Ge_{1+x}N_3$ obtained by Rietveld refinement, standard deviations in parentheses

Atom	Wyckoff site	*x*	*y*	*z*	U_{eq}	SOF
Li / Ca	4*a*	0	0.3161(7)	0.3911(10)	0.0086(2)	0.197(4) / 0.803(4)
Al / Ge	8*b*	0.1706(3)	0.1598(4)	0.9246(5)	0.0086(2)	0.401(2) / 0.599(2)
N1	8*b*	0.2083(8)	0.1406(21)	0.2832(10)	0.0086(2)	1
N2	4*a*	0	0.2738(15)	0.8723(16)	0.0086(2)	1

$Ca_{1-x}Li_xAl_{1-x}Ge_{1+x}N_3$ can be described as a solid solution of $CaAlGeN_3$ and $LiGe_2N_3$, in analogy to the previously described isostructural nitridosilicate $Ca_{1-x}Li_xAl_{1-x}Si_{1+x}N_3$, which is a solid solution of $CaAlSiN_3$ and $LiSi_2N_3$.[23] Li/Ca and Al/Ge are disordered on Wyckoff positions 4*a* and 8*b*, respectively. Further cation ordering was ruled out by selected area electron diffraction (SAED) and scanning transmission electron microscopy high-angle

annular dark-field imaging (STEM-HAADF), see section on transmission electron microscopy. Refinement of the site occupancy factors resulted in an occupancy of about 20 % Li / 80 % Ca and 40 % Al / 60 % Ge, corresponding to $x \approx 0.2$. This composition is in accordance with elemental analyses (see section below). Li/Ca are coordinated by five nitrogen atoms (2x N1, 3x N2) with bond lengths between 2.37 and 2.68 Å, while Al/Ge are tetrahedrally coordinated (3x N1, 1x N2) with distances between 1.82 and 1.92 Å. These bond lengths are in a similar range as in comparable nitridogermanates, e.g. Ca_4GeN_4, $Ca_7[GeN_4]N_2$ and $Ca_2Mg_5GeN_6$.[10,16,24] On the other hand, N1 is connected to three and N2 to two Al/Ge atoms, respectively. $(Al/Ge)N_4$ tetrahedra share corners to form a three-dimensionally extended network of *sechser* rings (Figure 2). The embedded counterions Li^+ and Ca^{2+} compensate the negative charge of the anionic framework.

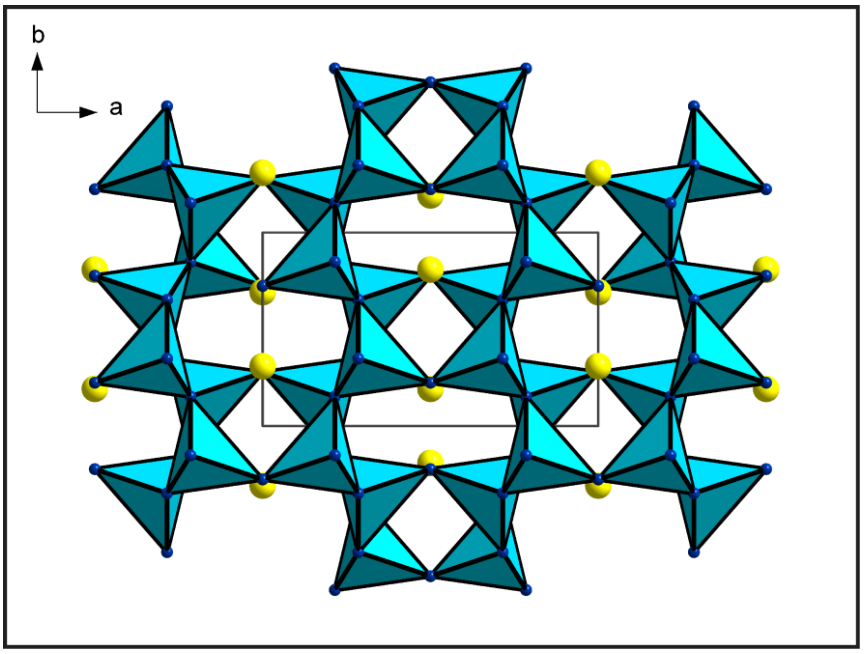

Figure 2. Crystal structure of $Ca_{1-x}Li_xAl_{1-x}Ge_{1+x}N_3$ viewed along [001] with $(Al/Ge)N_4$ tetrahedra depicted in light blue, Ca^{2+}/Li^+ in yellow and nitrogen in blue.

Temperature-programmed X-ray diffraction patterns up to 1270 K show that $Ca_{1-x}Li_xAl_{1-x}Ge_{1+x}N_3$ retains orthorhombic metrics up to ≈ 1000 K and degrades at higher temperatures as indicated by its vanishing reflections and emerging ones of decomposition products (see Figure S1 in the Supporting Information).

6.2.3 Elemental Analyses

The elemental composition of single crystals was determined by energy-dispersive X-ray spectroscopy (EDX). Additionally, inductively coupled plasma optical emission spectrometry (ICP-OES) was carried out to evaluate the Li content in the purified product. An atomic ratio of Ca/Al/Ge/N = 1.00(9):1.01(8):1.62(7):1.62(17) was determined by EDX which is consistent with the chemical formula $Ca_{0.8}Li_{0.2}Al_{0.8}Ge_{1.2}N_3$ derived from Rietveld refinement. Low nitrogen values within TEM-EDX may arise from defective surfaces of measured single crystals. No oxygen impurities were detected in these measurements. ICP data (Ca: 18.2 wt.-%, Li: 0.6 wt.-%, Al: 12.5 wt.-%, Ge: 48.2 wt.-%; atomic ratio Ca/Li/Al/Ge = 0.805:0.153:0.820:1.180) are in good agreement with calculated values for $x = 0.2$ in $Ca_{1-x}Li_xAl_{1-x}Ge_{1+x}N_3$ (Ca: 17.4 wt.-%, Li: 0.75 wt.-%, Al: 11.7 wt.-%, Ge: 47.3 wt.-%, N: 22.8 wt.-%). Nitrogen was not determined by ICP since the sample had to be dissolved in nitric acid for analysis.

6.2.4 Scanning Electron Microscopy (SEM)

SEM images of the purified product show needle-shaped crystals, similar to the morphology of ammonothermally synthesized $M AlSiN_3:Eu^{2+}$ (M = Ca, Sr) and $CaGaSiN_3:Eu^{2+}$.[21,25,26] However, considerably larger crystals with up to 15 µm in length grew (Figure 3 and Figure S2 in the Supporting Information), while crystallites of the reported nitridosilicates are rather in the nm range. This might be attributed to a higher solubility of Ge or respective intermediates in supercritical ammonia compared to silicon, or the use of $LiNH_2$ as mineralizer.

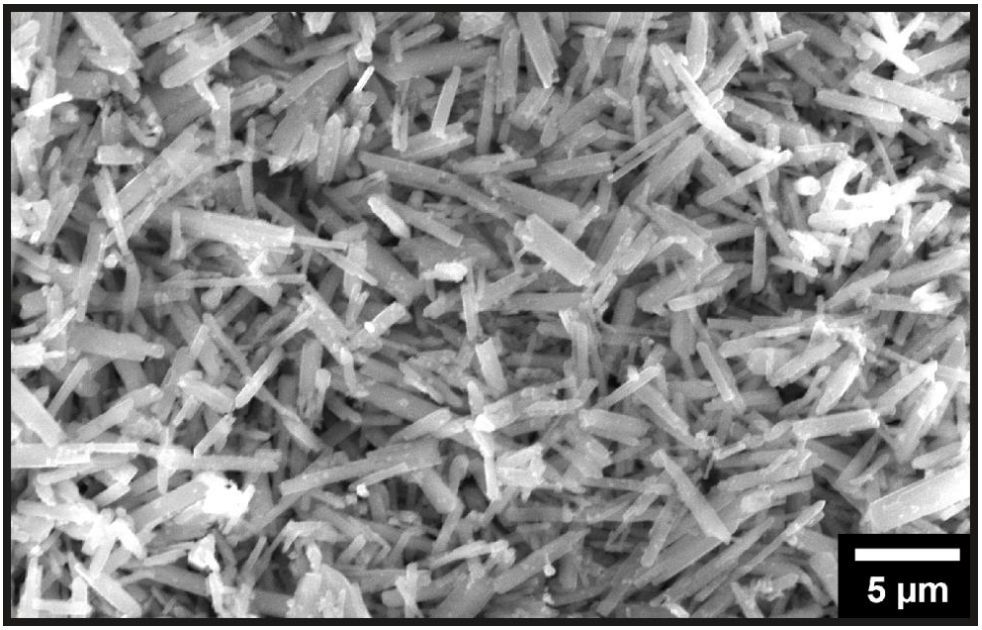

Figure 3. SEM secondary electron (SE) image of $Ca_{1-x}Li_xAl_{1-x}Ge_{1+x}N_3$.

6.2.5 Transmission Electron Microscopy (TEM)

Possible ordering of Al and Ge was analyzed by SAED and high resolution STEM-HAADF. SAED patterns did not show any superstructure reflections and comparison with simulated SAED patterns confirms the structure model of $Ca_{1-x}Li_xAl_{1-x}Ge_{1+x}N_3$. (Figure S3 in the Supporting Information). STEM-HAADF along [110] is suitable to differentiate between Ca, Al and Ge columns by *Z*-contrast imaging. Intensity deviations of different atom columns in line-scans are expected to show ordering of Al and Ge atoms, if present (Figure 4). The intensities were compared to three different structure models of $Ca_{1-x}Li_xAl_{1-x}Ge_{1+x}N_3$ in *translationengleiche* subgroups (*Cm*11, C1*c*1 and *C*11$2_1$) of *Cmc*2_1 (Figure 5). In all models, Al and Ge columns would be clearly separated in projections along [110], resulting in three different intensities along the line scan (Al weak, Ca intermediate and Ge strong). The absence of such intensity distributions confirms the absence of cation ordering in the structure model of $Ca_{1-x}Li_xAl_{1-x}Ge_{1+x}N_3$.

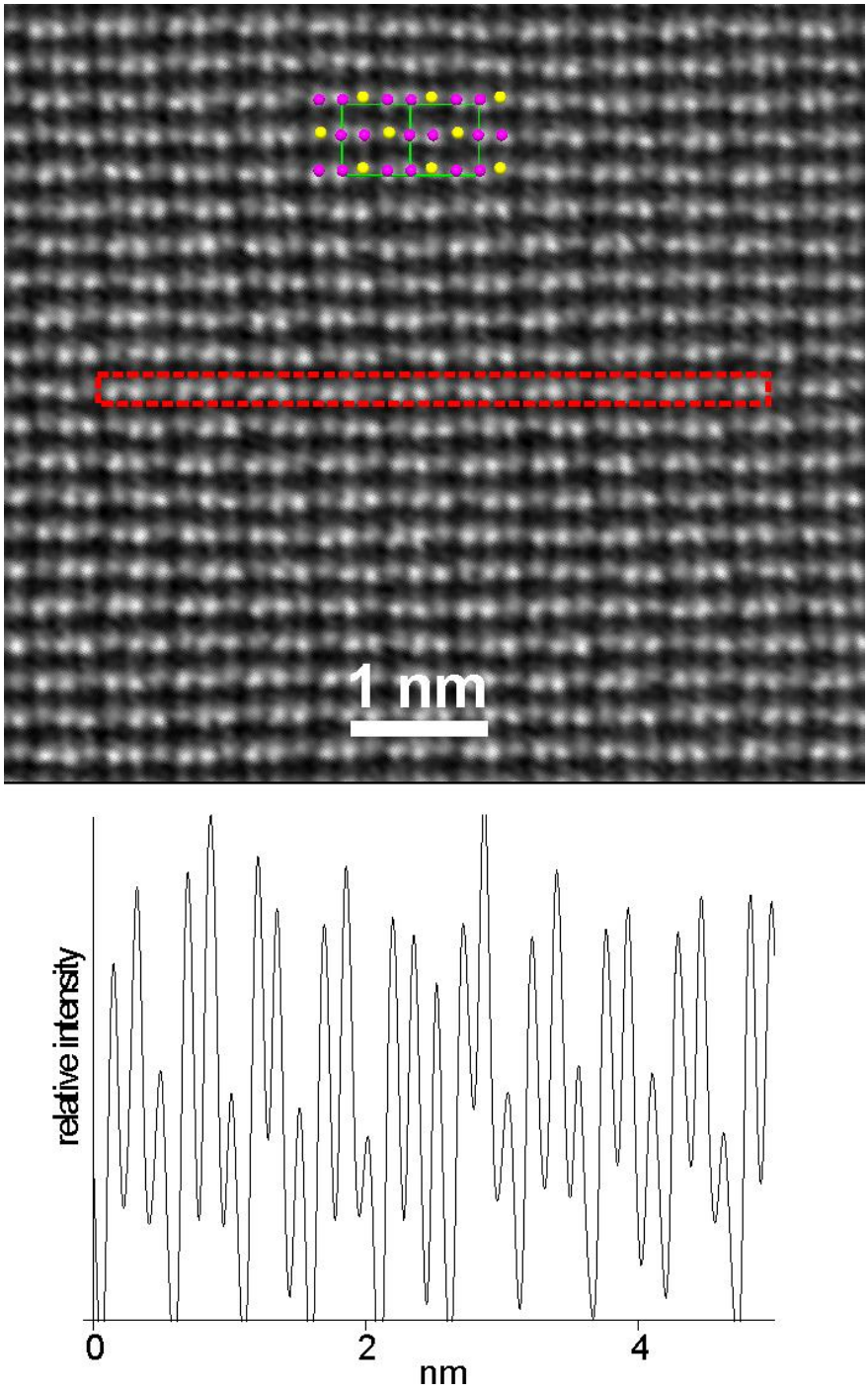

Figure 4. Fourier filtered STEM-HAADF image along zone axis [110]: brighter contrast corresponds to Al/Ge (purple) atom columns and darker contrast to Ca/Li (yellow) columns; area of linescan (red box) and corresponding intensities (bottom).

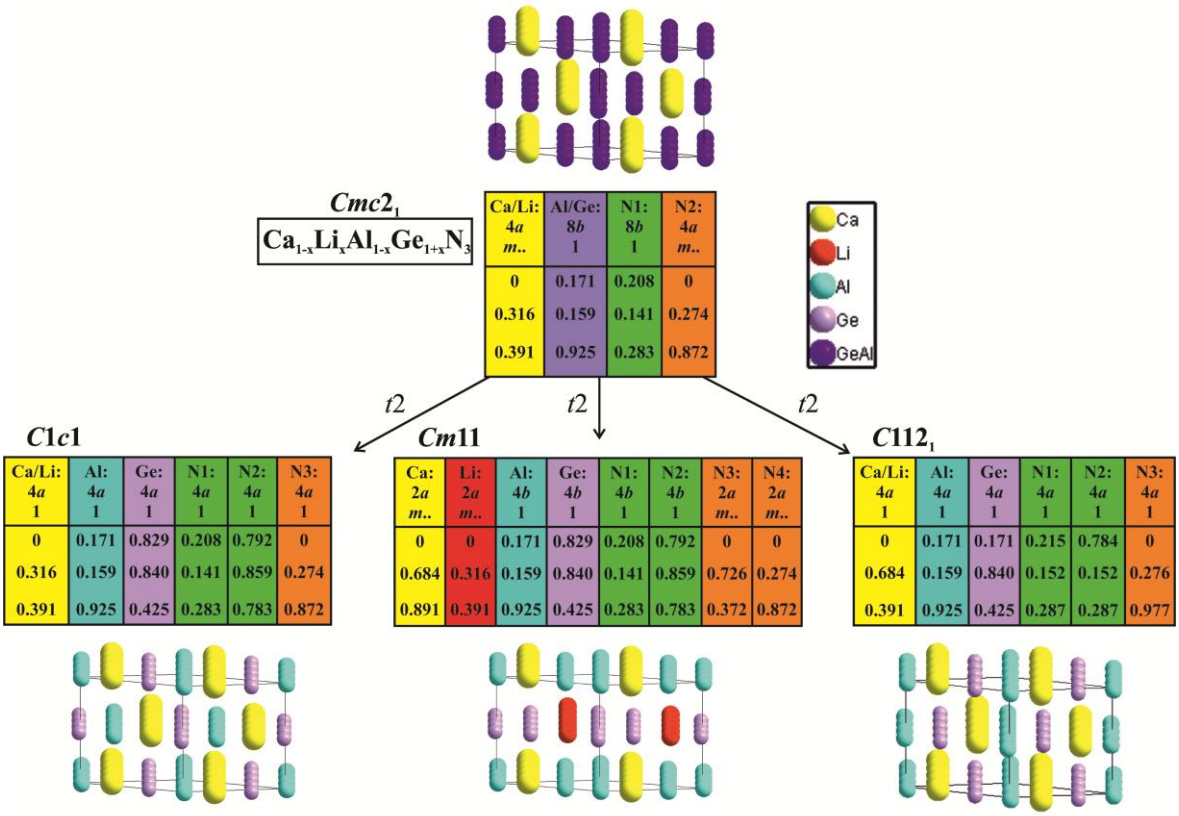

Figure 5. $Ca_{1-x}Li_xAl_{1-x}Ge_{1+x}N_3$ in space group $Cmc2_1$ (top) and hypothetical ordered models in *Cc* (bottom left), *Cm* (bottom middle) and $C2_1$ (bottom right). Structure projections in different space groups in direction ≈ [110]. Atom sites: Ca (yellow), Li (red), Al/Ge (purple), Al (turquoise) and Ge (lilac).

6.2.6 UV/Vis Spectroscopy

The diffuse reflectance spectrum of $Ca_{1-x}Li_xAl_{1-x}Ge_{1+x}N_3$ shows an absorption band in the UV region between 250 and 300 nm (Figure 6). The Kubelka–Munk function $F(R) = (1 - R)^2/2R$ (R = reflectance) was applied to convert the diffuse reflectance to a pseudo-absorption spectrum.[27] The band gap was then determined using the Tauc equation $(h\nu\alpha)^{1/n} = A(h\nu - E_g)$, where α denotes the absorption coefficient, A a proportional constant, E_g the band gap and n the nature of the sample transition (direct or indirect band gap).[28] An extensive linear region in the Tauc plot for $n = 1/2$ is observed, thus suggesting a direct band gap. The point of intersection of the aligned tangent and the horizontal axis yields an estimated optical band gap of 4.3 eV (see Figure 6).

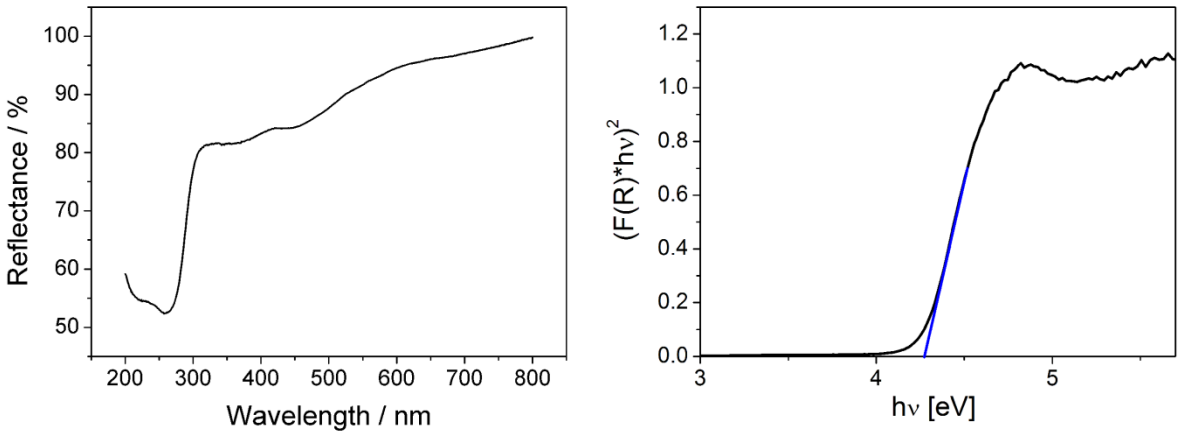

Figure 6. Diffuse reflectance spectrum (left) and Tauc plot $[F(R)\cdot h\nu]^2$ (right) of $Ca_{1-x}Li_xAl_{1-x}Ge_{1+x}N_3$ ($x \approx 0.2$).

6.3 Conclusions

Ammonothermal synthesis afforded the new nitridoalumogermanate $Ca_{1-x}Li_xAl_{1-x}Ge_{1+x}N_3$ with $x \approx 0.2$, which can be described as a solid solution of $LiGe_2N_3$ and hypothetical $CaAlGeN_3$. The crystal structure can be regarded as a distorted superstructure of the wurtzite type with orthorhombic space group $Cmc2_1$. Ordering of the Ca/Li or Al/Ge atoms was ruled out by SAED and STEM-HAADF. SAED patterns are in accordance with simulated ones and show no superstructure reflections. STEM-HAADF images confirmed the structural model and indicated no ordering either.

Syntheses of nitridogermanates are challenging due to their limited thermal stability in comparison to nitridosilicates. While virtually all known nitridogermanates have been synthesized employing the sodium azide route, the ammonothermal method proved to be a promising new approach as well. Inclusion of AlN_4 tetrahedra extends the diversity of possible structural units in nitridogermanates. Needle-shaped crystals with a diameter up to 15 µm were obtained at comparatively low temperature of 925 K. The well-defined morphology of the crystals indicates growth from solution, which is fundamental for future research on the ammonothermal crystal growth of quaternary and multinary nitrides.

While few compositions for $M^{II}M^{III}M^{IV}N_3$-type structures have been reported,[21,29,30] solid solutions with $M^{I}M^{IV}{}_2N_3$ nitrides additionally increase their variability. The formation of solid solutions as well as controlling their specific compositions will be addressed in future studies. Likewise, the feasibility of further wurtzite-derived nitridogermanates with

interesting optical and electronic properties has recently been predicted as well.[5] In this way, manifold perspectives for band-gap engineering of nitrides are opened up, which pave the way for the design of new semiconductor materials.

6.4 Experimental Section

All operations were carried out in flame-dried Schlenk-type glassware connected to a vacuum line (≤ 0.1 Pa) with argon and ammonia supply or in Ar-filled glove boxes (Unilab, MBraun, Garching, O_2 < 1 ppm, H_2O < 1 ppm) to exclude oxygen and moisture during syntheses. Gas purification cartridges (Micro Torr FT400-902 and MC400-702FV, SAES Pure Gas Inc., San Luis Obispo, CA, USA) were used for further purification of Ar (Air Liquide, 99.999 %) and NH_3 (Air Liquide, 99.999 %) providing a purity level of < 1 ppb H_2O, O_2 and CO_2.

6.4.1 Preparation of $Ca_3Al_2Ge_2$

Stoichiometric amounts of Ca (Sigma–Aldrich, 99.99 %), Al (Acros, 99.97 %) and Ge (smart-elements, 99.99 %) were placed in a tantalum ampule, which was sealed by arc melting under argon atmosphere. The ampule was placed in a fused silica tube, which was evacuated and inserted in a tube furnace. The ampule was then heated to 1325 K at a rate of 5 K/min, kept at this temperature for 50 h and cooled to room temperature with a rate of 0.5 K/min. The product was ground in an agate mortar and stored under argon.

6.4.2 Ammonothermal Synthesis

Custom-built autoclaves (10 mL internal volume) made of nickel-based superalloy (Haynes® 282®) were used for ammonothermal syntheses.[21] $Ca_3Al_2Ge_2$ (1 mmol) and Li (20 mmol, Alfa, 99 %) were placed in a niobium liner, which was then transferred into the autoclave. A sealing gasket (silver-coated Inconel 718 metal-C-rings, GFD seals) was inserted and the autoclave was assembled by tightening the screws of the flange connection. The head part, consisting of hand valve (SITEC), pressure transmitter (HBM P2VA1/5000 bar) and safety head with integrated bursting disc (SITEC), was connected to the autoclave lid via high-pressure pipes. The autoclave was evacuated and cooled with ethanol/liquid nitrogen to 198 K. Subsequently, ammonia was condensed into the autoclave via a pressure regulating valve. The autoclave body was heated in a custom-

built vertical tube furnace (type Loba, HTM Reetz) to 625 K with a rate of 3 K/min, kept at this temperature for 15 h, heated to 925 K with a rate of 1 K/min and held for further 75 h. The autoclave lid was heated to 625 K with a rate of 3 K/min using a separate heating zone and kept at this temperature during the remaining synthesis procedure. A maximum pressure of 135 MPa at 625 K and 185 MPa at 925 K was reached. During the heating period from 625 K to 925 K, the pressure was kept between 120 and 185 MPa and appropriately reduced when necessary. At the end of the synthesis, the autoclave was cooled to room temperature by switching off the furnace. The obtained product was suspended and purified in 100 % ethanol by ultrasonication for 30 min. The suspension was centrifuged for 10 min at 4000 rpm and the supernatant solution was disposed. This procedure was repeated with 100 % ethanol and three more times using 100 % acetic acid. After the last purification step, the microcrystalline beige-colored product was dried under vacuum and then stored under argon.

6.4.3 Powder X-ray Diffraction

The products were filled in glass capillaries (0.3 mm diameter, Hilgenberg GmbH). A Stoe STADI P diffractometer [Mo-$K_{\alpha1}$ radiation, Ge(111) monochromator, Mythen 1K detector, modified Debye–Scherrer geometry] was used for the PXRD measurements. Indexing and Rietveld refinement were carried out with the TOPAS package.[31] The peak shape function was described using fundamental parameters with direct convolution of source emission profiles, axial instrument contributions, crystallite size and microstrain effects.[32] Preferred orientation of the crystallites was described using spherical harmonics of fourth order.[33] Displacement parameters of N1 and N2 featured untypical standard deviations and were thus refined to one common value for all atoms. Site occupancy factors were refined in accordance with the composition of the solid solution $Ca_{1-x}Li_xAl_{1-x}Ge_{1+x}N_3$.

Temperature-programmed powder X-ray diffraction patterns were recorded using a Stoe STADI P diffractometer [Mo-$K_{\alpha1}$, λ = 0.70930 Å, Ge(111) monochromator, image-plate position-sensitive detector] equipped with a high-temperature graphite furnace. Measurements were conducted in steps of 50 K up to 1270 K with a heating rate of 5 K/min.

Further details on the crystal structure investigations may be obtained from the Fachinformationszentrum Karlsruhe, 76344 Eggenstein-Leopoldshafen, Germany (fax: +49-7247-808-666; E-mail: crysdata@fiz-karlsruhe.de), on quoting the depository number CSD-433751.

6.4.4 Scanning Electron Microscopy (SEM)

A FEI Helios G3 UC scanning electron microscope (field emission gun, acceleration voltage 30 kV) equipped with an energy-dispersive X-ray (EDX) detector for elemental analyses was used to investigate the morphology and chemical composition of the products. The samples were placed on an adhesive carbon pad and coated with a conductive carbon film using a high-vacuum sputter coater (BAL-TEC MED 020, Bal Tec AG).

6.4.5 Transmission Electron Microscopy

For sample preparation, crystals of $Ca_{1-x}Li_xAl_{1-x}Ge_{1+x}N_3$ ($x \approx 0.2$) were ground in absolute ethanol and drop-cast on copper grids covered with holey carbon film (S166-2, Plano GmbH, Germany). The grids were mounted on a double-tilt holder and transferred into a C_s DCOR probe corrected Titan Themis 300 (FEI, USA) TEM equipped with X-FEG, post-column filter (Enfinium ER-799), US1000XP/FT camera system (Gatan, Germany) and a windowless, 4-quadrant Super-X EDX detector. TEM images were recorded using a 4k × 4k FEI Ceta CMOS camera. The microscope was operated at 300 kV accelerating voltage for SAED and STEM-HAADF (convergence angle of 16.6 mrad, 50 µm aperture, detector inner half angle 63 mrad for 100 mm camera length). For evaluation of the TEM data, the following software was used: Digital Micrograph (Fourier filtering of STEM images), ProcessDiffraction7 (geometric calculations for SAED), JEMS (SAED simulations), and ES Vision (EDX spectra).[34-38] Given EDX data are averaged values of three single crystals.

6.4.6 ICP-OES

For quantitative elemental analysis, inductively coupled plasma optical emission spectrometry (ICP-OES) was conducted using a Varian Vista RL ICP-OES spectrometer. The sample was dissolved in HNO_3/HCl and hydrofluoric acid.

6.4.7 UV/Vis Spectroscopy

Diffuse reflectance measurements between 200 and 800 nm were carried out at room temperature using a Jasco V-650 UV/Vis spectrophotometer (Czerny-Turner mount, photomultiplier tube detector) equipped with deuterium (190 - 350 nm) and halogen (330 -

900 nm) lamps as light sources. The deuterium-halogen lamp switch at 330 nm was corrected for a reliable determination of the band gap.

6.5 References

[1] S. P. DenBaars, D. Feezell, K. Kelchner, S. Pimputkar, C.-C. Pan, C.-C. Yen, S. Tanaka, Y. Zhao, N. Pfaff, R. Farrell, M. Iza, S. Keller, U. Mishra, J. S. Speck, S. Nakamura, *Acta Mater.* **2013**, *61*, 945-951.

[2] R. Mueller-Mach, G. Mueller, M. R. Krames, H. A. Höppe, F. Stadler, W. Schnick, T. Jüstel, P. Schmidt, *Phys. Status Solidi A* **2005**, *202*, 1727-1732.

[3] P. Pust, V. Weiler, C. Hecht, A. Tucks, A. S. Wochnik, A. K. Henss, D. Wiechert, C. Scheu, P. J. Schmidt, W. Schnick, *Nat. Mater.* **2014**, *13*, 891-896.

[4] O. Boudrifa, A. Bouhemadou, N. Guechi, S. Bin-Omran, Y. Al-Douri, R. Khenata, *J. Alloys Compd.* **2015**, *618*, 84-94.

[5] Z.-H. Cai, P. Narang, H. A. Atwater, S. Chen, C.-G. Duan, Z.-Q. Zhu, J.-H. Chu, *Chem. Mater.* **2015**, *27*, 7757-7764.

[6] H. Yamane, F. J. DiSalvo, *Prog. Solid State Chem.* **2017**, https://doi.org/10.1016/j.progsolidstchem.2017.08.002.

[7] S. C. Junggeburth, O. Oeckler, W. Schnick, *Z. Anorg. Allg. Chem.* **2008**, *634*, 1309-1311.

[8] D. G. Park, Y. Dong, F. J. DiSalvo, *Solid State Sci.* **2008**, *10*, 1846-1852.

[9] C. Pösl, R. Niklaus, W. Schnick, *Eur. J. Inorg. Chem.* **2017**, *2017*, 2422-2427.

[10] C. Pösl, W. Schnick, *Z. Anorg. Allg. Chem.* **2016**, *642*, 882-886.

[11] H. Yamane, H. Morito, *J. Alloys Compd.* **2013**, *555*, 320-324.

[12] H. Yamane, F. J. DiSalvo, *J. Alloys Compd.* **1996**, *240*, 33-36.

[13] P. Pust, F. Hintze, C. Hecht, V. Weiler, A. Locher, D. Zitnanska, S. Harm, D. Wiechert, P. J. Schmidt, W. Schnick, *Chem. Mater.* **2014**, *26*, 6113-6119.

[14] Z. A. Gal, S. J. Clarke, *Chem. Commun.* **2005**, 728-730.

[15] S. J. Clarke, G. R. Kowach, F. J. DiSalvo, *Inorg. Chem.* **1996**, *35*, 7009-7012.

[16] S. J. Clarke, F. J. DiSalvo, *Inorg. Chem.* **2000**, *39*, 2631-2634.

[17] T. Richter, R. Niewa, *Inorganics* **2014**, *2*, 29-78.

[18] B. Wang, M. J. Callahan, *Cryst. Growth Des.* **2006**, *6*, 1227-1246.

[19] J. Häusler, S. Schimmel, P. Wellmann, W. Schnick, *Chem. Eur. J.* **2017**, *23*, 12275 - 12282.

[20] H. Jacobs, R. Nymwegen, *Z. Anorg. Allg. Chem.* **1997**, *623*, 429-433.

[21] J. Häusler, L. Neudert, M. Mallmann, R. Niklaus, A.-C. L. Kimmel, N. S. A. Alt, E. Schlücker, O. Oeckler, W. Schnick, *Chem. Eur. J.* **2017**, *23*, 2583-2590.

[22] H. Jacobs, R. Juza, *Z. Anorg. Allg. Chem.* **1972**, *391*, 271-279.

[23] L. Wang, R.-J. Xie, Y. Li, X. Wang, C.-G. Ma, D. Luo, T. Takeda, Y.-T. Tsai, R.-S. Liu, N. Hirosaki, *Light Sci Appl.* **2016**, *5*, e16155.

[24] S. C. Junggeburth, O. Oeckler, D. Johrendt, W. Schnick, *Inorg. Chem.* **2008**, *47*, 12018-12023.

[25] J. Li, T. Watanabe, N. Sakamoto, H. Wada, T. Setoyama, M. Yoshimura, *Chem. Mater.* **2008**, *20*, 2095-2105.

[26] T. Watanabe, K. Nonaka, J. Li, K. Kishida, M. Yoshimura, *J. Ceram. Soc. Jpn.* **2012**, *120*, 500-502.

[27] R. López, R. Gómez, *J. Sol-Gel Sci. Technol.* **2012**, *61*, 1-7.

[28] J. Tauc, R. Grigorovici, A. Vancu, *Phys. Status Solidi B* **1966**, *15*, 627-637.

[29] X. Piao, K.-i. Machida, T. Horikawa, H. Hanzawa, Y. Shimomura, N. Kijima, *Chem. Mater.* **2007**, *19*, 4592-4599.

[30] H. Watanabe, H. Yamane, N. Kijima, *J. Solid State Chem.* **2008**, *181*, 1848-1852.

[31] A. Coelho, *TOPAS Academic*, *Version 4.1*, Coelho Software, Brisbane (Australia), **2007**.

[32] R. W. Cheary, A. A. Coelho, J. P. Cline, *J. Res. Natl. Inst. Stand. Technol.* **2004**, *109*, 1-25.

[33] M. Jarvinen, *J. Appl. Crystallogr.* **1993**, *26*, 525-531.

[34] Gatan, Inc., Digital Micrograph, Pleasanton, California, USA, **1999**.

[35] J. L. Lábár, *Ultramicroscopy* **2005**, *103*, 237-249.

[36] P. A. Stadelmann, JEMS, CIME-EPFL, Saas-Fee, Switzerland, **2008**.

[37] Emispec Systems Inc., ES Vision, Tempe, Arizona, USA, **2002**.

[38] EDAX AMETEK, TEAM, Wiesbaden, Germany **2013**.

7 New perspectives for the ammonothermal synthesis and growth of ternary nitrides

Within the previous chapters, fundamental advances covering the ammonothermal synthesis of ternary and multinary nitrides were presented which strongly emphasize the high potential of this method. Significant findings that emerged within these systematic studies and have not yet been addressed will be briefly discussed in the following sections.

7.1 Ammonoacidic synthesis of $ZnGeN_2$

Up to now, reported ammonothermal syntheses of ternary nitrides were solely performed in ammonobasic environment. In chapter 3, synthesis of $ZnSiN_2$ and $ZnGeN_2$ was presented employing $LiNH_2$, $NaNH_2$ or KNH_2 as ammonobasic mineralizers. In this section, first ammonoacidic synthesis of the ternary nitride $ZnGeN_2$ will be demonstrated.

7.1.1 Experimental

Ammonoacidic syntheses of $ZnGeN_2$ and powder X-ray diffraction analyses were performed analogous to experiments described in section 3.4. To prevent severe corrosion of the autoclave walls, custom-built liners made of hot-pressed sintered Si_3N_4 (FCT Ingenieurkeramik GmbH) were used.[1] Zn (4.5 mmol, Alfa Aesar, 99.9%), Ge_3N_4 (1 mmol, Sigma-Aldrich, 99.99%) and NH_4F (22.5 mmol, Merck, 98%) were mixed and placed into the liner which was closed with a Si_3N_4 lid and then transferred into an Inconel 718 autoclave. The autoclave was closed, evacuated and cooled with ethanol / liquid nitrogen to 198 K. Ammonia was condensed into the autoclave via a pressure regulating valve. The autoclave body was heated to 870 K with a rate of 3.2 K / min and kept at this temperature for 195 h. A maximum pressure of 195 MPa was reached. The product was washed with 1 M HCl to remove residual mineralizer and intermediates and then dried at 350 K in air. $ZnGeN_2$ was obtained as beige polycrystalline powder.

7.1.2 Results and Discussion

$ZnGeN_2$ was successfully synthesized under ammonoacidic reaction conditions using ammonium fluoride as mineralizer. While ternary amides typically occur within ammonobasic syntheses of nitrides, recent studies on the aimed crystallization of Zn_3N_2 showed that fluoride ammoniates like $ZnF_2(NH_3)_2$ and $ZnF_2(NH_3)_3$ are formed during ammonoacidic reactions with NH_4F.[2] On the other hand, potential Ge containing intermediates have not been identified as yet. According to powder X-ray diffraction (Figure 1), the crystallinity is slightly lower compared to presented ammonobasic syntheses as indicated by broadened reflections, though this was likewise observed in analogous ammonobasic syntheses of $ZnGeN_2$ using Si_3N_4 liners. The thick wall could have an isolating effect lowering the reaction temperature and further affects convection within the autoclave. Recently, several other potential materials were screened with regard to their suitability as liners for ammonoacidic reactions. Next to Si_3N_4, molybdenum was suggested for NH_4F und NH_4Cl solutions, while silver was only suitable for syntheses with NH_4F.[1,3-4] The effect of different liner materials as well as employment of further ammonium halides as acidic mineralizers will be highly interesting for future studies.

The presented experiments demonstrate the first ammonoacidic synthesis of a ternary nitride and thus open up a wide range of new opportunities within ammonothermal research. With regard to the highly efficient crystal growth of GaN employing NH_4F as mineralizer, new perspectives for the development of growth processes for ternary nitrides, the formation of solid solutions as well as for possible p- and n-doping of GaN are established.[5-6]

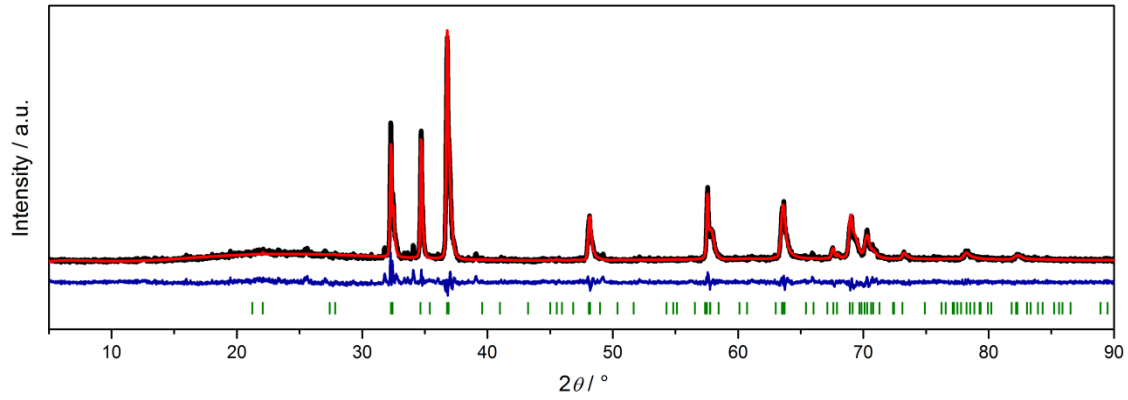

Figure 1. Rietveld refinement of $ZnGeN_2$ with experimental data (black line, Cu-Kα1 radiation, λ = 1.540596 Å), calculated pattern (red line), difference profile (blue line) and positions of Bragg reflections (green bars).

7.2 Ammonothermal growth of the ternary nitridotantalate $KTaN_2$

Presented results in previous chapters showed that crystallites in the µm range with well-defined morphology can be grown through ammonothermal reactions. However, growth of larger nitride crystals is hampered by low solubilities of Si or Ge containing species as well as the decomposition of ammonia at elevated temperatures. To promote crystal growth of addressed ternary and multinary nitrides, significantly higher pressures will be required for these reactions which in turn increase respective solubilities of ionic solids and inhibit ammonia decomposition at high reaction temperatures.[7-8] A proof of concept for crystal growth of the ternary nitridotantalate $KTaN_2$ will be demonstrated in the following.

7.2.1 Experimental

Growth of $KTaN_2$ single crystals was serendipitously observed during exploratory ammonothermal syntheses of $ZnSiN_2$. Synthesis, powder X-ray diffraction and scanning electron microscopy analyses were performed analogous to experiments described in section 3.4. Zn (7.5 mmol, Alfa Aesar, 99.9%), Si (7.5 mmol, Alfa Aesar, 99.99%) and KN_3 (15 mmol, Sigma-Aldrich, 99.9%) were mixed and placed into a tantalum liner (WHS Sondermetalle) which was transferred into a Haynes 282 autoclave. The autoclave was closed under argon, evacuated and cooled with ethanol / liquid nitrogen to 198 K. Ammonia was condensed into the autoclave via a pressure regulating valve. The autoclave body was heated to 670 K with a rate of 3 K / min, kept at this temperature for 20 h, heated to 1070 K with a rate of 0.05 K / min and held for further 140 h. The pressure was kept between 25 and 155 MPa during the heating periods. The product was washed with water to remove residual mineralizer and intermediates and then dried at 350 K in air. Green crystals were observed at the outer wall of the liner.

7.2.2 Results and Discussion

Powder X-ray analyses indicated that the targeted product $ZnSiN_2$ was slightly contaminated with $KTaN_2$ which emerged from the employed tantalum liner (Figure 2). At the outer wall of the liner, octahedron-shaped large crystals of $KTaN_2$ with diameters up to 100 µm and excellent crystal morphology were discovered (Figure 3, table 1). In contrast, only microcrystalline $KTaN_2$ was obtained in previous ammonothermal studies.[9] The well-defined crystals suggest growth proceeding from solution which is promoted by convection-driven chemical transport of the mineralizer KNH_2. The increasing temperature and the accompanying ammonia decomposition results in continuous supersaturation

during the heating periods. It can be assumed that the low applied heating rates of 3 K / h supported growth of isolated single crystals as supersaturation of the solution is kept very low. The tantalum liner apparently serves as substrate that further promotes the growth of well-defined single crystals. These results show that crystal growth of ternary nitrides from ammonothermal synthesis can be accomplished, while aspects like solubilities, supersaturation of supercritical ammonia solutions and chemical transport have to be taken into account.

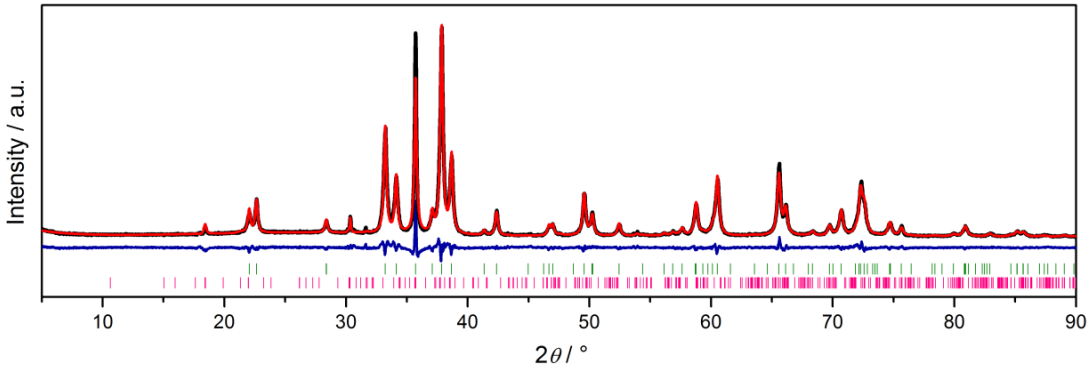

Figure 2. Rietveld refinement of obtained product with experimental data (black line, Cu-Kα1 radiation, λ = 1.540596 Å), calculated pattern (red line) and difference profile (blue line). Positions of Bragg reflections are represented with green bars for $ZnSiN_2$ and pink bars for $KTaN_2$.

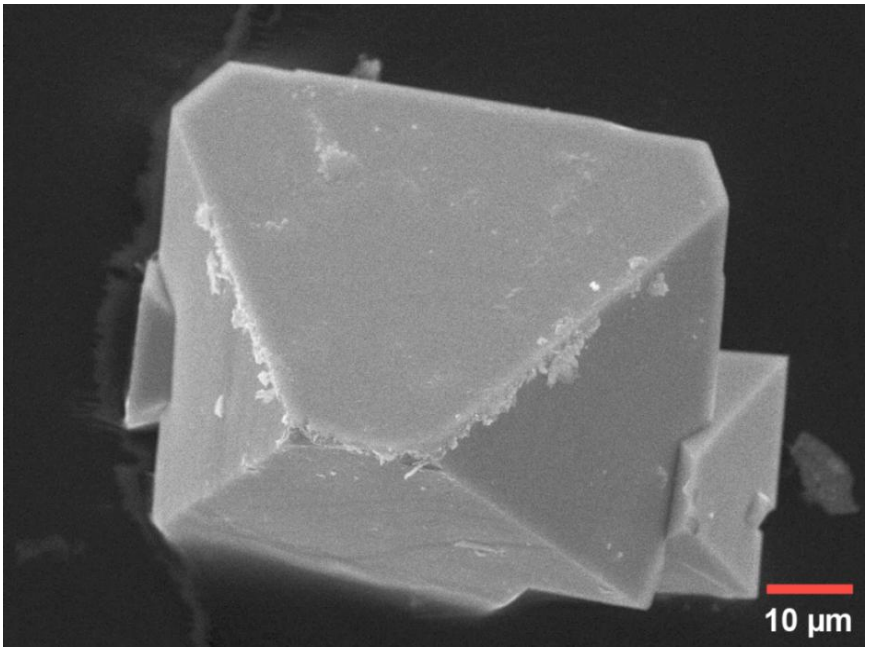

Figure 3. Scanning electron microscopy (SEM) image of $KTaN_2$.

Table 1. SEM EDX measurement of $KTaN_2$ single crystal in atom %. Little oxygen impurities presumably arise from the washing treatment

K	Ta	N	O
17.3	17.1	57.4	8.2

7.3 Ammonothermal synthesis of the rare earth nitridosilicate Eu_2SiN_3

Previous studies on the ammonothermal synthesis of nitridosilicates and -germanates are limited to main group elements, while rare earth metals have only been addressed with regard to amides, binary nitrides and dopants for luminescent materials.[7,10-11] Within this section, ammonothermal synthesis of the ternary rare earth nitridosilicate Eu_2SiN_3 will be presented.

7.3.1 Experimental

Eu_2SiN_3 was obtained within explorative ammonothermal syntheses of rare earth metal nitrides. Syntheses and powder X-ray diffraction were performed analogous to experiments described in section 5.4. The intermetallic precursor EuGaSi was synthesized from Eu (8.0 mmol, smart-elements, 99.99%), Ga (8.0 mmol, smart-elements, 99.999%) and Si (8.0 mmol, Alfa Aesar, 99.99%). The elements were placed into a tantalum ampule, heated to 1300 K at a rate of 5 K / min, kept at this temperature for 48 h and cooled down to room temperature with a rate of 0.5 K / min. EuGaSi (2.5 mmol) and NaN_3 (7.5 mmol, Acros, 99%) were transferred into a tantalum liner (WHS Sondermetalle) which was placed in a Haynes 282 autoclave. The autoclave was closed under argon, evacuated and cooled with ethanol / liquid nitrogen to 198 K. Ammonia was condensed into the autoclave via a pressure regulating valve. The autoclave body was heated to 770 K with a rate of 1 K / min, kept at this temperature for 20 h, heated to 1070 K with a rate of 1 K / min and held for further 5 h. The pressure was kept between 110 and 160 MPa during the heating periods. A black product with colorless plate-like crystals was obtained.

7.3.2 Results and Discussion

Reaction of intermetallic EuGaSi with NaN_3 under ammonothermal conditions yields the mixed valence europium nitridosilicate Eu_2SiN_3 next to GaN, $NaNH_2$ and minor unidentified side-phases (Figure 4). Eu_2SiN_3 is commonly obtained from europium metal and silicon diimide $Si(NH)_2$ at 1170 K in lithium flux.[12] Previous reactions in the Eu / $NaNH_2$ system at lower temperatures yielded divalent Eu^{2+} species like $Na_2Eu_3(NH_2)_8$, whereas employment of KNH_2 enables the formation of both Eu^{2+} and Eu^{3+} containing amides as well as crystal growth of EuN.[13-14] At 1070 K, no intermediate species were observed, while the mixed valence nitride Eu_2SiN_3 is preferably formed instead of possible wurtzite-type nitrides like $NaSi_2N_3$ or as yet unknown $EuGaSiN_3$. Eu_2SiN_3 crystallizes in orthorhombic space group *Cmca* (no. 64) containing one-dimensional infinite nonbranched *zweier* chains of corner-sharing SiN_4 tetrahedra, where europium is coordinated in a distorted pentagonal bipyramidal manner by nitrogen (Figure 5).[12] Plate-like crystals of Eu_2SiN_3 with up to 10 µm in length were observed by scanning electron microscopy (Figure 6, table 2). Apparently, growth rates are significantly higher compared to other nitridosilicates obtained from ammonothermal synthesis, in particular with regard to the short applied reaction time.[11,15-16] These findings open up numerous new opportunities for the discovery of novel rare earth nitrides and are thus highly promising for future ammonothermal studies within these systems.

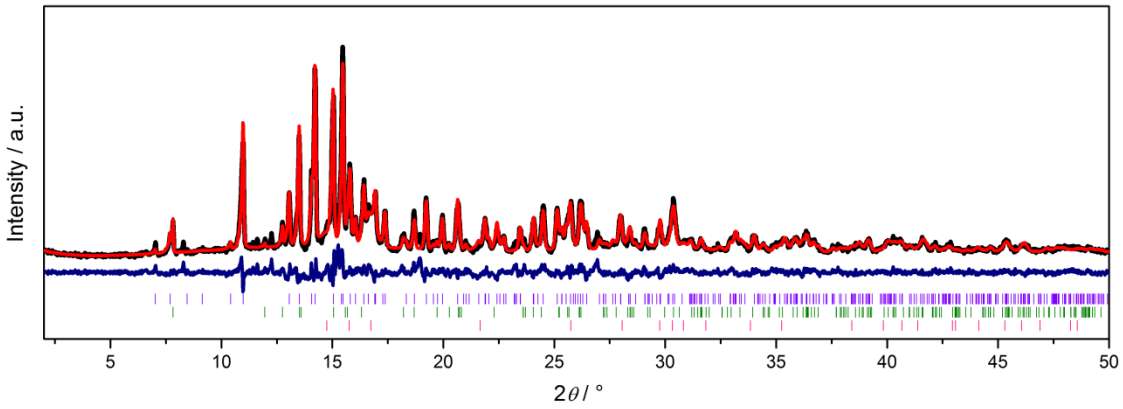

Figure 4. Rietveld refinement of obtained product with experimental data (black line, Mo-Kα1 radiation, λ = 0.70930 Å), calculated pattern (red line) and difference profile (blue line). Positions of Bragg reflections are represented with violet bars for Eu_2SiN_3 (51.8 wt%), green bars for $NaNH_2$ (26.6 wt%) and pink bars for GaN (21.6 wt%).

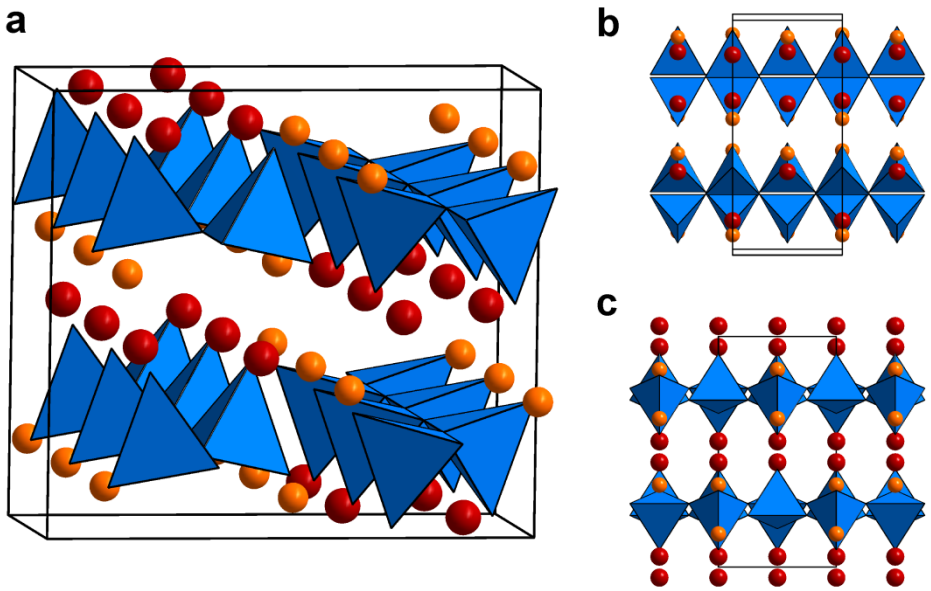

Figure 5. Crystal structure of Eu_2SiN_3 viewed along 100 (a), 010 (b) and 001 (c) with corner-sharing SiN_4 tetrahedra depicted in blue, Eu^{2+} in red and Eu^{3+} in orange.

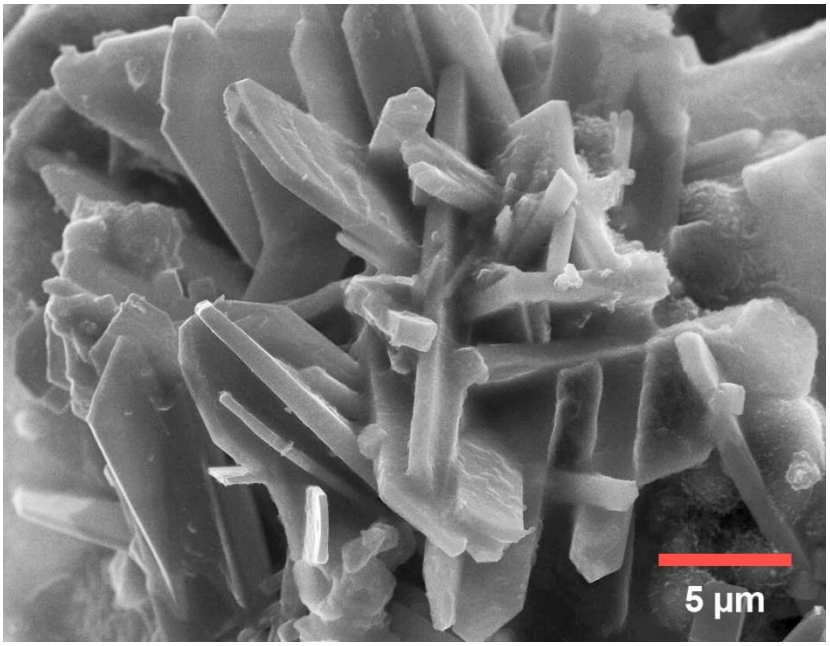

Figure 6. Scanning electron microscopy (SEM) image of Eu_2SiN_3.

Table 2. SEM EDX measurement of Eu_2SiN_3 crystals coated with decomposition products of $NaNH_2$ and intermediates in air, in atom %

Eu	Si	N	Na	O	Ga
12.7	8.5	40.7	10.6	26.9	0.6

7.4 Conclusion

In this chapter, new fundamental aspects for the ammonothermal synthesis and crystal growth of ternary nitrides were presented. The ammonoacidic approach greatly expands the synthetic potential of ammonothermal syntheses and establishes a virtually unexplored field within ammonothermal research. Moreover, the feasibility for crystal growth of ternary nitrides with excellent crystal morphology was demonstrated including $KTaN_2$ single crystals with up to 100 µm in diameter. Development of new autoclave systems could enable significantly higher pressures which in turn would strongly promote the growth of ternary nitrides. The extension of syntheses to rare earth elements further entailed promising perspectives for the discovery of new nitride materials as well. Therefore, an excellent fundament for future explorative ammonothermal studies and the development of growth processes for ternary nitrides was created.

7.5 References

[1] B. Hertweck, S. Schimmel, T. G. Steigerwald, N. S. A. Alt, P. J. Wellmann, E. Schluecker, *J. Supercrit. Fluids* **2015**, *99*, 76-87.

[2] T. M. M. Richter, S. LeTonquesse, N. S. A. Alt, E. Schlücker, R. Niewa, *Inorg. Chem.* **2016**, *55*, 2488-2498.

[3] B. Hertweck, S. Zhang, T. G. Steigerwald, N. S. A. Alt, R. Niewa, E. Schluecker, *Chem. Eng. Technol.* **2014**, *37*, 1835-1844.

[4] S. Pimputkar, T. F. Malkowski, S. Griffiths, A. Espenlaub, S. Suihkonen, J. S. Speck, S. Nakamura, *J. Supercrit. Fluids* **2016**, *110*, 193-229.

[5] D. Ehrentraut, R. T. Pakalapati, D. S. Kamber, W. Jiang, D. W. Pocius, B. C. Downey, M. McLaurin, M. P. D'Evelyn, *Jpn. J. Appl. Phys.* **2013**, *52*, 08JA01.

[6] T. Suehiro, M. Tansho, T. Shimizu, *J. Phys. Chem. C* **2017**, *121*, 27590-27596.

[7] T. Richter, R. Niewa, *Inorganics* **2014**, *2*, 29-78.

[8] S. Pimputkar, S. Nakamura, *J. Supercrit. Fluids* **2016**, *107*, 17-30.

[9] H. Jacobs, E. von Pinkowski, *J. Less Common Met.* **1989**, *146*, 147-160.

[10] H. Jacobs, D. Schmidt, *Curr. Top. Mater. Sci.* **1982**, *8*, 387-427.

[11] J. Häusler, L. Neudert, M. Mallmann, R. Niklaus, A.-C. L. Kimmel, N. S. A. Alt, E. Schlücker, O. Oeckler, W. Schnick, *Chem. Eur. J.* **2017**, *23*, 2583-2590.

[12] M. Zeuner, S. Pagano, P. Matthes, D. Bichler, D. Johrendt, T. Harmening, R. Pöttgen, W. Schnick, *J. Am. Chem. Soc.* **2009**, *131*, 11242-11248.

[13] H. Jacobs, U. Fink, *J. Less Common Met.* **1979**, *63*, 273-286.

[14] H. Jacobs, U. Fink, *Z. Anorg. Allg. Chem.* **1978**, *438*, 151-159.

[15] J. Li, T. Watanabe, N. Sakamoto, H. Wada, T. Setoyama, M. Yoshimura, *Chem. Mater.* **2008**, *20*, 2095-2105.

[16] T. Watanabe, K. Nonaka, J. Li, K. Kishida, M. Yoshimura, *J. Ceram. Soc. Jpn.* **2012**, *120*, 500-502.

8 Conclusion and Outlook

Prevailing synthesis methods for nitrides involve high-temperature or high-pressure techniques based on solid-state or metathesis reactions frequently with the aid of flux and nitriding agents. These procedures are suitable for synthesis of microcrystalline nitride powders, whereas growth of larger crystals is mostly hampered owing to the insufficient diffusion and fusibility of nitrides within these reactions. Moreover, nitrides with low thermal stability are difficult to access using these approaches which thereby impedes their discovery. In contrast, the ammonothermal method comprises solution-based reactions at rather moderate temperatures and is thus particularly promising for nitrides with limited thermal stability as well as crystal growth from solution employing well-soluble intermediates as transporting agents. Here, supercritical ammonia is used as reaction medium which provides enhanced solubilities of starting materials, high diffusivity of dissolved intermediates, low viscosity as well as near zero surface tension.[1-3] While hydrothermal syntheses are renowned for their great potential regarding crystal growth of inorganic materials and their scalable processes, the ammonothermal method is still on an early stage of development.

At present, ammonothermal research is primarily focused on the growth of gallium nitride and the enhancement of crystal qualities. Prior to this thesis, only very few examples of other nitrides from ammonothermal syntheses were available in literature. This thesis aimed to establish the ammonothermal method as powerful explorative tool for the synthesis of ternary and multinary nitrides. Experiments within autoclaves commonly used for GaN crystal growth revealed that these reactors barely provide the required parameters for the ammonothermal synthesis of other nitrides and rather lead to products with low crystallinity. Based on these preliminary studies, new high-pressure autoclaves made of superalloy Haynes 282 were developed that feature high tensile strength, yield strength and ductility at elevated process temperatures. In this way, maximum temperature and pressure limits could be significantly extended which proved to be the key to access highly crystalline ternary nitride semiconductors as well as novel multinary nitrides employing an ammonothermal approach.

Within this work, systematic syntheses of Grimm-Sommerfeld analogous ternary nitride semiconductors $MgSiN_2$, $MgGeN_2$, $MnSiN_2$, $MnGeN_2$, $ZnSiN_2$, $ZnGeN_2$, $LiSi_2N_3$ and $LiGe_2N_3$ (generally classified as II-IV-N_2 and I-IV_2-N_3 nitrides) from ammonobasic supercritical ammonia solutions were presented. The ammonothermal method proved to

be an excellent synthetic approach for this class of materials and enabled the preparation of pure products without observable side-phases within PXRD analyses. Experimental optical investigations included in chapters 3 and 4 demonstrate that a wide range of band gaps can be covered with these compounds. Noteworthy, the massively growing demand in GaN based semiconductors necessitates the search for earth-abundant materials as well-suited alternatives. The determined variability of optical and electronic properties coupled with a remarkable band gap tunability and high thermal stability makes these II-IV-N_2 and I-IV_2-N_3 nitrides very promising to replace currently used semiconductors based on scarce elements like gallium or indium. Superior properties compared to group 13 nitrides have already been ascertained, e.g. similar spontaneous polarization parameters of Zn(Si,Ge,Sn)N_2 which could suppress polarization fields in heterostructures.[4] Moreover, these materials feature promising optical properties for solar energy-conversion systems like photovoltaics or photocatalytical water splitting and further possess low carrier effective masses which is highly interesting for potential uses within power electronics.[5-7] II-IV-N_2 and I-IV_2-N_3 nitrides thus represent an intriguing class of semiconductors which could enable the development of new innovative devices. Still, most available data on these materials are based on theoretical calculations, while optical and electronic properties are virtually unexplored from an experimental point of view. Based on presented results in this work, detailed experimental investigation of further semiconductor characteristics can be performed on single crystals, e.g. charge carrier mobilities, concentrations and lifetimes as well as impurity and defect concentrations. In this regard, examination of suitable dopants for II-IV-N_2 and I-IV_2-N_3 nitrides within these bulk materials will be of great interest for future studies as well. Notably, the wide variability of these wurtzite-type superstructures provides numerous opportunities to implement p- and n-type conductivity, for instance by doping with monovalent or trivalent cations within II-IV-N_2 materials, respectively.[8]

Furthermore, novel multinary nitrides were discovered employing highly reactive intermetallic precursors and ammonobasic mineralizers as starting materials. On the one hand, the first nitridogallosilicate $CaGaSiN_3$ was prepared containing corner-sharing GaN_4 and SiN_4 tetrahedra within its three-dimensional framework. While nitridosilicates commonly require synthesis temperatures above 1300 K, stabilities of nitridogallates are quite limited concerning thermal decomposition.[9-11] Same holds for the gallium-containing nitridosilicate $CaGaSiN_3$ which decomposes below 1000 K at ambient pressure as established by high-temperature powder X-ray diffraction. Conventional high-temperature approaches are thus not applicable for the synthesis of such nitrides, while comparably moderate temperatures are sufficient for ammonothermal syntheses owing to the high

reactivity of supercritical ammonia and occurring intermediates. Besides, high pressures could additionally stabilize such potentially metastable compounds during these reactions. Apart from this, Eu^{2+} doped samples of $CaGaSiN_3$ show promising luminescence characteristics shifting the emission maximum from 650 to 620 nm compared to the industrially important red phosphor $CaAlSiN_3:Eu^{2+}$ (CASN). As the blue-shift reduces losses in the infrared region of emission within phosphor-converted LEDs, inclusion of Ga is a promising alternative for luminescence tuning of CASN-type materials.

On the other hand, the first nitridoalumogermanate $Ca_{1-x}Li_xAl_{1-x}Ge_{1+x}N_3$ was synthesized whose anionic framework is built up of corner-sharing AlN_4 and GeN_4 tetrahedra. While access to nitridogermanates is virtually limited to the sodium azide route,[11] the ammonothermal method proved to be a new highly promising approach for the discovery of novel nitridogermanates. Well-defined single crystals with diameters of up to 15 µm were obtained within short reaction periods which indicates remarkable growth rates from supercritical ammonia solution. While the exceptional thermodynamic stability of AlN and GaN often hampers syntheses of nitridoaluminates and -gallates and limits feasible synthetic approaches, it was shown that multinary Al- and Ga-containing nitrides can be accessed despite prevailing reaction conditions for the formation of the respective binaries.[12] These findings thus offer great potential for the discovery of further multinary nitridoaluminates and -gallates from ammonothermal syntheses.

Within this thesis, the number of ammonothermally accessible ternary and multinary nitrides was more than doubled revealing the high potential of explorative ammonothermal syntheses at elevated reaction temperatures and pressures. As nitrides crystallizing in wurtzite-derived superstructures seem to be preferably formed under ammonothermal reaction conditions, several other promising wurtzite-type nitride or oxonitride semiconductors could be readily accessible, such as $ZnTiN_2$, Zn_3WN_4 or ZnAlON.[7] According to considerations of Parthé, further compositions for fully condensed tetrahedral structures might be well feasible taking respective valence electron concentrations (VEC) into account, e.g. $M^{II}M^{III}{}_2M^{IV}N_4$, $M^{II}{}_2M^{III}M^{V}N_4$ or $M^{I}M^{III}M^{IV}{}_2N_4$.[13-14] For instance, the thermodynamic stability of quaternary nitride semiconductors $LiAlGe_2N_4$ and $LiGaGe_2N_4$ was recently predicted, while synthetic access to these materials was not accomplished so far.[15] As demonstrated for the rare earth nitridosilicate Eu_2SiN_3, inclusion of heavier countercations within these anionic frameworks or employment of other mineralizer systems is highly promising and further extends the structural variety of accessible nitrides. Moreover, Jacobs and coworkers already demonstrated the possible ammonothermal access to nitridophosphates, while reported crystal growth of

imidonitrides $Rb_8[P_4N_6(NH)_4](NH_2)_2$ and $Cs_5[P(NH)_4](NH_2)_2$ indicates the occurrence of well-soluble phosphorus containing intermediate species.[16-18] Taking advantage of the extended temperature regime, ammonothermal syntheses could thereby facilitate the discovery of novel nitridophosphates and further enable growth of macroscopic single crystals via convection-driven transport reactions.

Using newly developed high-temperature autoclaves, typical attainable crystal sizes of ternary and multinary nitrides were significantly increased compared to previous ammonothermal studies.[19-21] Exemplarily, single crystals of the nitridotantalate $KTaN_2$ with up to 100 µm in diameter and excellent crystal morphology were grown via controlled supersaturation of the present solution. Yet, growth rates are mostly limited by solubilities of starting materials and occurring intermediates. The ammonia equilibrium is significantly shifted to its decomposition products N_2 and H_2 at synthesis temperatures above 900 K which further hampers dissolution and diffusion of intermediate species. To this end, considerably higher pressures beyond 500 MPa will be required to inhibit ammonia decomposition and to enhance solubilities through an increased relative permittivity.[12,22-23] Dissolvabilities would be additionally improved by an increased density of supercritical ammonia thus promoting solution-based crystal growth of addressed nitrides. Presented in situ X-ray imaging experiments already provided a proof of principle for possible dissolution and recrystallization based growth of ternary nitrides. As conventional autoclave systems sustaining even higher pressures at temperatures of 1100 K are hardly feasible owing to materials limitations, alternative concepts including internally heated capsule based systems or techniques related to other high-pressure technologies have to be considered.[24-26]

Future experiments should cover the identification of dissolved intermediates as well as investigation of their formation and degradation conditions. With regard to strongly diverging solubilities of included elements and intermediate species, estimation of the latter is indispensable to enable controlled crystal growth. In situ Raman and UV-VIS spectroscopy can give information on the type of dissolved species, while in situ ultrasonic velocity measurements were recently developed to determine concentrations of dissolved mineralizer or intermediates.[27-28] The advancement of in situ technologies will thus be essential to gain a deeper understanding of occurring crystallization processes and to develop sophisticated growth techniques for nitrides. In this regard, the use of well soluble and highly reactive precursors as well as the extension to new mineralizer systems could significantly promote attainable growth rates. Notably, first demonstrated synthesis of a ternary nitride from ammonoacidic environment opens up vast new opportunities in

ammonothermal research. In particular with regard to the outstanding growth rates of GaN employing ammonium halides as mineralizers, the ammonoacidic regime is very promising to strongly enhance solubilities of the starting materials and occurring intermediates.[2,24,29] With respect to presented results in this work and the wide range of still unexplored fields within ammonothermal research, this re-established synthesis technique provides innumerable opportunities for the discovery of new functional nitride materials.

Final Remarks

The here reported findings represent fundamental advances in preparative solid-state chemistry and put forth new highly promising perspectives for the exploratory discovery of novel nitrides. The development and enhancement of new high-pressure autoclaves along with systematic explorations of mineralizers, precursors and synthesis parameters strongly extended the synthetic potential of the ammonothermal method. Within this thesis, ammonothermal syntheses emerged as powerful approach for the preparation of functional ternary and multinary nitrides, thus perfectly complement its high-temperature and high-pressure counterparts, and further revealed great potential for solution-based crystal growth of ternary and multinary nitride materials.

References

[1] L. Cornell, Y. C. Lin, W. H. Philipp, *NASA Technical Memorandum* **1990**, 102570.

[2] T. Richter, R. Niewa, *Inorganics* **2014**, *2*, 29-78.

[3] T. G. Steigerwald, N. S. A. Alt, B. Hertweck, E. Schluecker, *J. Cryst. Growth* **2014**, *403*, 59-65.

[4] T. R. Paudel, W. R. L. Lambrecht, *Phys. Rev. B* **2009**, *79*, 245205.

[5] P. Narang, S. Chen, N. C. Coronel, S. Gul, J. Yano, L.-W. Wang, N. S. Lewis, H. A. Atwater, *Adv. Mater.* **2014**, *26*, 1235-1241.

[6] T. Suehiro, M. Tansho, T. Shimizu, *J. Phys. Chem. C* **2017**, *121*, 27590-27596.

[7] Y. Hinuma, T. Hatakeyama, Y. Kumagai, L. A. Burton, H. Sato, Y. Muraba, S. Iimura, H. Hiramatsu, I. Tanaka, H. Hosono, F. Oba, *Nat. Commun.* **2016**, 7:11962.

[8] A. D. Martinez, A. N. Fioretti, E. S. Toberer, A. C. Tamboli, *J. Mater. Chem. A* **2017**, *5*, 11418-11435.

[9] C. Poesl, L. Neudert, W. Schnick, *Eur. J. Inorg. Chem.* **2017**, *2017*, 1067-1074.

[10] C. Poesl, W. Schnick, *Eur. J. Inorg. Chem.* **2017**, *2017*, 1498-1503.

[11] H. Yamane, F. J. DiSalvo, *Prog. Solid State Chem.* **2017**, DOI: 10.1016/j.progsolidstchem.2017.08.002.

[12] B. Wang, M. J. Callahan, *Cryst. Growth Des.* **2006**, *6*, 1227-1246.

[13] E. Parthé, *Z. Kristallogr. Cryst. Mater.* **1964**, *119*, 204.

[14] E. Parthé, *J. Phase Equilib.* **1991**, *12*, 404-408.

[15] Z.-H. Cai, P. Narang, H. A. Atwater, S. Chen, C.-G. Duan, Z.-Q. Zhu, J.-H. Chu, *Chem. Mater.* **2015**, *27*, 7757-7764.

[16] H. Jacobs, R. Nymwegen, *Z. Anorg. Allg. Chem.* **1997**, *623*, 429-433.

[17] F. Golinski, H. Jacobs, *Z. Anorg. Allg. Chem.* **1995**, *621*, 29-33.

[18] H. Jacobs, F. Golinski, *Z. Anorg. Allg. Chem.* **1994**, *620*, 531-534.

[19] S. Kaskel, M. Khanna, B. Zibrowius, H.-W. Schmidt, D. Ullner, *J. Cryst. Growth* **2004**, *261*, 99-104.

[20] J. Li, T. Watanabe, H. Wada, T. Setoyama, M. Yoshimura, *Chem. Mater.* **2007**, *19*, 3592-3594.

[21] J. Cho, B. K. Bang, S. J. Jeong, C. H. Kim, *RSC Adv.* **2014**, *4*, 23218-23222.

[22] M. P. D'Evelyn, H. C. Hong, D. S. Park, H. Lu, E. Kaminsky, R. R. Melkote, P. Perlin, M. Lesczynski, S. Porowski, R. J. Molnar, *J. Cryst. Growth* **2007**, *300*, 11-16.

[23] S. Pimputkar, S. Nakamura, *J. Supercrit. Fluids* **2016**, *107*, 17-30.

[24] D. Ehrentraut, R. T. Pakalapati, D. S. Kamber, W. Jiang, D. W. Pocius, B. C. Downey, M. McLaurin, M. P. D'Evelyn, *Jpn. J. Appl. Phys.* **2013**, *52*, 08JA01.

[25] A. Rabenau, *Angew. Chem.* **1985**, *97*, 1017-1032; A. Rabenau, *Angew. Chem. Int. Ed.* **1985**, *24*, 1026-1040.

[26] K. Byrappa, M. Yoshimura, *Handbook of Hydrothermal Technology*, William Andrew Publishing, New York, USA, **2001**.

[27] T. G. Steigerwald, J. Balouschek, B. Hertweck, A.-C. L. Kimmel, N. S. A. Alt, E. Schlücker, *J. Supercrit. Fluids* **2017**, DOI: 10.1016/j.supflu.2017.12.028.

[28] H. Baser, W. Schwieger, D. Freitag, T. G. Steigerwald, E. Schluecker, *Chem. Eng. Technol.* **2017**, *40*, 1101-1106.

[29] T. F. Malkowski, S. Pimputkar, J. S. Speck, S. P. DenBaars, S. Nakamura, *J. Cryst. Growth* **2016**, *456*, 21-26.

9 Summary

1. Ammonothermal Synthesis of Nitrides: Recent Developments and Future Perspectives

Jonas Häusler, and Wolfgang Schnick

Chem. Eur. J. **2018**, DOI: 10.1002/chem.201800115

This minireview illuminates the latest research findings covering the ammonothermal synthesis of nitrides and discusses future perspectives for the exploratory discovery of new functional materials. Within the last decade, growth rates and crystal quality of ammonothermal GaN were significantly improved enabling the development of optoelectronic devices with strongly increased semiconductor performances. Several years after the pioneering work of Jacobs and coworkers, the ammonothermal method was likewise rediscovered as versatile synthetic tool for the preparation and crystal growth of ternary and multinary nitride materials. New autoclave technologies enabled access to earth-abundant nitride semiconductors as well as novel nitrides with intriguing optical and electronic properties. The article further outlines synthesis strategies employing different precursors and mineralizers and describes future challenges for the crystal growth of nitride materials. Recently developed in situ technologies, which give fundamental insights into crystallization processes and allow solubility measurements of dissolved species, are briefly reviewed as well.

2. Ammonothermal Synthesis of Earth-abundant Nitride Semiconductors $ZnSiN_2$ and $ZnGeN_2$ and Dissolution Monitoring by In Situ X-ray Imaging

Jonas Häusler, Saskia Schimmel, Peter Wellmann, and Wolfgang Schnick

Chem. Eur. J. **2017**, *23*, 12275-12282.

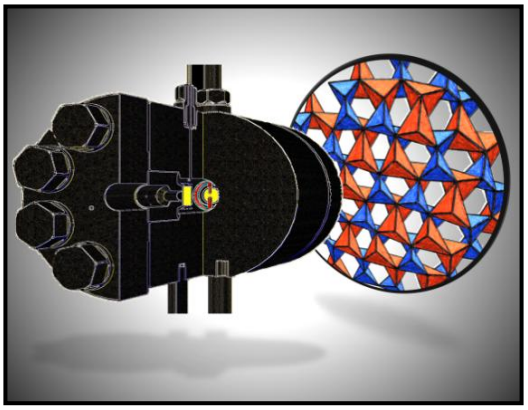

The first syntheses of $ZnSiN_2$ and $ZnGeN_2$ from solution are presented employing supercritical ammonia as solvent and nitriding agent. Different ammonobasic mineralizers MNH_2 (*M* = Li, Na or K) were used to increase solubilities of the starting materials promoting the formation of reactive intermediate species. In this way, phase-pure and highly crystalline products were obtained which are ideally suited for analyses of materials properties. Band gaps of $ZnSiN_2$ (3.7 eV) and $ZnGeN_2$ (3.2 eV) were determined by diffuse reflectance spectroscopy using the Kubelka-Munk function and corresponding Tauc plots. These Grimm-Sommerfeld analogous nitrides are of particular interest as next-generation semiconductor materials with regard to their promising optical and electronic properties as well as the earth-abundance of constituting elements. Further, in situ X-ray imaging experiments were carried out using specially designed high-pressure autoclaves equipped with sapphire windows to investigate the underlying mechanism of crystal growth. Dissolvability of $ZnGeN_2$ in basic supercritical ammonia was ascertained which emphasizes the feasibility of dissolution and recrystallization based crystal growth processes analogous to group 13 nitrides.

3. Ammonothermal Synthesis and Optical Properties of Ternary Nitride Semiconductors Mg-IV-N_2, Mn-IV-N_2 and Li-IV_2-N_3 (IV = Si, Ge)

Jonas Häusler, Robin Niklaus, Ján Minár, and Wolfgang Schnick

Chem. Eur. J. **2018**, *24*, 1686-1693.

A new ammonothermal approach was developed for the synthesis of ternary nitride semiconductors $MgSiN_2$, $MgGeN_2$, $MnSiN_2$, $MnGeN_2$, $LiSi_2N_3$ and $LiGe_2N_3$ employing custom-built high-pressure autoclaves. These Grimm-Sommerfeld

analogous nitrides are structurally related to industrially important group 13 nitrides (Al,Ga,In)N and potentially feature similar or even superior physical properties. However, material properties of these compounds are virtually unexplored and experimental data are scarcely available as yet. In this contribution, optical properties of $MgSiN_2$, $MgGeN_2$, $MnSiN_2$, $MnGeN_2$, $LiSi_2N_3$ and $LiGe_2N_3$ were examined experimentally and the results were further corroborated by DFT calculations. Besides, Bloch spectral functions were calculated using the SPRKKR formalism providing insights into electronic properties of these materials. The reported results demonstrate that these nitrides offer a wide range of attainable band gaps with manifold opportunities for band gap engineering and are thus very attractive for the design of new semiconductor materials.

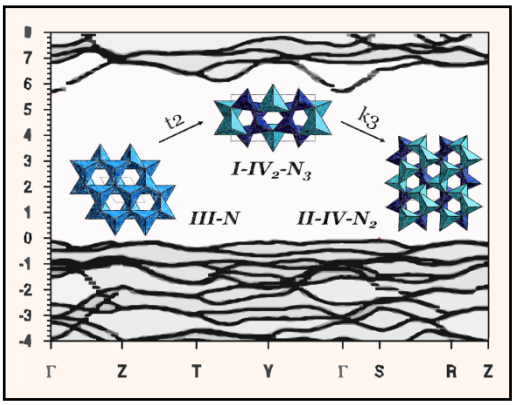

4. Ammonothermal Synthesis of Novel Nitrides: Case Study on $CaGaSiN_3$

Jonas Häusler, Lukas Neudert, Mathias Mallmann, Robin Niklaus, Anna-Carina L. Kimmel, Nicolas S. A. Alt, Eberhard Schlücker, Oliver Oeckler, and Wolfgang Schnick

Chem. Eur. J. **2017**, *23*, 2583-2590.

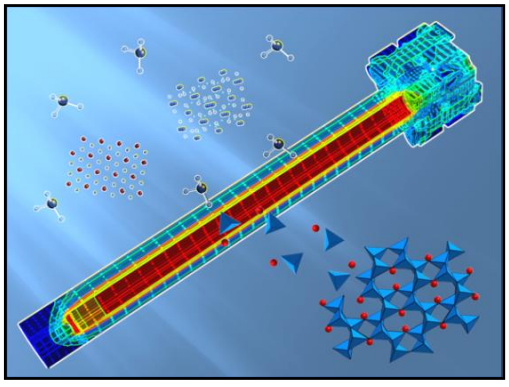

For the synthesis of $CaGaSiN_3$, new high-temperature autoclaves were developed which can be operated at pressures up to 170 MPa at a temperature of 1100 K. $CaGaSiN_3$ was synthesized from intermetallic CaGaSi and ammonobasic mineralizers $LiNH_2$ or $NaNH_2$ employing supercritical ammonia as the solvent. $CaGaSiN_3$ crystallizes in a wurtzite-derived superstructure in space group $Cmc2_1$ (a = 9.8855(11), b = 5.6595(1), c = 5.0810(1) Å, Z = 4) which was confirmed by powder X-ray diffraction and selected area electron diffraction (SAED). The structural results were further corroborated by ^{29}Si MAS-NMR and first-principle

DFT calculations. $CaGaSiN_3$ represents the first nitride comprising $(Ga,Si)N_4$-tetrahedra in its anionic framework. Eu^{2+} doped samples show red luminescence with an emission maximum of 620 nm when irradiated with UV light. Hence, the discovery of $CaGaSiN_3$:Eu^{2+} opens up new tuning opportunities of phosphors based on industrially important $(Ca,Sr)AlSiN_3$:Eu^{2+} (SCASN) type materials. The presented results demonstrate that the increase of parameter limits strongly extends the synthetic potential of the ammonothermal method further enabling the discovery of novel multinary nitrides.

5. Ammonothermal Synthesis and Crystal Structure of the Nitridoalumogermanate $Ca_{1-x}Li_xAl_{1-x}Ge_{1+x}N_3$ ($x \approx 0.2$)

Jonas Häusler, Lucien Eisenburger, Oliver Oeckler, and Wolfgang Schnick

Eur. J. Inorg. Chem. **2018**, *2018*, 759-764.

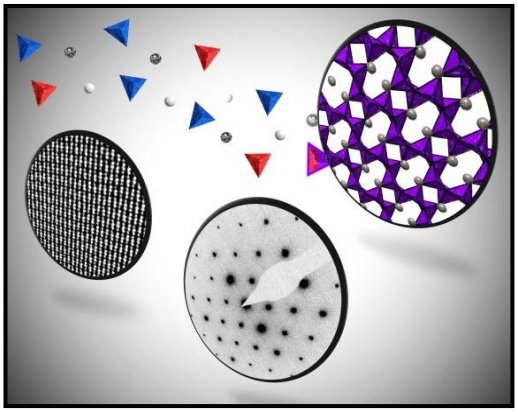

The first nitridoalumogermanate $Ca_{1-x}Li_xAl_{1-x}Ge_{1+x}N_3$ ($x \approx 0.2$) was synthesized by the ammonothermal method from intermetallic $Ca_3Al_2Ge_2$ employing Li as mineralizer. Its crystal structure was analyzed by powder X-ray diffraction, possible ordering phenomena were examined using selected area electron diffraction (SAED) and scanning transmission electron microscopy high-angle annular dark-field imaging (STEM-HAADF). $Ca_{1-x}Li_xAl_{1-x}Ge_{1+x}N_3$ ($x \approx 0.2$) crystallizes in orthorhombic space group $Cmc2_1$ (a = 9.9822(5), b = 5.7763(2), c = 5.1484(1) Å, Z = 4) and can be regarded as a solid solution of $LiGe_2N_3$ and hypothetical $CaAlGeN_3$. Needle-shaped crystals with up to 15 µm in length and well-defined morphology were obtained at a comparatively low temperature of 925 K. Besides, the band gap of $Ca_{1-x}Li_xAl_{1-x}Ge_{1+x}N_3$ ($x \approx 0.2$) was determined to be 4.3 eV at room temperature by diffuse reflectance spectroscopy. This study showed that the ammonothermal method represents a new promising approach for the synthesis of nitridogermanates with unprecedented elemental compositions. In addition, the investigations indicate that optical properties of quaternary $M^{II}M^{III}M^{IV}N_3$-type materials can be tuned by formation of solid solutions with $M^{I}M^{IV}{}_2N_3$ nitrides.

6. New perspectives for the ammonothermal synthesis and growth of ternary nitrides

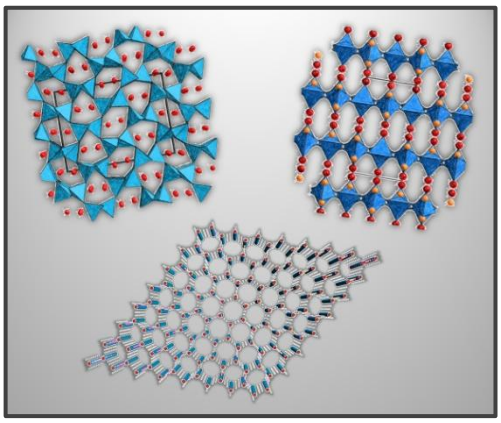

This chapter covers new important aspects for the ammonothermal synthesis and crystal growth of nitrides. The first ammonoacidic synthesis of a ternary nitride is demonstrated which entails a new virtually unexplored field within ammonothermal research. Ammonium fluoride was used as mineralizer for the ammonoacidic synthesis of $ZnGeN_2$, where custom-built liners made of hot-pressed Si_3N_4 prevented the formation of corrosion-induced byproducts. Moreover, a proof of concept for crystal growth of the ternary nitridotantalate $KTaN_2$ is presented attaining octahedron-shaped single crystals with up to 100 µm in diameter and excellent crystal morphology. Here, crystal growth is achieved via chemical transport of the mineralizer KNH_2 along with controlled supersaturation of the supercritical ammonia solution. These results are particularly promising for the development of crystal growth processes for ternary and multinary nitrides. Successful synthesis of the rare earth nitridosilicate Eu_2SiN_3 further extends the structural variety of accessible nitrides thus providing an excellent basis for future explorative ammonothermal studies.

10 Appendix

10.1 Supporting Information for Chapter 3

Jonas Häusler, Saskia Schimmel, Peter Wellmann, and Wolfgang Schnick

Chem. Eur. J. **2017**, *23*, 12275 - 12282.

Table S1. Wyckoff positions and atomic coordinates of $ZnSiN_2$ obtained by Rietveld refinement, standard deviations in parentheses

Atom	Wyckoff	*x*	*y*	*z*	SOF	U_{iso} (Å^2)
Zn	4*a*	0.4170(1)	0.1242(3)	0.0000(6)	1	0.0211(8)
Si	4*a*	0.0724(2)	0.1248(6)	0.5043(9)	1	0.0141(9)
N1	4*a*	0.0588(6)	0.0930(8)	0.1513(5)	1	0.0080(15)
N2	4*a*	0.1118(5)	0.6536(8)	0.0877(6)	1	0.0127(16)

Table S2. Wyckoff positions and atomic coordinates of $ZnGeN_2$ obtained by Rietveld refinement, standard deviations in parentheses

Atom	Wyckoff	*x*	*y*	*z*	SOF	U_{iso} (Å^2) §
Zn	4*a*	0.4183(7)	0.1173(5)	0.018(3)	1	0.0255(2)
Ge	4*a*	0.0773(6)	0.1236(5)	0.515(3)	1	0.0255(2)
N1	4*a*	0.070(3)	0.118(3)	0.148(5)	1	0.0255(2)
N2	4*a*	0.099(3)	0.641(3)	0.121(3)	1	0.0255(2)

§ Isotropic displacement parameters were refined to one common value for all four sites due to crystallite size induced overlapping of reflections

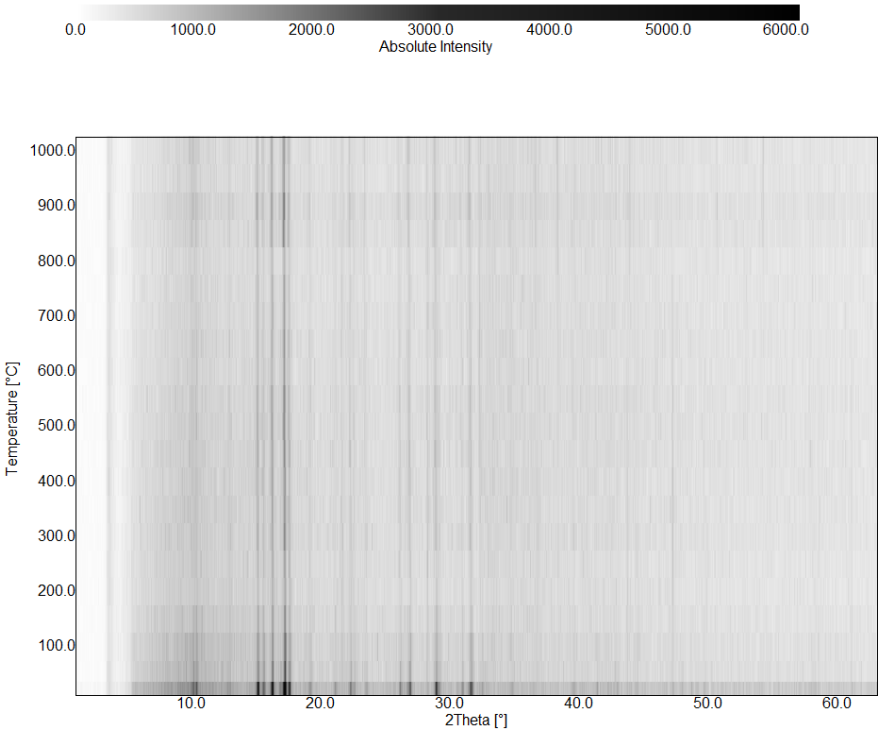

Figure S1. Temperature-programmed powder X-ray diffraction pattern of $ZnSiN_2$.

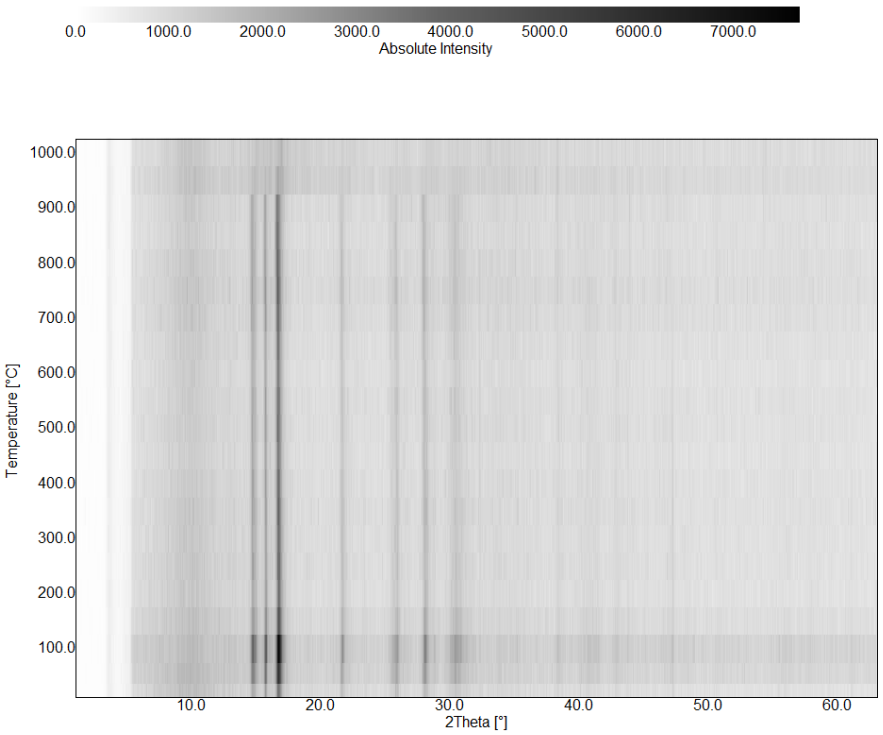

Figure S2. Temperature-programmed powder X-ray diffraction pattern of $ZnGeN_2$.

10.2 Supporting Information for Chapter 4

Jonas Häusler, Robin Niklaus, Ján Minár, and Wolfgang Schnick

Chem. Eur. J. **2018**, *24*, 1686-1693.

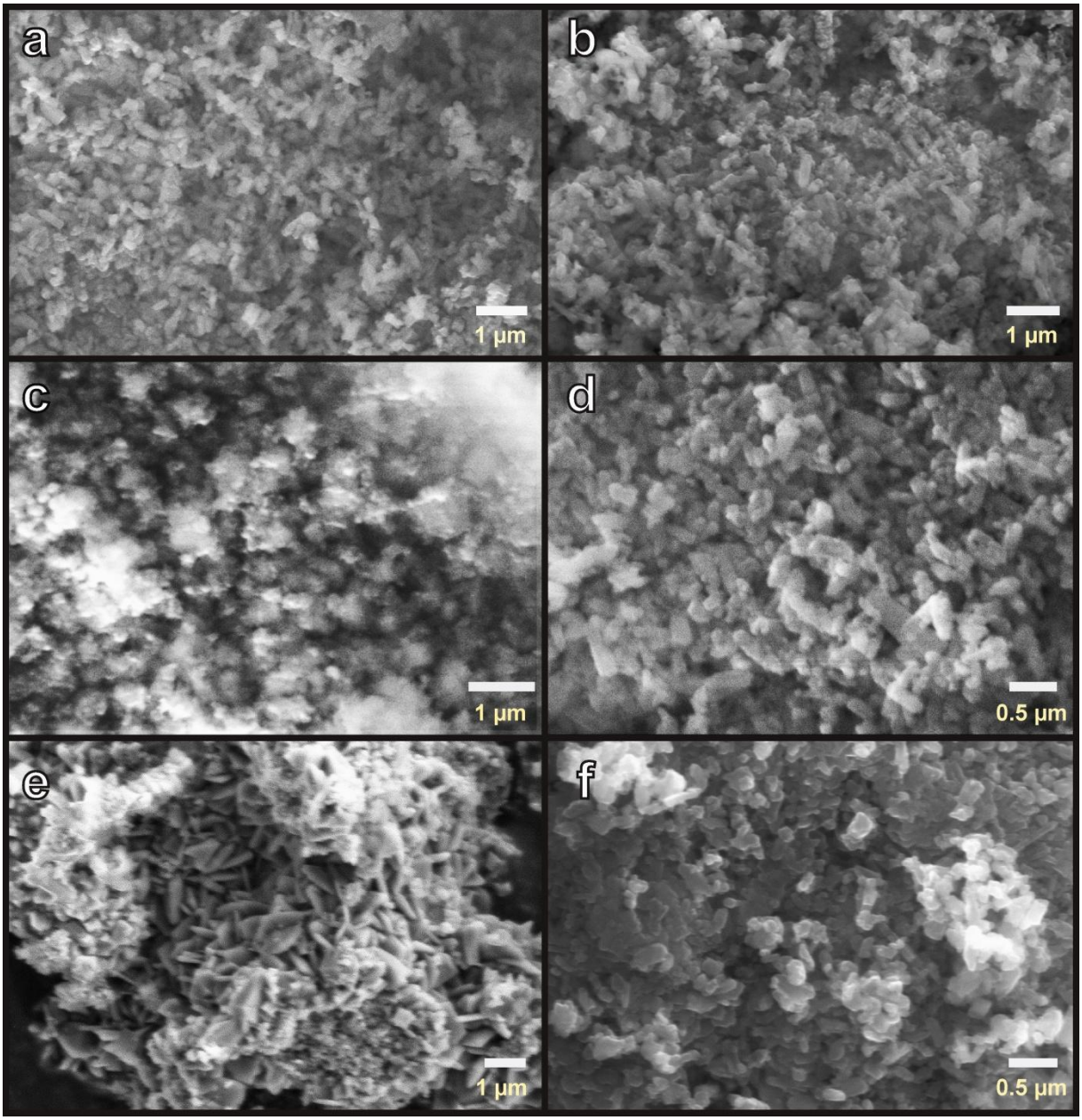

Figure S1. Scanning electron microscopy (SEM) images of $MgSiN_2$ (a), $MgGeN_2$ (b), $MnSiN_2$ (c), $MnGeN_2$ (d), $LiSi_2N_3$ (e) and $LiGe_2N_3$ (f).

Table S1. Wyckoff positions and atomic coordinates of $MgSiN_2$ obtained from Rietveld refinement, standard deviations in parentheses

Atom	Wyckoff	*x*	*y*	*z*	SOF	U_{iso} (Å^2)
Mg	4*a*	0.0861(5)	0.6192(7)	0.9945(13)	1	0.0061(3)
Si	4*a*	0.0689(4)	0.1246(6)	0.0063(11)	1	0.0061(3)
N1	4*a*	0.0530(15)	0.0894(12)	0.3634(18)	1	0.0061(3)
N2	4*a*	0.1059(12)	0.6581(10)	0.4213(18)	1	0.0061(3)

Table S2. Wyckoff positions and atomic coordinates of $MgGeN_2$ obtained from Rietveld refinement, standard deviations in parentheses

Atom	Wyckoff	*x*	*y*	*z*	SOF	U_{iso} (Å^2)
Mg	4*a*	0.0781(10)	0.6238(21)	0.0061(70)	1	0.0130(4)
Ge	4*a*	0.0745(3)	0.1255(7)	0.0063(25)	1	0.0130(4)
N1	4*a*	0.0860(25)	0.1462(23)	0.3917(29)	1	0.0130(4)
N2	4*a*	0.0849(26)	0.6521(23)	0.3988(18)	1	0.0130(4)

Table S3. Wyckoff positions and atomic coordinates of $MnSiN_2$ obtained from Rietveld refinement, standard deviations in parentheses

Atom	Wyckoff	*x*	*y*	*z*	SOF	U_{iso} (Å^2)
Mn	4*a*	0.0767(2)	0.6233(4)	0.9966(8)	1	0.0027(2)
Si	4*a*	0.0686(4)	0.1235(8)	0.9949(15)	1	0.0027(2)
N1	4*a*	0.1151(8)	0.6600(10)	0.4165(13)	1	0.0027(2)
N2	4*a*	0.0526(10)	0.0885(11)	0.3489(8)	1	0.0027(2)

Table S4. Wyckoff positions and atomic coordinates of $MnGeN_2$ obtained from Rietveld refinement, standard deviations in parentheses

Atom	Wyckoff	*x*	*y*	*z*	SOF	U_{iso} (Å^2)
Mn	4*a*	0.0786(6)	0.6245(16)	0.9867(24)	1	0.0101(3)
Ge	4*a*	0.0721(4)	0.1255(11)	0.9889(26)	1	0.0101(3)
N1	4*a*	0.0628(25)	0.1031(31)	0.3529(37)	1	0.0101(3)
N2	4*a*	0.1064(22)	0.6258(38)	0.3933(24)	1	0.0101(3)

Table S5. Wyckoff positions and atomic coordinates of $LiSi_2N_3$ obtained from Rietveld refinement, standard deviations in parentheses

Atom	Wyckoff	*x*	*y*	*z*	SOF	U_{iso} (Å^2)
Li	4*a*	0	0.3500(31)	0.9945(29)	1	0.0037(3)
Si	8*b*	0.1662(2)	0.8369(4)	0.0251(36)	1	0.0037(3)
N1	8*b*	0.1978(5)	0.8617(12)	0.3899(6)	1	0.0037(3)
N2	4*a*	0	0.2743(11)	0.4488(11)	1	0.0037(3)

Table S6. Wyckoff positions and atomic coordinates of $LiGe_2N_3$ obtained from Rietveld refinement, standard deviations in parentheses

Atom	Wyckoff	*x*	*y*	*z*	SOF	U_{iso} (Å^2)
Li	4*a*	0	0.336(9)	0.979(32)	1	0.0087(3)
Ge	8*b*	0.1657(3)	0.8280(5)	0.9795(1)	1	0.0087(3)
N1	8*b*	0.1883(13)	0.8216(33)	0.3452(14)	1	0.0087(3)
N2	4*a*	0	0.2940(30)	0.3873(18)	1	0.0087(3)

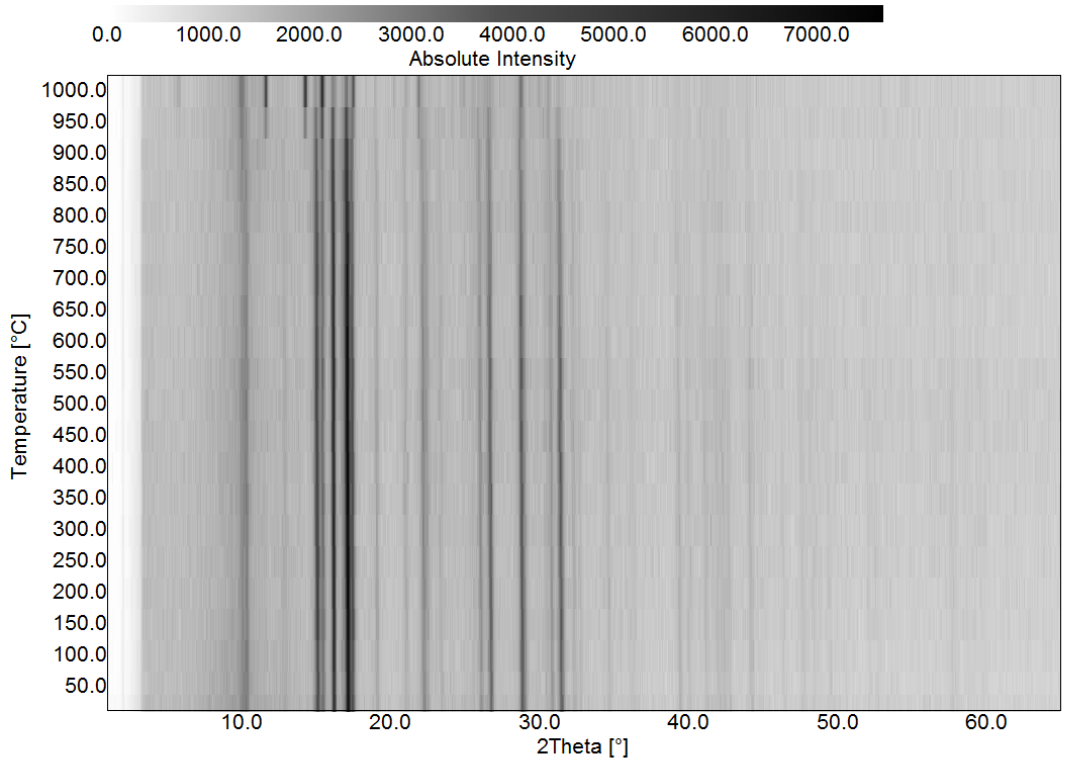

Figure S2. Temperature-programmed powder X-ray diffraction pattern of $MgSiN_2$.

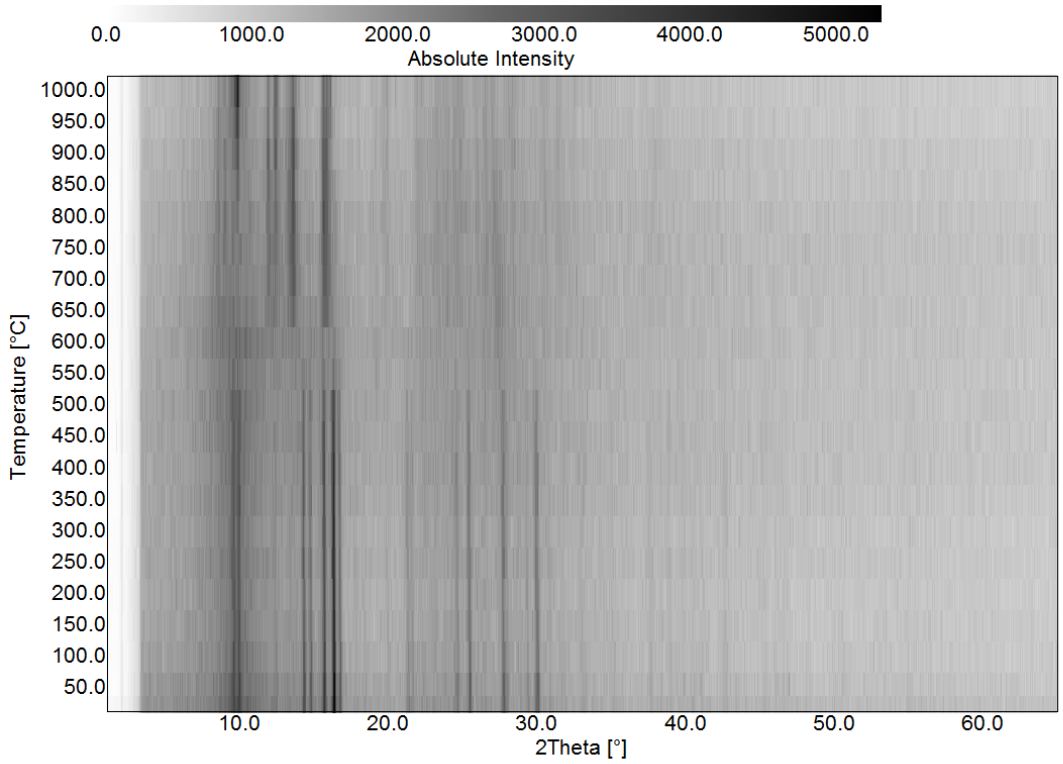

Figure S3. Temperature-programmed powder X-ray diffraction pattern of $MgGeN_2$.

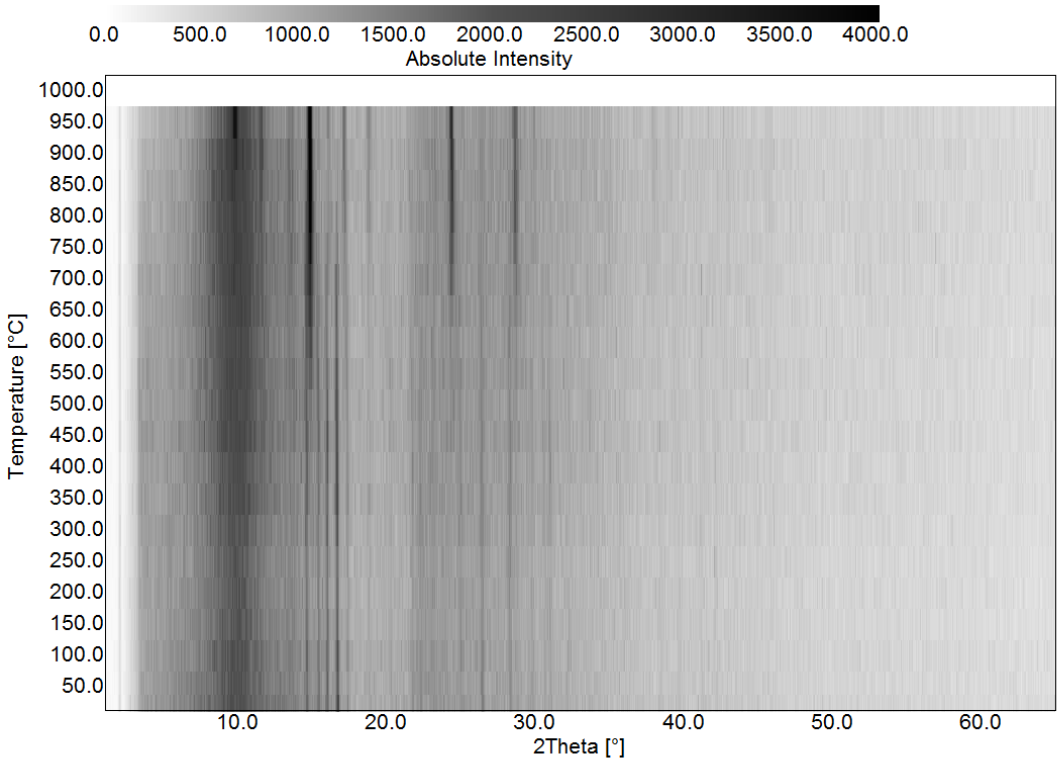

Figure S4. Temperature-programmed powder X-ray diffraction pattern of $MnSiN_2$.

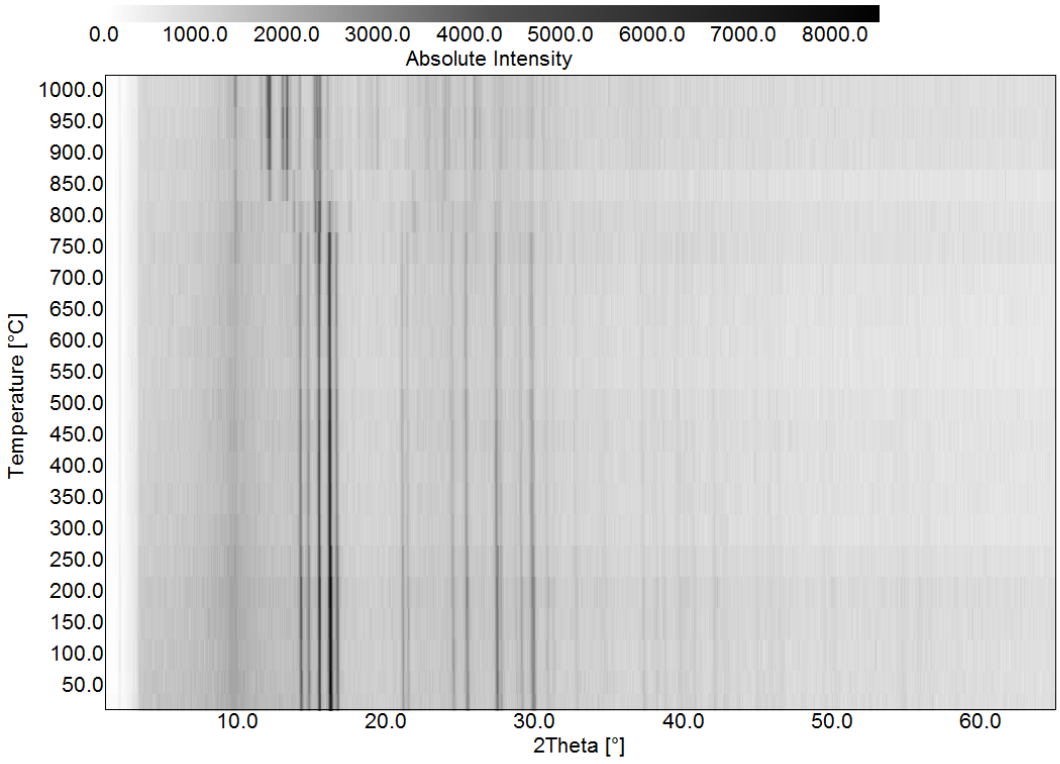

Figure S5. Temperature-programmed powder X-ray diffraction pattern of $MnGeN_2$.

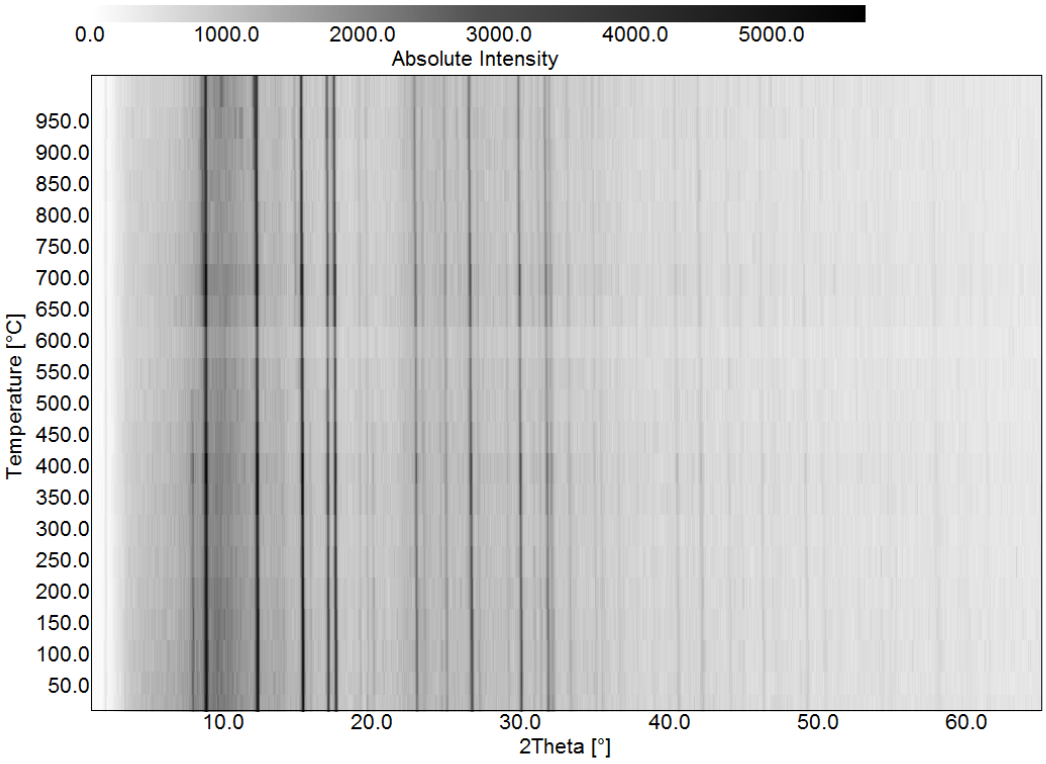

Figure S6. Temperature-programmed powder X-ray diffraction pattern of $LiSi_2N_3$.

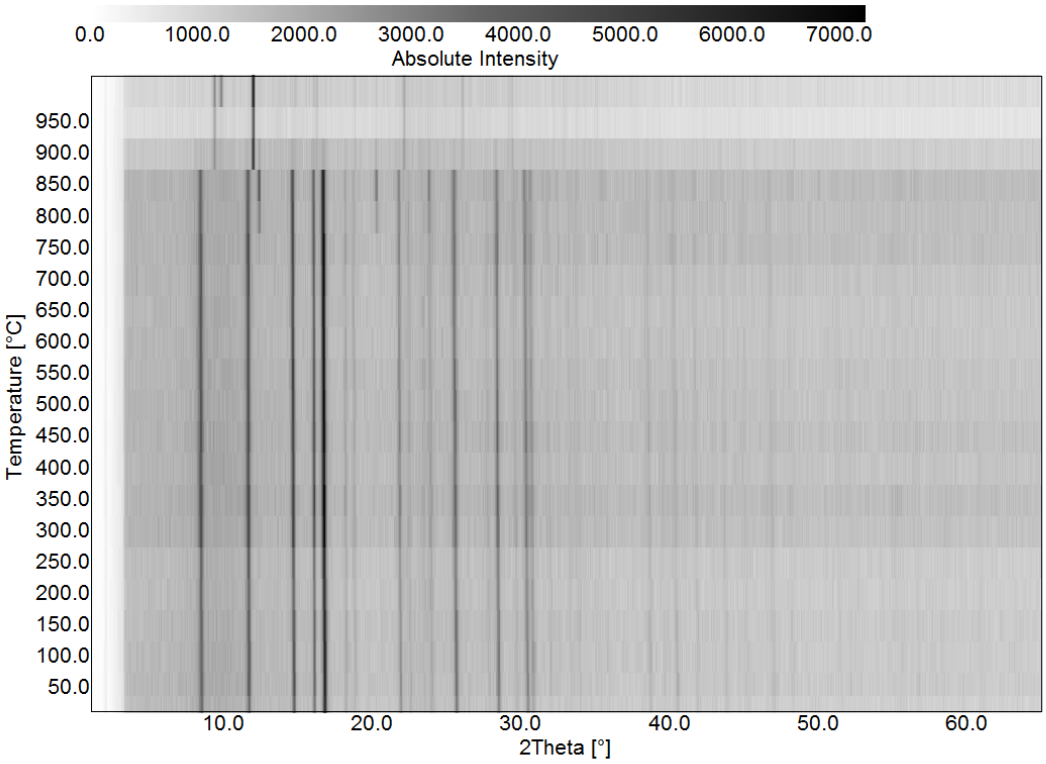

Figure S7. Temperature-programmed powder X-ray diffraction pattern of $LiGe_2N_3$.

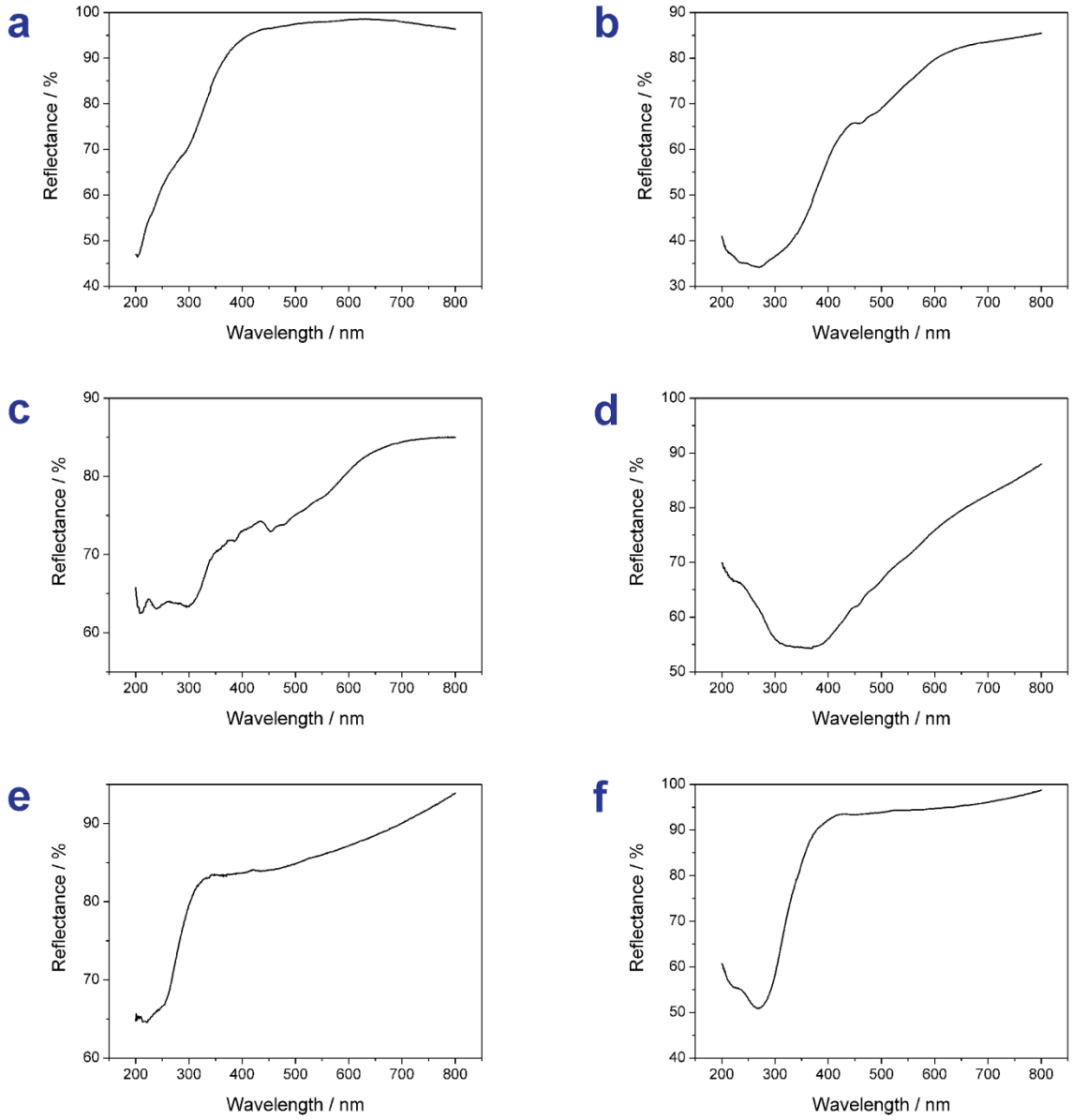

Figure S8. Diffuse reflectance spectra of $MgSiN_2$ (a), $MgGeN_2$ (b), $MnSiN_2$ (c), $MnGeN_2$ (d), $LiSi_2N_3$ (e) and $LiGe_2N_3$ (f).

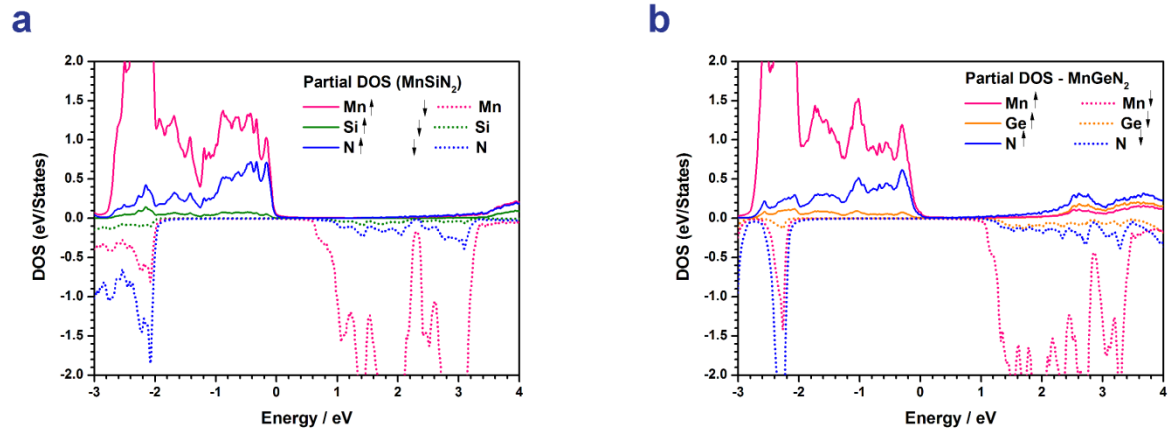

Figure S9. Enlarged section of total and atom resolved DOS of $MnSiN_2$ (a) and $MnGeN_2$ (b) within the SPRKKR formalism.

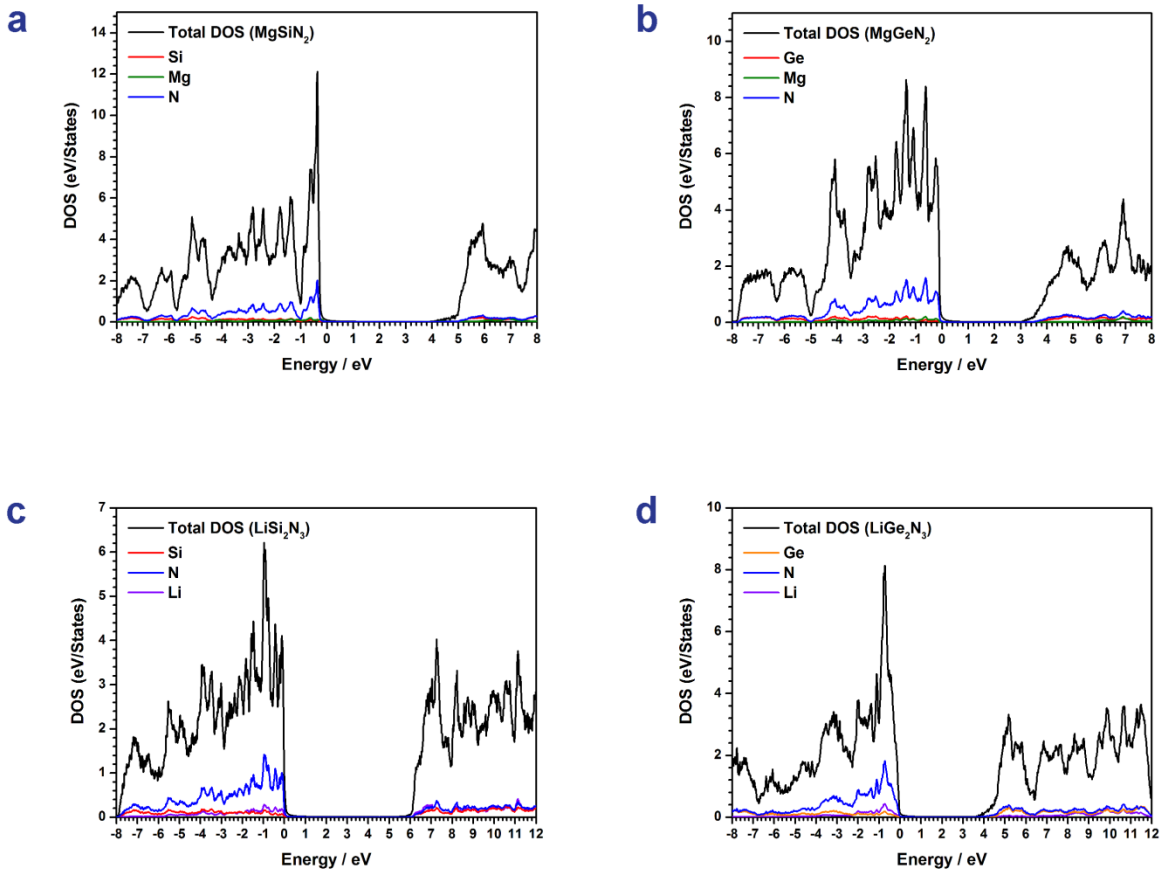

Figure S10. Total and atom resolved DOS of $MgSiN_2$ (a), $MgGeN_2$ (b), $LiSi_2N_3$ (c) and $LiGe_2N_3$ (d) within the SPRKKR formalism.

10.3 Supporting Information for Chapter 5

Jonas Häusler, Lukas Neudert, Mathias Mallmann, Robin Niklaus, Anna-Carina L. Kimmel, Nicolas S. A. Alt, Eberhard Schlücker, Oliver Oeckler, and Wolfgang Schnick

Chem. Eur. J. **2017**, *23*, 2583–2590.

Table S1. Wyckoff positions and atomic coordinates of $CaGaSiN_3:Eu^{2+}$ obtained by Rietveld refinement, standard deviations in parentheses

Atom	Wyckoff	*x*	*y*	*z*	SOF	B_{iso} (Å^2) [§]
Ca	4a	0	0.313(2)	0.473(8)	0.99	1
Eu	4a	0	0.313(2)	0.473(8)	0.01	1
Ga	8b	0.171(1)	0.161(1)	0.014(8)	0.5	1
Si	8b	0.171(1)	0.161(1)	0.014(8)	0.5	1
N1	8b	0.200(2)	0.114(4)	0.388(8)	1	1
N2	4a	0	0.234(5)	0	1	1

[§] Isotropic displacement parameters were fixed during the Rietveld refinement

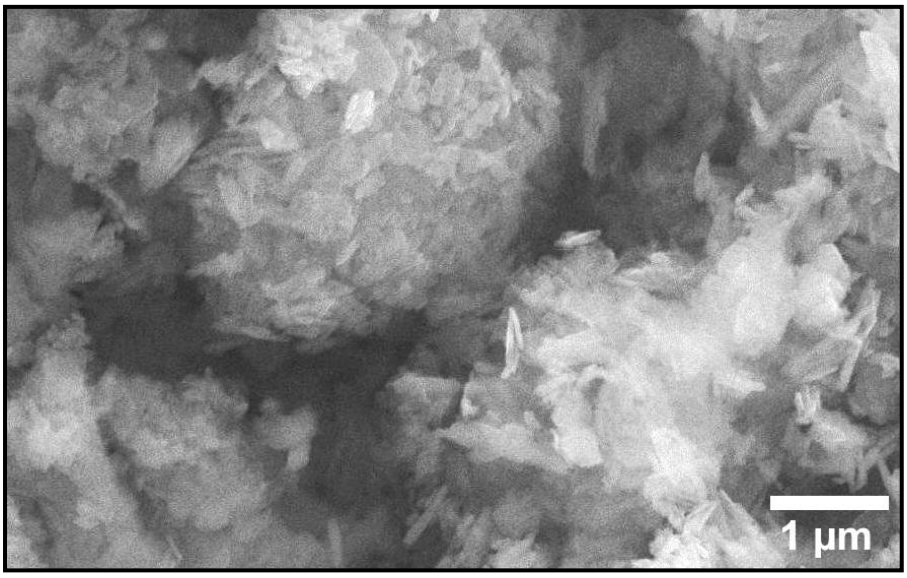

Figure S1. SEM image of plate- and needle-shaped crystallites of $CaGaSiN_3$.

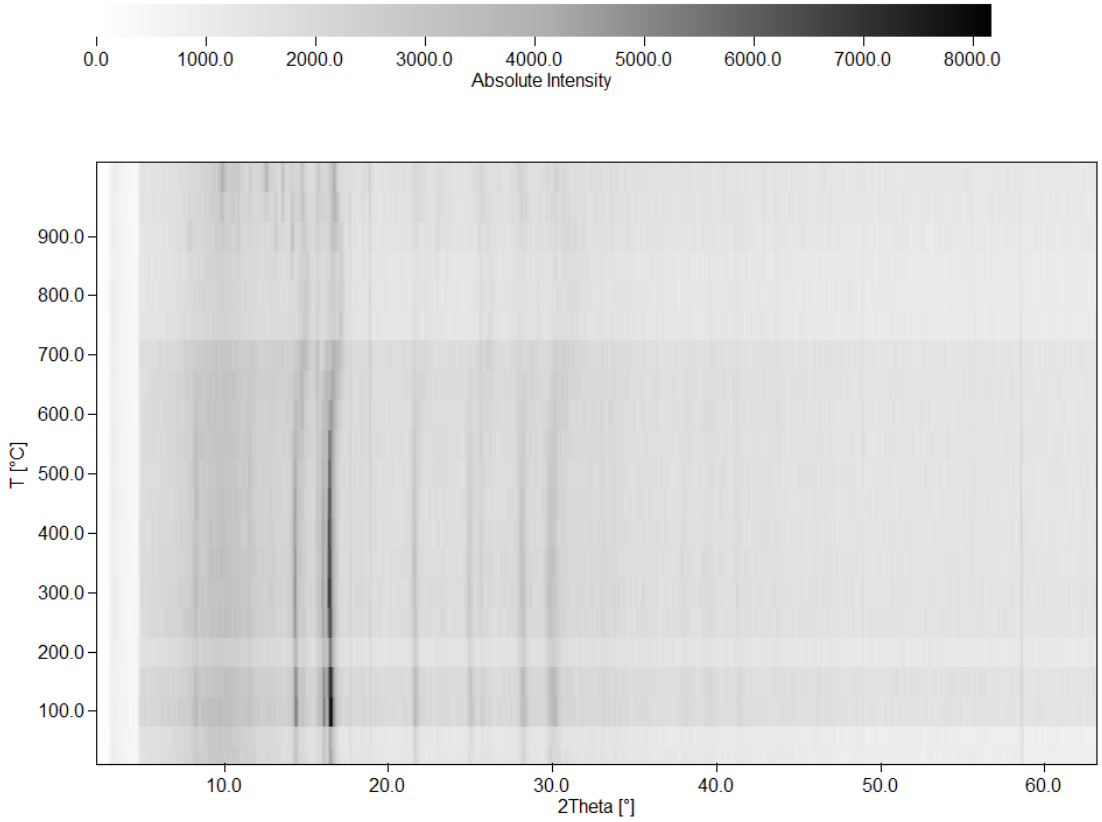

Figure S2. Temperature-dependent powder X-ray diffraction pattern.

10.4 Supporting Information for Chapter 6

Jonas Häusler, Lucien Eisenburger, Oliver Oeckler, and Wolfgang Schnick

Eur. J. Inorg. Chem. **2018**, *2018*, 759-764.

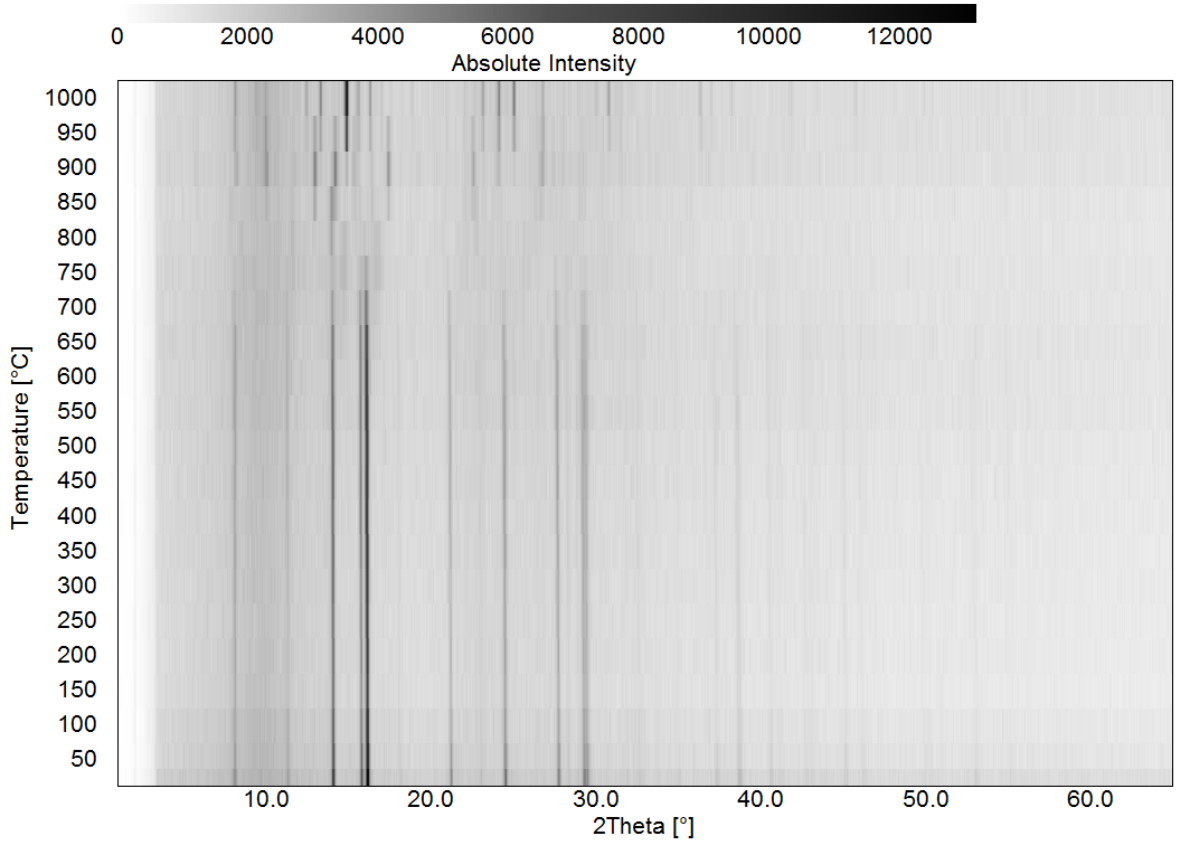

Figure S1. Temperature-programmed powder X-ray diffraction pattern of $Ca_{1-x}Li_xAl_{1-x}Ge_{1+x}N_3$ ($x \approx 0.2$).

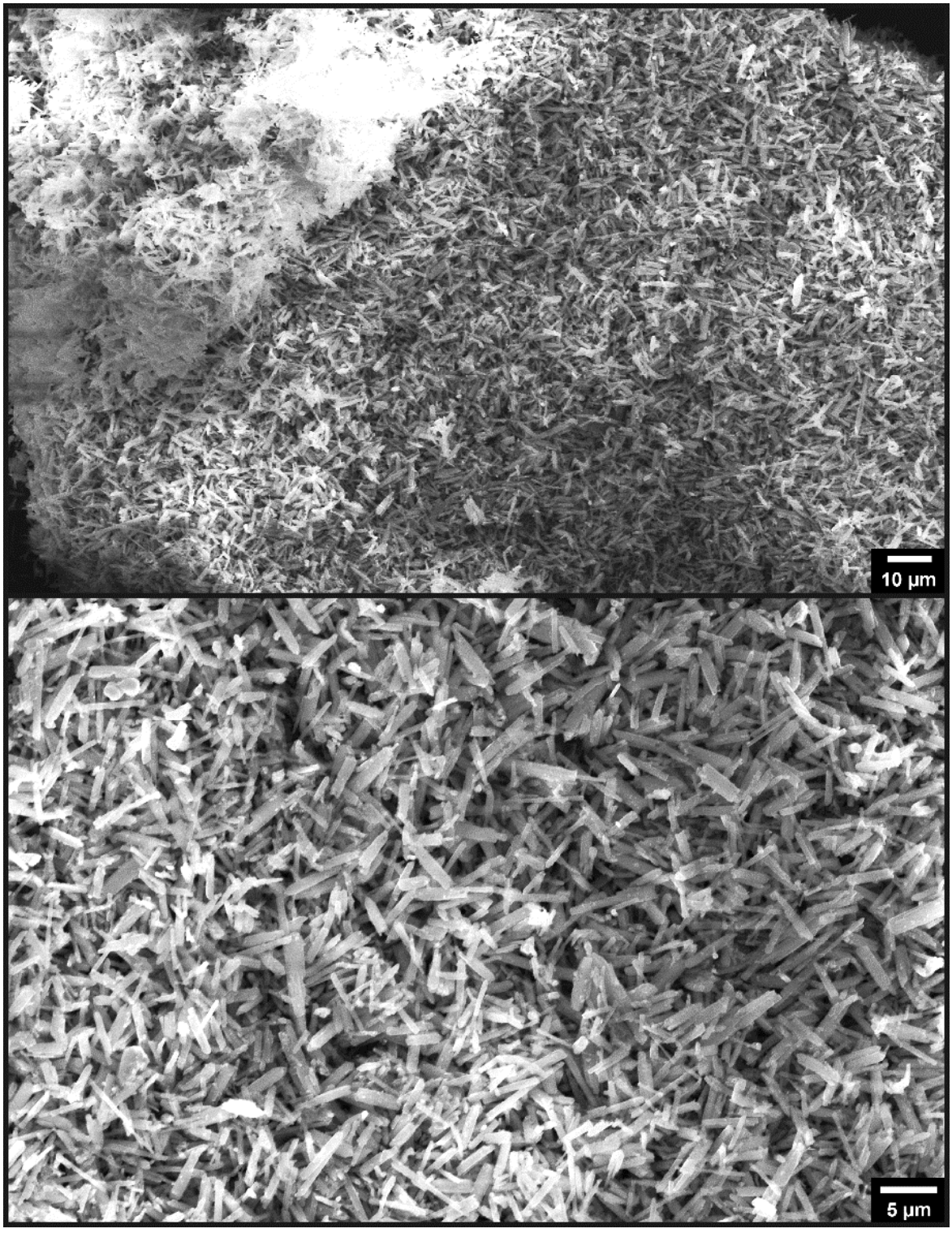

Figure S2. Scanning electron microscopy (SEM) secondary electron (SE) images of $Ca_{1-x}Li_xAl_{1-x}Ge_{1+x}N_3$.

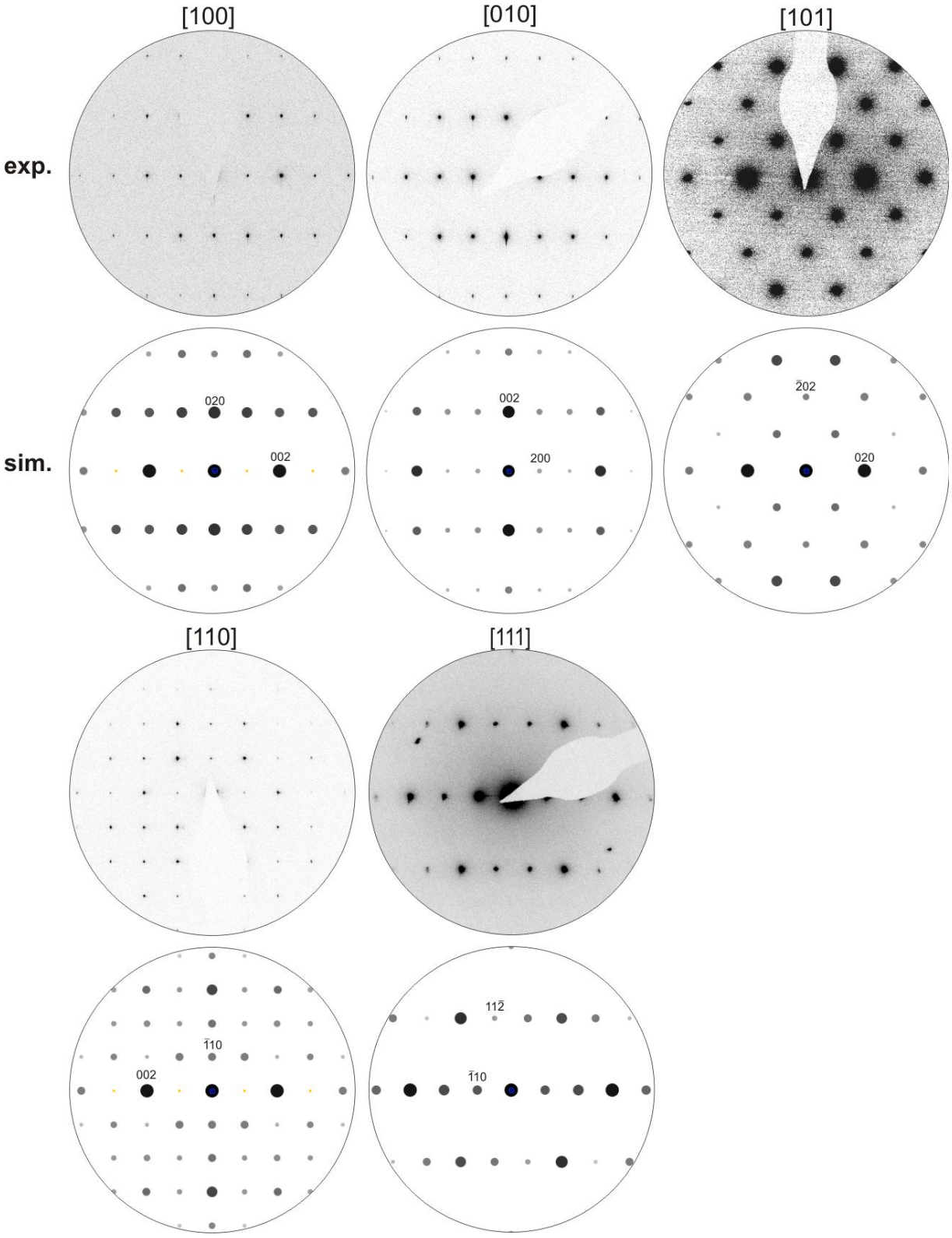

Figure S3. SAED patterns of $Ca_{1-x}Li_xAl_{1-x}Ge_{1+x}N_3$ with corresponding simulated patterns. Yellow reflections in simulations correspond to kinematically forbidden reflections.

11 Publications

11.1 List of publications within this thesis

1. **Ammonothermal Synthesis of Nitrides: Recent Developments and Future Perspectives**
   Jonas Häusler, and Wolfgang Schnick
   Chem. Eur. J. **2018**, DOI: 10.1002/chem.201800115

   Conceptualization of this review-type article, literature screening, writing of the manuscript and creation of graphical material was carried out by Jonas Häusler. Wolfgang Schnick revised the manuscript and supervised the research project.

2. **Ammonothermal Synthesis of Earth-abundant Nitride Semiconductors $ZnSiN_2$ and $ZnGeN_2$ and Dissolution Monitoring by In Situ X-ray Imaging**
   Jonas Häusler, Saskia Schimmel, Peter Wellmann, and Wolfgang Schnick
   Chem. Eur. J. **2017**, *23*, 12275-12282.

   For this contribution, ammonothermal syntheses, structure elucidation from powder X-ray diffraction data, Rietveld refinements, diffuse reflectance spectroscopy, band gap determination, literature research, writing of the main part of the manuscript, supporting dissolution experiments and sample preparation for in situ experiments were carried out by Jonas Häusler. In situ X-ray imaging, evaluation and discussion of the obtained data was done by Saskia Schimmel. Graphical material was created by Jonas Häusler and Saskia Schimmel. Peter Wellmann supervised the in situ experiments and Wolfgang Schnick directed and supervised the research project. All authors revised the manuscript.

3. Ammonothermal Synthesis and Optical Properties of Ternary Nitride Semiconductors Mg-IV-N_2, Mn-IV-N_2 and Li-IV_2-N_3 (IV = Si, Ge)

Jonas Häusler, Robin Niklaus, Ján Minár, and Wolfgang Schnick

Chem. Eur. J. **2018**, *24*, 1686-1693.

Literature screening, writing of the main part of the manuscript, sample synthesis, powder X-ray diffraction analyses, Rietveld refinements, spectroscopic measurements and band gap determination were carried out by Jonas Häusler. DFT calculations and evaluation of the data were done by Robin Niklaus under the supervision of Ján Minár. Graphical material was created by Jonas Häusler and Robin Niklaus. Wolfgang Schnick directed and supervised the work. All authors revised the manuscript.

4. Ammonothermal Synthesis of Novel Nitrides: Case Study on $CaGaSiN_3$

Jonas Häusler, Lukas Neudert, Mathias Mallmann, Robin Niklaus, Anna-Carina L. Kimmel, Nicolas S. A. Alt, Eberhard Schlücker, Oliver Oeckler, and Wolfgang Schnick

Chem. Eur. J. **2017**, *23*, 2583-2590.

For this article, literature research, writing of the major part of the manuscript, powder X-ray diffraction analyses, Rietveld refinements, luminescence measurements and evaluation of NMR data were carried out by Jonas Häusler. Sample syntheses and synthesis optimization was performed by Jonas Häusler and Mathias Mallmann. TEM investigations were carried out by Lukas Neudert under the supervision of Oliver Oeckler. Elucidation of the TEM data was performed by Lukas Neudert and Oliver Oeckler. Construction of ordered structure models and DFT calculations were done by Robin Niklaus. In close collaboration, Anna-Carina L. Kimmel developed new high-temperature autoclaves for syntheses up to 1070 K under the supervision of Nicolas S. A. Alt and Eberhard Schlücker. Wolfgang Schnick directed and supervised the research project. All authors revised the manuscript.

5. **Ammonothermal Synthesis and Crystal Structure of the Nitridoalumogermanate $Ca_{1-x}Li_xAl_{1-x}Ge_{1+x}N_3$ ($x \approx 0.2$)**
   Jonas Häusler, Lucien Eisenburger, Oliver Oeckler, and Wolfgang Schnick
   Eur. J. Inorg. Chem. **2018**, *2018*, 759-764.

   For this publication, preparation of intermetallic precursors, ammonothermal syntheses, powder X-ray diffraction analyses, Rietveld refinements, diffuse reflectance spectroscopy, writing the main part of the manuscript and literature research was performed by Jonas Häusler. TEM investigations were carried out by Lucien Eisenburger under the supervision of Oliver Oeckler. Elucidation of the TEM data was done by Lucien Eisenburger and Oliver Oeckler. Graphical material was created by Jonas Häusler and Lucien Eisenburger. Wolfgang Schnick directed and supervised the research project. All authors revised the manuscript.

11.2 Other publications

1. **Ammonothermal Synthesis of Novel Nitrides: Case Study on $CaGaSiN_3$ (Cover Picture)**
   Jonas Häusler, Lukas Neudert, Mathias Mallmann, Robin Niklaus, Anna-Carina L. Kimmel, Nicolas S. A. Alt, Eberhard Schlücker, Oliver Oeckler, and Wolfgang Schnick
   Chem. Eur. J. **2017**, *23*, 2479.

2. **Ammonothermal Synthesis of Alkali-Alkaline Earth Metal and Alkali-Rare Earth Metal Carbodiimides: $K_{5-x}M_x(CN_2)_{2+x}(HCN_2)_{1-x}$ (M = Sr, Eu) and $Na_{4.32}Sr_{0.68}(CN_2)_{2.68}(HCN_2)_{0.32}$**
   Mathias Mallmann, Jonas Häusler, Niklas Cordes, and Wolfgang Schnick
   Z. Anorg. Allg. Chem. **2017**, *643*, 1956-1961.

3. **First-principle and Experimental Characterization of the Electronic Properties of $CaGaSiN_3$ and $CaAlSiN_3$: The Impact of Chemical Disorder**
   Robin Niklaus, Ján Minár, Jonas Häusler, and Wolfgang Schnick
   Phys. Chem. Chem. Phys. **2017**, *19*, 9292-9299.

4. **Aggregated Molecular Fluorophores in the Ammonothermal Synthesis of Carbon Dots**
   Claas J. Reckmeier, Julian Schneider, Yuan Xiong, Jonas Häusler, Peter Kasák, Wolfgang Schnick, and Andrey L. Rogach
   Chem. Mater. **2017**, *29*, 10352-10361.

5. **The Existence of Tricyanomethane**
   Theresa Soltner, Jonas Häusler, and Andreas J. Kornath
   Angew. Chem. **2015**, *127*, 13979-13980; *Angew. Chem. Int. Ed.* **2015**, *54*, 13775-13776.

6. **Insight into the core-shell structures of Cu-In-S microspheres**
   Angela S. Wochnik, Anna Frank, Christoph Heinzl, Jonas Häusler, Julian Schneider, Ramona Hoffmann, Sonja Matich, Christina Scheu
   Solid State Sci. **2013**, *26*, 23-30.

11.3 Conference Contributions

1. **Ammonothermal method and metathesis reactions for the synthesis of binary and multinary nitrides (talk)**
   Jonas Häusler, and Wolfgang Schnick
   1. Obergurgl-Seminar für Festkörperchemie, Obergurgl (Austria), January 28 - 31, 2014.

2. **New insights into the ammonothermal synthesis of ternary and quaternary nitrides (poster presentation)**
   David Schmidl, Jonas Häusler, and Wolfgang Schnick
   Undergraduate Research Conference on Molecular Sciences (URCUP), Kloster Irsee (Germany), July 2 - 3, 2016.

3. **Band Gap and Electronic Structure of $Zn(Ge,Si)N_2$: Probing Defects Using XEOL (poster presentation)**
   Tristan de Boer, Philipp Strobel, Jonas Häusler, Wolfgang Schnick, and Alexander Moewes
   Advanced Light Source (ALS) User Meeting, Berkeley, California (USA), October 2 - 4, 2017.

4. **Cation disorder in $Ca_{1-x}Li_xAl_{1-x}Ge_{1+x}N_3$ ($x \approx 0.2$) by STEM-HAADF (talk)**
   Lucien Eisenburger, Jonas Häusler, Wolfgang Schnick, and Oliver Oeckler
   26th Annual Meeting of the German Crystallographic Society (DGK), Essen, Germany, March 5 - 8, 2018.

11.4 Deposited Crystallographic Data

Crystallographic data (CIF) of investigated compounds were deposited at the Fachinformationszentrum (FIZ) Karlsruhe, 76344 Eggenstein-Leopoldshafen, Germany (fax: +49-7247-808-666, e-mail: crysdata@fizkarlsruhe.de) and are available on quoting the following CSD depository numbers.

Compound	**CSD-Number**
$ZnSiN_2$	CSD-432701
$ZnGeN_2$	CSD-432702
$MgSiN_2$	CSD-433631
$MgGeN_2$	CSD-433632
$MnSiN_2$	CSD-433633
$MnGeN_2$	CSD-433634
$LiSi_2N_3$	CSD-433635
$LiGe_2N_3$	CSD-433636
$CaGaSiN_3:Eu^{2+}$	CSD-432259
$Ca_{1-x}Li_xAl_{1-x}Ge_{1+x}N_3$ ($x \approx 0.2$)	CSD-433751